Investigating the circulation of Southern Ocean deep water masses over the last 1.5 million years by geochemical fingerprinting of marine sediments

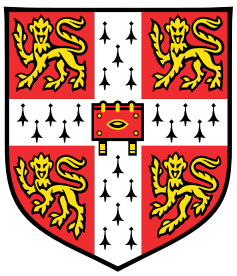

Thomas John Williams

Department of Earth Sciences and British Antarctic Survey
University of Cambridge

This dissertation is submitted for the degree of
Doctor of Philosophy

February 2018

Chris Cornell
1964 - 2017

Declaration

I hereby declare that except where specific reference is made to the work of others, the contents of this dissertation are original and have not been submitted in whole or in part for consideration for any other degree or qualification in this, or any other university. This dissertation is my own work and contains nothing which is the outcome of work done in collaboration with others, except as specified in the text and Acknowledgements. This dissertation contains fewer than 225 pages including appendices, bibliography, figures, tables and equations and fewer than 50 additional pages of data tables.

Thomas John Williams
February 2018

Acknowledgements

I am very grateful for the help and support offered by my supervisors, CD Hillenbrand, Alex Piotrowski and Claire Allen, who throughout my PhD have provided me with direction and support. Special thanks are reserved for CD, who first took me on as part a three-month contract back in January of 2012, and without whose guidance and patience across the last six years, this work would not have been possible.

I also owe a debt of gratitude to the members of Alex's lab group during my time in Cambridge: Natalie Roberts, Jake Howe, Rong Hu, Jo Clegg, Vicky Black, Yuting Li and Christina Larkin. Natalie, Jo, Jake and Rong were always on hand to provide assistance during my time in the department, and I will forever be grateful for their help. I would also like to thank Luke Skinner and Eric Wolff for providing guidance as academic friends, as well as the wider community of PhD students, postgraduates, lecturers, professors and support staff within the department who throughout my time there have helped foster scientific interests far beyond the immediate realm of this thesis. Special thanks are given to Jun Aizawa for help with computing throughout my PhD, and to Sarah Humbert for aid in all things bibliothèque.

I extend my thanks to the shipboard party of JR179, who collected core PC493, and to CD for providing data from the core for my PhD. I wish to thank Prof. Bob Anderson for aid in acquiring samples from cores NBP9802-04PC1 and NBP902-04PC1, and for helpful discussion of the data produced from these cores. Thanks are also extended to the core repository at the Lamont Doherty Earth Observatory for providing samples from cores NBP9802-04PC1 and NBP9802-06PC1, and the International Ocean Discovery Program's Kochi Core Centre for providing samples from Ocean Drilling Program Leg 121 Site 758. Processing of these samples was greatly helped by the assistance of Simon Crowhurst and everybody in the sedimentary laboratory, and Jason Day, Vicky Black, Sambuddha Misra and Ed Tipper are thanked for the assistance in running the mass spectrometers; Vicky and Sambuddha are especially thanked for giving up their time (often in the small hours of the morning) to provide assistance running the Neptune. Jason Day is thanked for analysing REE and Nd concentration samples on the Quadrapole ICPMS.

This work was funded through a NERC PhD studentship awarded to BAS. Additional funding for this project has been provided by two grants from the Trans Antarctic Association, and radiocarbon data collected as part of this thesis were funded by NERC and measured at the 14C Chrono Centre at Queens University, Belfast. The crew and scientific party aboard JR298 are thanked for making my time spent aboard the James Clerk Ross in the Southern Ocean a truly once in a lifetime experience, as are BAS for funding my place on the cruise.

I would like to thank the friends I have made at BAS and the Department of Earth Sciences, who are far too numerous to name individually but who have made my time in Cambridge special, and Kathy, whose love and support kept me sane and grounded throughout the writing of this thesis. Finally, I wish to thank my family: my brother Matt and my parents Gill and Dave, who have provided me with encouragement and support throughout.

Abstract

The Southern Ocean (SO) is a critical component in the global ocean conveyor. As the only conduit linking the Atlantic, Indian and Pacific Oceans, as well as an important region of upwelling and water mass formation, it is thought to have played a key role in modulating Earth's past climate. Changes in the circulation of SO deep and bottom waters over the last 1.5 million years are investigated using stable carbon isotope ($\delta^{13}C$) measurements made on the tests of the benthic foraminfer *Cibiciodes* ($\delta^{13}C_b$), and the rare earth element concentrations and Neodmium isotope (ε_{Nd}) values of marine sediments and their authigenic ferromanganese coatings. Being a proxy for past seawater nutrient contents, $\delta^{13}C_b$ provides important insights into both past ocean circulation and the potential storage of remineralised organic carbon within the deep ocean, while simultaneously providing information on the past ventilation state of the deep ocean interior. As seawater ε_{Nd} remains unaffected by biological fractionation or air-sea exchange processes, reconstructions of past deep and bottom water ε_{Nd} provides a tool with which to study past changes in the circulation and mixing of these water masses.

A suite of previously published late Holocene (0-6 ka) and Last Glacial Maximum (LGM; 18-24 ka) $\delta^{13}C_b$ data are used alongside newly acquired $\delta^{13}C_b$ data from the Amundsen Sea in the eastern Pacific sector of the SO to investigate past changes in the pattern of circum-Antarctic seawater carbon isotope composition. The $\delta^{13}C$ signature of deep and bottom waters was much more heterogenous during the LGM than the late Holocene, with negative $\delta^{13}C$ excursions occurring within the Atlantic and Indian sectors of the SO below c. 2-3 km water depth. Some of this negative $\delta^{13}C$ signal was advected through the SO to the Pacific sector, but this appears to have been restricted by bathymetric barriers within the SO.

$\delta^{13}C_b$ data spanning the last 800 ka from the Amundsen Sea show that bottom waters formed in the Pacific sector of the SO remained relatively enriched in 13C throughout this interval, compared with the negative $\delta^{13}C$ values observed in bottom waters from the Atlantic sector during past glacial periods. These data suggest differing modes of bottom water formation in the Atlantic vs Pacific sectors of the SO during glacial periods of the last 800 ka.

An authigenic ε_{Nd} record measured on sediments from a core located in the deep Indian Ocean is used to investigate the palaeocirculation history of modified Circumpolar Deep Water (mCDW) within the Indian Ocean during the last 1.5 million years. Shifts towards more radiogenic ε_{Nd} values during glacial periods are interpreted as reflecting a decreased entrainment of deep waters sourced in the North Atlantic (Northern Component Water, NCW) within CDW, which led to a reduced advection of an unradiogenic ε_{Nd} NCW signal to the core site. During the early stages of the Mid Pleistocene Transition (c. 1086-931 ka), a prolonged strengthening of this NCW signal is observed during glacial periods, which was followed by a weakening during Marine Isotope Stages 22-24, between c. 931 and 866 ka. Mixing calculations suggest that the advection of this NCW ε_{Nd} signature into the Indian Ocean during interglacials increased around 866 ka relative the interval between 1500-866 ka. I hypothesis that this represents an increase in the strength of global thermohaline circulation during interglacial periods after 866 ka.

ε_{Nd} and REE measurements made on sediments from two cores located on the Pacific-Antarctic Ridge in the western Pacific sector of the SO (to the north of the Ross Sea Embayment) are used to reconstruct the bottom water palaeocirculation in this region across the last 540 ka. The proportion and ε_{Nd} signature of Ross Sea Bottom Water (RSBW) bathing these core sites has fluctuated throughout the last 540 ka. These fluctuations do not follow the classical 'saw-tooth' pattern of glacial-interglacial cyclicity, but in general show shifts towards more radiogenic values during interglacials. Prior to the Holocene (11.5-0 ka), RSBW ε_{Nd} end member values were at least as radiogenic as c. -5.5 to -2.5 ε_{Nd}, compared with c. -6.5 ε_{Nd} today. Past changes in the production and ε_{Nd} end member values of RSBW are linked to changes in the extent of grounded and floating ice within the Ross Sea Embayment. These changes affected the rate and location of bottom water formation within the Ross Sea, and the supply of terrigenous material with radiogenic ε_{Nd} values, which has isotopically 'labelled' RSBW.

Table of contents

List of figures **xv**

List of tables **xix**

1 Introduction **1**
1.1 Quaternary palaeoclimate 1
1.2 Modern global ocean circulation 4
1.3 Southern Ocean circulation and water masses 5
1.4 Reconstructing past ocean circulation 8
1.4.1 Stable carbon isotopes 9
1.4.2 Neodymium isotopes 11
1.5 Thesis outline and objectives 14

2 Methods **17**
2.1 Core locations and typical sedimentary compositions analysed 17
2.2 Neodymium Isotope, minor and REE analyses 19
2.2.1 Sample processing for elemental separation 19
2.2.1.1 Processing of planktic foraminifera samples 19
2.2.1.2 Sediment and siliceous microfossil leachates 21
2.2.1.3 Detrital sediments 22
2.2.2 Column Chromatography 23
2.2.3 Analyses of minor and rare earth element concentrations 23
2.2.4 Neodymium isotopic analyses: Neptune Plus Multi-Collector ICP-MS 24
2.3 Stable oxygen and carbon isotope analyses on planktic and benthic foraminifera tests 27
2.4 Additional sedimentological, geochemical and palaeo magnetic analyses on core PC493 28

3 Late Quaternary stable carbon isotopes of Lower Circumpolar Deep Water (LCDW) in the Pacific sector of the Southern Ocean 31
3.1 Introduction . . . 31
3.1.1 Evidence for reduced ventilation of Southern Ocean sourced waters during past glacial periods . . . 31
3.2 Hydrographic setting of site PC493 . . . 34
3.3 Results . . . 36
3.3.1 Lithology . . . 36
3.3.2 Stable oxygen isotopes and age model . . . 36
3.3.3 Stable carbon isotopes of planktic and benthic foraminifera . . . 38
3.3.4 Neodymium isotopic composition of authigenic ferromanganese oxyhydroxide coatings of planktic foraminifera . . . 39
3.4 Discussion . . . 40
3.4.1 Productivity and hydrographic conditions at site PC493 during the Late Quaternary . . . 40
3.4.2 The δ^{13}C of deep and bottom water masses in the modern, late Holocene and Last Glacial Maximum Southern Ocean . . . 42
3.4.2.1 Location and possible sources of $^{13}C_b$ depletion in the LGM Southern Ocean . . . 45
3.4.2.2 LGM $\delta^{13}C_b$ and physical mixing within the glacial Southern Ocean . . . 51
3.4.3 δ^{13}C changes in deep and bottom water masses of the Southern Ocean during the glacial-interglacial cycles of the Late Quaternary . 56
3.4.4 Implications for AABW production during the Late Quaternary . . 59
3.4.5 Implications for nutrient cycling in the glacial ocean . . . 62
3.5 Conclusions . . . 63

4 A 1.5 million year neodymium isotope record of deep water circulation in the equatorial Indian Ocean 65
4.1 Introduction . . . 65
4.2 Location, chronology and previous work . . . 68
4.2.1 ODP 121 Site 758: hydrography and seawater ε_{Nd} . . . 68
4.2.2 Ocean Drilling Program Leg 121 Site 758 chronology . . . 70
4.2.3 Previous studies of ε_{Nd} at Ocean Drilling Program Leg 121 Site 758 70
4.3 Results . . . 71
4.4 Discussion . . . 76
4.4.1 Palaeocirculation of the deep Indian Ocean over the last 860 ka . . 76

4.4.2 Palaeocirculation of the deep Indian Ocean between 1500-800 ka: The Mid-Pleistocene Transition . . . 79
4.4.3 Quantifying the export of NCW into CDW throughout the last 1.5 Ma 83
4.4.4 Coupling of Neodymium and carbon isotopes at Site 758 . . . 91
4.5 Conclusions . . . 94

5 Deep water formation and palaeocirculation in the western Pacific sector of the Southern Ocean during the last 540 ka 97
5.1 Introduction . . . 97
5.2 Core locations and chronology . . . 98
5.2.1 Core location . . . 98
5.2.2 Chronology . . . 100
5.2.2.1 Radiocarbon Dates . . . 100
5.2.2.2 Litho- and Biostratigraphy . . . 102
5.3 Results . . . 105
5.3.1 Neodymium isotope composition of foraminifera Fe-Mn coatings, sediment leachates and terrigenous detritus . . . 106
5.3.2 Rare Earth Element concentrations of sedimentary leachates . . . 109
5.4 Discussion . . . 111
5.4.1 $\varepsilon_{Nd}{}^{leachate}$ as a recorder of bottom water ε_{Nd}. . . . 111
5.4.2 Potential water mass sources for radiogenic ε_{Nd} values recorded at sites NBP-04 and NBP-06 . . . 113
5.4.2.1 Pacific Deep Water . . . 114
5.4.2.2 Ross Sea Bottom Water . . . 116
5.4.2.3 Past and present sources of radiogenic Nd in the Ross Sea 117
5.4.2.4 Past regions of RSBW formation . . . 119
5.4.3 Changes in Bottom Water production in the Ross Sea over the last 540 ka . . . 120
5.4.4 Changes in deep water circulation and RSBW production in the SW Pacific Sector of the Southern Ocean during the last 55 ka. . . . 124
5.4.4.1 55 to 33.5 ka: From 'Intermediate Glacial' towards 'Peak Glacial' RSBW production . . . 124
5.4.4.2 33.5 to 13.9 ka : 'Peak Glacial' RSBW production . . . 127
5.4.4.3 13.9to 0 ka: Onset of 'Modern Interglacial' RSBW production . . . 129
5.5 Conclusions . . . 130

6 Synthesis of results **133**
6.1 Formation and palaeocirculation of Antarctic Bottom Water 133
6.2 Middle- to Late-Quaternary palaeocirculation history of modified Circumpolar Deep Water in the Indian Ocean 135
6.3 Targeting strategies for future work 136

References **139**

Appendix A Supplementary Figures **165**

Appendix B Supplementary Tables **171**

Appendix C Data Tables **179**

List of figures

1.1 Insolation at 65°N, the LR04 stack and past pCO_2^{atm} reconstructions and δD measurments from Antarctic ice cores . . . 2
1.2 Southern Ocean surface nitrate concentrations and modelled southern hemisphere dust transport . . . 4
1.3 Schematic global overturning circulation . . . 5
1.4 Schematic Southern Ocean overturning circulation . . . 6
1.5 AABW distrubution within the modern ocean . . . 7
1.6 $\delta^{13}C$, phosphate concentrations and total CO_2 within the modern oceans . . . 10
1.7 $^{143}Nd/^{144}Nd$ evolution of the Earth's crust and mantle . . . 12
1.8 Terrestrial and oceanic distribution of ε_{Nd} . . . 13

2.1 Map of core sites studied in this thesis . . . 18

3.1 Global compolation of Holocene (0-6 ka) and LGM (18-24 ka) $\delta^{13}C_b$ . . . 33
3.2 A map of the Southern Ocean and key sediment core sites . . . 35
3.3 PC493 stratigraphy . . . 37
3.4 $\varepsilon_{Nd}{}^{foram}$ at site PC493 . . . 40
3.5 Crossplots of $CaCO_3$ content, Ba/Ti ratios and $\delta^{13}C_b$ values from core PC493 41
3.6 Potential temperature-salinity plot with the $\delta^{13}C$ values of seawater in the modern Southern Ocean . . . 43
3.7 *C.* cf. *wuellerstorfi* and *N. pachyderma* (sin.) $\delta^{13}C$ and $\delta^{18}O$ values across the last two glacial terminations . . . 44
3.8 Southern Ocean records of $\delta^{13}C_b$ from the late Holocene (0-6 ka) and the LGM (18-24 ka) . . . 46
3.9 LGM $\delta^{13}C_b$ values as a function of the physical properties of modern deep and bottom water masses . . . 49
3.10 Cross sections of LGM (18-24 ka) $\delta^{13}C_b$ values in the Atlantic and Pacific sectors of the Southern Ocean . . . 50

3.11 Modern and LGM (18-24 ka) reconstructions of deep water potential temperature and salinity 52
3.12 LGM (18-24 ka) $\delta^{13}C_b$ and $\delta^{18}O_b$ data from Chatham Rise, SW Pacific Ocean 53
3.13 Contoured LGM (18-24 ka) $\delta^{13}C_b$ values in the Atlantic Southern Ocean . 55
3.14 Schematic depiction of modern and last glacial Southern Ocean circulation and $\delta^{13}C_{seawater}$ 56
3.15 Records of Southern Ocean $\delta^{18}O_b$ and $\delta^{13}C_b$ spanning the last 800 kyr . . 58
3.16 Stacks of Southern Ocean $\delta^{18}O_b$ and $\delta^{13}C_b$ spanning the last 800 kyr . . . 59
3.17 Spatial gradients in AABW $\delta^{13}C_{palaeoSW}$ values across the last 800 kyr . . . 60

4.1 The LR04 $\delta^{18}O_b$ stack alongside reconstructed sea level across the last 1.5 myr 66
4.2 The location of Ocean Drilling Program Leg 121 Site 758 69
4.3 ε_{Nd} records measured on the sediments of Site 758 72
4.4 Spectral analysis performed on the ε_{Nd} record of Site 758 74
4.5 $\delta^{18}O_b$, $\delta^{13}C_b$ and ε_{Nd} records of Site 758 75
4.6 Authigenic ε_{Nd} record of Site 758 over the last 860 kyr 77
4.7 Comparison between ε_{Nd} recorded at ODP sites 1088, 758, and RC11-83, TN057-21 and SK129-CR2 78
4.8 $\delta^{18}O_b$, $\delta^{13}C_b$ and ε_{Nd} recorded at Site 758 between 800-1500 ka 80
4.9 ε_{Nd} recorded at Site 758 and $\delta^{13}C_b$ records from the Atlantic Ocean and Southern Ocean 81
4.10 ε_{Nd} recorded at Site 758, Site 1088 and Site 1090, reconstructed sealevel and pCO_2^{atm} over the last 1.5 myr 82
4.11 Map of avaiable ε_{Nd} records spanning the Mid Pleistocene Transition . . . 84
4.12 Globaly distributed ε_{Nd} records crossing the MPT 85
4.13 The result of a mixing calculation showing the percentage of NCW vs PDW bathing Site 758, Site 929 and Site 1123 87
4.14 Advection of an unradiogenic ε_{Nd} signal from Site 929 to Site 758 during interglacials 89
4.15 Pacific $\delta^{18}O_b$ records and the LR04 $\delta^{18}O_b$ stack and North Altantic $\delta^{18}O_{sw}$ across the Mid Pleistocene Transition 90
4.16 Crossplot of $\delta^{13}C_b$ measured at Site 758 and percentage of NCW bathing Site 758 over the last 1.5 myr 92
4.17 Crossplot of $\delta^{13}C_b$ measured at Site 758 and percentage of NCW bathing Site 758 over the last 927 ka 93

5.1 Location of sediment cores NBP-4 and NBP-06 99

5.2 Age tie points used in the age models of cores NBP-04 and NBP-06 104
5.3 Age vs depth in cores NBP-06 and NBP-04 106
5.4 Crossplots of $\varepsilon_{Nd}{}^{foram}$ vs $\varepsilon_{Nd}{}^{leachate}$ and $\varepsilon_{Nd}{}^{detrital}$ vs $\varepsilon_{Nd}{}^{leachate}$ 107
5.5 ε_{Nd} records of cores NBP-04 and NBP-06 108
5.6 $REE^{leachate}$ records of cores NBP-04 and NBP-06 110
5.7 Cross plots of $\varepsilon_{Nd}{}^{leachate}$ vs Eu/Eu* and Ce/Ce* vs Y/Ho 113
5.8 Location of ε_{Nd} records shown in Fig. 5.9 114
5.9 $\varepsilon_{Nd}{}^{palaeoSW}$ reconstructions from cores within the Atlantic, Indian, Pacific and Southern oceans 115
5.10 Map of the Ross Sea Embayment 118
5.11 ε_{Nd} records of NBP-04 and NBP-06 vs modelled Antarctic ice volume acorss the last 550 ka 123
5.12 Records of palaeoclimatic and palaeoceanographic changes from the Southern Ocean and Antarctica during the last 60 ka 126

A.1 $\delta^{18}O_b$ from ODP Leg 121 Site 758 plotted on the age model used in this thesis 165
A.2 ε_{Nd} measurements made by Burton and Vance (2000) on reductively cleaned vs uncleaned planktonic foraminifera from ODP Leg 121 Site 758 166
A.3 ε_{Nd} measurements made by Burton and Vance (2000) on reductively cleaned planktic foraminifera vs ε_{Nd} leachate measurments of Gourlan et al. (2010) at ODP Leg 121 Site 758 167
A.4 Percentages of Northern Component Water (NCW) bathing ODP sites 929, 758 and 1123 168
A.5 $REE^{leachate}$ data from sites NBP-04 and NBP-06 169

List of tables

2.1 Location of sediment cores studied in this work 18
2.2 A summary of key analytical procedures performed on the marine sediment cores used in this thesis. 20
2.3 Typical internal and external errors achieved using differing analytical setups on the Neptune Plus MC-ICPMS in the Department of Earth Sciences, University of Cambridge. 26

4.1 End member ε_{Nd} and Nd concentrations used in the binary mixing calculation presented in section 4.4.4 86
4.2 Characterisation of $\delta^{13}C_b$ values and percentage of NCW bathing Site 758 across discrete intervals of the last 1.5 myr 94

5.1 Radiocarbon measurements made on the sediments of cores NBP-04 and NBP-06 101
5.2 Ce/Ce*, Eu/Eu*, MREE/MREE*, and HREE/HREE* averages and standard deviation of measurements made on sediment leachates from cores NBP-06 and NBP-04 111

B.1 Procedures for extraction of REE via column chromatography using 200 μL TRUSpec^{TM} resin (100-150 μm mesh size). 172
B.2 Procedures for purification of Nd via column chromatography using 5 mL LNSpec^{TM} resin (50-100 μm mesh size) 173
B.3 PC493 age model control points 174
B.4 ODP Leg 121 Ste 758 Age-depth tie points 175
B.6 A list of tie points used in the construction of age models for cores NBP9802-04 and NBP9802-06. MS denotes tie points linking magnetic susceptibility records to the record of dust flux to the EPICA Dome C ice core 177

C.1 Data from core PC493: stable oxygen and carbon isotopes, inclination of the Characteristic Remanent Magnetization (ChRM), $CaCO_3$ content and total organic carbon. 180
C.2 Details of sediment cores used in Holocene and LGM time slice compilations of *Cibicidoides* $\delta^{13}C_b$ in Figs. 3.8-3.10 196
C.3 Authigenic $\varepsilon_{Nd}{}^{leachate}$ measurements made on the sediments of ODP Leg 121 Site 758 as part of this thesis 202
C.4 Authigenic $\varepsilon_{Nd}{}^{leachate}$ measurements made on the sediments of NBP9802-04PC1 209
C.5 $\varepsilon_{Nd}{}^{foram}$ measurements made on NBP9802-04PC1 211
C.6 $\varepsilon_{Nd}{}^{detrital}$ measurements made on the sediments of NBP9802-04PC1 212
C.7 Authigenic $\varepsilon_{Nd}{}^{leachate}$ measurements made on the sediments of NBP9802-06PC1 212
C.8 Authigenic $\varepsilon_{Nd}{}^{foram}$ measurements made on NBP9802-06PC1 214
C.9 Authigenic $\varepsilon_{Nd}{}^{detrital}$ measurements made on the sediments of NBP9802-06PC1 215
C.10 Values used for PAAS-normalisation of REE concentrations. From Pourmand et al. (2012) 216
C.11 PAAS-normalised $REE^{leachate}$ data from core NBP9802-04PC1 217
C.12 PAAS-normalised $REE^{leachate}$ data from core NBP9802-04PC1 219

Chapter 1

Introduction

1.1 Quaternary palaeoclimate

The Earth's climate has been dominated by cycles of glaciation throughout the Quaternary, with glacial periods characterised by the presence of extensive ice sheets over much of North America and Eurasia, interspersed with relatively mild interglacial periods. The buildup and decay of these northern hemisphere ice sheets is ultimately paced by changes in the Earth's orbit around the Sun (Milankovich, 1941), which led to cyclical changes in the distribution of incoming solar radiation at the Earth's surface (i.e. insolation). However, it is clear from the magnitude and timing of the climatic response to these orbital cycles that past changes in the Earth's climate must have been amplified by internal feedbacks. Unraveling these internal feedbacks remains a challenge for the palaeoclimate community. Reconstructions of Antarctic air temperature closely match the saw-tooth pattern of atmospheric CO_2 concentrations (pCO_2^{atm}) and benthic foraminifera $\delta^{18}O$ ($\delta^{18}O_b$, which responds largely to changes in deep ocean temperature and global ice volume) over at least the last 800 ka (Bereiter et al., 2015; Jouzel et al., 2007; Lisiecki and Raymo, 2005), suggesting pCO_2^{atm} was key in modulating past global climatic change (Fig. 1.1).

The oceans play an important role in the redistribution of heat, both directly via the absorption of solar radiation at the ocean surface and the subsequent recirculation of this heat, and through changes in the Earth's albedo via the production and distribution of sea ice, and in the supply of moisture for the expansion of ice sheets at high latitudes. In addition to their role in the redistribution of heat and moisture, the oceans are a huge carbon reservoir, capable of interacting with the atmosphere on centennial to millennial time scales. For these reasons, it has long been proposed that a change in the partitioning of carbon between the ocean and the atmosphere may have played a key role in these pCO_2^{atm} fluctuations (e.g. Broecker (1982)).

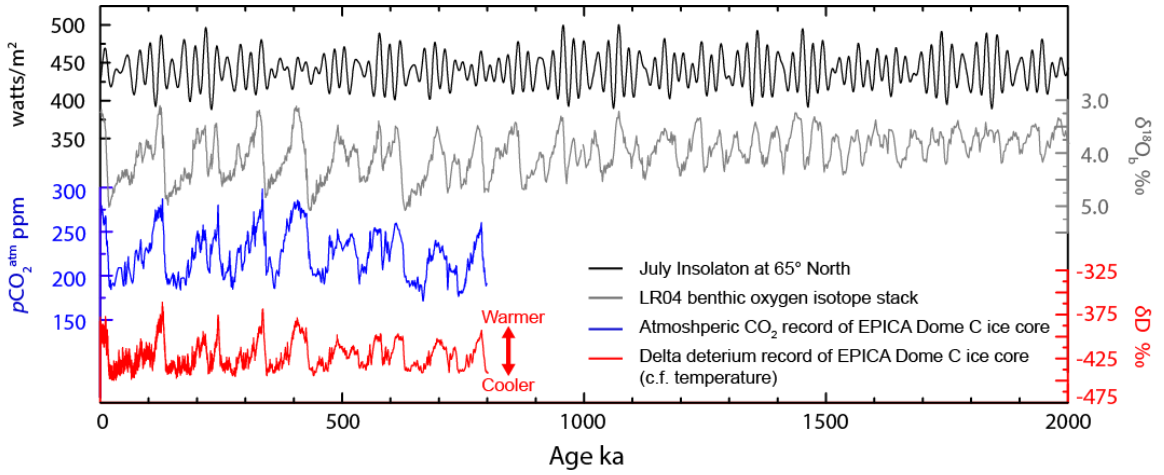

Fig. 1.1 Changes in incoming solar radiation (insolation) at 65°N, thought to be an important threshold in the advancement and retreat of northern hemisphere ice sheets, alongside palaeoclimate indicators through the Middle- and Late-Quaternary: the LR04 stack of global $\delta^{18}O_b$ records (Lisiecki and Raymo, 2005), largely reflecting the buildup [higher values] and decay [lower values] of terrestrial ice and changes in deep water temperature), and the pCO_2^{atm} (Augustin et al., 2004) and delta deuterium (a proxy for air temperature, Jouzel et al. (2007)) records of the EPICA Dome C ice core in East Antarctica (both records presented on the Antarctic Ice Core Chronology 2012 timescale (Bazin et al., 2013).

Oceans can change pCO_2^{atm} predominantly via two mechanisms. The first is the diffusion of CO_2 into the surface ocean, often termed the 'solubility pump'. The diffusion of CO_2 into surface waters is temperature dependant such that at 0°C surface water temperature the solubility of CO_2 is roughly twice as high as at 22°C (Carroll et al., 1991). When surface waters sink to form intermediate- or deep-water masses, the dissolved CO_2 is carried out of contact with the atmosphere and stored in the ocean interior until it returns, via upwelling waters, to the surface. The rate at which the ocean interior is flushed with deep waters that were recently in contact with the atmosphere is often termed its 'ventilation' state. The temperature dependence of diffusivity means high latitude surface oceans are a critical region of air-sea gas exchange. As the region where both the upwelling of deep water masses and the formation of intermediate- and deep-waters occurs, high latitude oceans exert a disproportionate control on the transfer of pCO_2^{atm} into the ocean interior (Gebbie and Huybers, 2011). As well as a thermodynamic control, there is also a kinetic control on the rate of air-sea gas diffusivity largely dependent on wind-driven mixing within the thermocline, surface water pCO_2 and salinity, which leads to a decrease in CO_2 partial pressure with increasing salinity. The physical properties of surface waters and the length of contact time between the sea surface and atmosphere in areas of deep water formation are therefore critical controls on the ability of the deep ocean to store pCO_2^{atm}. The capacity of glacial-time

cooling sea surface temperatures to account for the glacial-interglacial variability in pCO_2^{atm} is reduced due to the concurrent increase in whole-ocean salinity as northern hemisphere ice sheets expanded (Broecker, 1982). However, a reduction in air-sea gas exchange in the high latitude Southern Ocean (SO) due to increased sea-ice extent – and an associated increase in surface water stratification – may have reduced outgassing of CO_2 in areas of SO upwelling and in regions of bottom water formation (Ferrari et al., 2014; Stephens and Keeling, 2000), thereby increasing CO_2 storage within the ocean interior. Salinity can drive carbon storage in the ocean via another mechanism: increasing the density of deep waters reduces vertical diffusivity and mixing, and by increasing the salinity of the deep ocean interior it may be possible to reduce the transfer of carbon from the ocean interior to the atmosphere via mixing between water masses (Adkins, 2013; Bouttes et al., 2010). It has been hypothesised that increases in deep and bottom water salinity, coupled with a shoaling of deep water mass boundaries in the Atlantic and Atlantic SO above rough bathymetry due to a northward migration of upwelling deep water, reduced diapycnal mixing within the Atlantic basin. This would reduce the ventilation of abyssal waters via turbulent mixing with overlying well ventilated waters, and an expansion in relatively poorly ventilated SO-sourced deep waters (Ferrari et al., 2014).

The second mechanism for the transfer of carbon between oceanic and atmospheric reservoirs is the fixation of carbon by marine plankton and the subsequent removal of this organic carbon from the sea surface into the ocean interior, the so-called 'biological pump'. Although most organic carbon is respired to CO_2 in the surface ocean and returned to the atmosphere before it can enter the intermediate or deep ocean, a small proportion of organic matter or dissolved organic carbon either sinks as particulates or is mixed into the ocean interior before oxidation. Although small in proportion to the organic carbon that remains in the surface ocean, export productivity in the modern ocean is estimated at c. 6 PgC yr^{-1}, equivalent to rates of anthropogenic CO_2 release during the 1990s (Siegel et al., 2014). It's this export productivity which drives the storage of dissolved inorganic carbon (DIC) within the ocean interior via the biological pump. Today primary productivity in the SO is limited by the availability of the nutrient iron (Fe) within surface waters, resulting in an incomplete consumption of other available nutrients such as nitrogen and phosphorous (Martin, 1990) (Fig. 1.2). Fe-limitation represents an inefficiency in the biological pump's ability to sequester carbon: if the burden of reduced Fe availability were to be reduced or eliminated entirely, export productivity would increase and pCO_2^{atm} would decrease (Martin, 1990).

There is strong evidence that the dust-borne supply of Fe to the SO increased during past glacial periods (Lamy et al., 2014; Martínez-García et al., 2009, 2011), stimulating increased

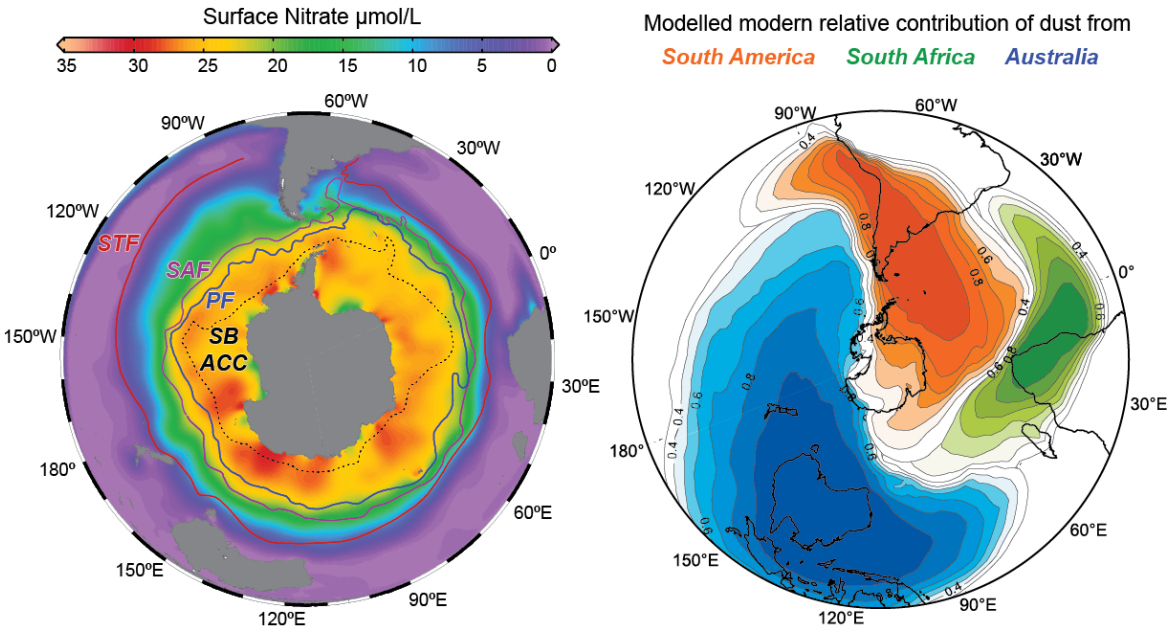

Fig. 1.2 Primary productivity within the surface of the SO is today limited by the supply of the micronutrient Fe, leading to incomplete utilisation of surface nitrate (left). An increase in Fe delivered to the surface ocean via dust from South America, South Africa and Australia to the SO is thought to have led to an increase in primary productivity during past glacial periods, leading to a more efficient biological pump and lowering pCO_2^{atm} (right). Surface nitrate concentrations plotted using Ocean Data View (Schlitzer, 2015) with data from the World Ocean Atlas 2013 (Garcia et al., 2014), and shown alongside major oceanographic fronts and boundaries after Orsi et al. (1995): the Subtropical Front (STF), Subantarctic Front (SAF), Polar Front (PF) and the southern boundary of the Antarctic Circumpolar Current (SB ACC). Modelled dust contribution modified from Lamy et al. (2014).

biological productivity and leading to a more efficient drawdown of pCO_2^{atm} via the biological pump (Martínez-García et al., 2014). Increasing the DIC content of the deep ocean would in turn increase the carbonate ion concentration ($[CO_3^{2-}]$), resulting in decreased $CaCO_3$ burial, a shoaling of the lysocline, an increase in whole-ocean alkalinity and an additional drawdown of pCO_2^{atm} into the ocean (Hain et al., 2010, 2014; Sigman et al., 2010)

1.2 Modern global ocean circulation

Large-scale circulation within the modern oceans is driven by i) the distribution of heat and salinity, which causes density differences between different water masses (so-called thermohaline circulation); ii) wind-driven currents which are normally confined to the uppermost few hundreds of meters of the water; and iii) tidal forcing from the sun and

moon (Lumpkin and Speer, 2007; Rahmstorf, 2002; Talley, 2013). Together with the current configuration of major land masses, these processes combine to produce a global circulation regime which is often likened to an oceanic 'conveyor belt' (Fig. 1.3): deep waters formed in the North Atlantic (NADW) flow south into the SO, where they mix with deep waters recirculating from the Indian and Pacific basins to form Circumpolar Deep Water (CDW). Around Antarctica, CDW upwells to the surface as, where buoyancy loss leads to downwelling of waters to form Antarctic Intermediate Water (AAIW) and Antarctic Bottom Water (AABW). AABW, AAIW and CDW flow into the major ocean basins via the deep western boundary currents, and return flow of intermediate and bottom waters north into the Atlantic ocean counterbalances the southward flow of NADW, completing once circuit of the oceanic 'conveyor belt' (Broecker, 1991). Approximately 15% of the surface ocean in the high latitude Atlantic and Southern oceans go on to fill 85% of the ocean interior (Gebbie and Huybers, 2011), making these regions of particular importance to global ocean circulation (Fig. 1.3).

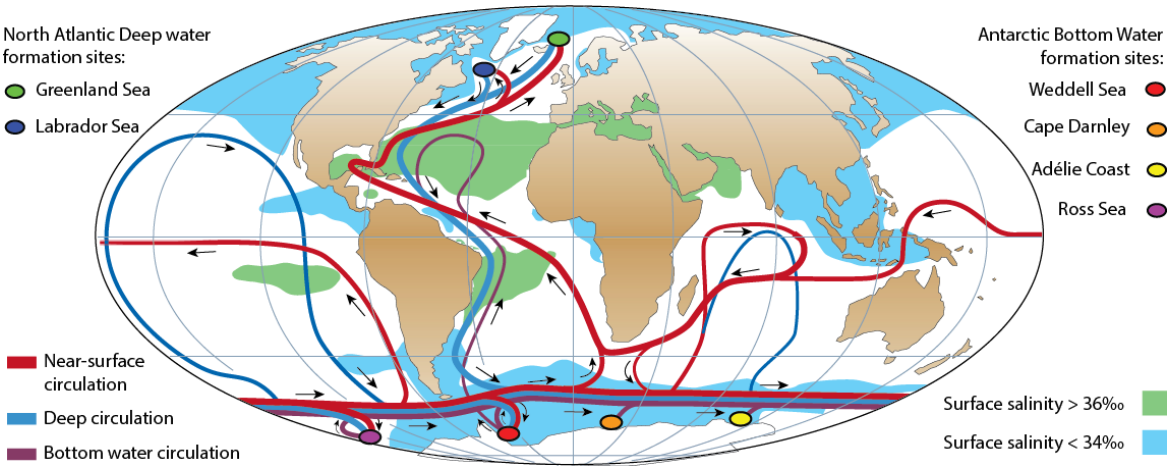

Fig. 1.3 A schematic depiction of global overturning circulation, modified from Rahmstorf (2002), after Broecker (1991). Although something of an oversimplification of global ocean circulation, this 'conveyor belt' schematic is a useful way to frame modern circulation when reconstructing past changes in large-scale ocean circulation.

1.3 Southern Ocean circulation and water masses

The SO is an important region linking ice sheets, ocean circulation and the atmosphere, and acts as a conduit connecting each of the major ocean basins. Circulation within the SO is dominated by the clockwise flowing Antarctic Circumpolar Current (ACC), the largest and longest oceanic current in the world, with an estimated transport of 147-152 Sv (1 Sv=

10^6 m^3 $s^{-}1$) at 58°E (Park et al., 2009) and a total estimated flow path of c. 24,000 km (Carter et al., 2008; Whitworth III, 1988). The ACC is largely driven by westerly winds, and generally reaches from surface ocean to seabed (Orsi et al., 1995), with flow concentrated along a series of oceanic fronts. To the south of the southern boundary of the ACC (SB-ACC), a counter-current flows west along the Antarctic coast, the Antarctic Coastal Current. The ACC is divided by two frontal systems, the Polar Front (PF), south of which very cold and relatively fresh Antarctic Surface Water (AASW) is found, and the Southern ACC Front (SACCF), which corresponds to a subsurface cold front within upwelling CDW (Orsi et al., 1995) (Fig. 1.4). To the north the ACC is bounded by the Subantarctic Front (SAF), beyond which lies the Subtropical Front (STF), where warmer subtropical waters mix with and override colder subantarctic waters. As the northern limit of subantractic waters, the STF is used to define the northern limit of the SO in this thesis.

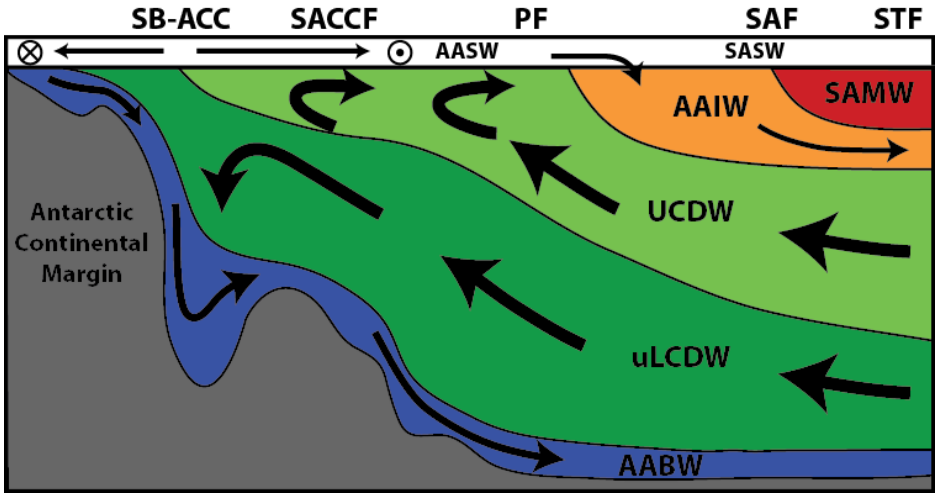

Fig. 1.4 Schematic depiction of overturning circulation within the Atlantic sector of the SO (modified after (Speer et al., 2000)). Shown are the locations of fronts defined by Orsi et al. (1995): the southern Antarctic Circumpolar Current (ACC) Front (SACCF); the Polar Front (PF); the Subantarctic Front (SAF) and the Subtropical Front (STF), along with the southern boundary of the ACC (SB-ACC). Surface water masses (white) are Antarctic and Subantarctic Surface Water (AASW and SASW, respectively). Intermediate- to deep-water masses are Subantarctic Mode Water (SAMW), Antarctic Intermediate Water (AAW), Upper Circumpolar Deep Water (UCDW), Lower Circumpolar Deep Water (LCDW) and Antarctic Bottom Water (AABW).

The largest water mass within the SO is CDW (Sverdrup, 1940). CDW can be split into two main water masses: Upper CDW (UCDW) is characterised by low oxygen and high nutrient content reflecting recirculation of deep waters from the Indian and Pacific basins. Lower CDW (LCDW) is characterised by a salinity maximum imparted by the inflow of

high-salinity NADW in the Atlantic sector of the SO (Reid and Lynn, 1971). AABW is a term encompassing all bottom waters formed around Antarctica, and is defined by Orsi et al. (1999) as all waters with a neutral density (γ^n) greater than 28.27 kg m^{-3} (Fig. 1.5). Despite sharing this common density characteristic, AABW formed in different regions around Antarctica possesses differing physical properties, reflecting diverse modes of formation and the physical properties of precursor water masses. AABW sourced in the Weddell Sea is the coldest, yet conversely, also the least saline SO bottom water, while AABW in the eastern Pacific sector of the SO is warmer and more saline, with bottom water in the eastern Indian sector having characteristics intermediate between the two. Mixing between CDW and AABW leads to a modified LCDW with physical properties similar to AABW; when discussing palaeocirculation of SO water masses it is therefore useful to distinguish between LCDW with a strong AABW component (lower LCDW, lLCDW) and LCDW with a strong NADW component (upper LCDW, uLCDW) (e.g. McCave et al. (2008); Russon et al. (2009)).

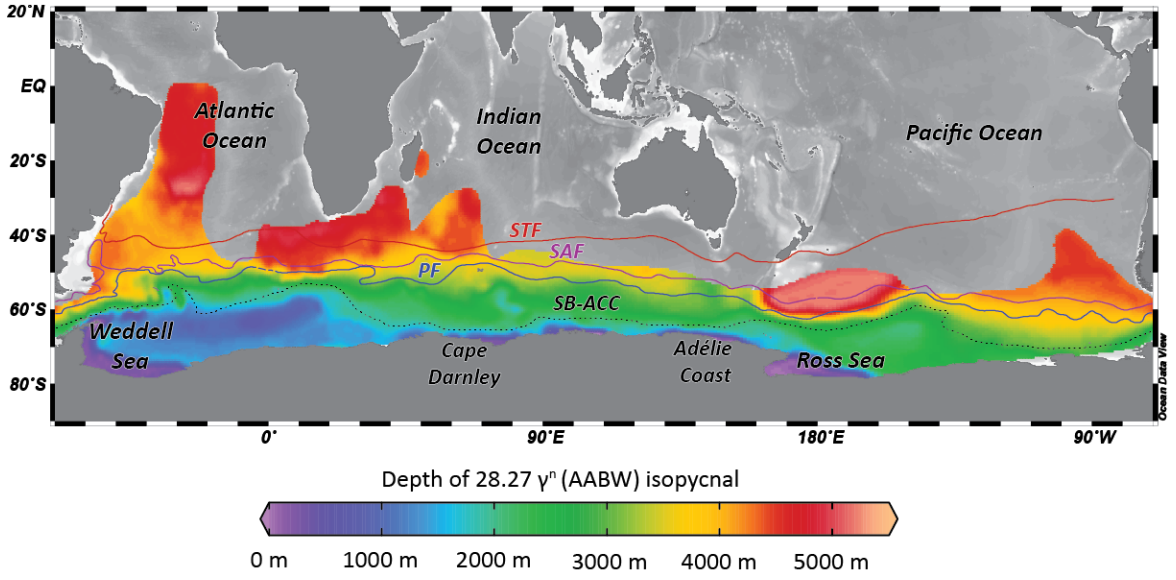

Fig. 1.5 The water depth of the 28.27 kg m^{-3} isopycnal, which delineates the upper surface of AABW (according to Orsi et al. (1999)). Bathymetric barriers imposed by mid ocean ridge systems play an important role in restricting the advection of AABW to lower latitudes, particularly in the Indian and Pacific basins. Also shown are the locations of major oceanographic fronts and boundaries after Orsi et al. (1995): the Subtropical Front (STF), Subantarctic Front (SAF), Polar Front (PF) and the southern boundary of the Antarctic Circumpolar Current (SB ACC) Plotted using Ocean Data View (Schlitzer, 2015) with hydrographic data from the World Ocean Atlas 2013 (Garcia et al., 2014).

SO surface waters can be divided into cold, relatively fresh AASW found south of the PF, and slightly warmer Subantarctic Surface Water (SASW), found between the PF and the STF. South of the SB-ACC, the counter-clockwise flowing Antarctic Coastal Current leads to Ekman transport of surface waters towards Antarctica, while north of the SB-ACC, the clockwise flowing ACC leads to Ekman transport away from Antarctica, creating the Antarctic Divergence in the region of the SB-ACC (Fig. 1.4). This divergence leads to the upwelling of CDW, where air-sea fluxes and, to a lesser extent, diapycnal mixing transform upwelling CDW into less dense AASW (Sloyan and Rintoul, 2001). Some of this AASW is transported poleward, cooled and subsequently goes on to form AABW, while some travels north. Where northward flowing AASW meets warmer, less dense surface water south of the SAF, these waters sink to form AAIW, which overlies denser CDW. North of the SAF, winter cooling of surface waters causes them to sink to water depths of $\sim$500 m and leads to the formation of Subantarctic Mode Water (SAMW) (Sloyan et al., 2010).

Owing to its high density, the circulation of AABW within the SO and its advection north into the Atlantic basin is strongly controlled by bathymetric barriers. AABW within the Atlantic Ocean is confined to the west by the presence of the Mid-Atlantic Ridge, while advection of AABW into the Indian and Pacific oceans is restricted by the presence of mid ocean ridge systems. In the western Pacific sector of the SO AABW spills over the Pacific-Antarctic Ridge and rapidly mixes with CDW to become lLCDW (Fig. 1.5).

AAIW, SAMW and AABW formation within the SO acts to ventialate the ocean interior with waters which have recently undergone air-sea gas exchange, thereby providing a connection pathway between the atmosphere and the ocean interior. While SAMW forms in the region of the SAF throughout the SO, AAIW formation is largely restricted to the eastern Pacific and western Atlantic sectors of the SO (Carter et al., 2008). From here, SAMW and AAIW flow northward at water depths between c. 800 and 1400 m, and play an important role in supplying nutrients to the subtropical thermocline (Sarmiento et al., 2004).

1.4 Reconstructing past ocean circulation

The study of modern oceanography relies heavily on the direct measurement of the physical properties such as temperature and salinity, or of chemical parameters such as nutrient contents. The direct measurement of variables such as these is impossible when studying the past oceans, and so instead we study marine sediments to indirectly reconstruct the properties of past water masses. As we are studying the physical or chemical characteristics of the past oceans by proxy, the techniques we employ are known as ‘proxies’. Two proxies employed extensively within this thesis are i) stable carbon isotopes measured on planktic

and benthic foraminifer shells (or tests); and ii) the neodymium isotopic values of various marine sedimentary phases.

1.4.1 Stable carbon isotopes

In the modern ocean, the distribution of nutrients can be used to characterise water mass circulation and mixing; by reconstructing the nutrient content of past water masses it is hoped that we can reconstruct palaeocirculation in a similar way. One such nutrient proxy is the ratio of the stable carbon isotopes ^{13}C and ^{12}C ($\delta^{13}C$) recorded in the calcium carbonate ($CaCO_3$) tests of planktic and benthic foraminifera. The $\delta^{13}C$ of seawater DIC ($\delta^{13}C_{seawater}$) in the ocean interior mirrors the distribution of nutrients, such that $\delta^{13}C$ can be used as a proxy for the nutrient content of seawater. This association arises due to the preferential uptake of ^{12}C during photosynthesis, leading to marine organic matter with $\delta^{13}C$ values typically between -20‰and -30‰. The preferential removal of ^{12}C by phytoplankton also leads to the carbon pool in the remaining surface waters being enriched in ^{13}C. Respiration of the ^{12}C-enriched organic matter during export to the ocean interior leads to an inverse relationship between $\delta^{13}C$ and nutrient content at depth. Thus, in the same way that different water masses have characteristic nutrient contents, $\delta^{13}C_{seawater}$ allows us to trace the circulation and mixing between water masses in the ocean, and by analysing the $\delta^{13}C$ of foraminiferal calcite we can reconstruct the nutrient contents and circulation of ancient water masses. As depletion of ^{13}C along a deep-water flow path is symptomatic of increased remineralisation of organic carbon, lower $\delta^{13}C$ values also correspond to increased carbon content within the modern ocean (Fig 1.6). $\delta^{13}C$ as recorded in the $CaCO_3$ tests of foraminifera therefore provides information on carbon sequestration via the biological pump, as well as the circulation and ventilation state of a given water mass.

The benthic foraminifera species most often used for reconstructions of past $\delta^{13}C$ of bottom waters are *Cibicidoides* and *Uvigerina*. The $\delta^{13}C$ of tests of the epifaunal foraminifer *Cibicidoides* largely reflects $\delta^{13}C$ of the ambient seawater, and can thus be used to reconstruct the past $\delta^{13}C$ of seawater DIC (Duplessy et al., 1984). It has been demonstrated that the $\delta^{13}C$ of tests of the epibenthic foraminifer *Uvigerina* is offset from $\delta^{13}C_{seawater}$, with the offset thought to reflect a local 'habitat signature', relating to the flux of organic matter to the core site and its subsequent decomposition within sediment pore waters (Belanger et al., 1981; Fontanier et al., 2006; Loubere, 1987; Mackensen and Licari, 2004; McCorkle et al., 1990; Woodruff et al., 1980; Zahn et al., 1986). There is evidence that *Uvigerina* species will opportunistically exploit short-lived episodes of heightened organic matter flux to the seafloor, potentially biasing $\delta^{13}C$ records measured on this genus to lighter values (Lutze and Coulbourn, 1984; Miller and Lohmann, 1982). Although a constant offset of +0.9‰ is often

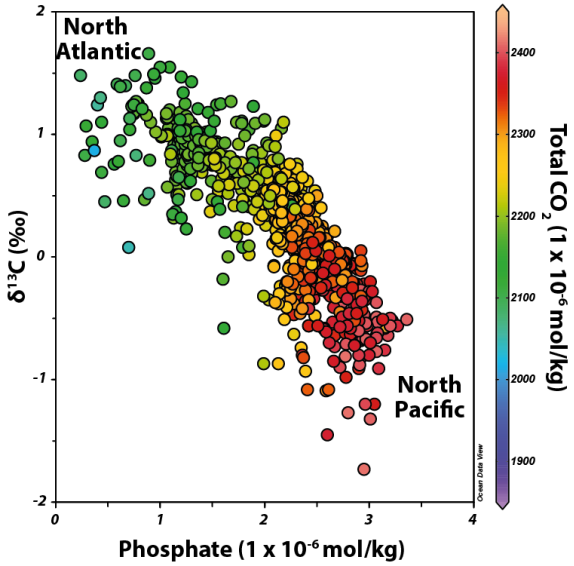

Fig. 1.6 Addition of nutrients phosphate and ^{12}C-enriched carbon due to remineralisation of organic matter along the flow path of the global thermohaline circulation from the North Atlantic to the North Pacific, leading to a decrease in $\delta^{13}C_{seawater}$ and an increase in phosphate and CO_2 contents. Data collected by the Geochemical Ocean Studies program from 1972 – 1978 (Ostlund et al., 1987) and plotted using Ocean Data View (Schlitzer, 2015).

applied to δ^{13}C values measured on *Uvigerina* to account for this habitat effect (Duplessy et al., 1984; Zahn et al., 1986), this approach does not take into account past variations in organic matter flux. It has been suggested that a variable offset to δ^{13}C values of *Uvigerina* needs to be applied using δ^{18}O values measured on the same specimens as an identifier of past climatic regime, the reasoning being that during past cold periods, such as during the Last Glacial Maximum (LGM, 18-24 ka), surface water productivity – and thus particulate organic matter flux to the seafloor – was increased, particularly in the SO (McCave et al., 2008; Pahnke and Zahn, 2005). The equation proposed by McCave et al. (2008) relating the difference between δ^{13}C measured on *C. wuellerstorfi* (which faithfully records δ^{13}C of bottom water) and *Uvigerina* to δ^{18}O measured on *Uvigerina* is:

$$\Delta\delta^{13}C_{Uvig-Cibs} = 0.464 \times \delta^{18}O_{Uvig} - 2.753 \tag{1.1}$$

Applying the above correction provides a R^2 correlation coefficient of 0.626 between *Cibicidoides wuellerstorfi* and *Uvigerina* spp. in sediment core MD97 2120 from the Chatham Rise region east of New Zealand (McCave et al., 2008). However, uncertainty remains as to the wider applicability of this offset: for example water masses sourced in different regions have different δ^{18}O values, and in an area with a complex hydrography this δ^{18}O variability

may lead to spurious calculated δ^{13}C values, while the relationship between changing organic flux and δ^{18}O is not expected to be uniform globally or temporally.

There is evidence that the decomposition of organic matter on the seafloor above the sediment-water interface can occur in regions of high surface ocean productivity. The degradation of this organic matter within a layer of phytodetritius on the sea floor may lead to the calcification of *C. wuellersetorfi* with δ^{13}C values lower than that of bottom water DIC, much in the same way *Uvigerina* spp. are affected by a microhabitat effect. This is referred to as a 'phytodetritus' or 'Mackensen' effect (Mackensen et al., 1993, 2001). Despite this possibility, considering the uncertainty in the *Uvigerina* δ^{13}C correction presented above, δ^{13}C measurements performed on *Cibicidoides* species are preferentially cited throughout this thesis, with *Cibicidoides wuellerstorfi* preferred when possible.

1.4.2 Neodymium isotopes

Although containing useful information on the cycling of nutrients within the ocean, the use of nutrient-based proxies such as δ^{13}C in reconstructing past water mass circulation and mixing is somewhat hampered by the fact that $\delta^{13}C_{seawater}$ can change independent from palaeocirculation, either via remineralization of organic carbon along a deep water flow path, or via air-sea gas exchange. This has led to the development of alternative palaeocirculation proxies, which behave independently of biological fractionation and air-sea exchanges. One such proxy is the ratio of the radiogenic, stable isotope neodymium-143 (^{143}Nd) to the stable, non-radiogenic isotope neodymium-144 (^{144}Nd), expressed in epsilon notation as the deviation of ^{143}Nd/^{144}Nd from a standard; in this case the chondritic uniform reservoir (CHUR; ^{143}Nd/^{144}Nd = 0.512638, Jacobsen and Wasserburg (1980)). As deviations from CHUR are small, they are expressed in epsilon notation multiplied by 10,000 (DePaolo and Wasserburg, 1976), according to equation 1.2:

$$\varepsilon_{Nd} = [(^{143}Nd/^{144}Nd_{sample})/(^{143}Nd/^{144}Nd_{CHUR}) - 1] \times 10000 \quad (1.2)$$

The ε_{Nd} of seawater ($\varepsilon_{Nd}{}^{seawater}$) is often referred to as a 'quasi conservative tracer of ocean circulation', in that seawater is isotopically labeled via boundary exchange along continental margins, but $\varepsilon_{Nd}{}^{seawater}$ within the ocean interior is determined by water mass mixing. The utility of Nd isotopes as a tracer of water masses therefore arises from the differing ε_{Nd} of terrigenous inputs in areas surrounding deep water formation.

Nd has seven naturally occurring isotopes, with ^{143}Nd formed via the alpha decay of samarium-147 (^{147}Sm), which occurs with a half-life of 106 Gyr. Over time, fractionation during partial melting of the mantle and fractional crystallization has led to an enrichment in

mantle Sm/Nd and a depletion in crustal Sm/Nd (Fig. 1.7). Lithologies derived from partial melting of the mantle (i.e. basic volcanic rocks) are relatively enriched in ^{147}Sm and its daughter isotope ^{143}Nd, whereas continental crust is relatively depleted in ^{147}Sm, and thus ^{143}Nd. This has led to a spatial heterogeneity in the ε_{Nd} of the global rock record, which is a function of the initial Sm/Nd ratio and the age of the rocks, with ancient continental crust, such as Greenland and the Canadian Shield, possessing a lower ^{143}Nd/^{144}Nd (more negative ε_{Nd}), while younger volcanic rocks, such as within and surrounding the Pacific Ocean, have a higher ^{143}Nd/^{144}Nd (more positive ε_{Nd}) (Fig 1.8a).

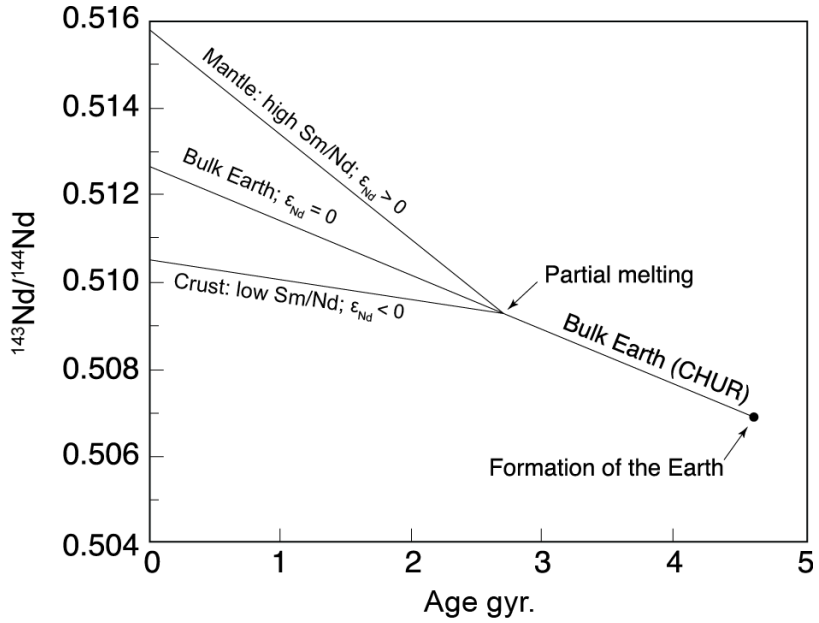

Fig. 1.7 A schematic depiction of the ^{143}Nd/^{144}Nd evolution of the Earth's crust and mantle from initial chondritic Sm/Nd values. After DePaolo and Wasserburg (1976).

This global heterogeneity in the ε_{Nd} of sedimentary inputs to the oceans leads to the 'labeling' of deep waters formed in the Labrador and Greenland seas and subsequently advected southwards as NADW with an unradiogenic (negative) ε_{Nd} signature. Conversely, boundary exchange within the Pacific Ocean leads to PDW with a more radiogenic (positive) ε_{Nd} signature (Fig 1.8). The observation that Nd residence times within the ocean are shorter than the whole ocean mixing time allows seawater ε_{Nd} to be utilized as a tracer of ocean circulation and water mass mixing within the modern ocean.

The neodymium isotopic composition of seawater is faithfully recorded in authigenic ferromanganese precipitates, which are ubiquitous within ocean sediments. Studies of the ε_{Nd} of slow growing (on the order of 10^{-1} years) Fe-Mn crusts offer a low-resolution record of changes in bottom water ε_{Nd} over long periods of time (Fig. 1.8 (Frank, 2002; O'Nions et al., 1978), but are ill suited to the study of palaeocirculation changes occurring at timescales

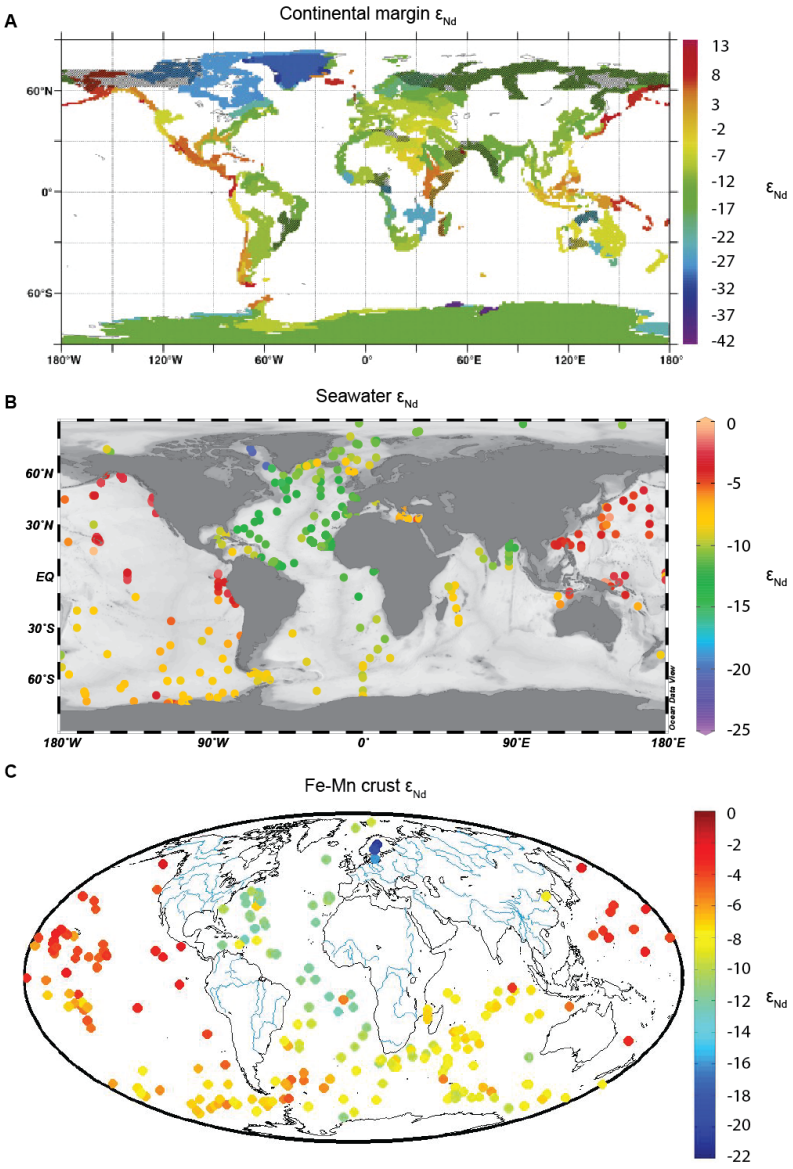

Fig. 1.8 (a) modelled ε_{Nd} of continental margin rocks based on a global compilation of ε_{Nd} (Jeandel et al., 2007); note that the modelled ε_{Nd} of much of Antarctica is based on relatively few data, and may not be accurate for the continental interior. (b) Deep water ε_{Nd} measurements: the deepest measurement was taken from each station in the seawater ε_{Nd} compilation of van de Flierdt et al. (2016). All data above 500 m water depth were excluded. (c) ε_{Nd} measurements carried out on scrapings of seafloor Fe-Mn crusts (Siddall, unpublished, after Frank et al. 2002). Deep water ε_{Nd} reflects mixing between the North Atlantic (c. -13.5) and Pacific (c. -3 to -4) ε_{Nd} end members, which are determined by terrigenous inputs to these regions, and bottom water ε_{Nd} is faithfully recorded by the Fe-Mn crust data.

of less than $10^{5\text{-}6}$ years. Alternative techniques have been developed for the leaching of authigenic Fe-Mn coatings of marine sediments, either from bulk sediment phases (Blaser et al., 2016; Chester and Hughes, 1967; Gutjahr et al., 2007; Rutberg et al., 2000) or from isolated phases such as the Fe-Mn coatings of foraminifer tests (Palmer and Elderfield, 1985; Roberts et al., 2010; Vance, 2004) or diagenetically altered fish debris (Martin and Haley, 2000; Staudigel et al., 1985). Concerns have been raised that leaching of bulk sedimentary phases can lead to the contamination of seawater ε_{Nd} signals by leaching of detrital Nd (Elmore et al., 2011; Roberts et al., 2010; Wilson et al., 2013). However, recent studies have demonstrated that it is possible to faithfully extract a seawater ε_{Nd} signal free of contamination, if care is taken to use a very weak leaching procedure (e.g. Blaser et al. (2016); see Chapter 2).

1.5 Thesis outline and objectives

The main aims of this thesis are i) to better characterise the past $\delta^{13}C$ and ε_{Nd} of the deep and bottom water masses within the SO; ii) to reconstruct the palaeocirculation history of deep and bottom water masses within the SO across the last 1.5 Ma; and iii) investigate the role of these deep and bottom water circulation changes in wider palaeoclimatic changes across this time period. To that end, the remainder of this thesis is divided into the following 5 chapters:

Chapter 2 provides details about the locations and composition of marine sediment cores analysed in this study, and the procedures employed in the analysis of sediments from these records.

In **Chapter 3** I present records of $\delta^{18}O$ and $\delta^{13}C$ measured on benthic and planktic foraminifer as well as the barium/titanium (Ba/Ti) ratios, total organic carbon contents and $CaCO_3$ contents of sediments of a piston core collected from the West Antarctic continental slope in the Amundsen Sea, eastern Pacific sector of the SO. The benthic $\delta^{13}C$ data (measured on *Cibicides* cf. *wuellerstorfi*) are first placed in the context of a compilation of all previously published $\delta^{13}C_b$ measurements conducted on *C. wuellerstorfi* from sediment cores south of 30°S during the current interglacial and the last glacial period. The full 800-kyr record of benthic $\delta^{13}C$ at site PC493 is then discussed in the context of SO palaeocirculation and the role of biological productivity and deep ocean ventilation in changes to the pCO_2^{atm} of the Late Quaternary.

In **Chapter 4** I present an authigenic ε_{Nd} record of deep water palaeocirculation changes from the equatorial Indian Ocean over the last 1.5 Ma. As deep waters in the Indian Ocean are sourced in the SO, this new data provides insights into the palaeocirculation history of

the Atlantic and Indian sectors of the SO. Emphasis is placed on studying the advection of deep waters sourced in the North Atlantic into the SO and the propagation of this chemical signature to the deep equatorial Indian Ocean.

In **Chapter 5** I present two new authigenic ε_{Nd} records measured on the Fe-Mn coatings of planktic foraminifera and sediments, as well as detrital ε_{Nd} data, from two cores in the western Pacific sector of the SO, north of the Ross Sea. These records provide insights into past changes in the ε_{Nd} composition and production of bottom waters formed in the Ross Sea, both at a low resolution over the last 540 kyr, and at a higher resolution across the last 56 kyr, with a particular emphasis on land-ice-ocean interactions across these intervals.

In **Chapter 6** I draw together the findings of the previous three chapters into a synthesis of SO palaeocirculation changes across the glacial-interglacial cycles of the last 1.5 Ma, and look ahead to the new research challenges presented by these findings.

Chapter 2

Methods

All sieving of marine sediment samples, picking of benthic and planktic foraminifera, picking of siliceous marine microfossils and leaching of sediment ferromanganese oxyhydroxides carried out during this PhD was performed in normal laboratory conditions. All detrital dissolution and column chemistry procedures were performed in a pressure- and temperature-controlled clean laboratory with air filtration systems. All chemical procedures for cleaning laboratory consumables, dissolution of detrital sediments and column chromatography were performed in ventilated fume hoods, and drying down of samples was carried out using air-tight dry down boxes. All neodymium isotope, minor and rare earth element concentration analyses and stable carbon and oxygen isotope analyses were performed using mass spectrometers in temperature and pressure controlled laboratories. Unless stated otherwise, all acids used in chemical procedures during this PhD were quartz distilled in a pressure- and temperature- controlled clean laboratory with air filtration systems. All centrifuge tubes used in work carried out as part of this thesis were first acid-cleaned using reagent-grade 20% nitric acid (HNO_3) at room temperature for a minimum of 24 hours. All Teflon vials used as part of this PhD were first cleaned with 50% reagent grade HNO_3 at 80°C for a minimum of 10 hours, then fumed with concentrated hydrochloric acid (HCl) on a hot plate at 80°C for a minimum of 10 hours.

2.1 Core locations and typical sedimentary compositions analysed

Samples from marine sediment cores collected at four sites were utilised for this study: Ocean Drilling Program (ODP) Leg 121 Site 758 located in the eastern equatorial Indian Ocean, NBP9802-04PC1 and NBP9802-06PC1 from the Pacific-Antarctic Ridge in the western

Pacific sector of the Southern Ocean (SO), and PC493 from the Amundsen Sea in the eastern Pacific sector of the SO (Figure 2.1. and Table 2.1.). All sites were chosen as they are today either bathed in Circumpolar Deep Water (CDW), or waters ultimately derived from CDW.

Table 2.1 Location of sediment cores studied in this work

Core Site	Latitude	Longitude	Water Depth	Water Mass	Average Sed Rate
PC493	71°07'50" S	119°54'49" W	2077 m	LCDW	0.4 cm/kyr
ODP 121-758	5°23'03" N	90°21'40" E	2935 m	m-CDW	1.5 cm/kyr
NBP9802-06PC1	61°52'00" S	169°58'00" W	3245 m	LCDW	3.8 cm/kyr
NBP9802-04PC1	64°12'00" S	170°05'00" W	2696 m	LCDW	1.4 cm/kyr

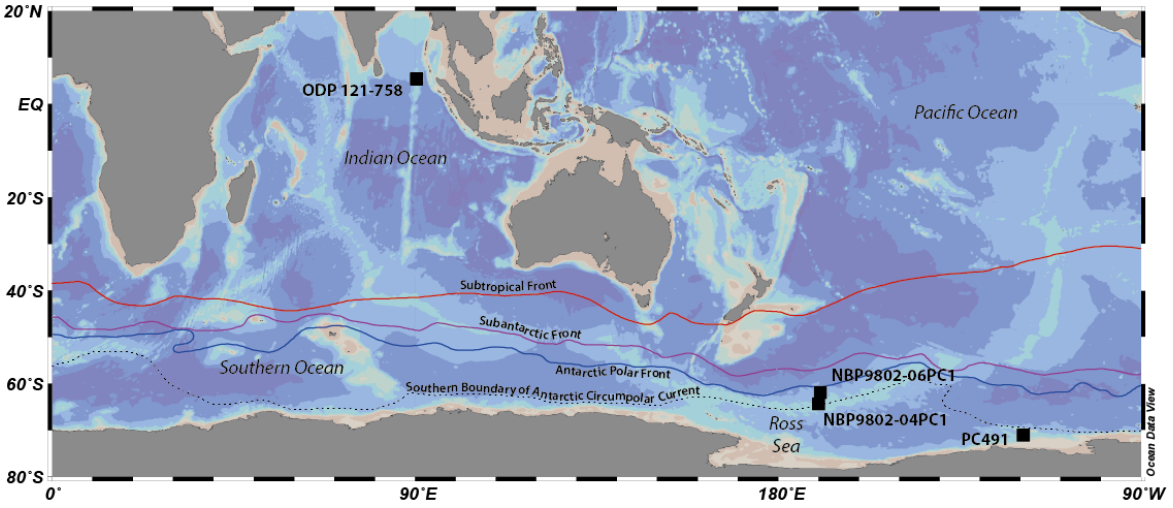

Fig. 2.1 A map of the core sites utilised as part of this work. Also shown are the location of major frontal positions and the southern limit of the Antarctic Circumpolar Current. Map created using Ocean Data View (Schlitzer, 2015)

The sediments of Site 758 consist of alternating light grey foraminiferal oozes with clay, and dark grey foramainiferal oozes with clay, and contain between 40-60 weight percent calcium carbonate. The sediments of cores NBP9802-04PC1 and NBP9802-06PC1 consist of siliceous oozes with clay and diatomaceous oozes with clay, with typical sedimentary opal contents of between 70-90 weight percent. Foraminiferal carbonate in both sediment cores NBP9802-04PC1 and NBP9802-06PC1 is limited to the upper core sections and the last glacial and penultimate glacial periods. Foraminifera are more prevalent in the sediments of core NBP9802-04PC1 than NBP9802-06PC1, reflecting the shallower water depth and better calcium carbonate preservation potential at this site. Site PC493 is situated on a

seamount in the Amundsen Sea, and its sediments consist of foraminiferal oozes, muds and foraminifera-bearing muds. The variable nature of sediments analysed as part of this work necessitated a variety of methodological approaches, which are summarised in table 2.2.

2.2 Neodymium Isotope, minor and REE analyses

2.2.1 Sample processing for elemental separation

2.2.1.1 Processing of planktic foraminifera samples

Bulk marine sediment samples were first wet sieved using reverse osmosis (RO) filtered water to separate <125 μm and >125 μm sediment size fractions (samples from sites NBP9802-06PC1, NBP980204PC1 and ODP Leg 121 Site 758) or <63 μm and >63 μm (samples from site PC493) sediment size fractions. To maximise the yield of foraminifera from the sediments of cores NBP9802-04PC1 and NBP9802-06PC1, sample volumes of 30 cubic centimetres (cc) each spanning 3 cm core depth (n= 101) and 50 cc across 5 cm core depth (n= 9) were utilised in this study. This represents an averaging of between 0.08-2.00 kyr (NBP9802-04, average 1.1 kyr) and 0.01-0.44 kyr (NBP9802-06, average = 0.20 kyr). The sediments of Site 758 and site PC493 both contain abundant foraminifera throughout and so samples spanning 1 cm core depth were used. Sample volumes of 14 cc (n= 4) and 7 cc (n= 150) from Site 758 and c. 5 cc from site PC493 were utilised in this study. Mixed species of planktic foraminifera – mostly the polar species *Neogloboquadrina pachyderma* sinistral (cores PC493, NBP9802-04PC1 and NBP9802-06PC1) and *Globigerinoides ruber*, *Pulleniatina obliquiloculata* and *Neogloboquadrina dutertrei* (Site 758) – were picked from the >125 μm or >63 μm size fraction for neodymium (Nd) isotopic analyses of authigenic ferromanganese oxyhydroxides using a fine paintbrush dipped in RO filtered water. Due to the general lack of foraminifera preserved in Southern Ocean sediments, no lower limit was placed on the foraminifera sample size picked for this work, however it was found that Nd isotope analyses were not possible on samples of less than c. 2.8 mg calcite.

A variety of studies have demonstrated that analyses of both 'chemically cleaned' and 'chemically uncleaned' planktic foraminifera record the neodymium isotope signature of bottom waters, rather than that of the surface seawaters in which they calcify (Piotrowski et al., 2012; Pomiès et al., 2002; Roberts et al., 2012, 2010; Tachikawa et al., 2013), as first suggested by Palmer and Elderfield (1985, 1986) following the findings of Boyle (1983). The method utilised in this work is that of Roberts et al. (2010), which excludes any chemical cleaning of the planktic foraminifera. Picked planktic foraminifera tests were first crushed between two glass plates separated by a 50 μm or 75 μm shim, for foraminifera of <c. 250

Table 2.2 A summary of key analytical procedures performed on the marine sediment cores used in this thesis.

	Core PC493	**Core NBP9802-04 PC1**	**Core NBP9802-06 PC1**	**Ocean Drilling Project Leg 121 Site 758**
ε_{Nd}: Planktic foraminifera authigenic ε_{Nd}	Mixed planktic from >63 μm size fraction	Mixed planktic from >125 μm size fraction	Mixed planktic from >125 μm size fraction	Mixed planktic from >125 μm size fraction
ε_{Nd}: Sediment leachate authigenic ε_{Nd}	-	< 125 μm size fraction in 0.02 mol/L HH and 4.4 mol/L acetic acid solution	< 125 μm size fraction in 0.02 mol/L HH and 4.4 mol/L acetic acid solution	Bulk sediment in 0.005 mol/L HH and 2.6 mol/L acetic acid solution
ε_{Nd}: Siliceous microfossil authigenic ε_{Nd}	-	-	Mixed sponge spicules, diatoms and radiolaria	-
ε_{Nd}: Detrital composition	-	< 125 μm size fraction	< 125 μm size fraction	-
δ^{13}C: Benthic foraminifera species	*C.* cf. *wueller-srtorfi*	Non present	Non present	-
δ^{13}C: Planktic foraminifera species	*N. pachyderma* sin.	-	-	-
δ^{18}O: Benthic foraminifera species	*C.* cf. *wueller-srtorfi*	Non present	Non present	-
δ^{18}O: Planktic foraminifera species	N. *pachyderma* sin.	-	-	-

μm and >c. 250 μm, respectively. Crushed foraminifera tests were then rinsed with Millipore Type 1 ultrapure Milli-Q deionised water with a resistivity of 18.2 MΩ·cm at 25°C (hereafter termed Milli-Q water) and sonicated to separate clay particles from calcite. The clay particles in suspension were pipetted off, and the sonication and pipetting processes repeated until the water appeared clear of clays. Crushed foraminifera tests were then poured into 15 mL centrifuge tubes, topped up with Mili-Q water, centrifuged at 3000 revolutions per minute (rpm) for 5 minutes and the supernatant pipetted to waste. The foraminifera calcite was dissolved via the addition of 100 μL aliquots of 1 mol/L reagent grade acetic acid up to a maximum of 1.5 mL, at which point samples were sonicated until dissolution was complete. To ensure any remaining detrital particles were removed, the solution containing dissolved foraminifera tests was then centrifuged at 4500 rpm for 10 minutes and the supernatant containing the dissolved sample pipetted into 1.5 mL centrifuge tubes. The sample was then centrifuged a final time at 10000 rpm for 10 minutes, and the supernatant containing the dissolved sample transferred into Teflon vials and dried down overnight at 60°C.

2.2.1.2 Sediment and siliceous microfossil leachates

For the dissolution of authigenic ferromanganese oxyhydroxides coatings of sediments from cores NBP9802-06PC1 and NBP9802-04PC1, approximately 2 g of the <125 μm sediment size fraction was leached in a 30 mL solution of 0.02 mol/L hydroxylamine hydrochloride (HH) in 4.4 mol/L acetic acid for 1 hour following the procedure of Wilson (2011). Samples were then centrifuged at 5000 rpm for 10 minutes and the supernatant containing dissolved ferromanganese oxyhydroxides decanted into 15 mL centrifuge tubes. Samples in solution were then again centrifuged at 6000 rpm and the supernatant containing the dissolved samples decanted into Teflon vials and dried down overnight at 60°C.

Sediment samples from Site 758 were split into two aliquots, one for sieving and separation of planktic foraminifera and one for leaching of the bulk sediment. The bulk sediments were then leached for 30 minutes in a 30 mL solution of 0.005 mol/L HH and 2.6 mol/L acetic acid. This weaker leaching solution and shorter leaching time follows the findings of Blaser et al. (2016), who showed that a weaker solution and shorter period of reactivity more reliably extracts authigenic Nd and reduces the likelihood of contamination by leaching of volcanogenic phases. Samples were then centrifuged at 5000 rpm for 10 minutes and the supernatant containing dissolved ferromanganese oxyhydroxides decanted into 15 mL centrifuge tubes. Samples in solution were then centrifuged at 6000 rpm and the supernatant containing the dissolved samples decanted into Teflon vials and dried down overnight at 60°C. No acetic acid decarbonation step was employed in any of these studies, as it has been shown that this can lead to leaching of detrital Nd (Wilson et al., 2013).

Between 5-12 mg of siliceous microfossils (a mixture of sponge spicules and mixed species of diatoms and radiolaria) was picked from the >125 μm size fraction of three opal-rich sediment samples from core NBP9802-06PC1 to assess the potential of opal as a carrier phase for ferromanganese oxyhydroxides. Siliceous microfossils were isolated and picked using a fine paint brush before being crushed between two glass plates and transferred to a beaker and rinsed with Milli-Q. The siliceous microfossils suspended in Milli-Q were sonicated to separate clay particles, and any clay particles in suspension were pipetted off. The sonication and pipetting processes was repeated until the water appeared clear of clays before transferal of the siliceous microfossil samples into 15 mL centrifuge tubes. The samples containing siliceous microfossils were then centrifuged and the supernatant decanted before addition of 10 mL of 0.02 mol/L HH in 4.4 mol/L reagent grade acetic acid to leach authigenic ferromanganese oxyhydroxides. The siliceous microfossils samples were then agitated on a vortex mixer and leached for two hours on a rotating wheel before centrifugation at 5000 rpm for 10 minutes and transferal into Teflon vials. To assess the proportion of authigenic ferromanganese oxyhydroxides leached using this procedure, the two hour 0.02 mol/L HH leaching process was then repeated twice more on the siliceous microfossil residue left in the 15 mL centrifuge tubes, with dissolved authigenic ferromanganese oxyhydroxides leachate, centrifuged and decanted into new Teflon vials each time. The samples contained within the Teflon vials were then dried down overnight at 60°C.

2.2.1.3 Detrital sediments

Following the leaching procedures outlined in section 2.3.1.2, sediments from the <125 μm size fraction were twice leached over a 24-hour period in a 0.005 mol/L HH solution to remove all remaining authigenic coatings. The <125 μm size fraction was chosen to allow a direct comparison between authigenic and detrital ε_{Nd} values. To remove any remaining HH solution and associated dissolved authigenic coatings, samples were first rinsed with Mili-Q water, centrifuged for ten minutes at 5000 rpm and the supernatant decanted, before being centrifuged a second time at 6000 rpm and the supernatant decanted. The remaining detrital sediment was then rinsed into Teflon vials using Milli-Q water and dried down at 60°C. Next, 12 mL of 5% hydrogen peroxide solution was added to remove organic matter and samples were dried down at 100°C. Samples were then digested in a solution of 3 mL concentrated HNO_3 and 1.5 mL 50% hydrofluoric acid (HF) at 110°C for 48 hours, before drying down overnight at 70°C. Samples were subsequently redissolved in 5 mL aqua regia, a mixture of concentrated HNO_3 and concentrated HCl at a molar ratio of c. 1:3, before drying down at 80°C for 24 hours.

2.2.2 Column Chromatography

Foraminifera, siliceous microfossil and sediment leachate samples were redissolved in 5 mL 0.33 mol/L HNO_3, and detrital samples were redissolved in 5 mL 1 mol/L HNO_3. An aliquot of 250 μL (5%) was taken from the redissolved samples for analyses of minor and rare earth element (REE) concentrations. All samples were then dried down at 60°C. REE were isolated using Eichron TRUspec^{TM} resin (100-150 μm mesh) in 100 μL Teflon columns. Nd was then extracted using Eichron LNspec^{TM} resin (50-100 μm mesh) in volumetrically calibrated Teflon columns. Appendix Tables B.1 and B.2 contain a more detailed account of column procedures.

2.2.3 Analyses of minor and rare earth element concentrations

A 5% aliquot from each foraminifera and leachate ε_{Nd} sample dissolved in 0.33 mol/L HNO_3 and each detrital ε_{Nd} sample dissolved in 1 mol/L HNO_3 was taken prior to column chemistry to determine the concentration of minor elements and REE. Analyses of Magnesium (Mg), Manganese (Mn), Zirconium (Zr), Barium (Ba), Hafnium (Hf), Lead (Pb), Strontium (Sr), Uranium (U) and REE concentrations was performed using a PerkinElmer SCIEX Elan DRC II Quadropole inductively coupled mass spectrometer in the Department of Earth Sciences, University of Cambridge. A linear calibration curve for each run of samples was constructed using 8 calibration standards of a known concentration. In turn, this calibration curve was used to determine the concentration of elements in each sample. Two additional standards with known REE concentrations and patterns were included between every 10 samples to allow external reproducibility to be calculated and to monitor oxide production. Errors in concentration measured on this standard were typically <2% and never exceeded 5% in any of the analyses performed as part of this study. Internal drift of count intensity was corrected throughout each run by adjusting measured intensities to expected values using Rhodium (Rh), Indium (In) and Rhenium (Re) standards.

All REE results presented in this thesis are normalised to Post Archean Australian Shale (PAAS; Pourmand et al. (2012); Taylor and McLennan (1985); non-normalised data are provided in appropriate appendix tables. Elemental anomalies are defined in equations (1.1), (1.2) and (1.3) below.

$$\frac{Ce}{Ce*} = \frac{Ce_{[PAAS]}}{0.5(La_{[PAAS]}) + 0.5(Pr_{[PAAS]})} \tag{2.1}$$

$$\frac{Eu}{Eu*} = \frac{Eu_{[PAAS]}}{(Sm_{[PAA]S} + Gd_{[PAAS]})^{0.5}} \tag{2.2}$$

$$\frac{MREE}{MREE*} = \frac{2MREE_{[PAAS]}}{LREE[PAAS]) + HREE[PAAS])} \tag{2.3}$$

Where $LREE = (LA_{[PAAS]} + Pr_{[PAAS]} + Nd_{[PAAS]})$; $MREE = Gd_{[PAAS]} + Tb_{[PAAS]} + Dy_{[PAAS]})$ and $HREE = (Tm_{[PAAS]} + Yb_{[PAAS]} + Lu_{[PAAS]})$.

In addition to the analyses of minor and REE, following the separation of Nd via the column chromatography techniques outlined in section 2.3.2., an aliquot was taken for the analyses of Nd concentrations prior to Nd isotopic analyses. This is a necessary step as Nd is unavoidably lost during elemental separation via column chromatography, and knowledge of the concentration of Nd within samples is required for appropriate standard bracketing, and to ensure that mass spectrometer Faraday cups are not overloaded by high Nd concentrations during analyses. Typical REE yields for TRUSpec were >95%, and yields for LNSpec were >90% for the majority of samples. Some LNSpec yields were between 80-90%, but the number of samples affected by this lower yield is estimated at fewer than 5% of samples measured in this study. For this samples were redissolved in 1 mL 2% HNO_3 and a 20 μL aliquot transferred into 0.5 mL centrifuge tubes, to which 380 μL of 2% HNO_3 was added. Nd concentrations were then measured using a PerkinElmer SCIEX Elan DRC II Quadropole inductively coupled mass spectrometer in the Department of Earth Sciences, University of Cambridge. A linear calibration curve was constructed using Nd standards of between 0.01 and 100 ppb Nd, which was then used to determine the concentration of Nd in each sample. A calibration curve was determined at the beginning and end of each analytical run, with additional curves produced every 50 samples when analysing >100 samples in a single analytical run. A standard with Nd concentrations of 0.25 ppb was analysed at the start and end of every analytical run, and between every 20 samples.

2.2.4 Neodymium isotopic analyses: Neptune Plus Multi-Collector ICP-MS

All samples in this work were analysed for Nd isotopes on a Neptune Plus multi-collector inductively coupled plasma mass spectrometer (MC-ICPMS) in the Department of Earth Sciences, University of Cambridge. Sediment leachates with >200 ng Nd were mainly analysed using an Elemental Scientific Inc. APEX IR desolvating nebuliser using an ACM membrane and nitrogen addition gas to minimise oxide formation. All foraminifera, detrital, and the remaining sediment leachate samples were analysed using an Aridus II system using nitrogen addition gas. Sample uptake rates were typically c. 80 μL/minute using the APEX ACM system and c. 45 μL/minute using the Aridus II system. Nickel Jet sample

cones and X skimmer cones were used for all analyses, and all samples were analysed in a matrix of 2% Teflon distilled HNO_3. Mass dependant fractionation effects were corrected for by normalising to $^{146}Nd/^{144}Nd$ of 0.7219 and applying an exponential correction. All samples were bracketed by a concentration matched solution of the reference standard JNdi-1, corrected to $^{143}Nd/^{144}Nd = 0.512115 \pm 7$ (Tanaka et al., 2000). Nd oxides were manually monitored throughout each analytical run, typically every 4-10 hours. When Nd oxide levels reached greater than 0.4% of Nd signal intensity, analyses parameters were adjusted to minimise oxides, typically by changing gas flow velocities, adjusting the torch position, or removal and cleaning of sample and skimmer cones. ^{147}Sm was also measured during all analyses to monitor for isobaric interference from ^{144}Sm, assuming a $^{147}Sm/^{144}Sm$ ratio of 4.83871. No samples in this work required correction for ^{144}Sm interference.

Samples containing more than 9 ng of Nd were measured in 30 separate analysis cycles each lasting 8 seconds. The $^{143}Nd/^{144}Nd$ ratio for each sample are the average of these 30 cycles of analyses; the internal error quoted in this work is double the standard error of the mean (S.E.M) of these analyses, as given by Equation 2.4 below.

$$S.E.M = \frac{s.d.}{\sqrt{n}} \tag{2.4}$$

Where $s.d.$ is the standard deviation of mean values and n is the number of analysis cycles (e.g. 30).

External errors are the external reproducibility of the reference standard JNdi-1, taken as double the standard deviation (2σ) of all standards within a single analytical run. Sample uptake time (the time between the initiation of an analysis and the actual measurement of $^{143}Nd/^{144}Nd$ ratio within a sample or standard) was 60 seconds for samples containing greater than 9 ng of Nd. An uptake time of 60 seconds was chosen to maximise analyses stability – and thus minimise internal error – without wasting too much sample. This analytical setup theoretically allowed for analyses of c. 400 μL of sample using the APEX ACM system and c. 225 μL of sample using the Aridus II. To allow for evaporation of samples prior to analyses, samples containing greater than 9 ng of Nd were prepared in volumes of 500 μL and 300 μL to be analysed using the APEX ACM system and Aridus II, respectively.

To allow for the analyses of more concentrated samples in smaller solutions whilst minimising internal error, samples containing less than 9 ng of Nd, all of which were analysed using the Aridus II, were measured in 40 cycles of 4.2 seconds, with an uptake time of 45 seconds. This allowed for the analyses of samples in volumes of c. 160 μL. To account for the loss of sample due to evaporation, samples were diluted to either 200 μL (samples containing 9 to 4 ng of Nd) or 180 μL (samples containing less than 4 ng of Nd).

External reproducibility of ε_{Nd} measured using the APEX ACM system and the reference standard JNdi-1 with 40 ng of Nd was between 0.05 and 0.26 epsilon units, averaging 0.11 for all analyses performed using this analytical setup in this thesis, while internal errors for samples across the same analytical runs using the APEX ACM system was between 0.04 and 0.26 epsilon units, and averaged 0.10. 2σ external reproducibility of ε_{Nd} measured with the Aridus II ranged from 0.08 to 0.42 epsilon units, while internal errors ranged from 0.06 to 0.76. Typical errors for different sample concentrations and analytical setups used during analyses performed as part of this thesis are shown in Table 2.3. below.

Table 2.3 Typical internal and external errors achieved using differing analytical setups on the Neptune Plus MC-ICPMS in the Department of Earth Sciences, University of Cambridge.

Nebuliser	**Method[1]**	**Approx. Nd Analysed**	**Internal Error (2*S.E.M)**	**External Error (2σ)**	**Reported Error**
APEX-ACM	30*8s	40 ng	0.10 ε_{Nd}	0.11 ε_{Nd}	0.11 ε_{Nd}
Aridus II	30*8s	20 ng	0.14 ε_{Nd}	0.19 ε_{Nd}	0.19 ε_{Nd}
Aridus II	30*8s	12 ng	0.17 ε_{Nd}	0.20 ε_{Nd}	0.20 ε_{Nd}
Aridus II	40*4.2s	6 ng	0.17 ε_{Nd}	0.13 ε_{Nd}	0.21 ε_{Nd}
Aridus II	40*4.2s	4.7 ng	0.22 ε_{Nd}	0.25 ε_{Nd}	0.25 ε_{Nd}
Aridus II	40*4.2s	4 ng	0.22 ε_{Nd}	0.22 ε_{Nd}	0.22 ε_{Nd}
Aridus II	40*4.2s	3.2 ng	0.31 ε_{Nd}	0.36 ε_{Nd}	0.36 ε_{Nd}
Aridus II	40*4.2s	2.5 ng	0.30 ε_{Nd}	0.39 ε_{Nd}	0.39 ε_{Nd}
Aridus II	40*4.2s	2 ng	0.29 ε_{Nd}	0.32 ε_{Nd}	0.32 ε_{Nd}
Aridus II	40*4.2s	1.5 ng	0.42 ε_{Nd}	0.42 ε_{Nd}	0.42 ε_{Nd}

[1] *refers to number of analysis cycles per sample and length of analysis time per cycle; e.g. 30 cycles of analyses each lasting 8 seconds.*

Both internal and external reproducibility were largely dependent on the concentration of the sample analysed, however, the relationship between internal and external errors and sample concentration in samples containing less than c. 6 ng Nd was not uniform between analytical runs. Samples containing less than 6 ng Nd were more susceptible to variations in tuning parameters or external variables such as changes in air pressure and/or temperature. This susceptibility to external factors led to more variable internal and external errors between analytical runs at lower concentrations; this is particularly pronounced in samples containing

less than c. 3.2 ng Nd (see table 2.3). The errors reported in figures and text in this thesis are the 2σ external reproducibility of JNdi-1 standards across each run of samples, unless the internal error is greater, in which case the reported error is the combined internal and external errors summed in quadrate, as given by Equation 2.5. below. Complete procedural Nd blanks averaged <24 pg (n = 10, from column chemistry stage onwards), or <1.6% of the smallest sample analysed in this work (1.5 ng).

$$Error = \sqrt{(2S.E.M)^2 + (2\sigma)^2} \tag{2.5}$$

2.3 Stable oxygen and carbon isotope analyses on planktic and benthic foraminifera tests

Planktic and benthic foraminifera samples for stable carbon (δ^{13}C) and oxygen (δ^{18}O) isotope analyses were picked from the sieved 63-2000 μm size fraction of core PC493 and the >125 μm size fraction for all other cores. Where possible 5-20 benthic foraminifera tests were picked, however there were often fewer than 5 tests present in a sample, and consequently some analyses had to be conducted on just 1 or 2 tests. Samples from core PC493 contained specimens which are similar in appearance to *C. wuellerstorfi* and most likely represent *C. wuellerstorfi* morphotypes. *Cibicidoides wuellerstorfi* was picked preferentially in samples from PC493, but in some cases the *C. wuellerstorfi* morphotypes had to be picked due to a lack of *C. wuellerstorfi*; specimens from this core are therefore identified as *C.* cf. *wuellerstorfi*. 10-25 tests *Neogloboquadrina pachyderma* sinistral were analysed in all planktic foraminifera samples. Analyses were performed at the Godwin Laboratory for Palaeoclimate Research at the Department of Earth Sciences, University of Cambridge. Both benthic and planktic foraminifera were first crushed and soaked in a solution of 3% H_2O_2 for 30 minutes, then acetone was added and the sample ultrasonicated for 10 seconds before the supernatant was decanted. Samples were then dried at 50°C overnight. Each vial was sealed with a septa and screw cap and analysed using a Micromass Multicarb sample preparation system attached to a VG SIRA Mass Spectrometer. Each run of 30 samples was accompanied by 10 samples of reference carbonates and 2 control samples. Stable carbon and oxygen isotope results are reported with reference to the international standard Vienna PeeDee Belemnite (VPDB) as given by Equations 2.6. and 2.7. below. External analytical precision for all samples presented in this thesis is better than $\pm$ 0.06‰ for δ^{13}C and $\pm$0.08‰ for δ^{18}O (1 sigma).

$$\delta^{13}C = (\frac{^{13}C/^{12}C_{sample}}{^{13}C/^{12}C_{reference}} - 1) * 1000 \tag{2.6}$$

$$\delta^{18}O = (\frac{^{18}O/^{16}O_{sample}}{^{18}O/^{16}O_{reference}} - 1) * 1000 \quad (2.7)$$

2.4 Additional sedimentological, geochemical and palaeo magnetic analyses on core PC493

Additional sedimentological, geochemical and palaeomagnetic data sets produced on sediments from core PC493 were made available for my PhD project, the methods for which are summarised here. Magnetic susceptibility and wet-bulk density were measured on the full diameter (unsplit) core sections using a GEOTEK multi-sensor core logger at the British Ocean Sediment Core Research Facility (BOSCORF) at the National Oceanography Centre in Southampton (UK). Afterwards the core sections were split length ways using a router system and cheese wire at the British Antarctic Survey in Cambridge (UK) and designated as working and archive halves. The sections were photographed and X-rayed, and the lithological composition and sedimentary structures were described visually, using X-radiographs and by microscopic analysis of smear slides. The split archive halves of the core were analysed using an Avaatech X-ray fluorescence (XRF) core scanner at the Department of Earth Sciences, University of Cambridge (UK), to obtain semi-quantitative elemental data at 2.5 mm spatial resolution. The core surface was carefully cleaned and covered with a 4 μm thin SPEXCertiPrep Ultralene foil to avoid contamination and reduce desiccation. XRF data were collected along the entire lengths of the core sections. The length and width of the irradiated surfaces were 10 and 12 mm, respectively. A Canberra X-PIPS Silicon Drift Model SXD 15C-150-500 with 150eV X-ray resolution detector and a Canberra Digital Spectrum Analyzer 1000 were used. Spectra were fitted with WinAxil software. The XRF scanning was undertaken to obtain Barium/Titanium ratios, an indicator for the palaeo-productivity proxy biogenic barium. Total carbon content (TC) was determined on ground bulk sediment samples using a Vario EL III Elementar analyser at the Institute for Geophysics and Geology, University of Leipzig (Germany). The organic carbon content (TOC) was measured with an Eltra METALYST-CS-1000-S after removal of the inorganic carbon with HCl, and CaCO3 contents were calculated from this TC and TOC data. Discrete orientated samples for palaeomagnetic investigations were taken continuously along the length of the core using plastic cubic boxes with a volume of 6.2 cm^3. Palaeomagnetic directions and magnetisation intensities were measured on a cryogenic magnetometer (model 2G Enterprises 755 HR) at the Department of Geosciences, University of Bremen (Germany). Natural remanent magnetisation was measured on each sample before these were subjected to a systematic

demagnetisation treatment involving 16 steps for each sample with a maximum alternating field intensity of 100 mT. A detailed vector analysis was applied to the results in order to determine the inclination of the characteristic remanent magnetisation (ChRM). Samples showing no systematic demagnetisation pattern were rejected.

Chapter 3

Late Quaternary stable carbon isotopes of Lower Circumpolar Deep Water (LCDW) in the Pacific sector of the Southern Ocean

3.1 Introduction

In this chapter, I will present a new benthic $\delta^{13}C$ ($\delta^{13}C_b$) record of deep water circulation from the Pacific sector of the Southern Ocean (SO). I will place this new record in the context of measurements made of the $\delta^{13}C$ of dissolved inorganic carbon in seawater ($\delta^{13}C_{seawater}$) from the modern SO, and seawater $\delta^{13}C$ reconstructions ($\delta^{13}C_{palaeoSW}$) for the SO from the Last Glacial Maximum (LGM, 18-24 ka) and throughout the Late Quaternary. I will then go on to discuss the implications of these $\delta^{13}C_{palaeoSW}$ reconstructions for Atlantic to Pacific palaeocirculation, SO deep water formation, and nutrient cycling through the last 800,000 years.

3.1.1 Evidence for reduced ventilation of Southern Ocean sourced waters during past glacial periods

Knowledge of the past geometry and rate of the oceanic global thermohaline circulation, in particular the connectivity of the deep ocean with the atmosphere, i.e. its ventilation state, is key to understanding changes in oceanic carbon storage via the 'solubility' and the 'biological' pumps (see section 1.1). As the formation region of Antarctic Intermediate Water

(AAIW) and Antarctic Bottom Water (AABW), the SO plays a critical role in determining the ventilation state of the deep ocean interior (Gebbie and Huybers, 2011; Knox and McElroy, 1984; Sarmiento and Toggweiler, 1984; Siegenthaler and Wenk, 1984). Today, widespread upwelling of deep water within the SO occurs south of the Antarctic Polar Front (APF) (Orsi et al., 1995). Formation and sinking of AAIW occurs north of the APF (Sloyan et al., 2010; Talley, 1996) while formation and sinking of AABW occurs far south of the APF Orsi et al. (1999) (see section 1.3). These newly formed southern-sourced water masses flow northwards, ventilating much of the ocean interior. Owing to the incomplete utilisation of available nutrients in modern SO surface waters, AAIW and AABW also play a critical role in redistributing preformed nutrients to lower latitudes.

Reconstructions of Atlantic Meridional Overturning Circulation (AMOC) during the last glacial period (Curry and Oppo, 2005; Gebbie, 2014; Howe et al., 2016a; Lippold et al., 2016) show a shallowing of North-Atlantic sourced waters (northern component water, NCW), with an expanded deep overturning cell comprised of primarily SO-sourced deep waters (southern component water, SCW). During the LGM, a sharp chemical boundary between SCW and NCW has been identified at c. 2.5 km water depth within the Atlantic Ocean based on $\delta^{13}C_b$ reconstructions (Fig. 3.1) (Curry and Oppo, 2005; Peterson et al., 2014). This boundary has been identified during multiple glacials (Hodell et al., 2003; Oliver et al., 2010), and suggests a pronounced physical stratification of the Atlantic Ocean interior and reduced vertical mixing during glacials. Temperature and salinity reconstructions suggest that this glacial-age stratification was established and maintained by an increase in the salinity of waters below this chemical divide (Adkins et al., 2002; Roberts et al., 2016), while the shoaling of the boundary between NCW and SCW to depths above rough bathymetry led to a reduction in turbulant mixing across this boundary (Ferrari et al., 2014). During glacials, reduced mixing between dense, poorly ventilated SCW and overlying NCW (Adkins et al., 2002; Curry and Oppo, 2005; Hoogakker et al., 2015; Jaccard et al., 2016; Peterson et al., 2014), coupled with a more vigorous sequestration of carbon via the biological pump drove down atmospheric carbon dioxide (pCO_2^{atm}) (Sigman and Boyle, 2000; Yu et al., 2014, 2016). The subsequent breakdown of this stratification during glacial terminations led to the release of large amounts of this stored carbon back into the atmosphere, driving a rapid transition from glacial to interglacial states (Anderson et al., 2009; Schmitt et al., 2012) and thus the characteristic saw-tooth pattern of late Quaternary climate cycles (Bereiter et al., 2015; Lisiecki and Raymo, 2005).

Currently, most proxy evidence for stratification and carbon storage within the SO comes from records located north of or close to the APF, i.e. predominantly from the Subantarctic Zone (SAZ) (Hodell et al., 2003; Jaccard et al., 2016; Krueger et al., 2012; Moy et al.,

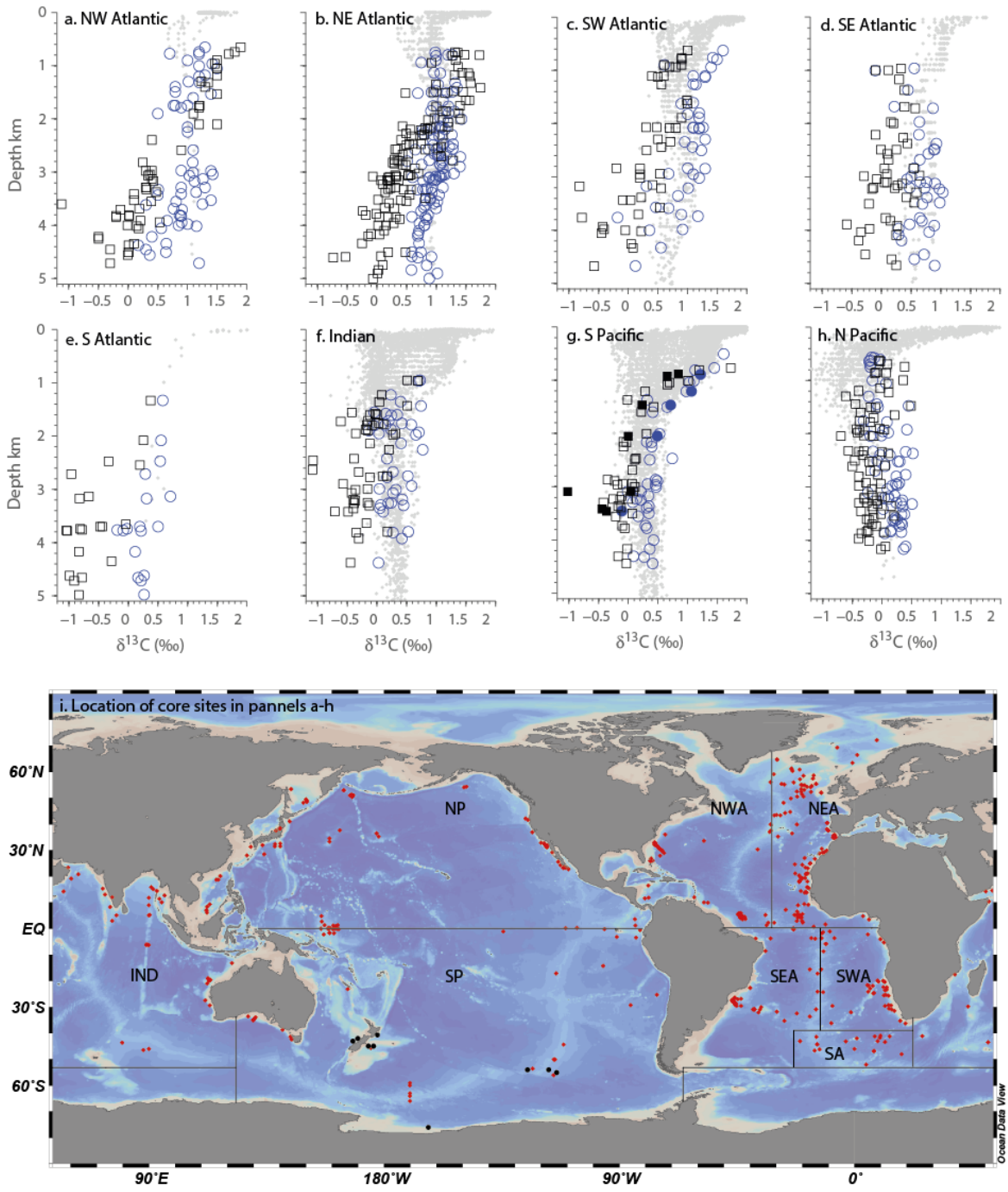

Fig. 3.1 a-h: δ^{13}C of dissolved inorganic carbon (DIC) in modern seawater (grey dots) and δ^{13}C of benthic foraminifera tests (*Cibicidoides* species) from the late Holocene (0-6 ka, blue circles) and LGM (18-24 ka, black squares) from different regions of the global ocean. Core sites in the Atlantic and, to a lesser extent, Indian oceans show evidence for a chemical boundary at c.2.5 km depth. Core locations (red and black dots) are shown in panel i. (NWA= North-West Atlantic; NEA= North-East Atlantic; SEA= South-East Atlantic; SWA= South-West Atlantic; SA= South Atlantic; Ind= Indian Ocean; SP= South Pacific; NP= North Pacific. Modified from data compilation of Peterson et al. (2014); additional data points from the South Pacific are highlighted as filled black squares and filed blue circles in panel g, and as black dots in panel i (Matsumoto et al., 2001; Molina-Kescher et al., 2016; Ronge et al., 2015; Ullermann et al., 2016). Map in panel i created using Ocean Data View (Schlitzer, 2015)

2006; Ullermann et al., 2016; Yu et al., 2014), where export productivity increased and fluctuated during past glacial periods (Chase et al., 2003; Lamy et al., 2014; Martínez-García et al., 2011). Variability in past export productivity hampers the use of nutrient-based palaeocirculation proxies, such as $\delta^{13}C_b$, as the relationship between $\delta^{13}C$ recorded in benthic foraminifer and the nutrient content of bottom waters can break down in regions of high seasonal productivity, leading to more negative $\delta^{13}C$ recorded in foraminiferal calcite (the 'phytodetritus' effect, Mackensen et al. (1993)). The paucity of records from areas south of the APF – in particular outside of the Atlantic sector – reflects a regional bias in the availability of foraminifera-based proxy archives in the SO, where carbonate is not as readily preserved as in other ocean basins. As the largest ocean basin, the Pacific Ocean must have played a crucial role in the drawdown and storage of pCO_2^{atm} during glacial periods. However, proxy evidence is still inconclusive as to whether the interior of the Pacific Ocean experienced a similar glacial-age stratification as the Atlantic. Available Pacific $\delta^{13}C_b$ values show no evidence for chemical stratification, and $\delta^{13}C_b$ values in in the deep South Atlantic were more ^{13}C-depleted than in the abyssal Pacific during the LGM; however this may due to the lack of $\delta^{13}C_b$ records from the central Pacific basin (Peterson et al. (2014); see Fig. 3.1). It is therefore still unclear how changes in the physical and chemical structure of water masses in the Atlantic propagated through the global ocean during the Late Quaternary glacial periods. In particular the glacial sources and pathways of bottom and deep-water masses in the SO are under debate (Adkins, 2013; Kobayashi et al., 2015; McCave et al., 2008). In this chapter I will present multi-proxy data from marine sediment core PC493 located 10° south of the APF in the Pacific sector of the SO, and examine circum-Antarctic connectivity and deep water formation in the SO, first during the last glacial period and then through the last 800 ka.

3.2 Hydrographic setting of site PC493

Piston core PC493 (71° 07'50" S 119°54'49" W, 2077 m. water depth, 10.4 m. recovery, of which 2.87 m. is presented here) was retrieved from the West Antarctic continental slope in the Pacific sector of the SO, during cruise JR179 aboard the RRS James Clark Ross in 2008 (Fig. 3.2). The core site is located on a seamount in the Amundsen Sea, a location previously reported to contain abundant calcareous foraminifera (cf. core PS2547 from the same site, see Hillenbrand et al. (2002)). In the modern Pacific sector of the SO, it is useful to subdivide Lower Circumpolar Deep Water (LCDW) into lower LCDW (a mixture of AABW and Circumpolar Deep Water [CDW] with a potential temperature of 0.0 to 0.7°C, hereafter lLCDW) and upper LCDW (a higher salinity mixture of CDW and North Atlantic

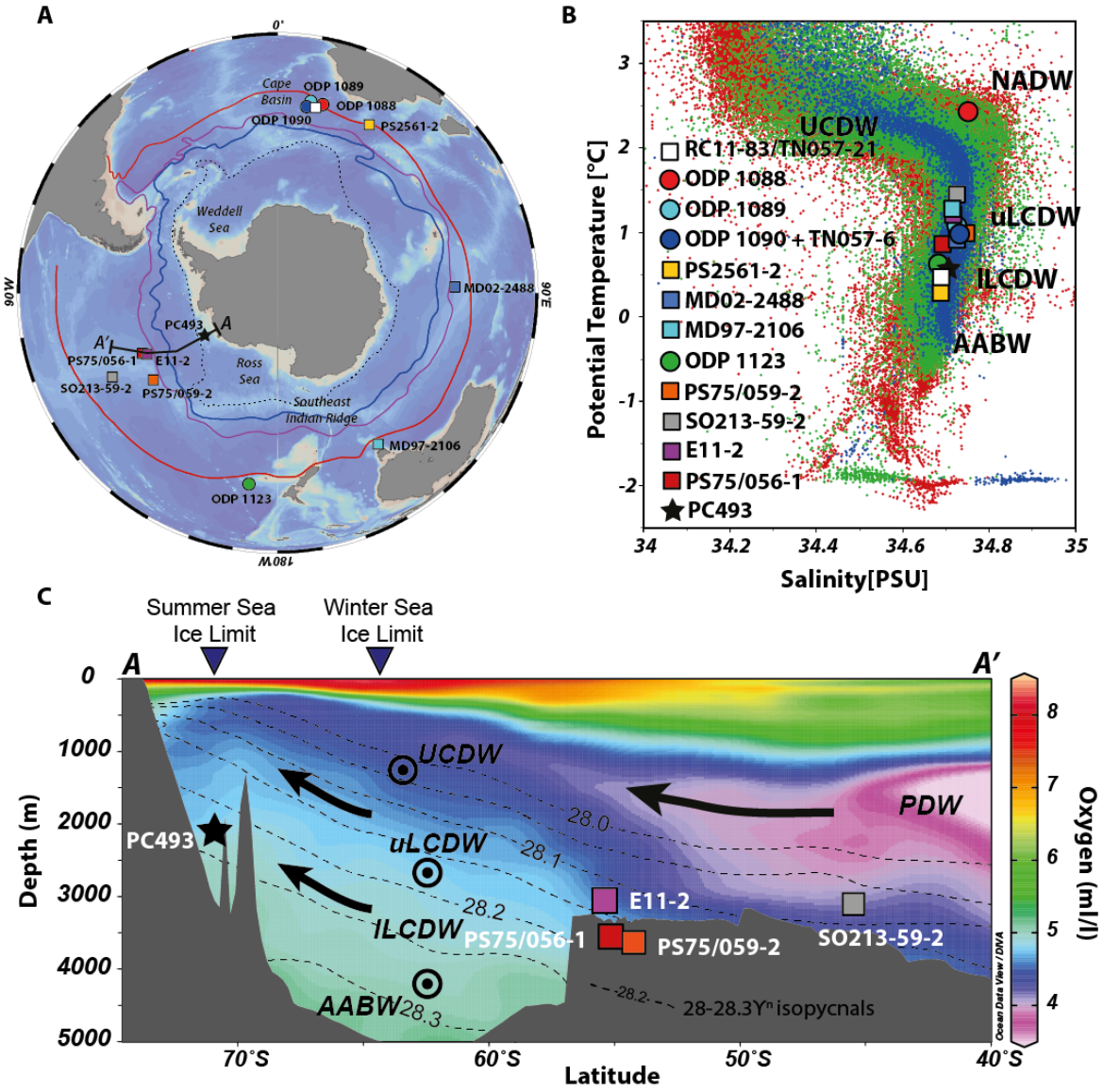

Fig. 3.2 A: Map of the SO and surrounding ocean basins. Key core sites discussed in the text are shown (for details see Table 3.1), as are the average positions of major oceanographic fronts (Orsi et al., 1995): the Subtropical Front (red), Subantartic Front (purple) and Antarctic Polar Front (blue), along with the position of the southern boundary of the ACC (black dashed line). B: Potential temperature and salinity of North Atlantic Deep Water (NADW), Upper Circumpolar Deep Water (UCDW), (upper/lower) Lower Circumpolar Deep Water ((u/l)LCDW) and AABW bathing core sites discussed in the text. Data from the SO's Atlantic sector are given in red, Indian sector in green and Pacific sector in blue. C: Hydrographic section of oxygen content across the central Pacific sector of the SO (line A-A' in panel A). Isopycnals highlight the upwelling of lLCDW and UCDW on the West Antarctica continental slope. PDW is characterised by low oxygen content, clearly distinguishable from LCDW and UCDW and AABW. The position of maximum summer and winter sea ice limits are also shown (Jacka, 1997). All plots created in Ocean Data View (Schlitzer, 2015), using hydropgraphic data from the Hydrographic Atlas of the Southern Ocean (panel B,Olbers et al. (1992) and World Ocean Atlas 2013 (panel C, Garcia et al. (2014).

Deep Water [NADW], hereafter uLCDW) (Carter et al., 2008). Located close to the modern maximum summer (February) sea-ice limit (Jacka, 1997), site PC493 is currently bathed in lLCDW as it upwells along the Antarctic continental margin south of the southern boundary of the clockwise flowing Antarctic Circumpolar Current (ACC) (Orsi et al., 1995) (Fig. 3.2). Site PC493 is located 'downstream' of inflowing NADW and AABW from the Weddell and Ross seas to the ACC, but 'upstream' of the main inflow of Pacific Deep Water (PDW) to the SO in the central and eastern Pacific (Talley, 2013), so is well situated to monitor the mixture of SO-sourced deep waters.

3.3 Results

3.3.1 Lithology

The top 2.87 m. of sediments recovered at site PC493 comprise a condensed but continuous sequence of olive brown, foraminiferal oozes, muds and foraminifera-bearing muds. The condensed nature of the sequence reflects the reduced supply of sediment to the site, in part owing to its position atop a seamount. The sediments contain varying amounts of planktic foraminifera (a nearly monospecific assemblage of *Neogloboquadrina pachyderma* sinistral), and low abundances of calcareous benthic foraminifera (mainly *Cibicidoides* cf. *wuellerstorfi*). A lithological log of the upper 3 m. and summary of results is provided in Fig. 3.3, and a complete list of data from core PC493 are provided in Appendix table C.1.

3.3.2 Stable oxygen isotopes and age model

The age model for core PC493 is constrained by the presence of the Bruhnes-Matuyama boundary (780 ka) at 277-284 cm core depth. Based on this, the age model is further refined via tuning of both *N. pachyderma* sin. and *C.* cf. *wuellerstorfi* δ^{18}O data to the global benthic δ^{18}O ($\delta^{18}O_b$) LR04 stack (Lisiecki and Raymo, 2005) (Fig. 3.3). It has been noted in numerous previously published studies that δ^{18}O measured on *C. wuellerstorfi* does not match equilibrium seawater, and an offset of 0.64‰ has been suggested to correct for vital effects (Shackleton, 1974), although this may be an over estimate (Marchitto et al., 2014) and may not be uniform in all ocean basins (Keigwin, 1998). The vital offset for *N. pachyderma* sin. δ^{18}O is less well characterised, with estimates ranging from 0.5 to 1.5‰ (Hendry et al., 2009; Pados et al., 2015). The range in these estimates may reflect variable calcification depths within the upper c.20-200 m. of the water column (Kohfeld et al., 1996), where fluctuations in temperature and salinity may result in a variable δ^{18}O of calcite within the life cycle of a single foraminifer. On the other hand, there is evidence that *N. pachyderma* sin.

migrates vertically within the water column to maintain constant temperature and salinity conditions (Simstich et al., 2003). Neither the benthic nor planktic δ^{18}O data of site PC493 presented here have been corrected for these possible offsets.

δ^{18}O age-depth tie points for core PC493 were taken mainly at the transition dates between glacial and interglacial Marine Isotope Stages (MIS) as defined by the LR04 stack (Lisiecki and Raymo, 2005). Other tie points, such as MIS 5e peak interglacial at 123 ka and the glacial δ^{18}O peak at 294 ka (cf. substage 8.6 of Imbrie et al. (1984)), were also used. A full list of tie points is provided in Appendix Table B.3. The full glacial-interglacial δ^{18}O amplitude caused by the global ice volume effect is recorded in the $\delta^{18}O_b$ data for most glacial-interglacial cycles at site PC493, possible exceptions being the interglacials MIS 1, MIS 13 and MIS 15, where $\delta^{18}O_b$ values do not reach peak interglacial values seen in the LR04 stack. Planktic δ^{18}O ($\delta^{18}O_p$) values, however, do reach values similar to other

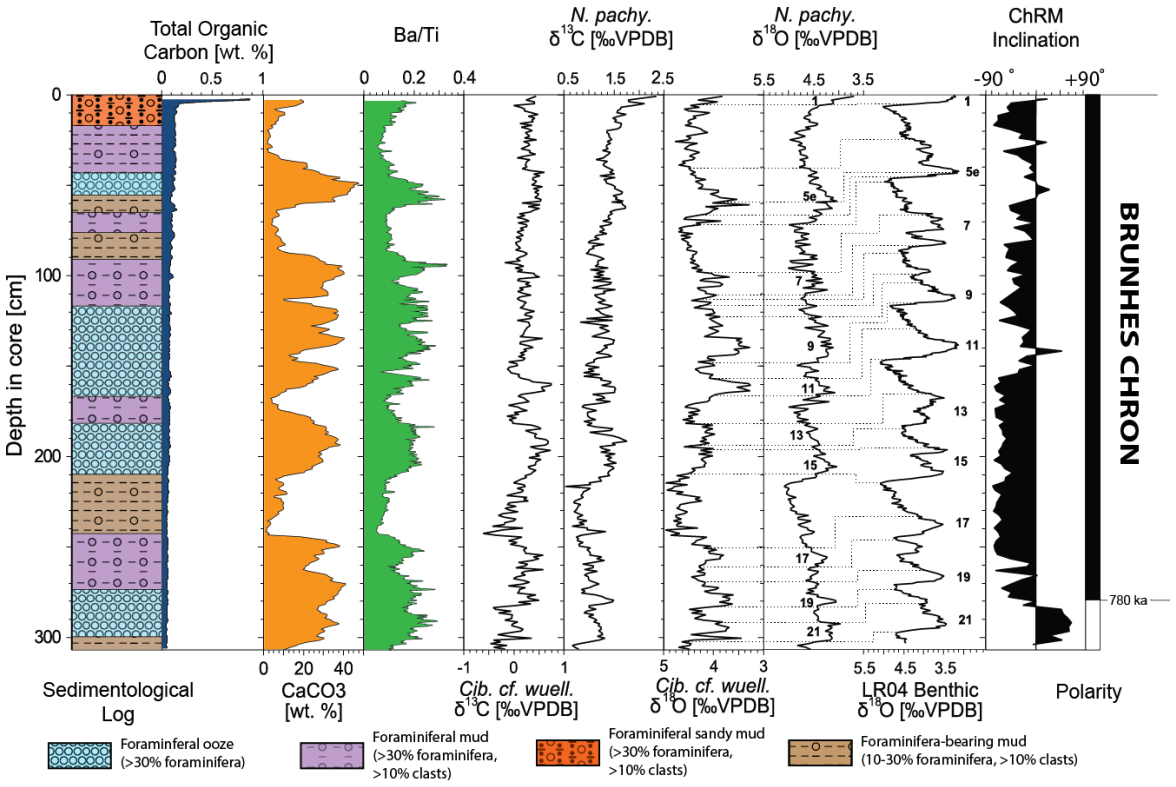

Fig. 3.3 Lithology, palaeoproductivity proxies (total organic carbon [TOC], $CaCO_3$ content, Barium/Titanium [Ba/Ti] ratio) and inclination of the Characteristic Remanent Magnetization (ChRM) with magnetic polarity, and δ^{13}C and δ^{18}O isotope data measured on planktic (*Neogloboquadrina pachyderma* sinistral) and benthic (*Cibicidoides* cf. *wuellerstorfi*) foraminifera from core PC493. The LR04 benthic δ^{18}O stack (Lisiecki and Raymo, 2005) with numbers giving interglacial Marine Isotope Stages (MIS) and age-depth tie points (indicated by dotted lines) are also shown.

interglacials during MIS 1 and MIS 15, while both the ratios of Barium and Titanium (Ba/Ti) and the $CaCO_3$ contents of sediments at site PC493 exhibit expected interglacial values during MIS 13 and MIS 15 (see 3.4.1 below), indicating these interglacials are present in the core. It should also be noted that MIS 13 and MIS 15 are muted interglacials within the global LR04 stack itself, and that the $\delta^{18}O_b$ values of core PC493 may in fact represent peak interglacial conditions at this site.

The total organic carbon (TOC) content in core PC493 is 0.4-0.9 wt. % at the core top and <0.1-0.2 wt. % down core, which is low when compared to typical down-core values of 0.1-0.4 wt. % at other sites from the Amundsen Sea (Hillenbrand et al., 2002) and the western Antarctic Peninsula margin (Pudsey and Camerlenghi, 1998). This possibly reflects a low flux of organic material to the seafloor combined with its poor preservation in the sediments (DeMaster and Ragueneau, 1996), in keeping with the low sedimentation rates at site PC493. A study of organic particulate flux to the seafloor in the seasonal sea ice zone of the Amundsen Sea recently demonstrated greatly reduced concentrations of organic matter content within the water column during periods of persistent sea ice cover compared with open water conditions (Kim et al., 2015). Given the proximity of site PC493 to the modern summer sea ice limit (Jacka, 1997), it can be assumed that this site experienced prolonged periods of persistent sea-ice cover, and thus reduced supply of organic matter to the sea floor. Low organic matter content likely inhibited the establishment of an abundant benthic community at the core site, and along with the absence of infaunal foraminifera species, such as *Uvigerina*, probably prevented deep bioturbation of the sediments in core PC493.

3.3.3 Stable carbon isotopes of planktic and benthic foraminifera

Multiple studies have demonstrated that of all benthic foraminifera taxa, *C. wuellerstorfi* forms its tests closest to equilibrium with $\delta^{13}C_{seawater}$, and is therefore the preferred benthic species for bottom water $\delta^{13}C_{seawater}$ reconstructions (Belanger et al., 1981; Duplessy et al., 1984; Graham et al., 1981; Woodruff et al., 1980; Zahn and Mix, 1991). In contrast, the $\delta^{13}C$ values of planktic *N. pachyderma* sin. in the high latitude SO display an offset from equilibrium surface $\delta^{13}C_{seawater}$. The offset between core-top *N. pachyderma* sin. and modelled preindustrial equilibrium $\delta^{13}C_{seawater}$ has been shown to increase from c.1‰ at 70° S to c.2.8‰ at 43° S in the Atlantic sector of the SO (Charles and Fairbanks, 1990; Kohfeld et al., 2000). The variable offset is the result of changes in i) dietary $\delta^{13}C$, ii) seawater carbonate ion concentrations ($[CO_3^{2-}]$), and iii) seawater temperature – all of which may have fluctuated at site PC493 throughout the last 800 ka. Based on the modelled preindustrial offset from equilibrium surface $\delta^{13}C_{seawater}$ at 70°S (Kohfeld et al., 2000), a correction of +1.0‰ is applied to all *N. pachyderma* sin. $\delta^{13}C$ data presented here.

The $\delta^{13}C_b$ values of core PC493 typically range from 0.5‰ to 0.7‰ during peak interglacials and from -0.2‰ to 0.2‰ during glacial maxima (Fig. 3.3). The amplitude of $\delta^{13}C_b$ changes at glacial terminations varies between 0.7‰ and 0.2‰, and the average amplitude of 0.39±0.16‰ across all terminations is close to the 0.38±0.08‰ whole ocean (0.5-5 km water depth) $\delta^{13}C_{seawater}$ shift of 0.38±0.08‰ across the last deglaciation estimated by Peterson et al. (2014). $\delta^{13}C_p$ values range from 1.3‰ to 1.7‰ during peak interglacials and from 0.8‰ to 1.2‰ during glacial maxima, while the amplitude across terminations varies from 0.2‰ to 0.6‰. The average amplitude in $\delta^{13}C_p$ values across all terminations is 0.43±0.11‰. The $\delta^{13}C_p$ values are higher in the Holocene than at any other point during the last 800 ka, with peaks of 2.33‰ (0.5 cm) and 2.11‰ (4.5 cm) being particularly high.

3.3.4 Neodymium isotopic composition of authigenic ferromanganese oxyhydroxide coatings of planktic foraminifera

The neodymium isotopic composition of authigenic ferromanganese oxyhydroxide coatings of planktic foraminifera ($\varepsilon_{Nd}{}^{foram}$) were measured on 5 samples from core PC493 spanning MIS 1-5. Unfortunately, $\varepsilon_{Nd}{}^{foram}$ at site PC493 does not faithfully record a bottom water signature, which is evident from its offset from nearby seawater towards more radiogenic values (Fig. 3.4). Given site PC493s low sedimentation rate and position atop a volcanic seamount, this offset is most likely caused by a combination of contamination with highly radiogenic volcanogenic detritus during ε_{Nd} extraction, and/or boundary exchange with volcanic sediments.

The apparent cyclicity within $\varepsilon_{Nd}{}^{foram}$ measured on core PC493 suggests changes across glacial-interglacial cycles, with more radiogenic values of 1.20±0.36 and less radiogenic values of -1.99±0.36 during the Holocene and -2.20±0.36 during MIS 5e (Fig. 3.4). This cyclicity may reflect either changes in glacial bottom water ε_{Nd} towards more radiogenic values prior to modification by boundary exchange, and/or a climatologically-driven modulation of boundary exchange processes, perhaps via changes in the detrital provenance of sediments at site PC493 on glacial-interglacial timescales, which have been reported for other cores from the continental margin in the Amundsen Sea (Hillenbrand et al., 2009, 2002).

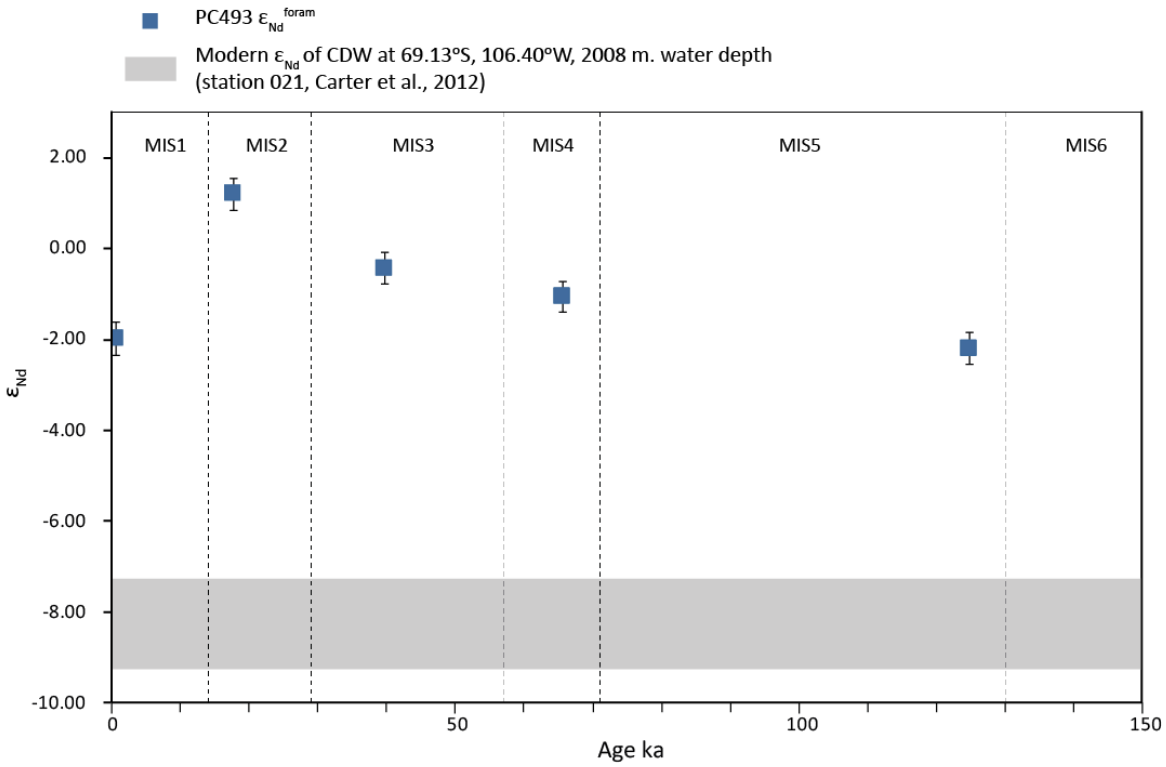

Fig. 3.4 The neodymium isotopic composition of authigenic Fe-Mn coatings of planktic foraminifera ($\varepsilon_{Nd}{}^{foram}$) from core PC493 across the last glacial cycles. Core top $\varepsilon_{Nd}{}^{foram}$ is clearly offset from modern seawater values measured nearby (grey bar, Carter et al. (2012)

3.4 Discussion

3.4.1 Productivity and hydrographic conditions at site PC493 during the Late Quaternary

The Ba/Ti ratio of sediments reflects the content of biogenic barium, which is the most reliable productivity proxy in sediments from the Antarctic continental margin (Bonn et al., 1998; Hillenbrand et al., 2009, 2002) and south of the APF (Jaccard et al., 2013; Nürnberg et al., 1997). The correlation coefficient (R^2 of 0.78 for $CaCO_3$ against Ba/Ti, Fig. 3.5) shows that the $CaCO_3$ record of core PC493 reflects primary biological productivity at the core site, and that this productivity signal has not been substantially overprinted by carbonate dissolution. The lack of carbonate dissolution overprinting demonstrates that site PC493 remained above the lysocline throughout the last 800 ka. The low correlation coefficient (R^2 = 0.28) between the $CaCO_3$ content and $\delta^{13}C_b$ at site PC493 (Fig. 3.5) furthermore indicates that the $\delta^{13}C_b$ signal records changes in water mass chemistry rather than local productivity

effects (e.g. Mackensen et al. (1993), and demonstrates that carbonate dissolution has not affected the $\delta^{13}C_b$ record (McCorkle et al., 1995).

The $CaCO_3$ and the Ba/Ti records indicate that primary productivity at site PC493 was reduced during glacial periods. The location of PC493 close to the modern summer sea ice limit made it sensitive to increasing sea-ice coverage during past glacial periods, and the concomitant decrease in biological productivity was probably caused by the site being covered by sea ice almost all year round (Benz et al., 2016; Bostock et al., 2013; Kim et al., 2015), as was also observed in other SO sectors (e.g. Allen et al. (2011); Gersonde et al. (2005)). However, the continuous presence of planktic and benthic foraminifera in the sediments of core PC493 even during glacial periods of permanent sea ice cover also implies that polynyas must have opened up at least episodically above the site during glacial periods and allowed phytoplankton production (Lu et al., 2016; Smith et al., 2010). The formation of glacial polynyas above site PC493 can be attributed to upwelling of relatively warm deep water on the northward flank of the seamount (Thatje et al., 2008), in a process analogous to modern-day open ocean polynya formation at Maud Rise (a prominent seamount in the Atlantic sector of the SO; Bersch et al. (1992)). This glacial polynya formation depended on the continued upwelling of deep waters along the Antarctic margin, as occurs along the Amundsen Sea continental slope today (e.g. Jenkins et al. (2016)). Planktic Iodine/Calcium (I/Ca) reconstructions of upper ocean oxygen (O_2) concentration from the same core site (cores TC493 and PS2547) indicates O_2 depletion during the last glacial period (Lu et al.,

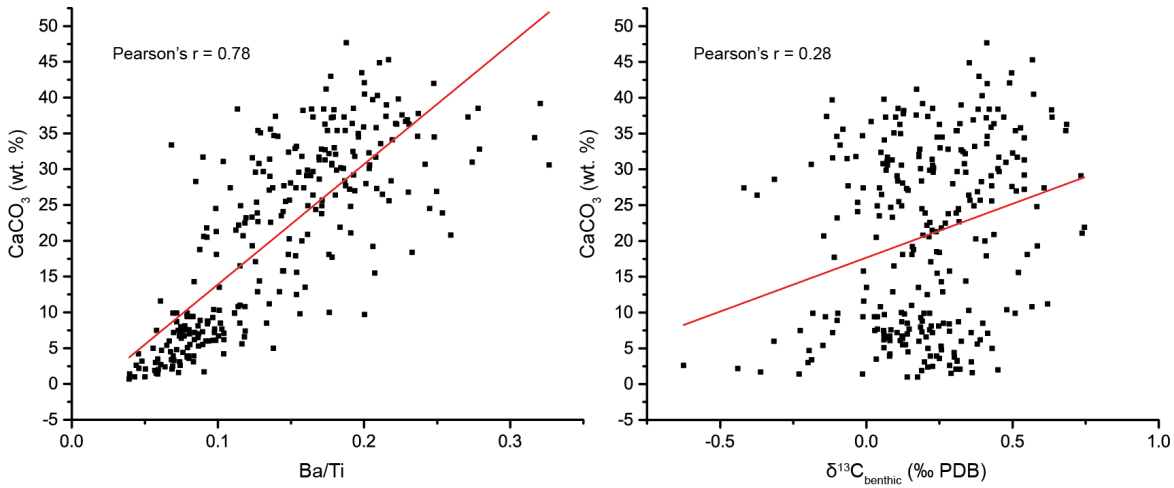

Fig. 3.5 $CaCO_3$ content and Ba/Ti ratios in core PC493 show a good correlation, confirming that the $CaCO_3$ record primarily reflects changes in productivity at site PC493. There is only a weak correlation between benthic δ^{13} values and $CaCO_3$ content, suggesting that dissolution of $CaCO_3$ did not affect the site and providing evidence against a local productivity control on benthic $\delta^{13}C$.

2016), providing further evidence for persistent upwelling of a poorly oxygenated deep water mass at this location during past glacials. The presence of glacial polynyas at site PC493 relies on upwelling of deep water, and is incompatible with down-welling of brines over this site, which may have formed in these polynas. Any dense bottom waters that may have originated from the continental shelf or the shelf edge would bypass regions of elevated bathymetry, as is observed at modern sites of deep water formation and transport, such as the Adélie Land and George V Land continental margins (Williams et al., 2010). Any bottom waters originating on the continental shelf or shelf edge and flowing down the continental slope would therefore bypass site PC493 due to its elevated position on a seamount. The seamount position of site PC493 also explains the lack of turbidites in core PC493, which are abundant in nearby cores (Hillenbrand et al., 2002). To date, all the evidence points towards continuous upwelling of deep waters to site PC493 throughout the glacial-interglacial cycles of the Late Quaternary.

3.4.2 The $\delta^{13}C$ of deep and bottom water masses in the modern, late Holocene and Last Glacial Maximum Southern Ocean

Today the SO is well mixed due to a combination of strong meridional and longitudinal circulation and intense diapycnal mixing, particularly in areas of rough bathymetry, such as the Scotia Sea in the Atlantic sector of the SO (Heywood et al., 2002). This mixing leads to a condensed temperature/salinity field and a homogenisation of water mass tracers such as $\delta^{13}C_{seawater}$, which today averages 0.4±0.1‰ within CDW (Kroopnick, 1985) (Fig. 3.6).

The $\delta^{13}C_b$ record of PC493 shows no significant difference between the LGM (average $\delta^{13}C_b$= 0.35‰, σ= 0.14‰) and the late Holocene (average $\delta^{13}C_b$= 0.33‰, σ= 0.13‰); this contrasts with the increase in $\delta^{13}C_b$ of 0.47‰across the penultimate glacial termination (Fig. 3.7). A muted LGM-late Holocene change is also evident in the $\delta^{18}O_b$ record of site PC493, which decreased from an LGM maximum of 4.58‰, to a late Holocene minimum of 3.83‰($\Delta\delta^{18}O_b$= -0.75 ‰). This again contrasts with the penultimate deglaciation, which saw a $\delta^{18}O_b$ decrease of 1.32‰ (Fig. 3.7). On the other hand, $\delta^{18}O_p$ decreases by 0.99‰ and $\delta^{13}C_p$ increases by 0.86‰between the LGM and the late Holocene, indicating that the Holocene and LGM similarities in $\delta^{13}C_b$ at site PC493 are unlikely to be due to bioturbation, and reflect bottom water $\delta^{13}C_{seawater}$ values at the time. This interpretation is reinforced by a shift toward more negative $\delta^{13}C_b$ values during the last deglaciation, from a peak of 0.48‰ at 22.9 ka, to a minimum of -0.01‰ 14.3 ka, before recovering into early Holocene values of 0.41‰. At no point during the last glacial period did $\delta^{13}C_b$ values fall below -0.01‰.

The similarity of late Holocene and LGM $\delta^{13}C_b$ values, and the persistent presence of bottom waters relatively enriched in ^{13}C during the LGM and previous glacial periods at site PC493 is at odds with many previous studies of SO deep and bottom water masses, which largely describe heterogenous, ^{13}C-depleted deep and bottom water masses within the glacial SO (e.g. Curry and Oppo (2005); Oliver et al. (2010); Peterson et al. (2014)). As site PC493 provides $\delta^{13}C$ data from a previously under-sampled region of the SO, I have compiled all available $\delta^{13}C$ data measured on tests of the benthic foraminifer *Cibicidoides* from marine sediment cores collected from water depths >500 m. and south of 30°S, to investigate the spatial pattern of LGM and late Holocene $\delta^{13}C_b$ values and provide context for the $\delta^{13}C_b$ record of site PC493 (Figs. 3.8, 3.9, and 3.10). The compilation presented here builds upon – but is largely the same as – that presented by Peterson et al. (2014). All sample values within

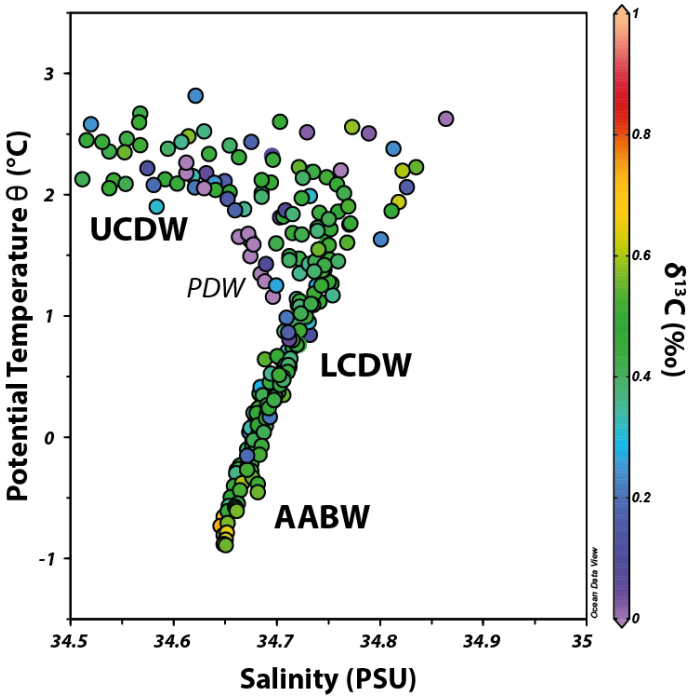

Fig. 3.6 Potential temperature-salinity plot showing the stable carbon isotopic values of seawater in the modern SO interior (>300 m. water depth south of 30°S). Strong meridional circulation coupled with intense vertical mixing within the SO acts to homogenise physical and chemical tracers, leading to SO water masses, i.e. Antarctic Bottom Water (AABW), Lower Circumpolar Deep Water (LCDW) and Upper Circumpolar Deep water (UCDW), having similar $\delta^{13}C$ values. Inflow of Pacific Deep Water (PDW) between 30°S and 40°S in the eastern Pacific sector of the SO is expressed by isotopically lighter $\delta^{13}C$ values, reflecting the position of PDW further along the path of thermohaline circulation. Data collected by GEOSECS program between 1972-1978 (Ostlund et al., 1987) and plotted using Ocean Data View (Schlitzer, 2015)

time slices of 18-24 ka (LGM) and 0-6 ka (late Holocene) were averaged for each sediment core, and the core locations categorised into three regions: the southern Atlantic and Atlantic sector of the SO (hereafter Atlantic sector; 70°W to 50°E, n= 46), the southern Indian Ocean and Indian sector of the SO (hereafter Indian sector; 50°E to 165°E, n= 17) and the South Pacific and Pacific sector of the SO (hereafter Pacific sector; 165°E to 70°W, n= 20). Only previously published age models were used for all cores. Carbon isotope data measured on the infaunal foraminifer *Uvigerina* spp. have not been included in this compilation because it was previously shown that δ^{13}C data measured on various species of this genus do not

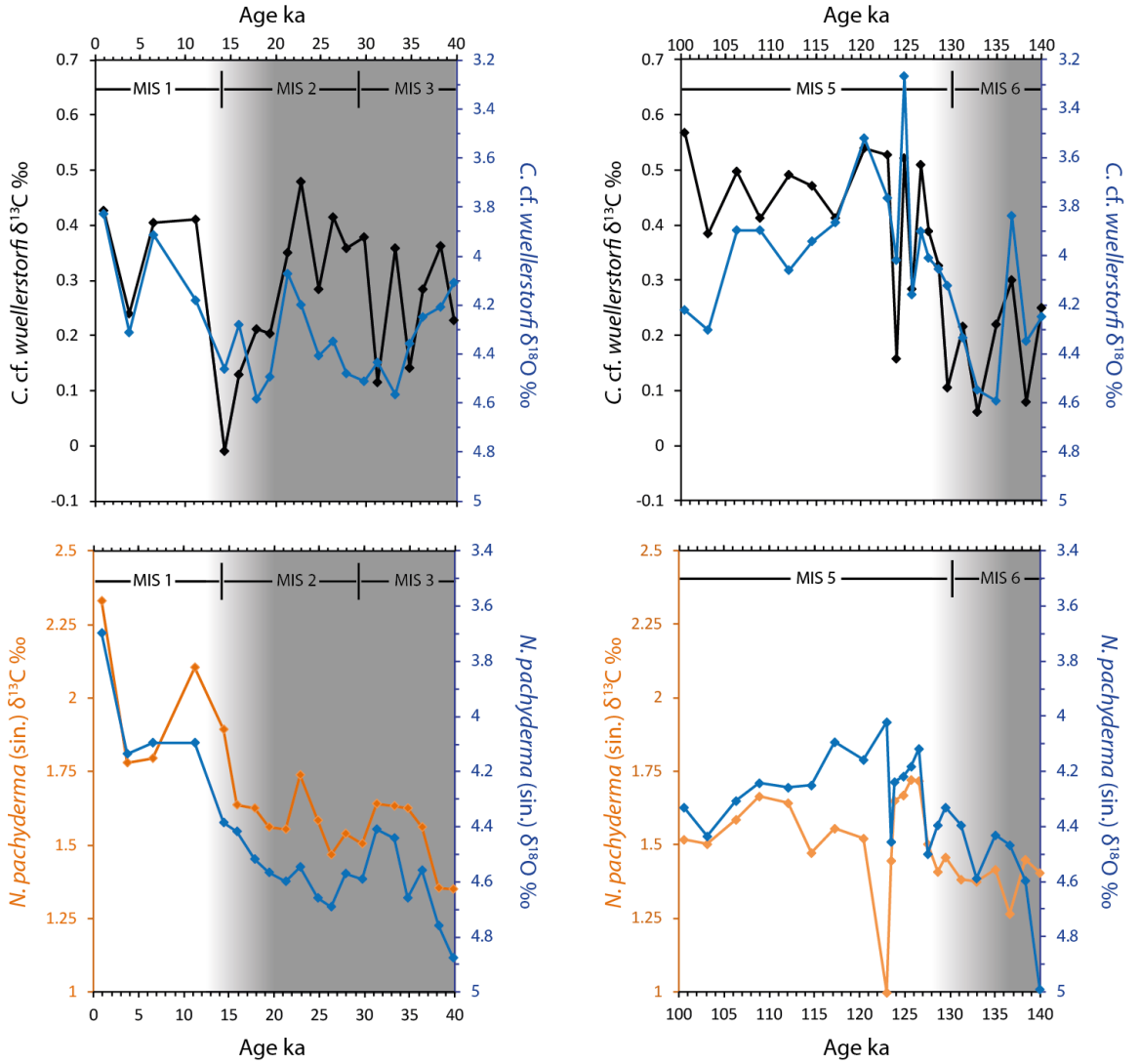

Fig. 3.7 Records of *C.* cf. *wuellerstorfi* (upper panels) and *N. pachyderma* (sin.) (lower panels) δ^{13}C and δ^{18}O across the last glacial period into the Late Holocene (left panels), alongside the penultimate deglaciation for comparison (right panels).

faithfully reflect $\delta^{13}C_{seawater}$ (Zahn et al., 1986). Where $\delta^{13}C$ data from *Uvigerina* are shown for comparison, both offsets discussed in section 1.4.1 are applied. For a full list of core sites, averaged $\delta^{13}C$ data and references used in the compilation presented here, see Appendix Table C.2.

Late Holocene $\delta^{13}C_b$ values reflect the well mixed nature of the SO interior (average Atlantic sector= 0.49±0.31‰, Indian sector= 0.67±0.37‰, Pacific sector= 0.54±0.34‰), with AABW and CDW values varying between 0.0 and 0.5‰, and AAIW values ranging between 1.0 and 1.5‰ (Fig. 3.8 b-f). The isotopically heavier AAIW $\delta^{13}C$ values are a consequence of i) air-sea gas exchange between the atmosphere and Antarctic Surface Water (AASW), the precursor to AAIW, and ii) the effect of biological productivity in the surface water, which both drive AAIW to isotopically higher values (Lynch-Stieglitz et al., 1995; Zhang et al., 1995). In the Atlantic and Indian sectors, the effects of NADW mixing into the ACC north of 42°S is also apparent in some cores, where values are elevated to c. 0.5 to 1.0‰.

3.4.2.1 Location and possible sources of $^{13}C_b$ depletion in the LGM Southern Ocean

During the LGM, the most depleted $\delta^{13}C_b$ values are found between 15°W and 12°E in the deep Cape Basin of the Atlantic sector, where values reach as low as -1.03‰ (average 15°W-12°E, > 2000 m. water depth= -0.47‰, σ= 0.46‰). This $\delta^{13}C_b$ depletion gives way to gradually more ^{13}C-enriched values along the flow path of the ACC, with minimum $\delta^{13}C_b$ values in the Indian sector being -0.71‰ (average >2000 m. water depth= -0.19‰, σ= 0.34‰) and in the central Pacific sector (southern East Pacific Rise) being -0.43‰ (average between 125°W and -111°W, >2000 m. water depth, including site PC493= -0.10‰, σ= 0.27). The LGM $\delta^{13}C_b$ value of -1.09‰ at site MD97-2121 in the western Pacific sector (off New Zealand) records southward flowing PDW, and so does not reflect a SO-sourced water mass (McCave et al., 2008; Skinner et al., 2015) (Fig. 3.12). There is also a latitudinal pattern in the LGM distribution of $\delta^{13}C_b$: In the Atlantic sector the most depleted values occur between 40°S and 55°S, in the region of the LGM SAZ and APF (Gersonde et al., 2005). Increased supply of Fe to the glacial SAZ – which is today more Fe-limited than the region south of the APF (e.g. Sigman et al. (2010)) – led to greatly enhanced biological productivity in this region during the LGM when compared with the Holocene (Jaccard et al., 2013; Kohfeld et al., 2005; Lamy et al., 2014), providing an enhanced supply of ^{13}C-depleted organic matter to the abyssal ocean. However, enhanced productivity in the glacial SAZ also made *Cibicidoides* tests there more prone to lowering of $\delta^{13}C$ due to the increased supply of ^{12}C-enriched phytodetritus, with seasonally high fluxes of organic matter to the seabed in the seasonal ice zone possibly leading to even lower $\delta^{13}C$ values ('Mackensen effect';

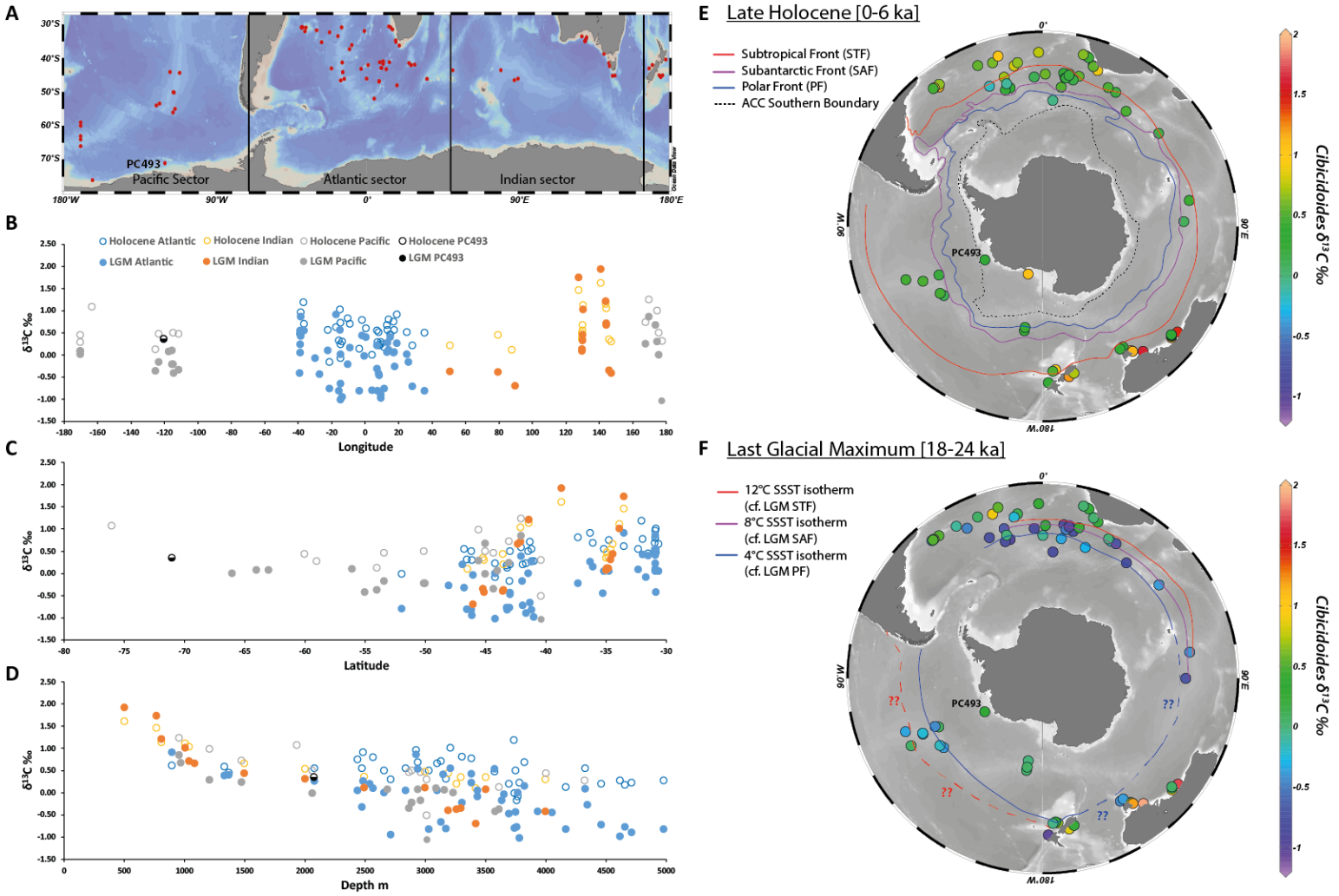

Fig. 3.8 Records of $\delta^{13}C_b$ from the late Holocene (0-6 ka) and/or the LGM (18-24 ka) measured on *Cibicidoides*. All core locations shown in panel A. All measurements are shown vs. longitude (B), latitude (C) and water depth (D). The location of each $\delta^{13}C_b$ value, alongside modern and reconstructed LGM fronts (Benz et al., 2016; Gersonde et al., 2005)) are presented in panels E and F, respectively. Areas with uncertain LGM frontal positions are dashed. N.B. the location of the LGM SAF is unknown between c. 90°E and c. 25°W and is therefore absent from this figure.

Mackensen et al. (1993)). While a glacial increase in biological surface water productivity may have played a role for some individual core sites, it is unclear if it could cause sustained depletion in $\delta^{13}C$ data throughout the LGM across a large area, and it is unable to explain the apparent depth-dependency of $\delta^{13}C$ depletion observed in the Atlantic sector (Fig. 3.8.d). If the $\delta^{13}C_b$ depletion were to be entirely explained by glacial productivity increase, one would not expect to see similar negative $\delta^{13}C_b$ values in cores from south of the APF, where productivity was reduced during the LGM compared to the Holocene (e.g., Bonn et al. (1998); Bradtmiller et al. (2009); Hillenbrand and Cortese (2006); Jaccard et al. (2013); Kohfeld et al. (2005); Nürnberg et al. (1997)). Summer sea surface temperature (SSST) reconstructions from the Atlantic sector suggest that the LGM APF was positioned at c. 46°S during the LGM (Gersonde et al., 2005). $\delta^{13}C_b$ data from south of this region are sparse, however the core site furthest south of the LGM APF in the Atlantic sector records average LGM $\delta^{13}C_b$ values of -0.81‰ (TN057-15: 51.9°S, 4.5°E, 3744 m. water depth; Curry and Oppo (2005); Ninnemann and Charles (2002)). The location of this core site far south of the LGM APF suggests that the LGM $\delta^{13}C_b$ depletion recorded there is water mass signature, and not the result of productivity increases associated with frontal positions. Another factor which may contribute to this latitudinal control on LGM $\delta^{13}C_b$ in the Atlantic sector is the inflow of less $\delta^{13}C$-depleted NCW at shallower water depths. A recent ε_{Nd} study has shown that, although NCW shoaled during the last glacial period, it still penetrated the SO as far as 46°S at 2500 m. water depth during the LGM (Howe et al., 2016b), where it was entrained within the flow of the ACC (Hu et al., 2016b). This tongue of relatively ^{13}C-rich NCW led to a strong latitudinal gradient in $\delta^{13}C_b$ between 35°S to 40°S during the LGM. Also in the Pacific sector there was apparently a latitudinal control on $\delta^{13}C_b$ during the LGM. Average $\delta^{13}C_b$ values in cores south of 55°S do not fall below 0‰, in line with values recorded at site PC493 (0.34‰), whereas $\delta^{13}C_b$ values north of 55°S reach -0.43‰, and are even more ^{13}C-depleted during previous glacial periods (see section 3.4.3 below). Although LGM frontal positions in the Pacific sector are poorly constrained, all data exhibiting relatively depleted $\delta^{13}C$ values come from close to or north of the reconstructed position of the APF, which was located at c.55°S (Benz et al., 2016). Although higher glacial productivity in this northerly area (Bradtmiller et al., 2009; Lamy et al., 2014) may have lowered $\delta^{13}C$ values of *Cibicidoides* tests at these sites, it is also possible that cores south of 55°S were bathed in southern-sourced waters during the LGM, which were better ventilated than more northerly deep waters. A potential source region for such a ventilated LGM water mass is the Ross Sea, where Ross Sea Bottom Water (RSBW) is formed today. This scenario has previously been proposed based on $\delta^{13}C$ measurements of *Cibicidoides* and *Uvigerina* tests from a transect of cores across Chatham Rise, east of New Zealand (McCave et al., 2008) (Fig. 3.12). This would

require an expansion in RSBW production during the last glacial period, and/or a decrease in the proportion of AABW formed in the Weddell Sea (and possibly along the Adélie coast) admixed into CDW and advected through to the Pacific sector; I make the argument that both occurred during past glacial periods in chapter 5 of this thesis. Finally, there is also a strong depth-dependency of the LGM $\delta^{13}C_b$ data in all three sectors, with $\delta^{13}C$ values <-0.5‰ occurring exclusively below 2.5 km water depth. This depth dependency appears most pronounced in the Atlantic sector, corroborating the findings of previous studies (Curry and Oppo, 2005; Oliver et al., 2010; Peterson et al., 2014), although this may be due to a lack of cores from >4000 m. water depth in the Indian and Pacific sectors.

Given the $\delta^{13}C_b$ variability between core sites in different sectors, and to help differentiate between possible productivity effects and variations in $\delta^{13}C_{seawater}$, it is useful to frame the LGM $\delta^{13}C_b$ data measurements in relation to the physical properties (i.e. potential temperature, salinity and density) of the modern deep and bottom water masses bathing the core sites (Figs. 3.9 and 3.10). The most depleted LGM $\delta^{13}C_b$ values are found at sites in the Atlantic sector that are today bathed in AABW and LCDW. In contrast, core sites in the Atlantic sector that are today bathed in NADW do not show the same level of $\delta^{13}C_b$ depletion during the LGM as those bathed in AABW/LCDW, reflecting the continued flow of NCW (low in remineralised nutrients and carbon) into the SO. The pattern in the Indian sector is similar, with core sites today bathed in LCDW having been more depleted in $\delta^{13}C_b$ during the LGM, and core sites today bathed in a mixture of LCDW, UCDW and NADW having been less ^{13}C-depleted during the LGM. The LGM pattern of $\delta^{13}C_b$ in the Indian sector reflects the entrainment and mixing of NCW into the ACC at intermediate water depths during the LGM (Hu et al., 2016b). Core sites from the Pacific sector which are today bathed in lLCDW do not show the same level of ^{13}C-depletion during the LGM as observed in LCDW/AABW from the abyssal Atlantic sector. Sites today bathed in uLCDW in the Pacific sector show ^{13}C-depletion during the LGM compared with core sites bathed in lLCDW, pointing to either i) the advection and/or admixture of SCW from the Atlantic sector into the ACC and subsequent transport into the intermediate-to-deep (i.e. uLCDW) Pacific sector, ii) addition of remineralised carbon to uLCDW in the Pacific sector, or iii) lowering of $\delta^{13}C_b$ north of the glacial APF in the Pacific sector due to increased productivity. If core sites in the Pacific sector which are today bathed by lLCDW also recorded a modified AABW signal during the LGM, the lack of significant ^{13}C-depletion in the $\delta^{13}C_b$ data at core sites south of 55°S in the Pacific sector would reflect a heterogeneity in the $\delta^{13}C$ of AABW formed in the Atlantic and Pacific sectors of the SO.

The relatively ^{13}C-rich bottom waters identified in the Pacific sector south of 55°S exclude glacial deep water formation in this region as the source of the extremely $\delta^{13}C$-depleted,

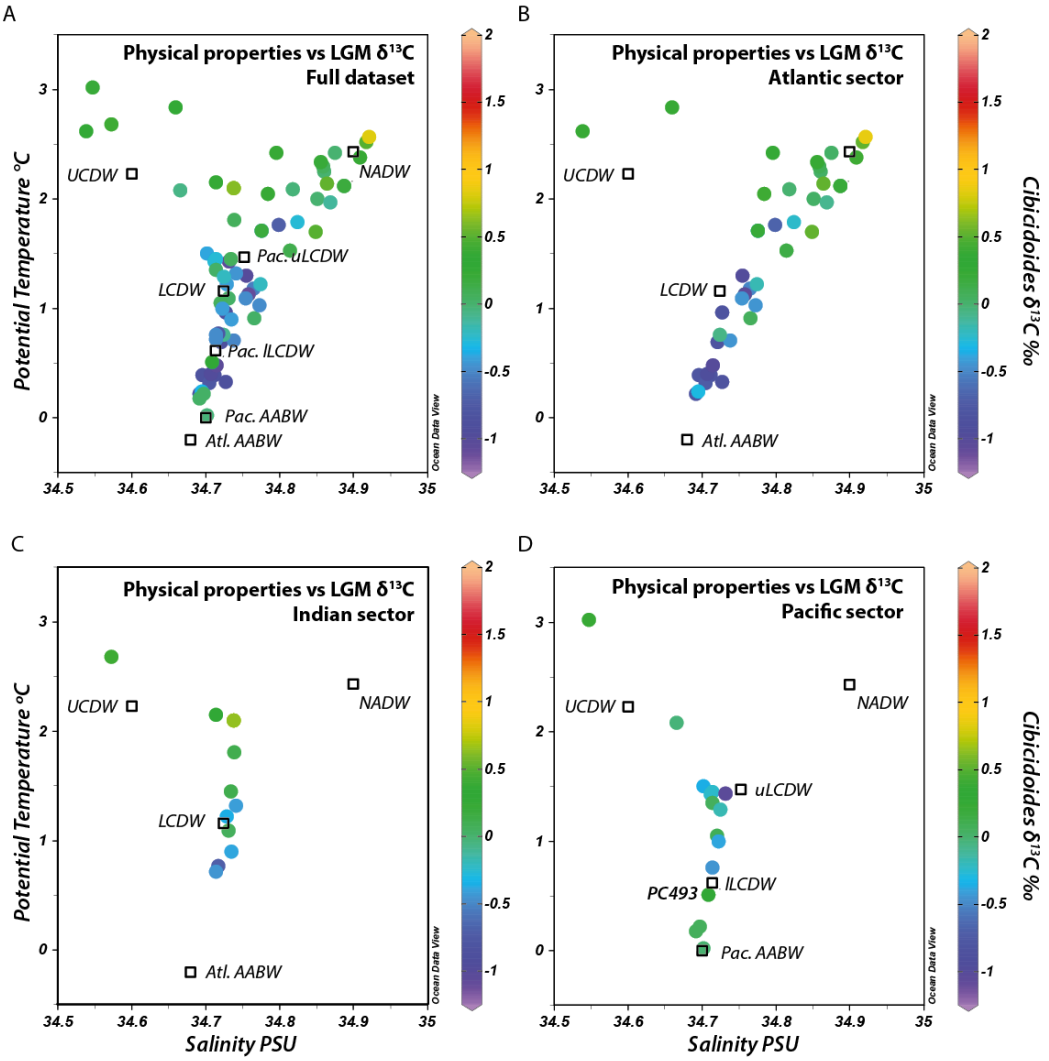

Fig. 3.9 Average LGM $\delta^{13}C_b$ values measured on *Cibicidoides* as a function of the physical properties of modern deep and bottom water masses bathing (A) all core sites south of 30°S, (B) core sites in the Atlantic sector, (C) core sites in the Indian sector and (D) core sites in the Pacific sector. Physical properties of water masses at core locations were compiled using the Hydrographic Atlas of the Southern Ocean (Olbers et al., 1992). Plots produced using Ocean Data View (Schlitzer, 2015).

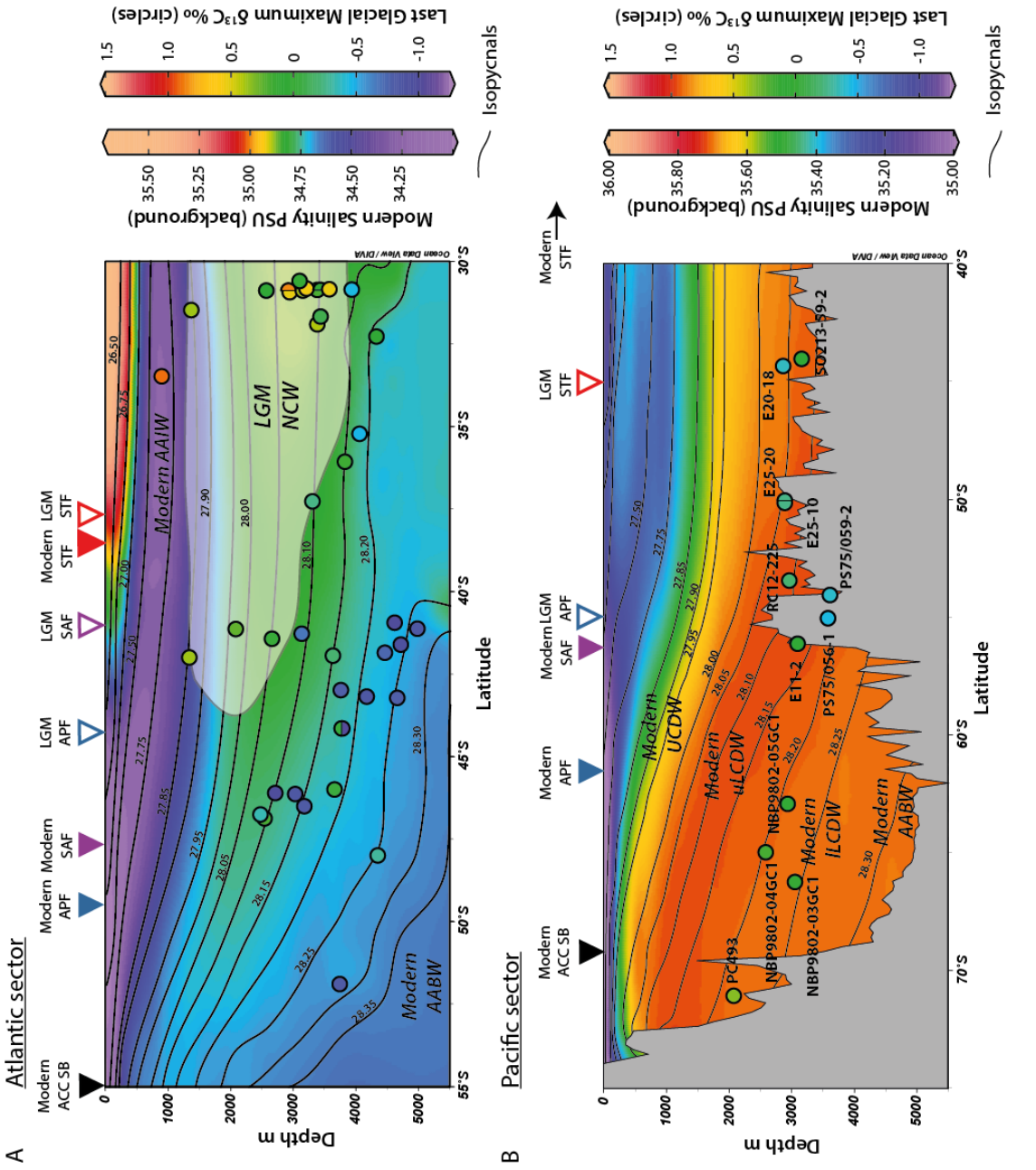

Fig. 3.10 LGM $\delta^{13}C_b$ data (coloured circles) alongside modern water salinity (background colours) and density (contours) in the Atlantic and Pacific sectors. In the LGM Atlantic sector (panel A), inflowing NCW (shaded region, based on $\delta^{13}C_b$ data) is expressed as a ^{13}C-enrichment (δ^{13}C c. 0-0.5‰) compared to SCW (δ^{13}C c.-0.5‰ to -1‰) SCW in the Pacific sector (panel B) does not show a similar level of ^{13}C-depletion as the Atlantic sector, and all $\delta^{13}C_b$ values south of the LGM APF are >0‰. Salinity and density in the Atlantic sector are a gridded weighted-average of values across all core sites based on data from the World Ocean Circulation Experiment Hydrographic Programme (Schlitzer, 2000). Salinity, density and bathymetry in the Pacific sector are based on a weighted-average of all values across a transect running north at 120°W. The modern hydrography in the region of New Zealand/Chatham Rise is too dissimilar from this, so data from those cores have been omitted. All reconstructed frontal positions are after Gersonde et al. (2005) and Benz et al. (2016). In panel B the exact position of the SAF during the LGM is unclear, although it must have been located between the LGM APF and STF, and probably lay north of site E25-20.

CO_2-rich water mass observed in the glacial Atlantic basin. Some of the glacial $\delta^{13}C_b$ minima observed in the deep Atlantic basin may have been influenced by PDW inflow to the SO. PDW in the equatorial eastern Pacific during the LGM had a $\delta^{13}C$ of -0.3‰ (Lisiecki, 2010; Mix et al., 1995). Remineralisation of organic matter along the return flow path of PDW to the SO probably lowered its $\delta^{13}C$ further, leading to average LGM $\delta^{13}C_b$ values of -1.09±0.28‰ recorded in core MD97-2121, which is located off the eastern coast of New Zealand and was bathed in PDW during the LGM (McCave et al., 2008; Skinner et al., 2015) (Fig. 3.12). Assuming a similar effect of remineralisation on the $\delta^{13}C$ of PDW that flowed into the SO off the coast of South America, $\delta^{13}C_b$ values of -1‰ recorded in the abyssal Atlantic sector would require core sites in this region to have been bathed in 100% PDW during the LGM. However, during the LGM core sites in the abyssal Atlantic sector were bathed in a water mass with less radiogenic ε_{Nd} values (c.-6 ε_{Nd} Howe et al. (2016b)) than those of the PDW end member (ε_{Nd}= -3.5 to -4) or of modified PDW that flowed back into the SO from the Eastern Equatorial Pacific (ε_{Nd}= -2, Hu et al. (2016b)), implying that the isotopically light $\delta^{13}C_b$ values in the deep Atlantic sector cannot have been sourced in the Pacific basin. At the LGM, processes operating in the Atlantic sector must have been responsible for lowering the $\delta^{13}C$ of AABW to much lower values than those of AABW in the Pacific sector. These processes may have included glacial reductions in (i) the production of deep waters, (ii) air-sea gas exchange (due to sea ice expansion and/or surface water stratification), and (iii) vertical advection of – and mixing between – SO water masses

If the mid-depth 'bulge' of relative ^{13}C depletion in the Pacific sector (Figs. 3.8-3.10, 3.12), which had been previously identified by McCave et al. (2008), represents circulation of the same dense water mass observed in the abyssal Atlantic sector, it raises the question of how such a dense water mass could overly AABW formed in the Pacific sector. The answer must lie either in i) a higher density of AABW formed in the Pacific sector than of AABW produced in the Atlantic sector, or ii) diapycnal mixing of dense waters produced in the Atlantic sector with overlying CDW of a lower density, leading to uLCDW in the Pacific sector with a lower density than AABW and lLCDW. Reconstructions of temperature and salinity during the LGM show that AABW in the Atlantic sector was by far the densest water mass in the global ocean (Adkins et al., 2002; Roberts et al., 2016) (Fig. 3.11).

3.4.2.2 LGM $\delta^{13}C_b$ and physical mixing within the glacial Southern Ocean

The increased density of the deep and bottom waters in the Atlantic sector during the LGM was salinity-driven, with the reconstructed salinity at 4548 m. water depth being c.37.1‰ practical salinity units (PSU). This water was 1‰ PSU more saline than the LGM North Atlantic at intermediate depth (c.36.1‰ PSU, 2184 m. water depth), and c.2.4‰ PSU more

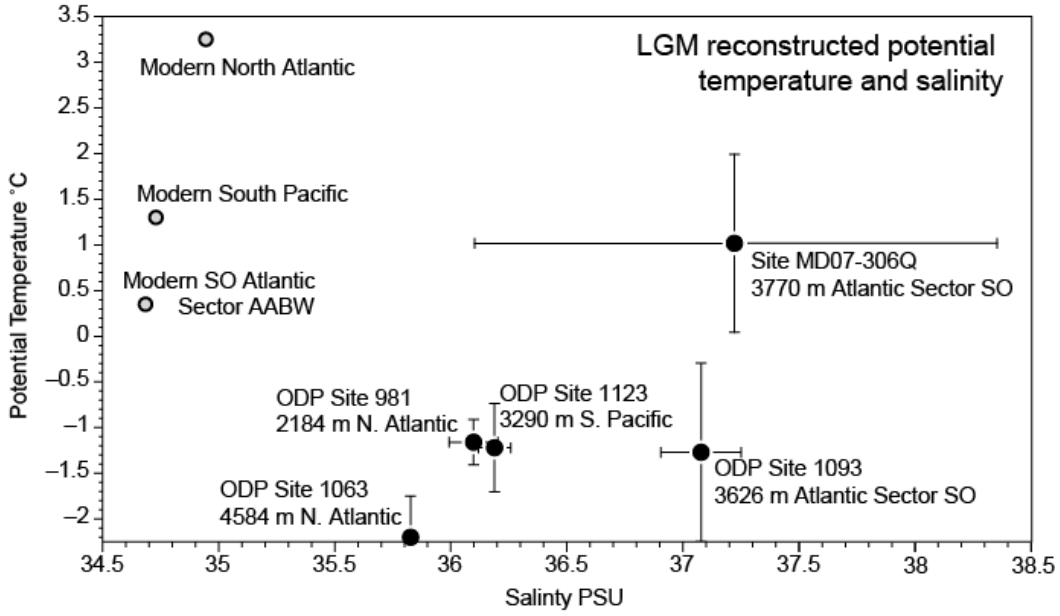

Fig. 3.11 Potential temperature and salinity of deep and bottom waters reconstructed for the LGM (black dots) in comparison to those of modern deep and bottom waters (grey dots) (modified from Adkins et al. (2002), with data from Roberts et al. (2016)).

saline than modern AABW in the Atlantic sector of the SO (c.34.67‰ PSU, Orsi et al. (1999)). Outflow of uLCDW from the SO into the SW Pacific within the Deep Western Boundary Current (DWBC) is constrained by Ocean Drilling Program Leg 181 Site 1123 located at 3290 m. water depth on Chatham Rise in the western Pacific sector (Hall et al., 2001). δ^{13}C ratios measured on the infaunal foraminifer species Uvigerina peregrina and converted to '*Cibicidoides* equivalent' δ^{13}C values (McCave et al. (2008); see section 1.4.1) from Site 1123 yield average LGM values between -0.06‰ (+0.9‰ offset applied) and -0.52‰ (McCave et al. (2008) offset applied), indicating that Site 1123 was bathed in the same uLCDW as core sites located north of the APF between c.2800 m. to 3600 m. water depth on the East Pacific Rise (110°W-130°W) (Figs. 3.8.d and 3.10.b) (Matsumoto and Lynch-stieglitz, 1999; Ninnemann and Charles, 2002; Ullermann et al., 2016).

LGM temperature and salinity reconstructions from Site 1123 yield salinities of c.36.2‰ PSU, within error of values from the intermediate North Atlantic (Adkins et al., 2002). This may be evidence against the admixture of extremely dense, relatively ^{13}C-depleted AABW in the Atlantic sector up through the water column into overlying CDW as it flows via the ACC into the Pacific sector. It is likely that the bathymetric barrier imposed by the Southeast Indian Ridge, and to a lesser extent Kerguelen Plateau (for locations see Fig. 3.14), prevented the advection of dense AABW from the Atlantic sector into the Pacific basin, as suggested by modelling studies of dense shelf water spreading within the modern SO (Kusahara et al.,

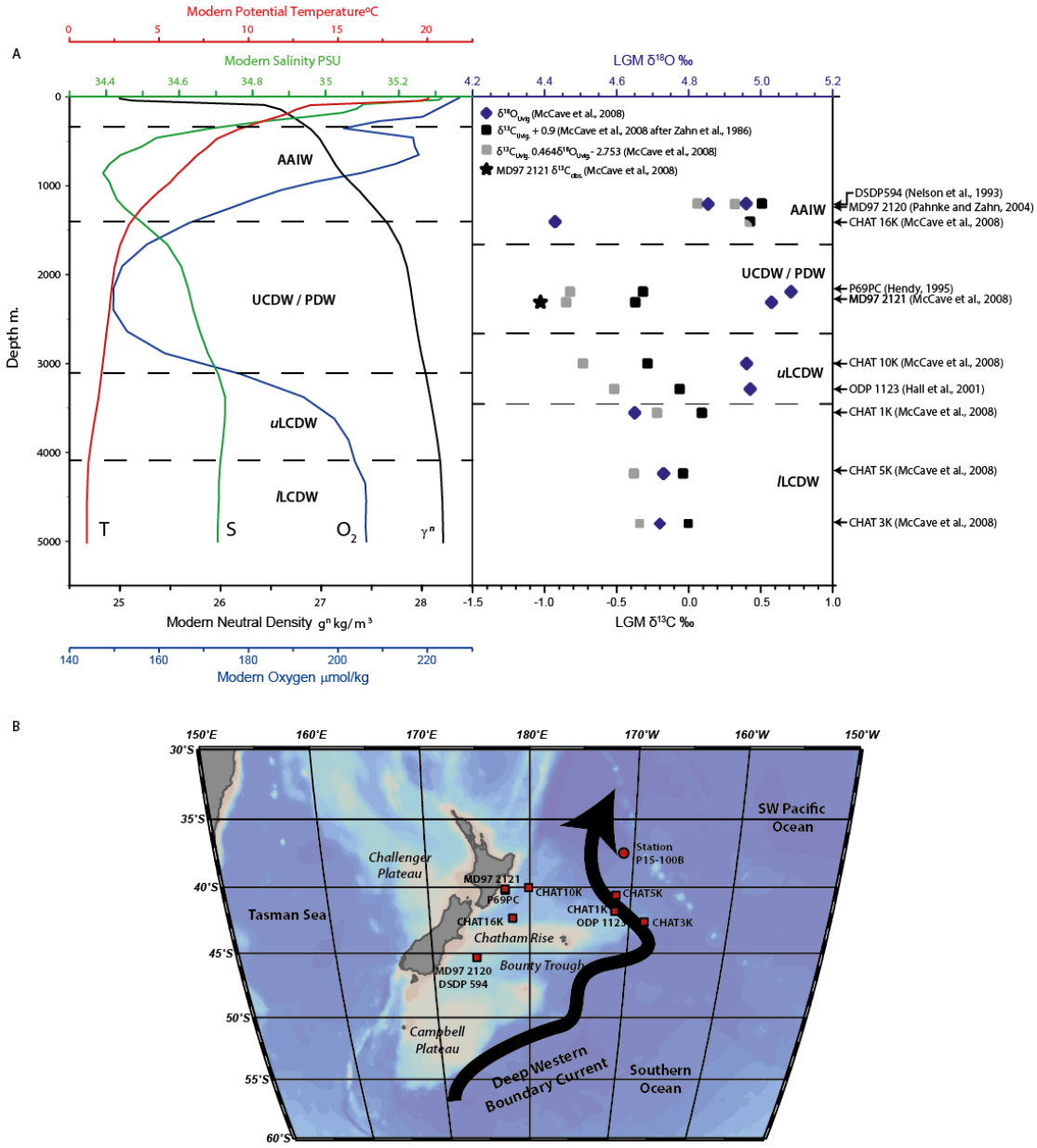

Fig. 3.12 A: (Left panel): A hydrographic profile of World Ocean Circulation Experiment cruise P15 at station 100B (Schlitzer, 2000) showing properties of major water masses in the Deep Western Boundary Current (DWBC) in the western Pacific sector. Note UCDW mixes with southward flowing PDW in this region. (Upper right panel): $\delta^{13}C^{b}$ and $\delta^{18}O^{b}$ data during the LGM from a transect of cores located along the DWBC as it flows across Chatham Rise. All data were measured on the infaunal foraminifer *Uvigerina* spp. (diamonds and squares), except the data from core MD97-2121, which were obtained from *Uvigerina* and *Cibicidoides* (star) independently. To account for *Uvigerina* habitat effects, their $\delta^{13}C$ data have been converted to 'Cibicidoides equivalent' using both a uniform correction of 0.9‰ (black data points, after Zahn et al. (1986) and a variable offset related to the $\delta^{18}O$ data measured on the same foraminifer tests, which is used as an approximation for glacial state and therefore particulate organic matter flux (grey data points, after McCave et al. (2008)).B: Location map with core sites and seawater station 100B.

2017). On the other hand, these same bathymetric highs may also have promoted diapycnal mixing between AABW originating from the Atlantic sector and overlying CDW. LGM salinity reconstructions from sites bathed in UCDW in the Atlantic sector and/or NCW as it flowed into the Atlantic sector are required to better constrain the mixing ratio of CDW and AABW from the Atlantic sector as it flowed into the Pacific sector; however, the low $\delta^{13}C_b$ values recorded in uLCDW from the Pacific sector suggest that some mixing occurred.

As discussed previously, an alternative possibility to account for the spatial pattern of SO $\delta^{13}C_b$ during glacial periods is that the low glacial $\delta^{13}C$ values observed in the Pacific sector and/or Atlantic sector were caused by high seasonal productivity north of the APF during times of increased airborne input of the micronutrient Fe via dust. This hypothesis is not supported by the data from the Atlantic sector, however, as this mechanism is unable to explain the observed $\delta^{13}C$ decrease with increasing water depth. It is clear from the LGM compilation of $\delta^{13}C_b$ data presented in Figs. 3.8 and 3.10 that cores in close proximity to each other record different LGM $\delta^{13}C$ values depending on their water depth – i.e. cores above c.2.5 km water depth are ^{13}C-enriched relative to cores below c.2.5 km water depth. It therefore seems that the low $\delta^{13}C$ values recorded in cores from the deep Atlantic sector represent a true water mass signature. LGM $\delta^{13}C_b$ data from the Pacific sector are sparse, but there seems to be a strong latitudinal control on the $\delta^{13}C$ signal of cores from this region, with the lowest $\delta^{13}C$ values found in the region close to or north of the APF, where productivity was enhanced during the LGM (Bostock et al., 2013; Bradtmiller et al., 2009; Lamy et al., 2014). Although this trend could be interpreted as a result of glacial increase in surface water productivity north of the APF influencing the $\delta^{13}C_b$ record, the coherence of the $\delta^{13}C$ records from this region during the last 500 ka (see section 3.4.3 below) seems to rule out the scenario that the glacial lowering of the $\delta^{13}C_b$ values results entirely from a concomitant productivity increase.

Another possibility is that SO overturning circulation was greatly reduced during the last glacial period, with no upwelling around the Antarctic continental margin. This would imply that all the cores with low LGM $\delta^{13}C_b$ values from the Atlantic, Indian and Pacific sectors were bathed in the same water mass. If this were the case, the relatively ^{13}C-enriched LGM values recorded at site PC493 would reflect a position of this core above a chemocline at c.2.5 km depth, below which resided the nutrient-rich deep glacial water mass with high CO_2 contents and low $\delta^{13}C_{seawater}$. As discussed in section 3.4.1, there are several lines of evidence demonstrating that upwelling of lLCDW at site PC493 has been a persistent feature during the last 800 ka: 1) the presence of polynyas above site PC493 is indicative of upwelling of a (relatively warm) deep water mass to the surface ocean; 2) this is supported by a planktic I/Ca reconstruction of upper ocean oxygen concentrations from the same site, documenting

the upwelling of a low-oxygen water mass during the LGM (Lu et al., 2016); 3) It is unclear whether it is physically possible to "flatten" isopycnals in the SO and prevent upwelling of deep water, considering that the SO overturning circulation is driven by i) wind-driven Ekman transport and ii) buoyancy fluxes between the atmosphere and surface ocean. During glacial periods of more expanded sea ice cover, the location of northward Ekman transport and regions of surface ocean buoyancy loss and gain to the atmosphere migrated further north (Watson et al., 2015). SO overturning circulation would therefore continue under glacial conditions, with upwelling of deep waters along the Antarctic continental margin (Böning et al., 2008). If anything, glacial time waters bathing site PC493 under these conditions would have been sourced from greater water depths than today. Assuming that δ^{13}C seawater acts as a conservative water mass tracer over relatively short distances within the SO, δ^{13}C of DIC would trace isopycnals. Thus, the LGM δ^{13}C compilation shown here would allow us to test the hypothesis that upwelling around the Antarctic continental margin occurred during the LGM. In the Atlantic sector, the hypothesis of tilted isopycnals and continued upwelling during the LGM appears to be consistent with the pattern of glacial $\delta^{13}C_b$ values, although there is some scatter in the data, partly due to averaging across the entire South Atlantic basin (Fig. 3.13). Unfortunately, there are too few data points to perform the same exercise in the Pacific sector. However, it seems reasonable to assume that the same physical process leading to upwelling in the Atlantic sector during past glacial periods would also have been active in the Pacific sector.

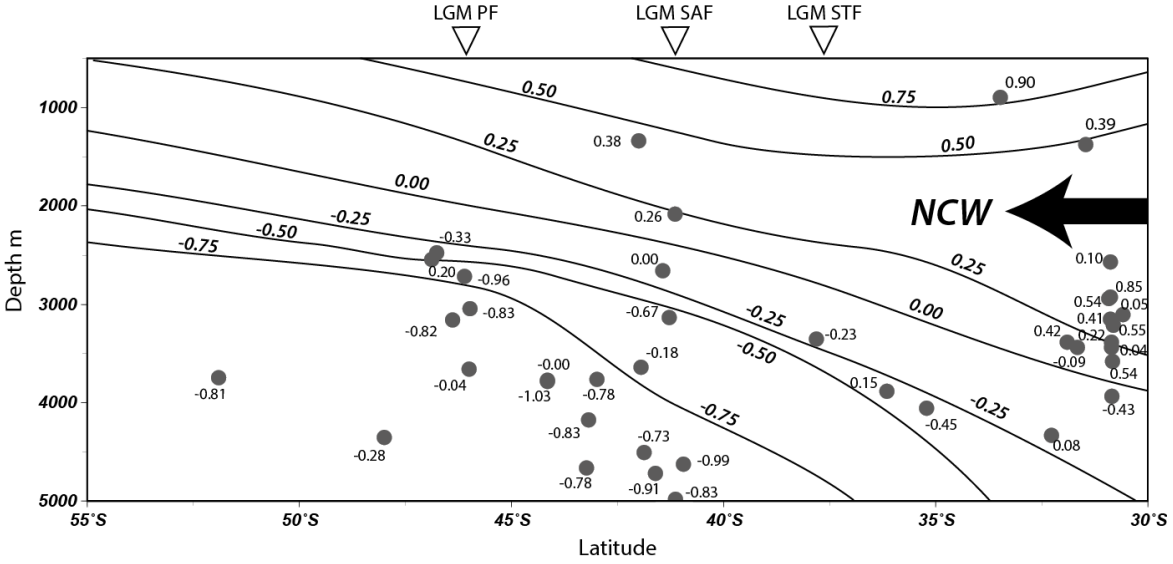

Fig. 3.13 Contoured LGM $\delta^{13}C_b$ values measured on *Cibicidoides* tests from the Atlantic sector. Although there is scatter in the data, it is possible to discern inflowing NCW at c.2000 m. water depth and the tilt of contours towards the Antarctic continent.

Given the spatial pattern of $\delta^{13}C_b$ values during the LGM, the most likely scenario for palaeocirculation in the glacial SO is that of reduced admixture of abyssal waters depleted in ^{13}C from the Atlantic sector into overlying waters and into the abyssal Pacific sector. While some vertical mixing and advection of relatively ^{13}C-depleted AABW/LCDW from the Atlantic sector into the Pacific sector must have occurred (as it is evidenced by the presence of uLCDW with lowered $\delta^{13}C$ signature), the abyssal Pacific sector was not entirely bathed by the relatively extremely ^{13}C-depleted, CO_2-rich water mass observed in the glacial Atlantic basin (Fig. 3.14).

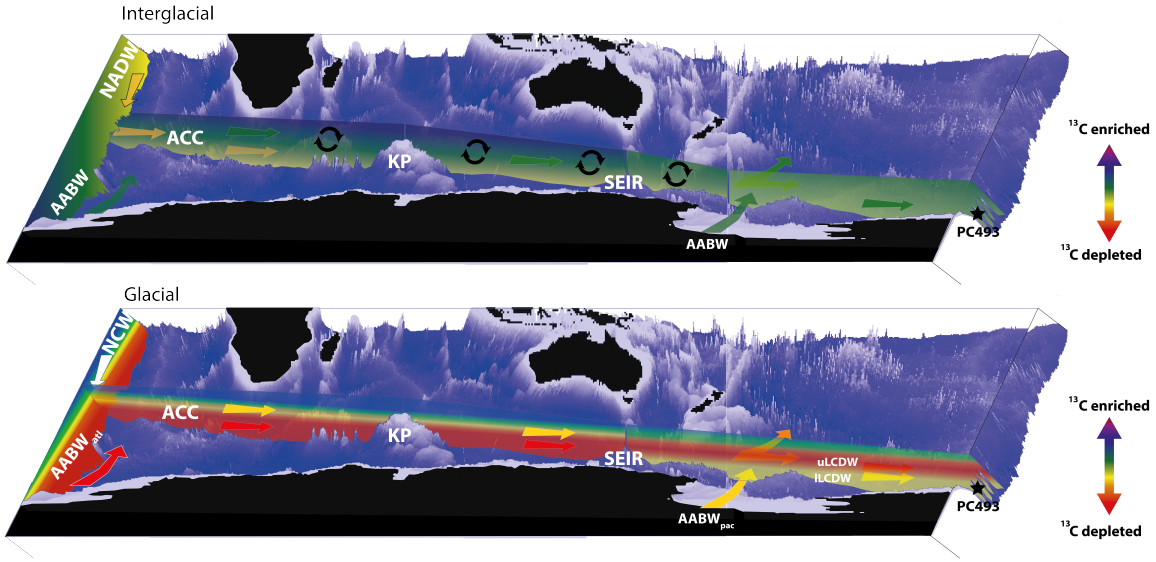

Fig. 3.14 Schematic depiction of SO circulation and $\delta^{13}C_{seawater}$ during the current interglacial (top panel) and last glacial period (bottom panel). Coloured arrows represent circulation and black arrows denote strong vertical mixing

3.4.3 $\delta^{13}C$ changes in deep and bottom water masses of the Southern Ocean during the glacial-interglacial cycles of the Late Quaternary

The benthic $\delta^{13}C_b$ record of core PC493 can be compared with records from other areas of the SO to elucidate the spatial advection of deep water masses across the glacial-interglacial cycles of the past 800,000 years. The spatial coverage of sediment cores providing palaeoceanographic information stretching back multiple glacial cycles within the SO is sparse, but there are a few key core sites which, along with the new $\delta^{13}C_b$ record of PC493, provide insights to SO palaeocirculation. Ocean Drilling Program Leg 177 sites 1090 (Hodell et al.,

2003), and 1089 (Venz and Hodell, 2002), core TTNO57-6 (Hodell et al., 2003) and the composite record of sites RC11-83/TN57-21 (Ninnemann and Charles, 1997, 2002) recovered from the SAZ in the Atlantic sector, along with Indian sector cores PS2561-1 collected from the SE flank of Agulhas Plateau (Krueger et al., 2012) and MD02-2488 recovered from the South Indian Ridge (Govin et al., 2009) all document the glacial-age presence of the abyssal dense, salty, nutrient-rich water mass with high CO_2 contents and low $\delta^{13}C$ discussed in the previous section. Inflow of nutrient- and carbon-poor NCW with relatively high $\delta^{13}C$ values at intermediate water depths into the SO is monitored by Ocean Drilling Program Leg 177 Site 1088 located on Agulhas Ridge (Hodell et al., 2003), while outflow of LCDW from the SO into the SW Pacific is constrained by Site 1123 located on Chatham Rise (Hall et al., 2001) Fig. 3.12). uLCDW from the SAZ of the Pacific sector is constrained by cores E11-2 (Ninnemann and Charles, 2002), SO213-59-2 (Molina-Kescher et al., 2016), PS75/059-2 and PS75/056-1 (Ullermann et al., 2016). The age models for all cores discussed in this section are as originally published, except for Site 1090, whose $\delta^{18}O_b$ record has been correlated with the global LR04 $\delta^{18}O_b$ stack (Lisiecki and Raymo, 2005). All core locations are shown in Fig. 3.2, and the stable carbon and oxygen isotope records of the cores mentioned above are shown in Fig. 3.15. To explore the long-term trends in SO palaeocirculation, I averaged and smoothed the records from the deep Atlantic and Indian sectors (which have been bathed in a mixture of AABW and LCDW throughout the Late Quaternary), and Pacific sector (bathed in uLCDW) at 2 kyr resolution to create 'stacks' for comparison with the records from sites PC493 (lLCDW in the Pacific sector) and Site 1088 (a mixture of UCDW and NCW as it flows into the SO).

Despite the noise within the individual datasets, the $\delta^{18}O_b$ stacks compare well with the global LR04 stack, providing confidence that the average values are representative of each sector (Fig. 3.16). Between the end of MIS 7 and the beginning of the Holocene, $\delta^{13}C$ values in the Pacific sector were consistently offset from that of the deep Atlantic and Indian sectors by c.+0.2‰. Both stacks exhibit the same structure throughout this time interval, with increased $\delta^{13}C$ depletion during the penultimate glaciation (MIS 6) relative to the last glacial period. This suggests a similar control on this 'baseline' glacial $\delta^{13}C$ value and that the ^{13}C-depletion observed in uLCDW of the Pacific sector originates in the abyssal Atlantic sector. A synthesis of global $\delta^{13}C$ data shows that this pattern of increased $\delta^{13}C$ depletion during MIS 6 relative to MIS 2 is observed throughout the global ocean (Oliver et al., 2010), and may in fact reflect changes in the carbon budget of the terrestrial biosphere.

If AABW/LCDW from the Atlantic sector did exert a control on the $\delta^{13}C$ of uLCDW in the Pacific sector, the positive $\delta^{13}C$ offset in the Pacific sector along the flow path of the ACC must reflect admixture between AABW from the Atlantic sector and a better ventilated

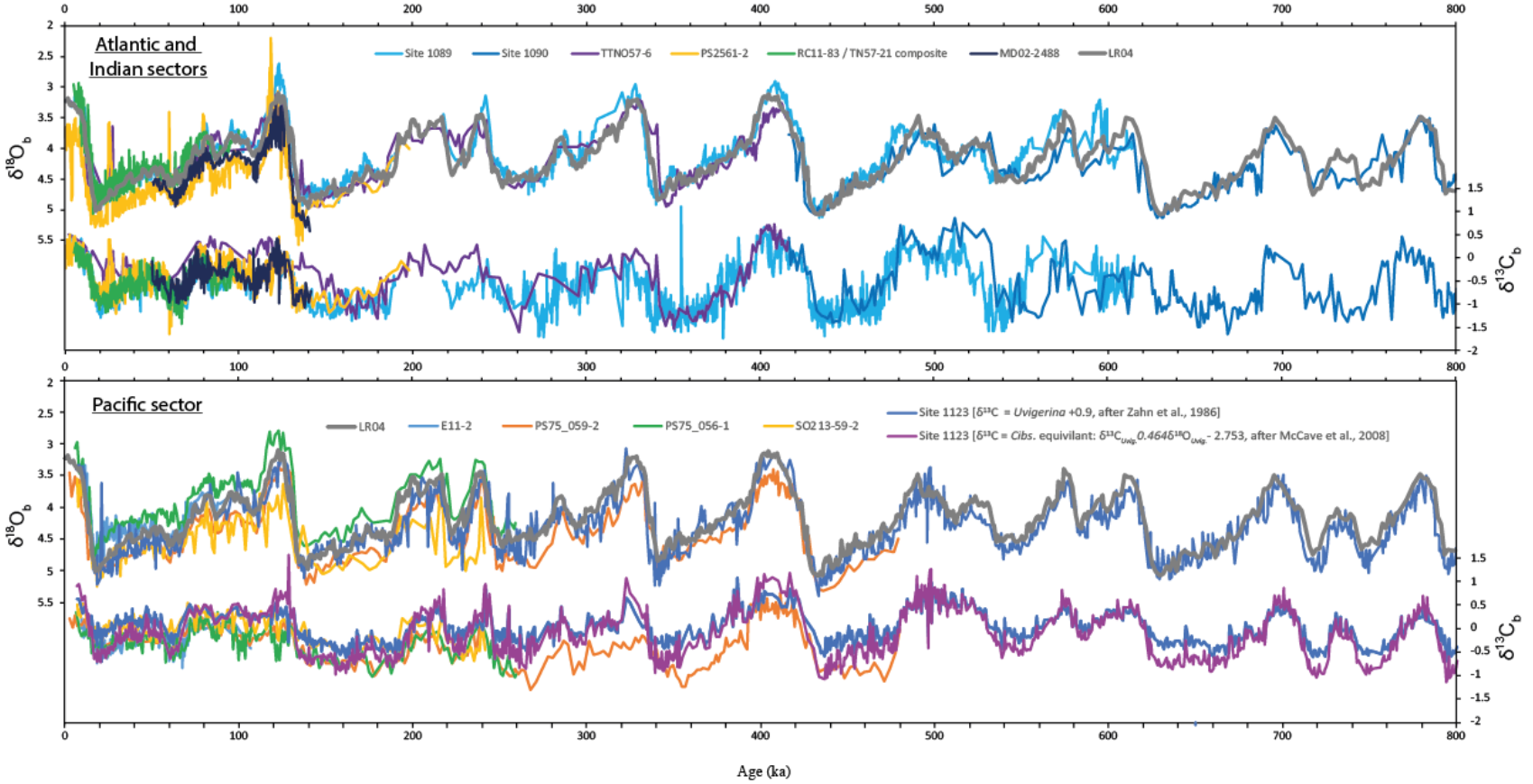

Fig. 3.15 Records of $\delta^{18}O_b$ and $\delta^{13}C_b$ from the Atlantic and Indian (upper panel) and Pacific (lower panel) sectors used to create composite 'stacks' shown in Fig. 3.16. The global LR04 $\delta^{18}O_b$ stack is shown for comparison. Also shown are data from Site 1123, located on Chatham Rise off New Zealand. This $\delta^{13}C_b$ record was measured on *Uvigerina*, to which I have applied a uniform correction of +0.9‰ (Zahn et al., 1986) (blue curve) and a variable offset related to the $\delta^{18}O_b$ value of *Uvigerina*, after McCave et al. (2008). Due to uncertainties in the offset of *Uvigerina* $\delta^{13}C_b$ from $\delta^{13}C_{seawater}$ this record was not included in the stack of records shown in Fig. 3.16. It is included in this figure to demonstrate that the mode of glacial-interglacial $\delta^{13}C_b$ variation in the Pacific sector remained constant throughout the last 800 ka.

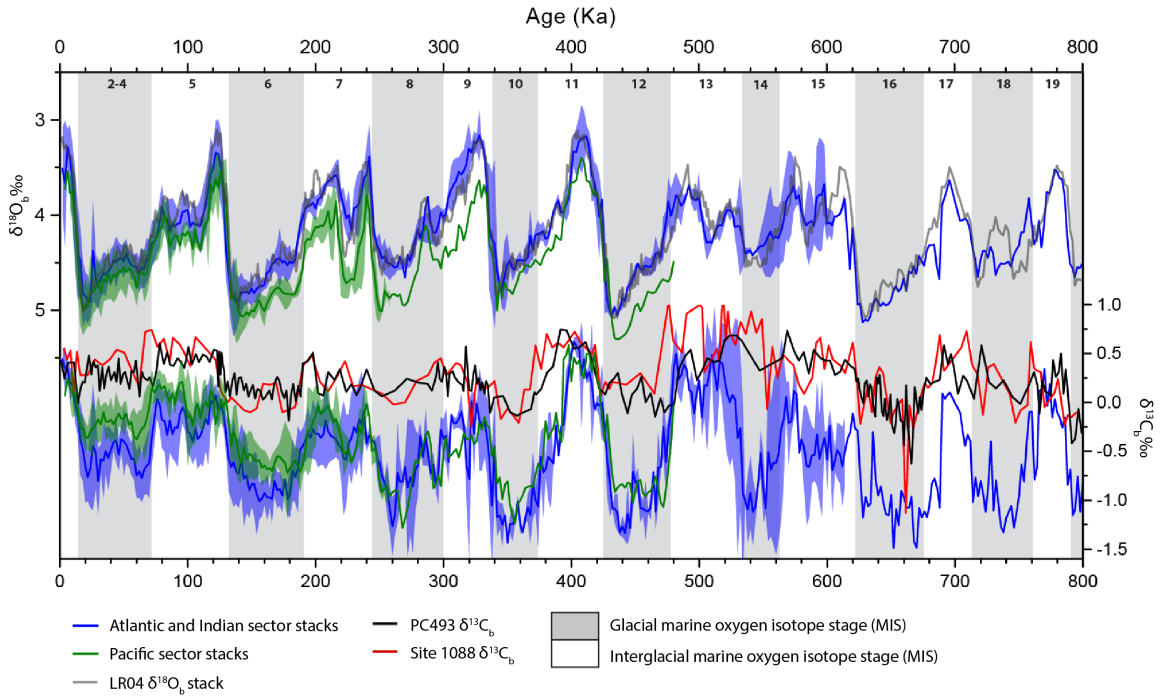

Fig. 3.16 Comparison of the PC493 $\delta^{13}C_b$ record with composite $\delta^{13}C_b$ 'stacks' for AABW/LCDW in the Atlantic and Indian sectors (blue) and uLCDW within the Pacific sector (green) produced by averaging and smoothing the individual deep water records displayed in Fig. 3.15 at 2 kyr resolution. The $\delta^{18}O_b$ data of the stacks and the global LR04 stack are also shown. Shading represents the standard deviation of records used to construct each composite stack. Also shown here are the $\delta^{13}C_b$ data from Site 1088 that records inflow of NCW as it mixes with SO waters to form CDW.

water mass. During the three glacial cycles prior to MIS 6 (MIS 8 to MIS 12) the $\delta^{13}C$ values in the abyssal Atlantic and uLCDW in the Pacific sector co-varied, although $\delta^{13}C$ depletion during the glacial maxima of MIS 10 and 12 was more severe in the Atlantic and Indian sectors than in the Pacific sector. The difference in $\delta^{13}C$ of AABW from the Atlantic sector and lLCDW recorded at site PC493 in the Pacific sector indicates different deep water formation mechanisms in the Atlantic and Pacific sectors during past glacial periods.

3.4.4 Implications for AABW production during the Late Quaternary

The absence of significant periods of relative $\delta^{13}C$ depletion in lLCDW bathing site PC493 indicates that the source of the $\delta^{13}C$ depleted glacial water mass observed in the Atlantic sector must have been deep waters forming there during glacial periods throughout the last 800,000 years. If – as it is the case today – AABW influences the $\delta^{13}C$ of deep waters

bathing site PC493, it is possible to gauge the heterogeneity of AABW formed in different sectors of the SO during glacial periods of the Late Quaternary (Fig. 3.17).

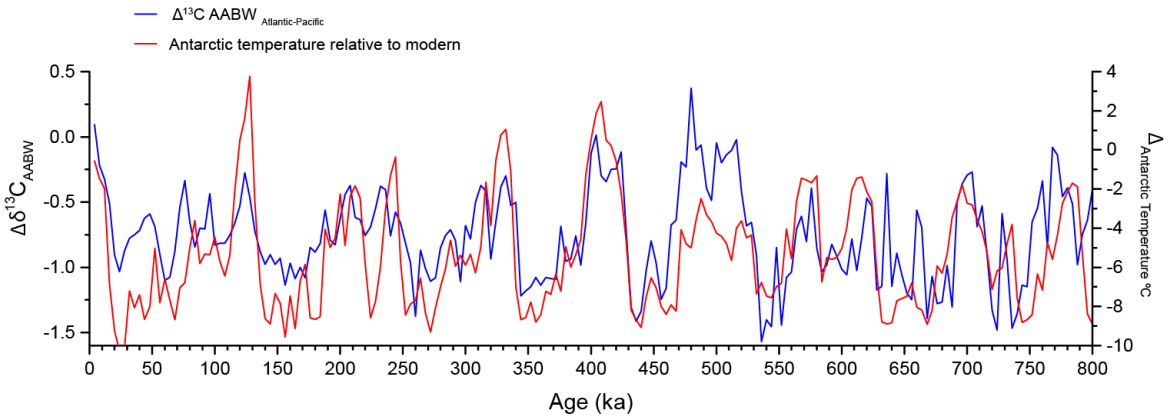

Fig. 3.17 Difference between δ^{13}C of AABW formed in the Atlantic sector (taken here as the average value of the Atlantic and Indian sector deep water δ^{13}C stack) and δ^{13}C values at site PC493. Assuming the $\delta^{13}C_b$ values recorded at site PC493 monitor the δ^{13}C of AABW formed in the Pacific sector, the $\Delta\delta^{13}$C signal provides a measure for the heterogeneity in AABW δ^{13}C in the SO. Also shown is the Antarctic temperature relative to modern values reconstructed using deuterium measurements on the EPICA Dome C ice core (Jouzel et al., 2007). Both records smoothed to 4 kyr resolution

Increases in the heterogeneity of SO bottom water δ^{13}C occurred throughout the glacial periods of the last 800,000 years and were driven by changes in δ^{13}C of AABW in the Atlantic sector ($AABW_{atl}$). Stephens and Keeling (2000) hypothesize that during the LGM waters upwelling in the SO froze at the sea surface, thereby increasing sea ice cover and reducing air-sea gas exchange. It does appear that increased heterogeneity in AABW occurred during cold periods in Antarctica (Fig. 3.17), lending weight to the hypothesis that air-sea gas exchange between upwelling deep water and the atmosphere was limited during these periods, at least in the Atlantic sector. At low temperatures, the thermodynamic fractionation in δ^{13}C that occurs during air-sea exchange drives $\delta^{13}C_{seawater}$ to higher values (Zhang et al., 1995). The δ^{13}C depletion observed in $AABW_{atl}$ during the LGM therefore implies a reduction in air-sea exchange during bottom water formation (Mackensen et al., 1996). Today, most $AABW_{atl}$ forms in the Weddell Sea. There, the precursor water masses for $AABW_{atl}$ are produced via two mechanism: dense waters form via i) brine rejection in regions of sea-ice formation and polynyas, and ii) supercooling of waters beneath floating ice shelves. The first mechanism leaves a high thermodynamic imprint on $AABW_{atl}$, leading to $AABW_{atl}$ with elevated δ^{13}C values, while the second mechanism minimises the impact of this thermodynamic imprint. Thus, increasing the relative proportion of bottom water production via mechanism (ii) compared with the modern would lead to a decrease in

bottom water $\delta^{13}C$ (Mackensen et al., 1996). An increase in $AABW_{atl}$ formation beneath ice shelves is at odds with evidence from submarine glacial geomorphology and marine sediment cores which suggest that during the LGM the continental shelf in the southern Weddell Sea may have been entirely covered by grounded ice (Hillenbrand et al., 2014, 2012), preventing sub-ice shelf formation of precursor water masses for $AABW_{atl}$. However, increased sub-ice shelf production of $AABW_{atl}$ would be consistent with constraints from terrestrial geological data (mainly cosmogenic exposure dates) from the hinterland of the Weddell Sea embayment, which indicate that the LGM ice sheet was not thick enough to cause grounding in the deep bathymetric troughs extending across the Weddell Sea shelf, and that ice shelves may have persisted there through the LGM (Bentley, 2010; Hein et al., 2011; Hillenbrand et al., 2014). On the other hand, the process of brine rejection in the seasonal sea-ice zone, which had expanded equator-ward in the Atlantic sector during the last glacial period (Collins et al., 2012; Gersonde et al., 2005), and also in polynyas on the Antarctic continental margin (e.g. Smith et al. (2010)), is likely to have taken place at the LGM. According to Stephens and Keelings' (2000) hypothesis, brine rejection would actually have increased the thermodynamic fractionation and raised $\delta^{13}C_{seawater}$. The answer to this paradox may therefore lie in a reduction in the formation of AABW in the Atlantic sector during glacial periods, thereby reducing the ability of thermodynamic fractionation during air-sea exchange to ventilate, or 'reset', the $\delta^{13}C$ of deep waters in this region. A reduction in AABW formation in the Atlantic sector is at odds with the increased salinity of deep waters in the Atlantic sector, which requires a significant increase in AABW formed via brine rejection during sea-ice formation, but would be consistent with a glacial reduction in AABW flow speed as it was reconstructed from deep water cores recovered in the Weddell Sea and the subantarctic Atlantic sector of the SO, respectively (Diekmann et al., 2003).

In contrast, deep water formation mechanisms within the Pacific sector of the SO maintained elevated $\delta^{13}C$ throughout glacial periods of the last 800,000 years. Only a minor proportion of modern day RSBW production is attributed to the supercooling of waters beneath floating ice shelves within the Ross Sea Embayment, with the majority of RSBW production occurring the western Ross Sea Embayment via brine rejection during sea ice formation (Orsi and Wiederwohl, 2009). Reconstructioned limits of grounded ice within the Ross Sea Embayment suggest these regions of bottom water production were overridden by ice sheets during past glacial periods (see Anderson 2014 for a recent review). However, the presence of polynyas in the north western Ross Sea Embayment have been inferred from the deposition of planktic foraminifera-bearing sediment layers enriched in ice-rafted debris (IRD) (Bonaccorsi et al., 2007; Smith et al., 2010), which remained ice free during past glacials. RSBW formation within these polynyas would provide a mechanism for the

continued production of bottom waters with an elevated δ^{13}C signal during past glacial periods. The history of RSBW formation is explored further in chapter 5.

3.4.5 Implications for nutrient cycling in the glacial ocean

Partially or completely restricting the flow of AABW formed in the Atlantic sector of the SO through the ACC and into the Pacific sector and/or reducing formation of $AABW_{atl}$ during glacial periods would have had important implications for the cycling of nutrients within the ocean interior. In the modern ocean, the most important water mass in setting the chemical composition of CDW is inflowing NCW. The similarity of benthic δ^{13}C data from Site 1088 – recording the admixture of NCW into UCDW – during both interglacial and glacial periods, and the δ^{13}C signal of lLCDW at site PC493 illustrates that UCDW from the Atlantic sector – and therefore NCW – may have played an important role in setting the preformed nutrient concentrations of AABW formed in the Pacific sector during past glacial periods. Surface waters in the North Atlantic which go on to form NCW are sourced in low latitudes, where utilization of surface nutrients is near complete, imposing a low preformed nutrient content on NCW. In contrast, surface waters around Antarctica today experience incomplete nutrient utilization, imposing a much higher preformed nutrient content on the ocean interior that is ventilated by AABW. Palaeoproductivity indicators suggest a decrease in glacial productivity south of the APF (Bradtmiller et al., 2009; Jaccard et al., 2013; Kohfeld et al., 2005; Lamy et al., 2014), while diatom-bound and deep sea coral nitrogen isotopes suggest more complete utilization of nutrients in surface waters in this region (Robinson and Sigman, 2008; Wang et al., 2017). Taken together, these lines of evidence point to NCW with a low preformed nutrient content feeding the surface waters of the polar SO during glacial periods. Any nutrients left unused by organisms in the surface ocean represent an inefficiency in the cycling of organic carbon from the surface ocean to the interior. If – as appears to be the case based on the δ^{13}C record of core PC493 – NCW was ultimately the precursor water mass to AABW formed in the Pacific sector, this would represent an increase in the efficiency of the global biological pump during glacial periods compared with the modern. Box models (Hain et al., 2014; Sigman et al., 2010) show that increasing the volume of the abyssal ocean ventilated by AABW with a low preformed nutrient content decreases pCO_2^{atm}. If the lLCDW observed in Pacific sector played a significant role in ventilating the Pacific basin, this would therefore increase the efficiency of the global biological pump, driving down pCO_2^{atm}.

3.5 Conclusions

In this chapter, I have presented benthic and planktic foraminifera $\delta^{13}C$ and $\delta^{18}O$ records and palaeo-productivity proxy data (Ba/Ti ratios, TOC and $CaCO_3$ contents) from core PC493 that was recovered in the Pacific sector of the SO and spans the last 800,000 years. The Ba/Ti and $CaCO_3$ records demonstrate reduced productivity at this location during past glacials, due to the site being nearly permanently covered by sea ice. I have documented the evidence for the continued upwelling of deep waters and for the presence of polynyas at site PC493 during past glacial periods.

For comparison with the $\delta^{13}C_b$ record of lLCDW at site PC493, I extended Peterson et al. (2014)'s compilation of late Holocene and LGM $\delta^{13}C_b$ data measured on *Cibicidoides* from sediment cores located south of 30°S, and compiled 'stacks' of AABW/LCDW $\delta^{13}C$ from the Atlantic sector and uLCDW $\delta^{13}C$ from the Pacific sector of the SO during the Late Quaternary. Using this data I could demonstrate that the extensive glacial depletion of AABW/LCDW $\delta^{13}C$ observed in the Atlantic sector of the SO is a water mass signature, and cannot be attributed to glacial increases in biological productivity and the 'Mackensen effect'. Although these processes may have affected individual core sites north of the APF in the Pacific sector, the coherence of $\delta^{13}C$ records from this region provides evidence that also there the glacial $\delta^{13}C$ decrease is a true water mass signal.

The lLCDW $\delta^{13}C$ record at site PC493 shows no evidence for the $\delta^{13}C$ depletion observed in the Atlantic sector of the SO during the LGM, suggesting a different mode of deep and bottom water formation in the Atlantic sector versus the Pacific sector during glacial periods. These different 'modes' of deep and bottom water formation may have been driven by changes in the formation of AABW in the Atlantic sector, and are consistent across glacial periods throughout the last 800,000 years. Changes in AABW formation in the Atlantic sector during past glacial periods may have included a reduction in the formation of precursor water masses on the Antarctic continental shelf, or differences in the relative proportion of dense shelf waters formed under ice shelves and in polynyas to AABW formation. Evidence for increased salinity and an expansion of the seasonal sea ice zone in the Atlantic sector is consistent with increased deep water formation via brine rejection during sea ice formation. This, however would lead to an increase in the thermodynamic fractionation of carbon isotopes during air-sea gas exchange and an increase in the $\delta^{13}C$ of deep waters, the opposite of what is observed in the $\delta^{13}C$ recorded in benthic foraminifera.

Evidence for a mid-depth $\delta^{13}C_{palaeoSW}$ 'bulge' in the Pacific sector during glacial periods demonstrates that the relatively ^{13}C-depleted, CO_2-rich deep water from the Atlantic sector was – at least partially – advected into uLCDW in the Pacific sector. The abyssal Pacific

sector, however, was not bathed entirely by this ^{13}C-depleted deep water mass. The precursor water mass for deep and bottom waters formed in the Pacific sector may have been NCW sourced with a low preformed nutrient content. If bottom waters formed in the Pacific sector went on to ventilate a large portion of the deep ocean interior, for example the abyssal Pacific basin, this low preformed nutrient content would indicate a significant increase in the efficiency of the global biological pump during glacial periods compared with the modern ocean, providing a mechanism to lower glacial pCO_2^{atm}.

Chapter 4

A 1.5 million year neodymium isotope record of deep water circulation in the equatorial Indian Ocean

4.1 Introduction

The Earth has undergone both gradual and abrupt shifts in its climate states throughout the last 1.5 Ma. Between c.1250-750 ka, there was a shift in the periodicity of glacial-interglacial cyclicity from an obliquity-driven 41 kyr pacing, to a quasi-100 kyr cyclicity after (Clark et al., 2006). This time interval, known as the Mid Pleistocene Transition (MPT), is characterised by an abrupt expansion in terrestrial ice volume around 900 ka (Elderfield et al., 2012) and a more gradual increase in the amplitude of climatic shifts between interglacial and glacial states (Fig 4.1). A wide variety of changes in Earth's climate system is inferred from palaeoclimate proxy archives across the MPT, and several mechanisms have been proposed to explain these changes. Following the MPT, the amplitude of glacial-interglacial climatic oscillations increased once again at c. 430 ka, a climatic transition termed the Mid-Bruhnes event (MBE) driven by an increased warming during interglacial periods, although the global extent of this event is debated (Candy and McClymont, 2013; Lang and Wolff, 2011).

The identification of an orbital control on the stable oxygen isotopes (δ^{18}O) recorded in benthic foraminifera ($\delta^{18}O_b$) was a key validation of the Milankovitch hypothesis for an orbital control on Pleistocene glaciation (Hays et al., 1976; Milankovich, 1941). It quickly became apparent that the dominant 100 kyr cyclicity observed through the Late Pleistocene emerged during the MPT (Shackleton and Opdyke, 1976); prior to this, the dominant periodicity in $\delta^{18}O_b$ records corresponded to the 41 kyr orbital obliquity cycle

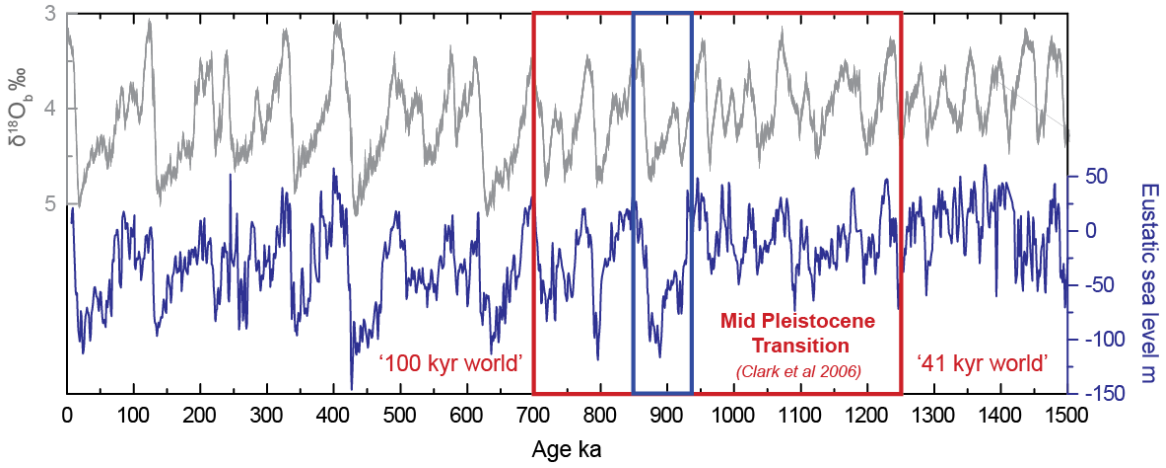

Fig. 4.1 The LR04 stack of stable oxygen isotope data measured on benthic foraminifera ($\delta^{18}O_b$, grey line) (Lisiecki and Raymo, 2005) alongside sea level relative to today (blue line), calculated by Elderfield et al (2012, supplementary online materials) using $\delta^{18}O_b$ and Mg/Ca palaeothermometry to deconvolve the $\delta^{18}O$ of seawater at a core site in the SW Pacific. The red box denotes the Mid Pleistocene Transition as defined by Clark et al. (2006), who identified the emergence of 100 kyr cyclicity in the LR04 $\delta^{18}O_b$ stack between 1250-700 ka, while the blue box denotes the rapid expansion in global ice volume across 936-866 (MIS 24-22) identified by Elderfield et al. (2012)

(Lisiecki and Raymo, 2005). This shift in $\delta^{18}O_b$ was originally identified in Pacific core V28-239 (3.25°N, 159.1°E, 3490 m.) as a step-change to higher values between c. 900-866 ka, interpreted as a major expansion of Northern Hemisphere glaciation (Shackleton and Opdyke, 1976). Subsequent studies have inferred a more gradual increase in global $\delta^{18}O_b$, beginning at c. 1250 ka, and completed by 700 ka (e.g. Clark et al. (2006); Lisiecki and Raymo (2005)).

The debate surrounding the timing and cause of the MPT is still ongoing. Based on the nature of $\delta^{18}O_b$ changes across the MPT, a number of hypotheses for the cause of the MPT and the onset of 100 kyr glacial-interglacial cyclicity call for an increase in global ice volume through this interval. These hypotheses invoke either an expansion in northern hemisphere ice sheets, which are more resistant to waxing and waning on 41 kyr timescales (Abe-Ouchi et al., 2013; Clark et al., 2006; Clark and Pollard, 1998; Crowley and Hyde, 2008), and/or ice sheet expansion in the southern hemisphere, causing a transition from a deglaciated Antarctic continental margin sensitive to southern hemisphere insolation forcing, to marine-based Antarctic ice sheets more sensitive to changes in sea level driven by northern hemisphere insolation forcing (Elderfield et al., 2012; Raymo et al., 2006). Attempts have been made to investigate changes in global ice volume across the MPT using Mg/Ca palaeothermometry to determine bottom water temperatures, so as to deconvolve the $\delta^{18}O_{palaeoSW}$ component from

$\delta^{18}O_b$ (Elderfield et al., 2012; Ford et al., 2016; Sosdian and Rosenthal, 2009). Although each of these studies agrees that global ice volume crossed a critical threshold across the MPT, leading to a change in the response of the global climate system to orbital forcing and ushering in the '100 kyr world', they disagree as to the nature of this change. $\delta^{18}O_{palaeoSW}$ reconstructions from the Atlantic Ocean (Ford et al., 2016; Sosdian and Rosenthal, 2009) suggest only a modest, gradual increase in ice volume across the MPT, which occurred as part of a longer-term trend, while $\delta^{18}O_{palaeoSW}$ reconstructed from the SW Pacific suggest a sharp increase in global ice volume at c. 900 ka.

It has been argued that moisture supply to the high latitude northern hemisphere played a critical role in the expansion of northern hemisphere ice sheets during glacial periods (e.g. McClymont et al. (2008)). In general, Pleistocene records of sea surface temperature (SST) show a gradual decrease in surface temperatures across the MPT, or an acceleration in a pre-existing cooling trend (see McClymont et al. (2013) for a review), with a pronounced cooling event between c. 936-866 ka. This trend towards cooler SST across the MPT is not uniform globally, but greatest in regions of upwelling and at higher latitudes, with little change in the western equatorial Pacific warm pool (McClymont et al., 2013). These steeper gradients in SST may have strengthened trade winds and increased the supply of moisture for ice sheet growth in the high latitudes, with the major decrease in SST between 936 and 866 ka leading to an intensification of ice sheet growth at this time (McClymont and Rosell-Melé, 2005).

Many hypotheses for the cause of the MPT invoke changes in ocean circulation, in particular changes in the poleward transferal of heat and moisture associated with the strength of the Atlantic Meridional Overturning Circulation (AMOC), and changes in the proportion of southern component water (SCW, high in remineralised carbon) filling the abyssal ocean, with increases in SCW argued to cause an expansion of the oceanic carbon pool at the expense of the atmospheric carbon pool (e.g. Pena and Goldstein (2014). In this chapter, I will use neodymium isotopes measured on marine sediment authigenic leachates to investigate oceanographic changes in the equatorial Indian Ocean, first over the last 860 ka and then the last 1.5 Ma. The goal of this chapter is to investigate changes in global thermohaline circulation (THC) before, during and after the MPT, and discuss potential explanations for the observed changes.

4.2 Location, chronology and previous work

4.2.1 ODP 121 Site 758: hydrography and seawater ε_{Nd}

Ocean Drilling Program (ODP) Leg 121 Site 758 is located on Ninetyeast Ridge, in the eastern equatorial Indian Ocean (5°23.05'N, 90°21.67'E, 2925 m. water depth; Fig. 4.2; Farrell and Janecek (1991)). Today, Site 758 is bathed in waters ventilated by northward-flowing modified Circumpolar Deep Water (mCDW) (Fig. 4.2) (Reid, 1995; You, 2000). The northward flow of mCDW in the Indian Ocean is concentrated in two branches: one in the west at c. 55°E, along the Madagascar and Somali Basins; and the other in the central Indian Basin at c. 70-80°E. Waters bathing Site 758 are advected to the core site via the central circulation pathway, which enters the Indian Ocean to the east of Kerguelen Plateau at c. 100°E and flows along the eastern edge of the Southeast Indian, Mid-Indian and Chagos-Laccadive ridges, before flowing east towards Site 758 (Fig. 4.2C and 4.2D). mCDW from the deep western Indian Ocean, where seawater ε_{Nd} reconstructions from the last deglacial period have been affected by boundary exchange with sediments along the Madagascan margin (Wilson et al., 2012), does not contribute to deep waters at Site 758.

Previous studies have argued that seawater ε_{Nd} in the region of Site 758 is controlled by boundary exchange with sedimentary inputs from the Ganges and Brahmaputra river systems, and that seawater ε_{Nd} at this site is therefore ultimately controlled by Himalayan weathering intensity (Burton and Vance, 2000; Gourlan et al., 2010; Stoll et al., 2007). However, measurements of seawater Nd concentrations and ε_{Nd} from the Bay of Bengal show that the ε_{Nd} signature of waters bathing Site 758 is derived from mixing between mCDW and modified North Atlantic Deep Water (mNADW) (Singh et al., 2012). Mixing calculations performed by Singh et al. (2012) suggest that c. 90% of the water bathing Site 758 is sourced in the Atlantic (mNADW) and Southern (mCDW) Oceans. Singh et al. (2012) report only a minor contribution from North Indian Deep Water (NIDW), and no contribution from Bay of Bengal Subsurface Waters (BBSW) or Himalayan river-derived waters (Ganges-Brahmaputra Bay of Bengal Low Salinity Surface Water, GB-BBLS, Fig. 4.2B). There is some evidence for release of Nd from sediments of the Bengal Fan (Singh et al., 2012), however, Site 758 is elevated some 1200 m. above Bengal fan sediments, and is therefore unlikely to be affected by boundary exchange. Past changes in the ε_{Nd} composition of waters bathing Site 758 reflect changes in mCDW with a strong influence from mNADW, making Site 758 well placed to monitor changes in the advection of NADW (hereafter termed Northern Component Water, NCW when referring to the palaeo-water mass) into CDW within the SO. As Site 758 represents the only marine sedimentary record from within the

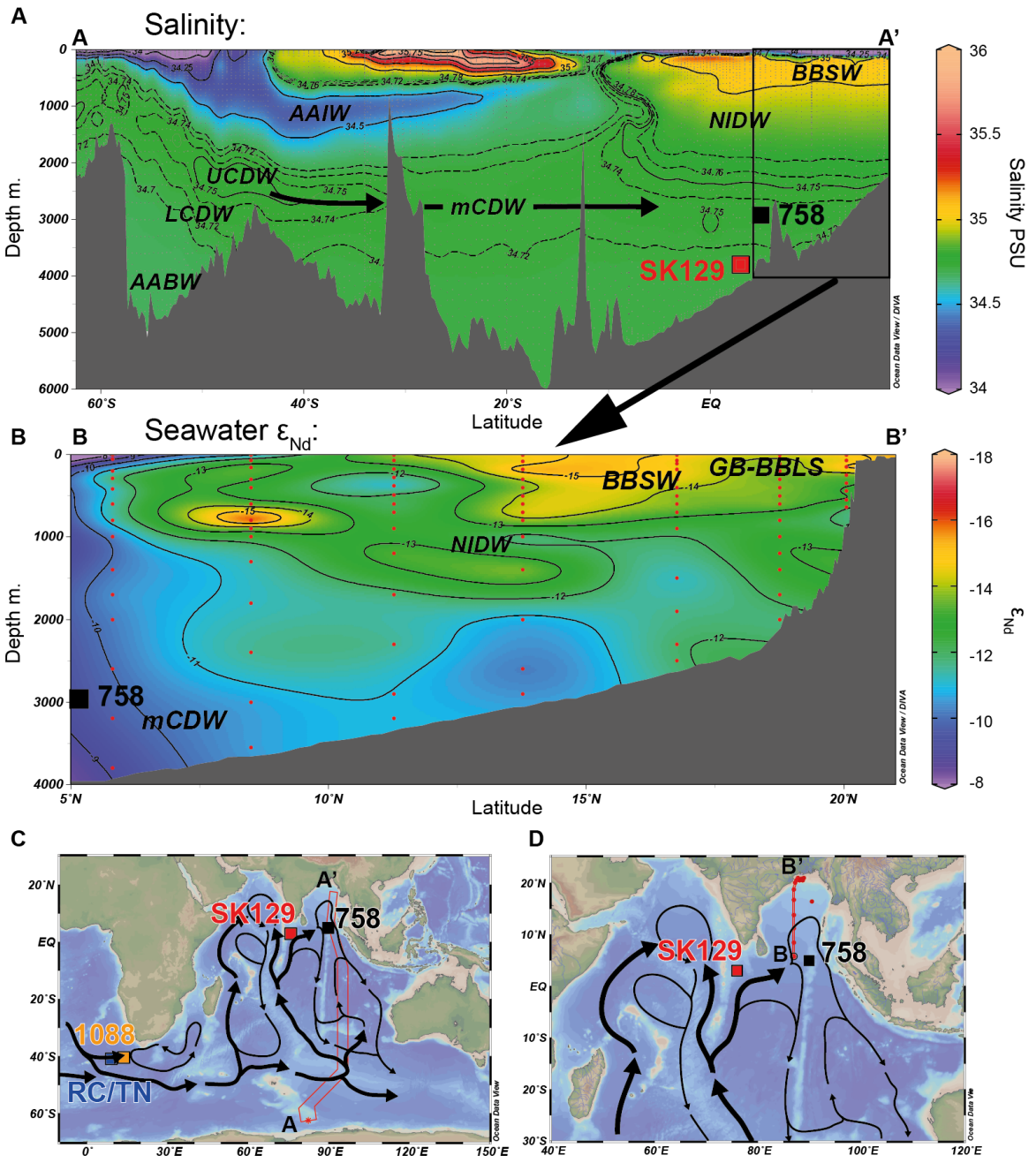

Fig. 4.2 Cross sections of salinity (A, location of section in panel C) and seawater ε_{Nd} (Singh et al., 2012) (B, location of section in panel D). The addition of North Atlantic Deep Water (NADW) to Upper Circumpolar Deep Water (UCDW) is evidenced by the salinity maximum at c. 50°S, which can be traced within mCDW through the Indian Ocean to Site 758. Seawater ε_{Nd} at Site 758 is not influenced by Himalayan river-derived waters (Ganges-Brahmaputra Bay of Bengal Low Salinity Surface Water, GB-BBLS and Bengal Subsurface Waters, BBSW). Also shown are Lower Circumpolar Deep Water (LCDW), Antarctic Bottom Water (AABW), and North Indian Deep Water (NIDW). Locations of Site 1088 (2082 m.) and the composite record of cores RC11-83 and TN057-21 (4800 m.), and SK129-CR2 (3800 m.) are shown in panel C. Major circulation pathways of CDW/mCDW within the ACC and deep western boundary currents within the SO/Indian Ocean are shown by thick black arrows in C and D, while recirculation of CDW within the Agulhas Current retroflection and mCDW within the Indian Ocean are shown by thin black arrows (after You (2000)).

Indian Ocean spanning the entire Pleistocene epoch, this site is uniquely placed to examine the admixture of NCW into CDW and its advection via mCDW through the SO and into the Indian Ocean during this time interval.

4.2.2 Ocean Drilling Program Leg 121 Site 758 chronology

This study examines sediments deposited over the last 1.5 Ma at Site 758, and the age model for this time period was constructed by tying a previously published $\delta^{18}O_b$ record measured on *Cibicidoides wuellerstorfi* (Chen et al., 1995) to the LR04 $\delta^{18}O_b$ stack (Lisiecki and Raymo, 2005). The majority of $\delta^{18}O_b$ measurements between 1.5-0 Ma from Site 758 were performed on samples from Hole 758A (n= 328), with coring gaps from Hole 758A filled with samples measured on Hole 758B (n= 37) and spliced into a composite record. Where multiple $\delta^{18}O_b$ measurements were made on samples from the same depth, an average of these samples was taken for construction of the age model. The age model is largely the same as that used in the construction of the LR04 stack (Lisiecki and Raymo, 2005); the minor differences between the age model used here and that produced as part of the LR04 stack relate to the averaging of multiple $\delta^{18}O_b$ measurements carried out on samples from the same depth, except for a shift of the MIS 13 $\delta^{18}O_b$ minimum at Site 758 to 488 ka (LR04: 491 ka), which brings the Site 758 $\delta^{18}O_b$ into better alignment with the LR04 $\delta^{18}O_b$ stack. A list of age-depth tie points is provided in Appendix Table B.4, and a comparison between the LR04 age model of Site 758, the age model used here, and the full LR04 stack are provided in Appendix A Fig. A.1. The sedimentation rate at Site 758 averages 1.53 cm/kyr throughout the last 1.5 Ma, and ranges from 0.63 to 2.86 cm/kyr, with sedimentation rates varying between 1 and 2 cm/kyr throughout most of this period.

4.2.3 Previous studies of ε_{Nd} at Ocean Drilling Program Leg 121 Site 758

Burton and Vance (2000) attempted to reductively clean the Fe-Mn coatings of planktonic foraminifera from Site 758 in order to measure the ε_{Nd} of the foraminiferal calcite, in theory providing a record of past surface water ε_{Nd}, in order to investigate the past flux of riverine waters delivered to the surface waters of the Bay of Bengal. However, Burton and Vance (2000) failed to demonstrate that reductively cleaned (i.e. recording surface water ε_{Nd}) and uncleaned (i.e. recording bottom water ε_{Nd}) planktonic ε_{Nd} values were systematically different (Appendix A Fig. A.2). Pomiès et al. (2002) argued that in fact these ε_{Nd} measurements made on 'cleaned' planktic foraminifera reflect the composition of authigenic ferromanganese oxyhydroxides (Fe-Mn) coatings of the foraminifera, owing to

the difficulty in completely removing the Fe-Mn phase. Pomiès et al. (2002)'s interpretation has been reinforced by subsequent studies showing that Nd concentrations are much higher in foraminiferal Fe-Mn coatings than within calcite (Roberts et al., 2012; Tachikawa et al., 2013). Recent studies of seawater ε_{Nd} from the Bay of Bengal show that surface and deep waters at Site 758 are expected to show the same ε_{Nd} value, perhaps explaining the similarity of the 'cleaned' and 'uncleaned' foraminifera ε_{Nd} measurements. However, this similarity stems from the fact that the surface waters at the core site are unaffected by ε_{Nd} inputs from the Ganges-Brahmaputra (evident in Fig. 4.2C), undermining the argument of Burton and Vance (2000) for a riverine control on ε_{Nd} at Site 758. The arguments of Burton and Vance (2000) also fail to account for the LGM similarity of 'cleaned' and 'uncleaned' ε_{Nd}.

The work of Burton and Vance (2000) was expanded by Gourlan et al. (2010), who demonstrated that a 1N acetic acid leaching of the carbonate-rich sediments of Site 758 (sediment $CaCO_3$ contents= 50-75% throughout the last 1.5 Ma, Farrell and Janecek (1991)) yielded ε_{Nd} values within error of those performed on reductively cleaned planktonic foraminifera by Burton and Vance (2000), providing further evidence that the ε_{Nd} data collected by Burton and Vance (2000) reflect the composition of authigenic Fe-Mn coatings of planktonic foraminifer tests (Appendix A Fig. A.3). Gourlan et al. (2010) recognised that the ε_{Nd} values they measured reflected those of Fe-Mn coatings of foraminifera rather than foraminiferal calcite. Although Gourlan et al. (2010) argued that these Fe-Mn coatings are acquired within the upper 1000 m. of the water column, and therefore reflect riverine inputs to the Bay of Bengal, Roberts et al. (2012) demonstrated that the authigenic phases acquired by foraminifera in the upper water column are easily remineralised, and concluded that the dominant ε_{Nd} signature in fossil foraminifera (>90 % of the signal) is acquired at or close to the sediment-water interface, thus recording the ε_{Nd} signature of bottom waters. Based on these findings, the ε_{Nd} records produced by Burton and Vance (2000) and Gourlan et al. (2010) have been subsequently reinterpreted as recording bottom water ε_{Nd} (Wilson et al., 2015a, 2013), and are incorporated into the bottom water ε_{Nd} record presented in this chapter.

4.3 Results

The authigenic ε_{Nd} data from Site 758 produced as part of this thesis were measured on a weak, 0.005 mol/L HH leachate after Blaser et al. (2016), and are concentrated in the period between 1500-500 ka. As I will also re-interpret the previously published data of Burton and Vance (2000) and Gourlan et al. (2010), I will present and discuss the full record covering the last 1500 ka. The individual records are shown alongside the composite record in Fig.

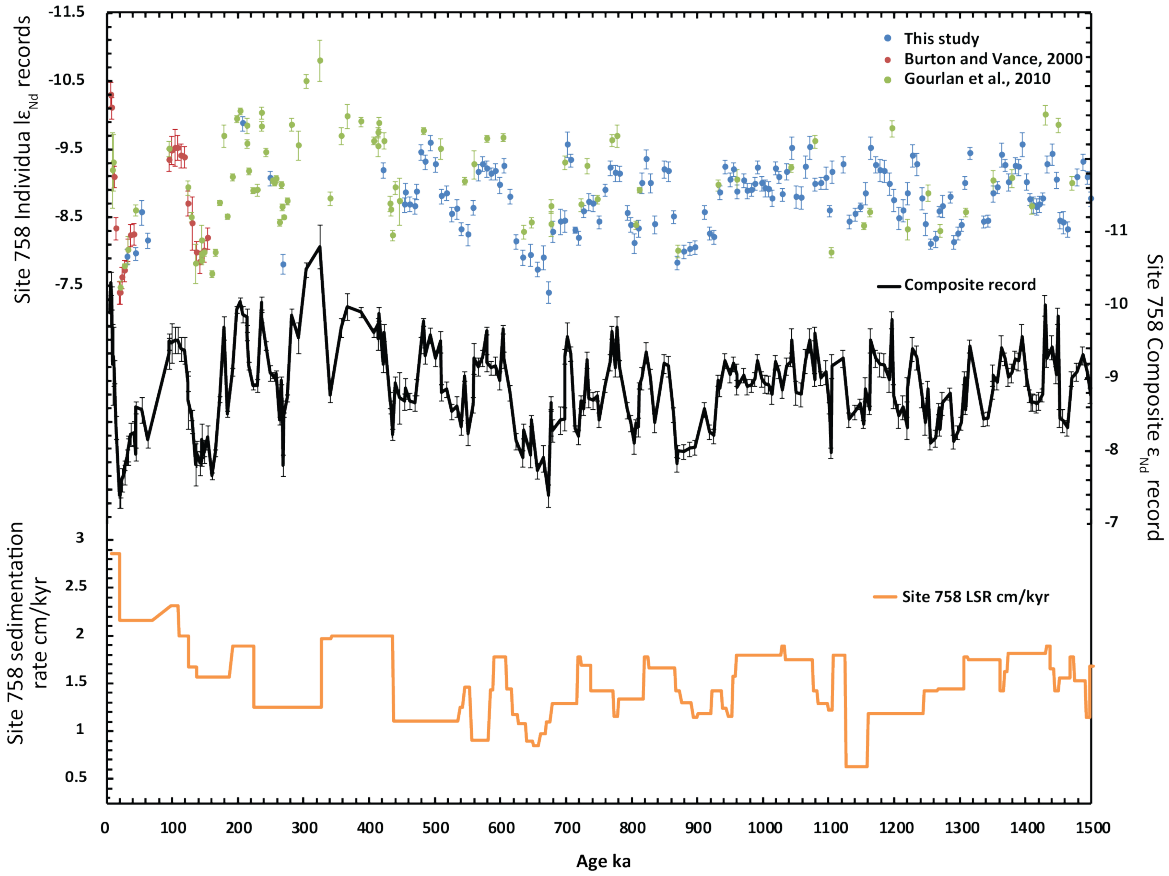

Fig. 4.3 Individual ε_{Nd} records produced by Burton and Vance (2000), Gourlan et al. (2010) and as part of this thesis (upper left Y-axis) measured on the sediments of Site 758, alongside a composite record of all three studies (right Y-axis). Also shown are linear sedimentation rates (LSR) for Site 758.

4.3. All ε_{Nd} data measured on sediments from Site 758 as part of this thesis are provided in Appendix Table C.3.

The ε_{Nd} record of Site 758 during the last 1.5 Ma is characterised by a clear glacial-interglacial cyclicity, with less radiogenic values during interglacials and more radiogenic values during glacials (Figs. 4.3 and 4.4). The amplitude of variations across glacial terminations ranges from -0.3 to -1.52 epsilon units between c. 1500-1081 ka, +0.1 to -0.4 epsilon units between c. 1062-900 ka, -0.9 to -1.77 epsilon units between c. 866 and 424 ka and -1.56 to -2.5 epsilon units between c.374 and 0 ka. The ε_{Nd} record of Site 758 between c. 1096-931 demonstrates greatly reduced variability, with ε_{Nd} values between -8.79 and -9.61. This reduced variability is largely driven by a shift towards less radiogenic peak glacial ε_{Nd} values, although the period from c. 1043-931 ka is also characterised by slightly more radiogenic ε_{Nd} peaks during interglacials when compared to the times before

and after. Although only covered by two data points, interglacial MIS 9 (337-300 ka) is characterized by the least radiogenic ε_{Nd} values recorded at any point over the last 1500 years (ε_{Nd}= -10.49 to -10.80). MIS 9 does not stand out as a particularly strong interglacial in the benthic foraminifera carbon isotope record (measured on *Cibicidoides wuellerstorfi*, $\delta^{13}C_b$) nor the $\delta^{18}O_b$ record of Site 758 (Fig. 4.5), nor is there a major change in sedimentation rates at this time (Fig. 4.3). Between 621-340, ε_{Nd} peaks (i.e. glacial MIS 14, 12 and 10) are not as radiogenic as during the later glacial periods (i.e. MIS 8, 6 and 4-2), although the sampling resolution of the glacial-time sediments between 374-337 ka (MIS 10) is low (12 kyr spacing across MIS 10, compared with 5 kyr spacing between 337-0 ka).

Spectral analysis was performed on the ε_{Nd} record of Site 758, which was first interpolated at a 6 kyr resolution, the results of which are presented in Fig. 4.4 below. As the sampling resolution between 406-160 ka is lower than 6 kyr, the record between 406-0 ka was omitted from this analysis. The ε_{Nd} record between 700-406 ka is dominated by a relatively long wavelength periodicity, in the order of the 100 kyr orbital eccentricity cycle. Prior to this, between 1096-706 ka the presence of a 41 kyr cycle is clearly visible, which is attributed to the 41 kyr orbital obliquity cycle, along with a higher wavelength signal, again in the order of 100 kyr. In the interval between 1498-1102, there is no strong 100 kyr cycle, and the ε_{Nd} signal is dominated by a periodicity of between 41 kyr and c. 61 kyr. The 'smearing' of this signal can in part be attributed to the less radiogenic ε_{Nd} values during the glacial period at c. 1375 ka (MIS 44) and more radiogenic ε_{Nd} values during the interglacial period at c. 1285 ka (MIS 39) when compared to other glacials/interglacials through the interval from 1498-1102.

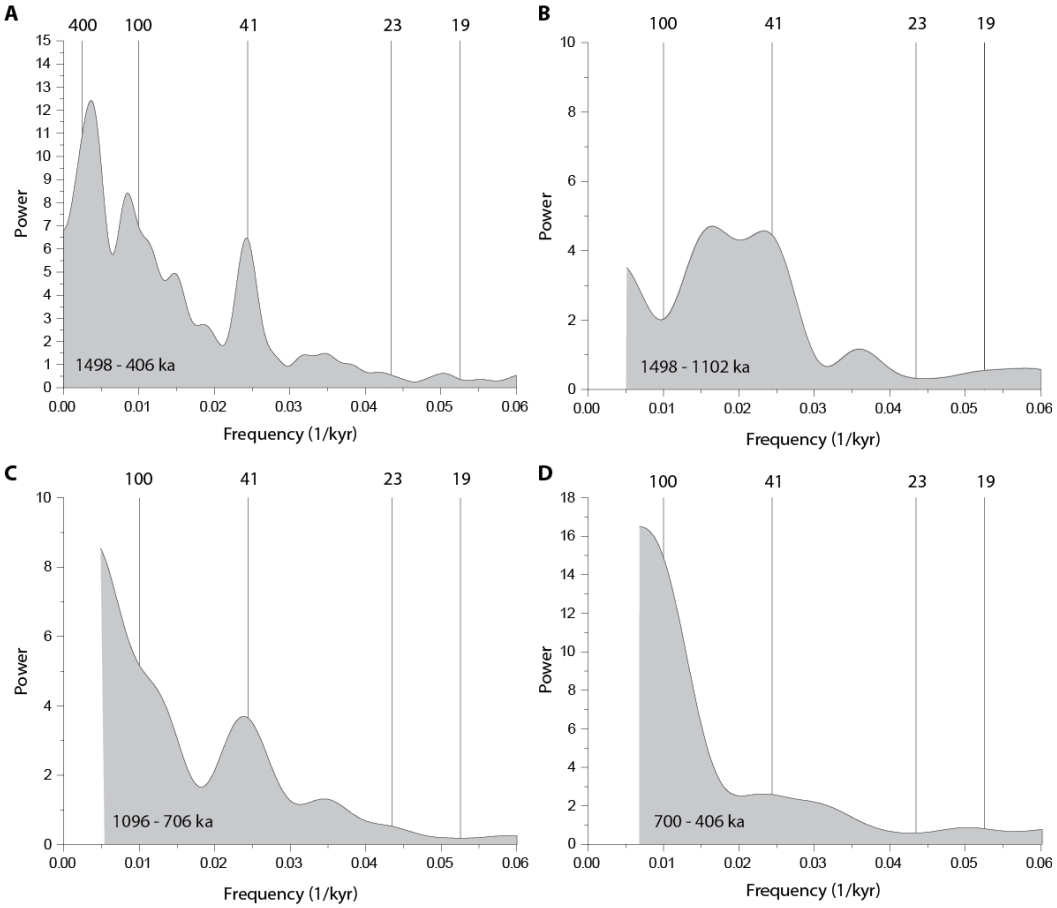

Fig. 4.4 Spectral analysis performed on the 6-kyr interpolated ε_{Nd} record of Site 758 between 1498-406 ka. (A), between 1498-1102 ka (B), between 1096-706 ka (C) and between 700-406 ka (D). These intervals were chosen to demonstrate the transition from a c. 41 kyr cyclicity (B and C) towards a c. 100 kyr cyclicity (D). Frequencies related to 400, 100, 41, 23 and 19 kyr periodicities are highlighted by vertical lines. N.B. some time windows are omitted (e.g. 706-700 ka.) due to the 6kyr interpolation, while the interval between 406-0 ka was omitted due to a low sampling resolution between 374-337 ka. Spectral analysis was performed using the Blackman-Tukey method utilizing a Bartlett window, with the AnalySeries software v. 2.0 (Paillard et al., 1996).

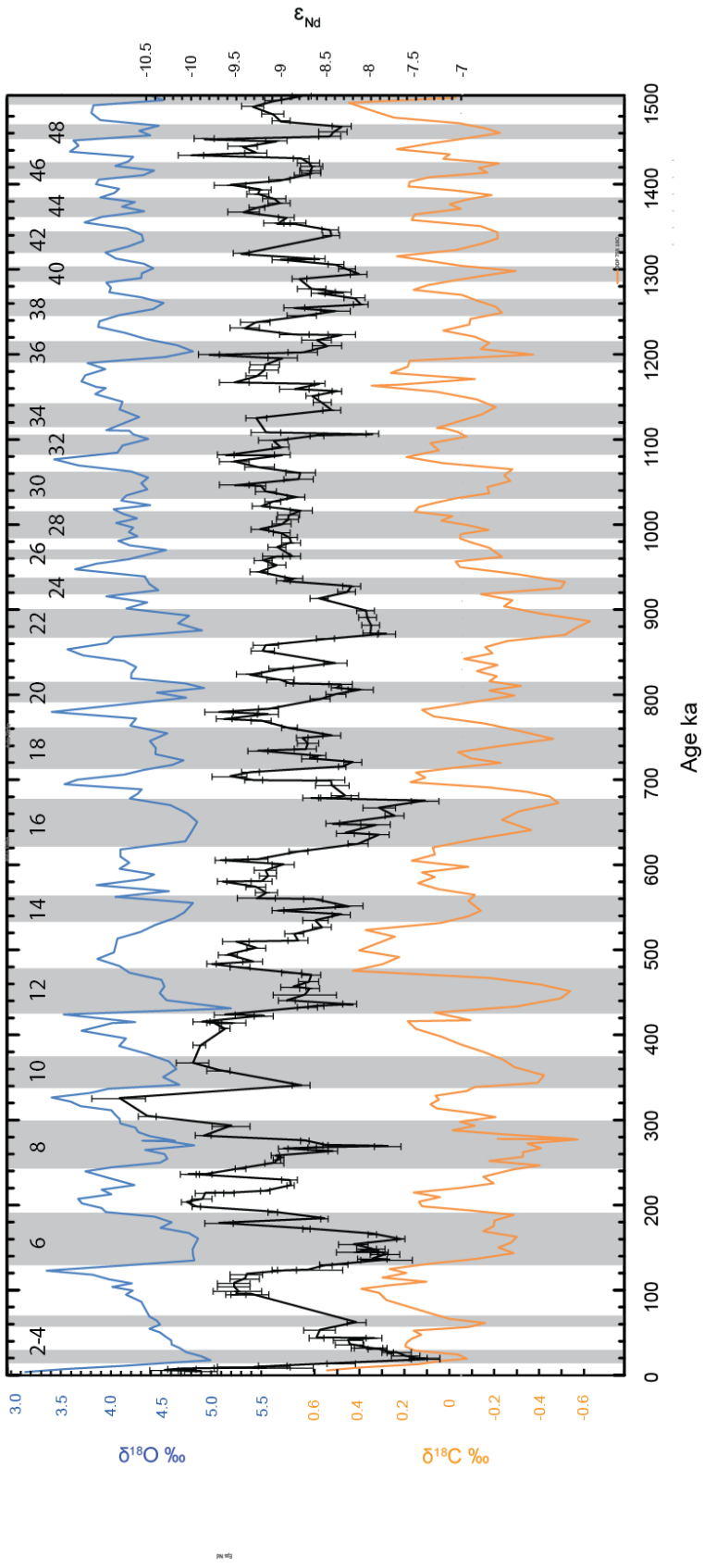

Fig. 4.5 Stable oxygen (blue) and carbon (orange) isotope values measured on the epibenthic foraminifera species *Cibicidoides wuellerstorfi* from Site 758 (Farrell and Janecek, 1991), alongside a composite record of ε_{Nd} measured at Site 758 (black). Glacial marine isotope stages are shaded grey and labelled according to Lisiecki and Raymo (2005).

4.4 Discussion

4.4.1 Palaeocirculation of the deep Indian Ocean over the last 860 ka

ε_{Nd} recorded in the Late Holocene sediments of Site 758 (ε_{Nd}= -9.89±0.18, dated to 5.4 ka) is within error of modern seawater data (ε_{Nd} of c. -10 to -9.7) measured nearby (Singh et al., 2012), Figs. 4.6 and 4.7), providing confidence that ε_{Nd} recorded in these sediments reflects a bottom water signature. The expansion of deep waters modified by the addition of Ganges and Brahmaputra river waters with an unradiogenic signature would lead to a shift towards less radiogenic values, which is not observed during past glacial periods. The more radiogenic ε_{Nd} values recorded at Site 758 during glacials of the last 860 ka therefore largely reflect a reduced outflow of NCW into the SO during these periods, leading to a shift towards more radiogenic ε_{Nd} values in UCDW within the Atlantic sector of the SO. This signal is then propagated through the ACC and to Site 758 via northward-flowing mCDW. The peaks in ε_{Nd} recorded at Site 758 are not the same for each glacial or interglacial period throughout the last 860 ka, which reflects variable contributions from NCW to mCDW bathing the core site during different glacial/interglacial peaks. For example, modern seawater ε_{Nd} values of c. -10 to -9.7 (Singh et al. (2012), Fig. 4.2) are c. 0.5 epsilon units less radiogenic than ε_{Nd} values during the penultimate interglacial, but identical to the preceding peaks (immediately prior to MIS 6.5 at c. 179 ka, and 7.1-7.3 and 7.5 between c. 198-237 ka, see Figs. 4.6 and 4.7).

The ε_{Nd} peak during the penultimate interglacial (ε_{Nd}= -9.52, between 104.5-108.5 ka) is more radiogenic than the peak Holocene value (ε_{Nd}= -10.3, 6.5 ka) which may be caused a temporary shift in the end member ε_{Nd} composition of NCW during the early- to mid-Holocene towards unradiogenic values, rather than a change in the proportion of NCW reaching the SO. This transient early- to mid-Holocene ε_{Nd} shift in the NCW end member has been attributed to either changes in the relative contribution of the precursor water masses to NCW (Böhm et al., 2014; Roberts et al., 2010), or the input of poorly weathered, unradiogenic sediments into the North Atlantic region during the retreat of the Laurentide Ice Sheet (Howe et al., 2016c). The signal of this temporary early-Holocene shift in NCW ε_{Nd} is observed in the mid-depth Atlantic SO (at ODP Leg 177 Site 1088, Hu et al. (2016a)), and can be traced along the path of the 'ocean conveyor' to sites SK129-CR2 and Site 758 in the deep equatorial Indian Ocean (see Fig. 4.7 below), and into the SW Pacific Ocean at 3556 m. water depth (site CHAT 1k on Chatham Rise, Hu et al. (2016a)), supporting the assertion that waters bathing Site 758 have a strong contribution from NCW, and records past changes in palaeocirculation rather than riverine inputs from the Ganges-Brahmaputra basin.

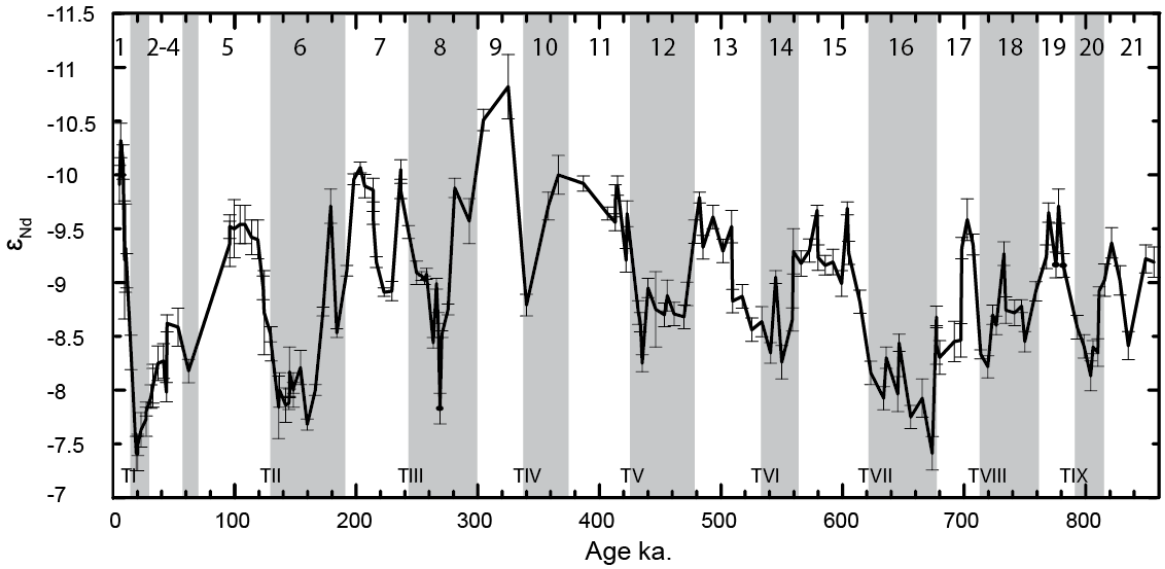

Fig. 4.6 The composite record of authigenic ε_{Nd} measured on sediments from Site 758 over the last 860 ka. Glacial marine isotope stages (MIS) are shaded grey and MIS 1-21, as defined by Lisiecki and Raymo (2005), are numbered, as are glacial terminations (TI-TIX).

The advection of NCW vs SCW into the Atlantic sector of the SO and north to Site 758 over the last 260 ka can be examined by comparing the ε_{Nd} record of Site 758 to those of SK129-CR2 in the deep equatorial Indian Ocean (3800 m., Fig. 4.7) (Piotrowski et al., 2009; Wilson et al., 2015b), the spliced composite record of cores RC11-83 and TN057-01 from the deep Cape Basin (c. 4800 m., Fig. 4.7; Piotrowski (2005); Piotrowski et al. (2012), and Site 1088 (2082 m., Fig. 4.7) (Hu et al. (2016a) from the intermediate water depth in the Cape Basin. These cores all record more radiogenic ε_{Nd} values during glacials compared with interglacials, with broadly the same amplitude of ε_{Nd} variability as Site 758 suggesting a common control on ε_{Nd}, although the deeper core sites of RC11-83/TN057-01 and SK129-CR2 show consistently more radiogenic ε_{Nd} values than Site 758 during glacial periods. The interpretation of these shared characteristics as a reduction in the advection of NCW into the SO during glacial periods is in agreement with other ε_{Nd} records of NCW production and advection from the Atlantic Ocean, which show reduced flow of NCW during the last glacial period (Böhm et al., 2014; Howe et al., 2016b; Lippold et al., 2016; Roberts et al., 2010). The deepest records of RC11-83/TN057-01 and SK129-CR2 show millennial scale variability during the last two glacial periods that is largely absent from the shallower sites 758 and 1088. At these shallower sites the absence of millennial-scale variability may in part be due to the lower sedimentation rates (average over last 260 kyr = 2.0 cm/kyr at Site 758 and 1.1 cm/kyr at Site 1088) compared with TN057-21 (14.5 cm/kyr) and RC11-83 (21.2 cm/kyr). However, the observation of this variability at the deeper, low sedimentation site

SK129-CR2 within the Indian Ocean (average sedimentation rate = 2.1 cm/kyr) suggests that there is a depth-dependency to this millennial-scale variability, with periods of expanded AABW/lower Lower Circumpolar Deep Water (lLCDW) (i.e. Southern Component Water, SCW) contribution to these deeper core sites which do not affect the shallower sites. This suggests that Site 758 (as well as Site 1088) is sensitive to changes in the proportion of NCW entering the SO, while the deeper RC11-83 and SK129-CR2 sites are recording both a reduction in NCW during glacial periods, and an expansion in SCW relative to NCW during millennial-scale cooling events.

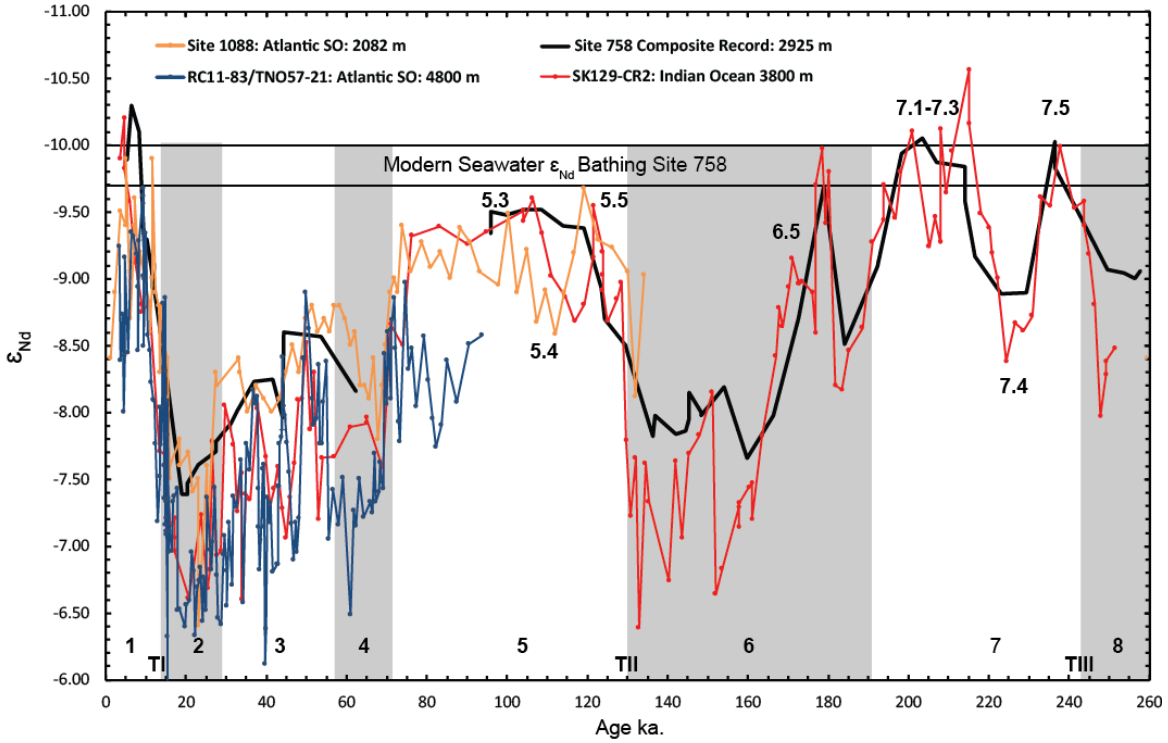

Fig. 4.7 Authigenic ε_{Nd} values measured at Site 758 (black line, Burton and Vance (2000); Gourlan et al. (2010); this study), the deep Cape Basin composite record of RC11-83/TN057-21 (Piotrowski, 2005; Piotrowski et al., 2012), the intermediate depth Cape Basin Site 1088 (Hu et al., 2016a) and the deep equatorial Indian Ocean core SK129-CR2 (Piotrowski et al., 2009; Wilson et al., 2015a). All core locations are provided in Fig. 4.2. The deeper cores RC11-83/TN057-21 and SK129-CR2 are apparently sensitive to expanded SCW during peak glacial conditions of MIS 2-4, 6 and MIS 8, while the shallower core sites 758 and 1088 monitor the continuous outflow of NCW into the SO throughout. Modern seawater ε_{Nd} values measured close to Site 758 are shown (Singh et al., 2012).

This interpretation is supported by the observation that, although all of these records show similar glacial-interglacial variability in ε_{Nd} values, the absolute ε_{Nd} values of the deeper sites RC11-83/TN057-21 and SK129-CR2 are more radiogenic than the shallower

sites during glacial periods (Fig. 4.7) This is exemplified by comparing the record of Site 758 to that of SK129-CR2: during warm intervals over the last 260 ka, the ε_{Nd} records of SK129-CR2 and Site 758 exhibit similar values, suggesting that both sites are bathed by the same water mass. The depth range of these cores (2925-3800 m.) requires the advection of a homogenous, well mixed mCDW to both core sites during these intervals. The development of an offset in ε_{Nd} between these two sites during past glacials indicates the presence of two distinct water masses within the equatorial Indian Ocean at these times, with mCDW containing a larger proportion of NCW overlying a water mass with an increased contribution from SCW, with the boundary between these two water masses located between 2925-3800 m. water depth. The establishment of this water mass boundary may indicate an increased physical stratification of water masses in the deep Indian Ocean during glacials (Adkins et al., 2002), although more ε_{Nd} records from water depths between 2925 and 3800 m. in the Indian Ocean are required to determine whether this water mass boundary represents a diffuse change in ε_{Nd}, or a sharp boundary, as identified in $\delta^{13}C_b$ records from the deep South Atlantic and Atlantic sector of the SO during the last glacial period. The development of an ε_{Nd} offset between SK129-CR2 and Site 758 during glacials can be interpreted as either i) a reduction in NCW mixing to abyssal depths within the SO, ii) an increase in production of AABW, or iii) a mixture of both these processes.

4.4.2 Palaeocirculation of the deep Indian Ocean between 1500-800 ka: The Mid-Pleistocene Transition

ε_{Nd} recorded at Site 758 underwent two shifts between 1500-860 ka, a period of time coinciding with the MPT, a major reorganisation of glacial-interglacial climatic variability, which has been linked to an expansion of Northern and/or Southern hemisphere ice sheets (Clark and Pollard, 1998; Elderfield et al., 2012) and an apparent reduction in THC identified between 923-879 ka (Pena and Goldstein, 2014). The onset of the MPT is apparent in the $\delta^{13}C_b$ and $\delta^{18}O_b$ records of Site 758 at c. 1200 ka, when $\delta^{13}C_b$ values reach -0.39‰ and $\delta^{18}O_b$ values reach >4.8‰ for the first time (Fig. 4.8), suggesting an intensification of glacial conditions. Glacial intensification is followed by the first truly saw-tooth pattern of glacial-interglacial cyclicity in the $\delta^{18}O_b$ record of Site 758 across, 1141-1114 ka (Lisiecki and Raymo, 2005). The first changes in authigenic ε_{Nd} associated with the MPT at Site 758 occurs at 1058 ka, when the amplitude of glacial-interglacial cyclicity is greatly reduced (Fig. 4.8). Between c. 1086-931 ka there is a prolonged period of reduced variability, with ε_{Nd} values fluctuating between -8.83 and -9.24 (except one data point at 1044 ka where ε_{Nd}= -9.51), in contrast to the preceding 457 ka, when glacial ε_{Nd} values typically reached c. -8.1

to -8.5, while peak interglacial values typically range from -9.5 to -10. This prolonged period of deep water circulation somewhere between a full glacial and a full interglacial is also reflected in the $\delta^{18}O_b$ record, which shows muted changes compared with the LR04 $\delta^{18}O_b$ stack throughout this period.

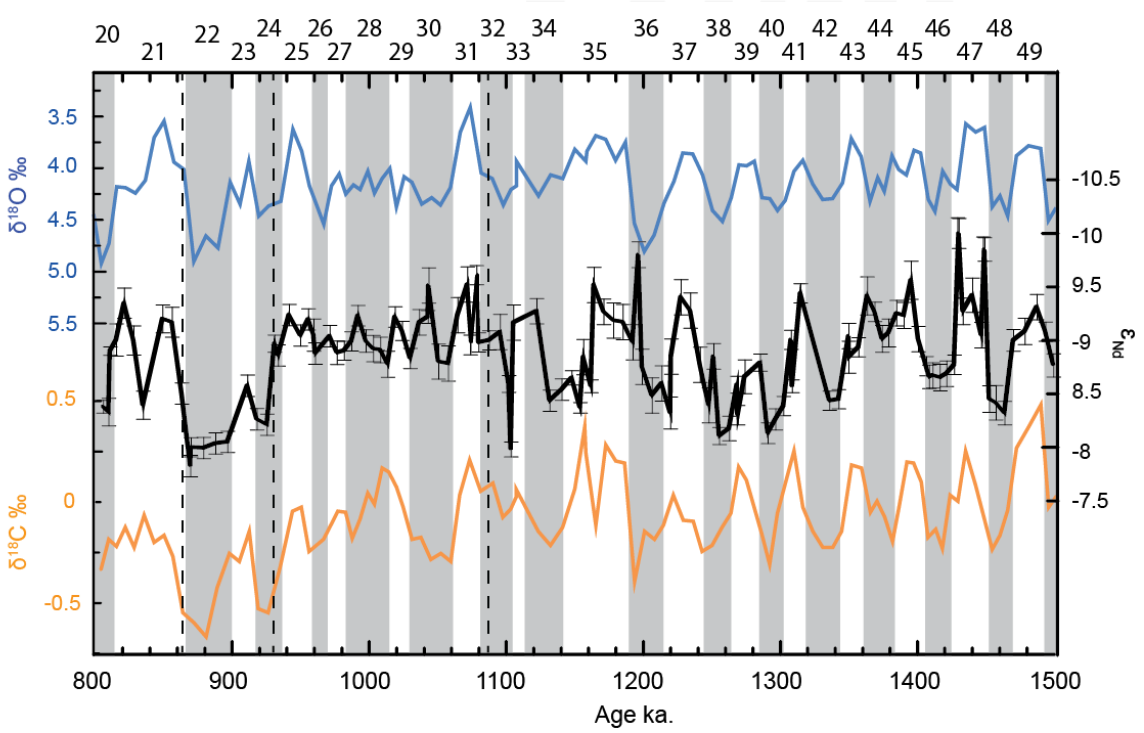

Fig. 4.8 $\delta^{18}O_b$ (blue curve), ε_{Nd} (black curve) and $\delta^{13}C_b$ (orange curve) measured at Site 758 from 1500-800 ka, with MIS numbered 20-49. A prolonged period of stability in is ε_{Nd} evident between c. 1086-931, in the early stages of the MPT, followed by a prolonged shift to more radiogenic values between c. 936-866 ka (dashed windows).

The muted glacial-interglacial variability in deep water circulation at c. 1086-931 ka represents a slight reduction in the advection of NCW to Site 758 during peak interglacials, but also a continued contribution of NCW – and therefore a relatively reduced contribution of SCW/Pacific Deep Water (PDW) – during glacial periods. The continued advection of NCW to Site 758 during glacial periods between c. 1086-931 ka represents stability in THC across glacial-interglacial cycles at this time. Diekmann and Kuhn (2002) suggested a strengthening of THC and an expansion of SCW through the same period in the Atlantic sector of the SO from around 1200 ka based on the increased amplitude of glacial-interglacial variations in sediment compositional ratios (kaolinite/chlorite and quartz/feldspar) measured at Site 1090. Variability in surface ocean nutrient content in the same core has been attributed to

a shallowing of Antarctic Intermediate Water (AAIW) through 1081-936 ka, suggesting a continued and stable AMOC configuration during this period (Marino et al., 2009). The identification of a strong North-South $\delta^{13}C_b$ gradient between Site 1090 in the deep Cape Basin and sites 929 and 607 in the equatorial and North Atlantic between 1048-943 ka (Lisiecki, 2014; Venz and Hodell, 2002) suggests a reduced flow of SCW into the Atlantic, consistent with a suppression of SCW vs NCW during glacial periods at Site 758 at this time (Fig. 4.9). Reduced glacial-interglacial variability through 1066-941 ka is also observed in the low resolution ε_{Nd} records of Site 1090 (Atlantic SO, 3702 m.) and Site 1088 (Atlantic SO, 2082 m.) (Pena and Goldstein, 2014), however as these records do not go back beyond 1066 ka, it is not clear if the low glacial-interglacial variability through this period is part of a longer trend (Figs. 4.10 and 4.12).

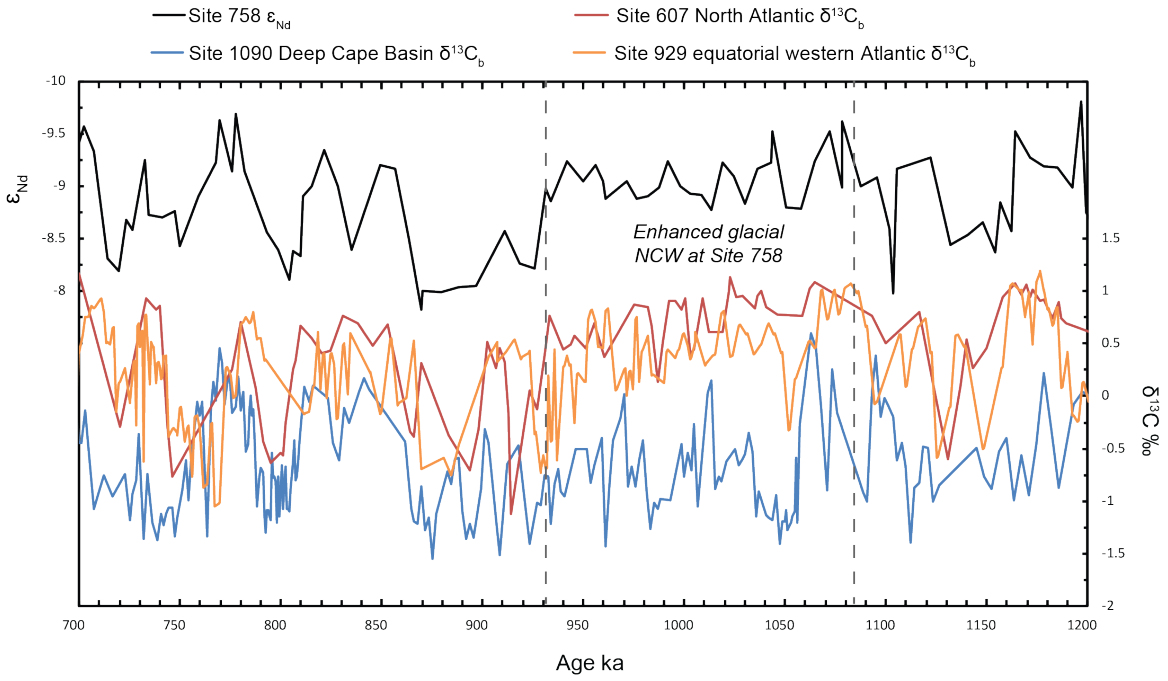

Fig. 4.9 ε_{Nd} measured at Site 758 (black) shows a continued contribution of unradiogenic NCW bathing the core site throughout glacial and interglacial periods between 1086-931 ka (dashed lines). Also shown are $\delta^{13}C_b$ records from the Atlantic SO (Site 1090, dark blue – Hodell et al. (2003), equatorial Atlantic (Site 929, orange - Bickert et al. (1997) and high latitude North Atlantic (Site 607, red - Raymo et al. (1989), showing the existence of a gradient in $\delta^{13}C_b$ between the Atlantic sector of the SO and the mid-to-high latitude Atlantic during the same interval.

The second major shift in ε_{Nd} at Site 758 across the MPT occur between c. 936-866 ka (MIS 24-22), when there is a prolonged period of glacial-like conditions of reduced NCW contribution to mCDW. This prolonged glacial across MIS 24-22 effectively marks the

beginning of 100 kyr glacial-interglacial cycle during the Pleistocene (Pena and Goldstein, 2014; Raymo et al., 1997), and coincides with the THC 'crisis' identified by Pena and Goldstein (2014) in cores Site 1090 and Site 1088 across 923-879 ka, when NCW advection to these sites was greatly reduced. Rather than a 'crisis' in THC, this period of reduced NCW entrainment into mCDW bathing Site 758 effectively marks the first prolonged glacial of the late Pleistocene, and is comparable to conditions during other glaciations of the Late

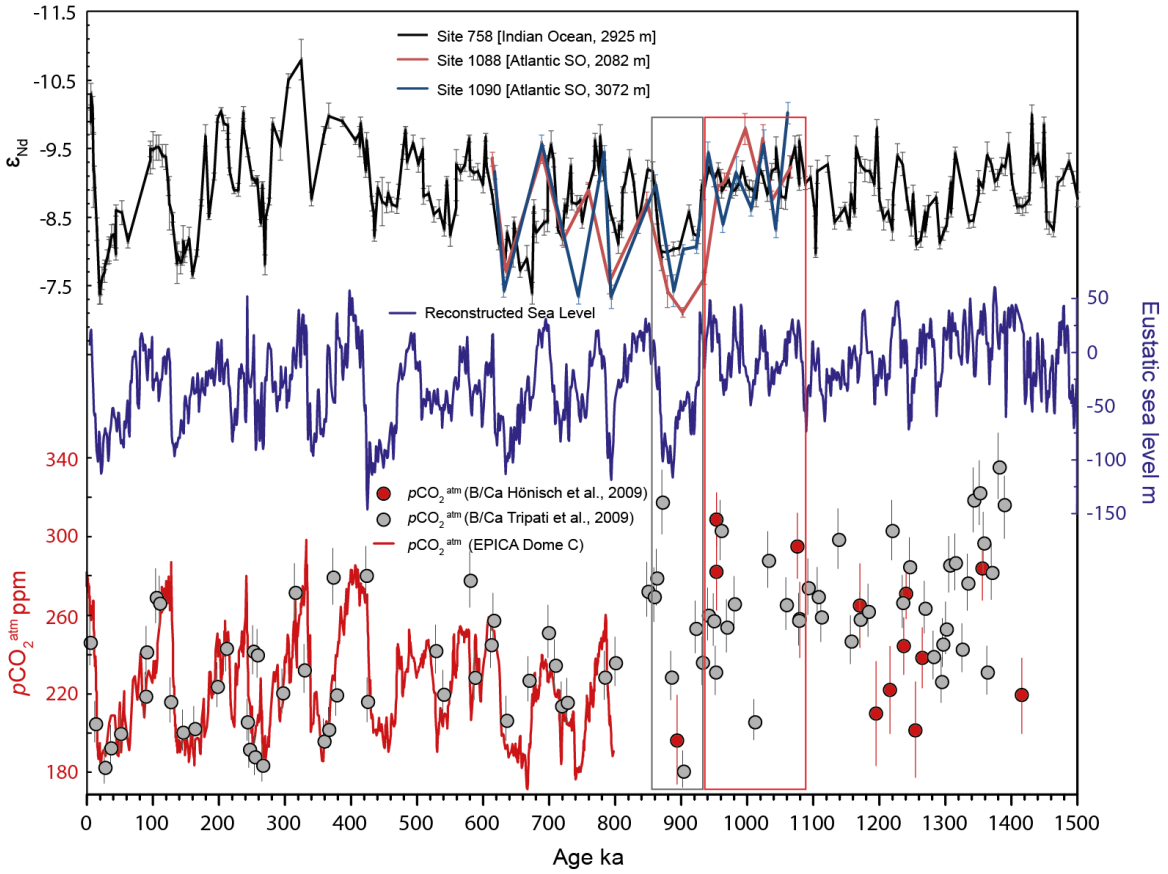

Fig. 4.10 ε_{Nd} recorded at Site 758 (black line), Site 1088 (red line, Pena and Goldstein (2014)) and Site 1090 (blue line, Pena and Goldstein (2014)) alongside reconstructed sea-level across the MPT (blue, Elderfield et al., 2012 supplementary online materials) and pCO_2^{atm} measured in the EPICA Dome C, ice core (red curve, Augustin et al. (2004) and reconstructed from boron isotope measurements made on planktonic foraminifera (grey dots, Tripati et al. (2009) and red dots, Hönisch et al. (2009). There appears to be a tight coupling between changes in THC, pCO_2^{atm} and ice sheet growth across the MPT: continued glacial advection of NCW during glacial periods between 1088-936 ka coincides with elevated sea level and pCO_2^{atm} (red box), while the prolonged reduction in NCW between c. 936-866 ka coincides with lower sea levels (increased global ice volume) and lower pCO_2^{atm} (grey box)

Pleistocene between c. 674-623 ka (MIS 16), c. 166-136 ka (MIS 6) and c. 18-37 ka (MIS2-3).

The expansion of global ice volume identified at c. 900 ka by Elderfield et al. (2012) occurs around the same time as the prolonged reduction in the contribution of NCW to mCDW documented at Site 758 (Fig. 4.10). Elderfield et al. (2012) suggest this increase in ice volume was driven by an expansion of Antarctic ice, due to the anomalously low interglacial summer insolation at c. 917-900 ka. The reduction in NCW advection into the SO documented in $\varepsilon_{\mathrm{Nd}}$ at Site 758, and by inference the expansion in SCW across this interval, supports the assertion of Pena and Goldstein (2014) that an expansion of SCW led to a drawdown of $p\mathrm{CO}_2^{atm}$, as hypothesized to occur during glacial periods of the Late Pleistocene (Chapter 3) (Fig. 4.10). The preceding prolonged period of relative stability in the advection of NCW into mCDW bathing Site 758 between c. 1086-931 also coincides with a period of elevated sea level and $p\mathrm{CO}_2^{atm}$ (red box in Fig. 4.10), suggesting a tight coupling between palaeocirculation and other palaeoclimatic boundary conditions across the MPT.

4.4.3 Quantifying the export of NCW into CDW throughout the last 1.5 Ma

To quantitatively asses past changes in the advection of NCW from the Atlantic to Site 758 a mixing calculation has been performed, assuming binary mixing between NCW and PDW end members, following equation 4.1 below:

$$\%NADW = \frac{\varepsilon_{Nd}^{NCW} \cdot [Nd]^{PDW} - \varepsilon_{Nd}^{PDW} \cdot [Nd]^{PDW}}{\varepsilon_{Nd}^{NCW} \cdot [Nd]^{PDW} - \varepsilon_{Nd}^{PDW} \cdot [Nd]^{PDW} - \varepsilon_{Nd}^{NCW} \cdot [Nd]^{NCW} + \varepsilon_{Nd}^{NCW} \cdot [Nd]^{PDW}} \tag{4.1}$$

Although this is a simplification of global circulation in that it does not acknowledge a SO-sourced end member, the fact that NCW appears to exert a dominant control on the $\varepsilon_{\mathrm{Nd}}$ of bottom waters bathing Site 758, and that the site appears to remain above the main body of SCW during past glacial periods (see section 4.4.1), suggest this simplification is justified. End member $\varepsilon_{\mathrm{Nd}}$ values and seawater Nd concentrations used in this calculation are provided in Table 4.1. End member values of PDW have remained constant for several million years (Albarède and Goldstein, 1992; Goldstein and O'Nions, 1981; Hu et al., 2016b; O'Nions et al., 1978; Piepgras et al., 1979), and probably for as long as the last 65 million years (Thomas, 2004). NCW end member values are also thought to have stayed largely constant throughout the last 2 million years (Burton et al., 1999; Foster et al., 2007; Reynolds et al.,

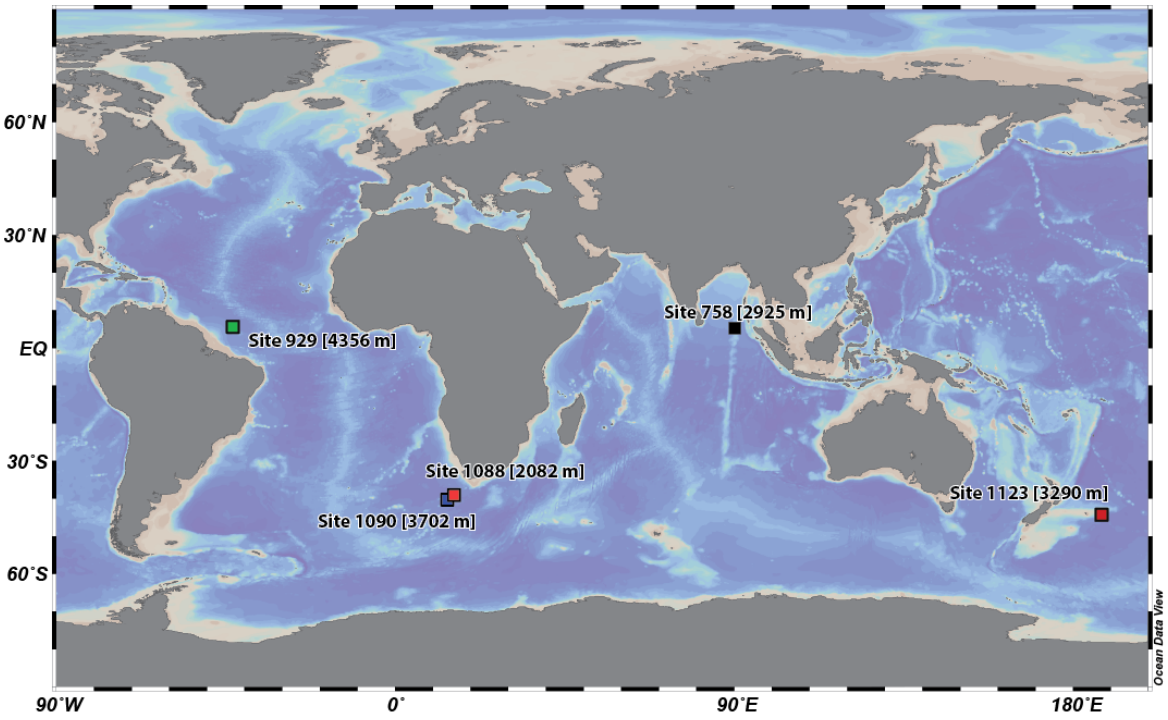

Fig. 4.11 The location of marine sediment cores from which reconstructions of past seawater ε_{Nd} spanning the MPT have been produced: Site 929 (Howe et al., unpublished); Site 1090 and Site 1088 (Pena and Goldstein, 2014), Site 758 (this study) and Site 1123 (Piotrowski et al., unpublished).

1999), although transient changes in the ε_{Nd} of NCW advected from the North Atlantic have been identified during the early- to mid-Holocene (Böhm et al., 2014; Howe et al., 2016c; Roberts et al., 2010).

The same mixing calculations have been performed on two other ε_{Nd} records which cover the MPT: from the Atlantic, a record of ε_{Nd} measured on fish debris and the Fe-Mn coatings of mixed planktonic foraminifera from ODP Leg 154 Site 929, located at 4356 m. water depth on the Ceara Rise (Fig. 4.11) in the equatorial western Atlantic close to the modern mixing zone between SCW and NCW (Curry et al., 1995); Howe et al., unpublished), and from the SW Pacific Ocean an ε_{Nd} record measured on the Fe-Mn coatings of mixed planktonic foraminifera from ODP Leg 181 Site 1123, located off Chatham Rise at 3290 m. water depth (Hall et al., 2001); Piotrowski et al., unpublished), which is today bathed in upper Lower Circumpolar Deep Water (uLCDW). Along with the ε_{Nd} records of Site 1088 and Site 1090, these are the only other ε_{Nd} records yet produced which span the MPT, and together allow for the first time the investigation of ε_{Nd}-reconstructed palaeocirculation from the Atlantic basin, through the Southern and Indian Oceans and into the Pacific basin. By quantifying the propagation of NCW from the North Atlantic to the equatorial Atlantic, into

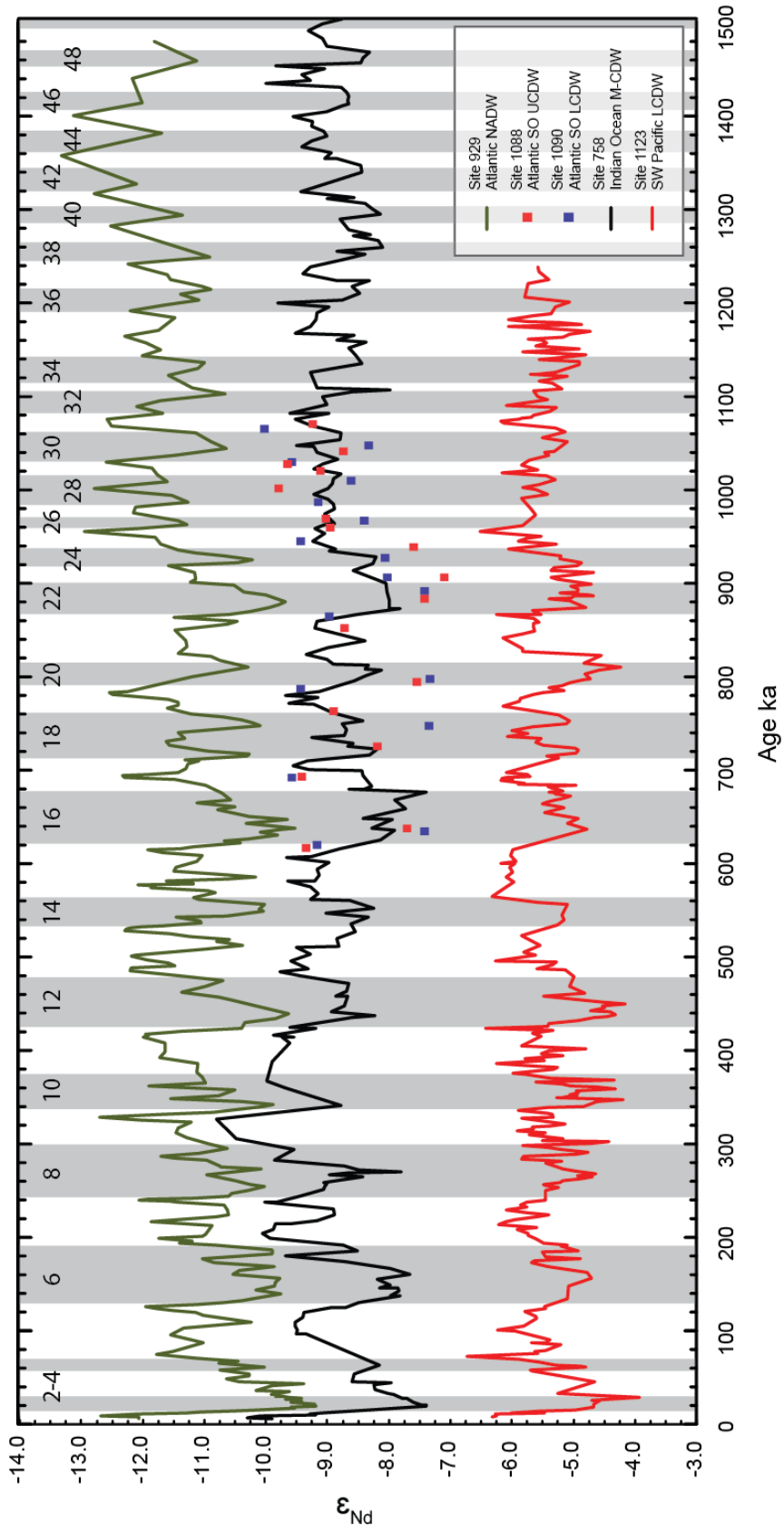

Fig. 4.12 Globally distributed ε_{Nd} records crossing the MPT - for locations see Fig. 4.11. Site 929: Howe et al., (In prep.); Sites 1088 and 1090 from (Pena and Goldstein, 2014), Site 758 this work along with data from (Burton and Vance, 2000; Gourlan et al., 2010), and Site 1123 Piotrowski et al., (In prep.)

the Southern and Indian oceans, and from the SO into the SW Pacific, it should be possible to explore changes in the palaeocirculation between these basins.

Table 4.1 End member ε_{Nd} and Nd concentrations used in the binary mixing calculation presented in section 4.4.4

Water mass	ε_{Nd}	**Concentration**	**Reference**
NCW	-13.2	17.6 pmol/kg	(Lambelet et al., 2016)
PDW	-3.9	39 pmol/kg	(Amakawa et al., 2009)

As ε_{Nd} behaves conservatively away from continental margins, this mixing calculation essentially allows the treatment of NCW as a 'dye tracer' through the ocean conveyor, and treating it as such enables me to gauge the strength of THC in the past, in the same way ocean circulation models utilize passive tracer experiments to explore ocean circulation pathways (e.g. Stevens and Stevens (1999)). There are a number of reasons why the transferal of NCW from the Atlantic into the Southern, Indian and Pacific oceans may have changed in the past, including i) a change in the physical properties of water masses, leading to more/less mixing between water masses; ii) changes in the rate of mixing between water masses due to physical mixing mechanisms (i.e. eddy diffusivity); iii) a change in the frontal positions of the SO, which could affect the location of NCW admixture into CDW, and thus the entrainment and transport of NCW within the ACC, or change the strength of the Agulhas Undercurrent (the deep expression of the Agulhas Current, responsible for the advection of NCW around the southern tip of South Africa); iv) a change in the speed of the ACC, which may impact the propagation of NCW from the Atlantic SO into the Indian and Pacific oceans; and v) changes in the production rate of SCW, which are not accounted for in this mixing calculation. Most (or all) of these factors can be thought of as affecting the movement of a parcel of water through the ocean conveyor, from the Atlantic to Pacific oceans, i.e. affecting the 'strength' of global THC. Therefore, I will refer to the propagation of this NCW signal from Site 929 into the SO and to Site 758, and on to Site 1123 in the SW Pacific, as reflecting the 'strength' of global THC: by this definition, a decrease in the 'strength' of the global THC does not necessitate that overturning circulation slowed down, but that the propagation of NCW from one oceanic basin to another decreased.

There is a very close relationship between changes in the proportion of NCW reaching Site 758 and NCW reaching Site 1123, suggesting that both core sites are recording fluctuations in the propagation of NCW through the global THC 'conveyor' (Fig. 4.13). The reduction in glacial-interglacial variability in the percentage of NCW at Site 758 between c. 1086-931 is matched by reduced variability in the percentage of NCW bathing Site 1123 across the same interval. Prior to c. 923 ka, glacials in equatorial Atlantic core Site 929 are characterised

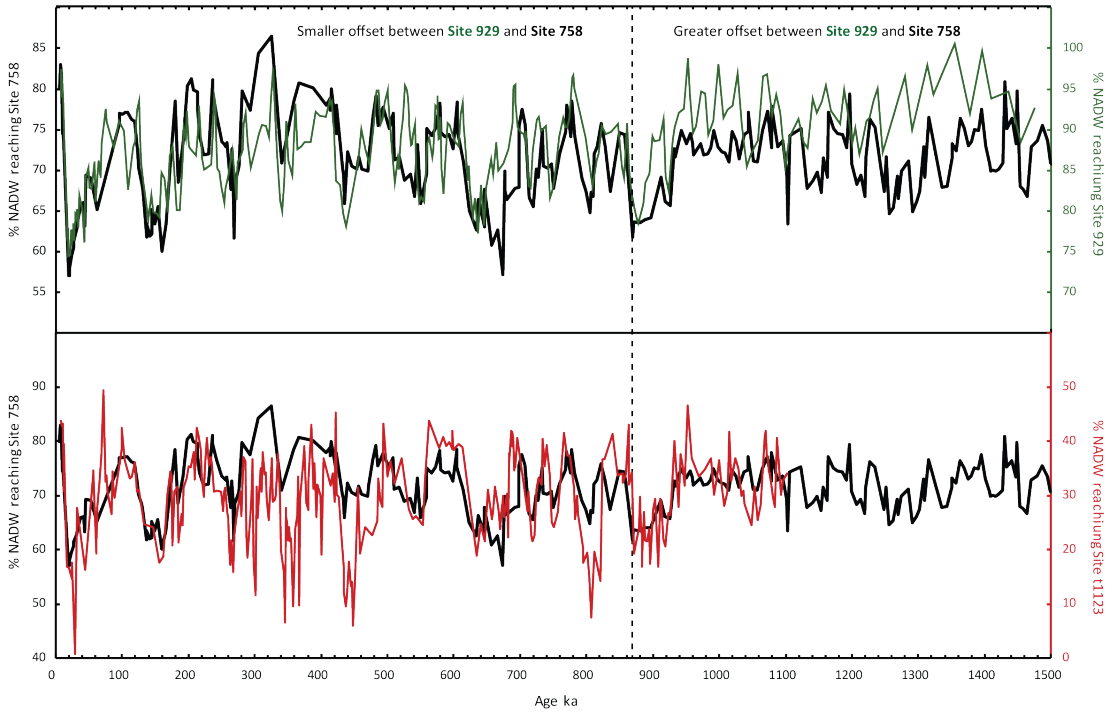

Fig. 4.13 The result of a mixing calculation showing the percentage of NCW vs PDW bathing Site 758 (black solid line, upper and lower panel) and Site 929 in the deep equatorial Atlantic (green line, upper panel) and Site 1123 in the SW. Pacific (red line, lower panel). Note the difference in the Y-scales: the % NCW at Site 929 is offset by +15% from Site 758 in the upper panel and Site 1123 is offset by -40% from Site 758 in the lower panel. All records are shown on the same Y-Axis in Appendix A figure Fig. A.4

by lower proportions of SCW, and interglacials by higher NCW, compared with the period following c. 923 ka. The percentages of NCW at Equatorial Atlantic Ocean Site 929, Indian Ocean Site 758, and SW Pacific Ocean Site 1123 show an NCW reduction in waters bathing the sites across c. 936-866 ka. The amount of NCW recorded at Site 929 is apparently as great during the interglacial period of 917-900 ka (MIS 23) as in the following interglacial period across 866-814 ka (MIS 21). However, NCW percentages at Site 758 and Site1123 were greatly reduced across 917-900 ka (MIS 23) compared with the following interglacial (866-814 ka, MIS 21), indicating a reduction in the strength of global THC across this interval.

Following the period from 936-866 ka, the trends in glacial-interglacial variability in the proportion of NCW reaching Site 758 match the trends in the variability of NCW reaching Site 929, which contrasts with the previous c. 500 kyrs, when the trends were less similar between the two core sites, and there was a greater offset in the NCW percentages bathing the two sites (Fig. 4.13). The fact that i) the equatorial Atlantic Ocean was apparently bathed

in a greater proportion of NCW prior to 936 ka compared to the period following 866 ka, and ii) the proportion of NCW bathing sites 758 and 1123 was not higher prior to 936 ka, suggests a weaker THC prior to 936 ka.

To further analyse the propagation of NCW from Site 929 to Site 758, a mixing calculation has been performed using Site 929 as an end member for NCW, with the ε_{Nd} values of unradiogenic interglacial peaks at Site 929 and the modern Nd concentration of seawater close to the core site of 29.7 pmol/kg (Piepgras and Wasserburg, 1987). During glacial periods, it is likely that part of the ε_{Nd} signal recorded at Site 929 reflects advection of SCW to the core site on the Ceara Rise, causing offsets towards more radiogenic ε_{Nd} values and making these intervals unsuitable for the use of Site 929 as an end member for NCW: as such the mixing calculation performed between Site 929 and Site 758 only incorporates interglacial ε_{Nd} minima. To account for variations in the age models of the two cores, differing sampling intervals, and lags in signal propagation due to variable ocean circulation rates, unradiogenic peaks in ε_{Nd} between the records of Site 929 and Site 758 have been manually correlated. The differences in ages between unradiogenic peaks in Site 929 and Site 758 are largely <3.1 kyrs (n= 21 of 31 peaks identified in both records), lower than the sampling resolution of Site 758 (average resolution = 5-6 kyr) and Site 929 (average resolution = 4-5 kyr). The differences in absolute ε_{Nd} values between the two sites are also shown (lower panel in Fig 4.14).

Using this approach, it is clear that the weakening in global THC pre-dates the 'THC crisis' identified as occurring between 936-866 ka by Pena and Goldstein (2014), which in fact represents a reduction in NCW production and expansion in SCW. Indeed, a reduced strength of global THC appears to be a pervasive feature of interglacial periods prior to c. 868 ka. The interglacial at 1108 ka (MIS 33) appears an outlier, with a greater proportion of NCW (as defined by the ε_{Nd} recorded at Site 929) advected to Site 758 (Fig. 4.14); however, this interglacial is a period of particularly radiogenic ε_{Nd} values at Site 929, suggesting that at this time, Site 929 was not bathed purely in NCW, and as such may not reflect true NCW ε_{Nd} end member values. This mixing calculation assumes that i) Nd concentrations of waters bathing Site 929 during peak interglacials of the past were the same as today, ii) PDW end member ε_{Nd} values and Nd concentrations also remained stable in the past. It also assumes that the contribution from SCW to Site 929 has remained consistently low during past interglacials (which is probably not the case during MIS 23 at c. 900 ka and MIS 33 at c. 1108 ka). However, the trends in the offsets of absolute ε_{Nd} values between the two core sites are similar to those of the mixing calculation (Fig 4.14), suggesting that the direction and magnitude of changes identified in this mixing calculation are reasonable. As discussed in Chapter 3 (section 3.4.5.), box models suggest that increasing the proportion of NCW –

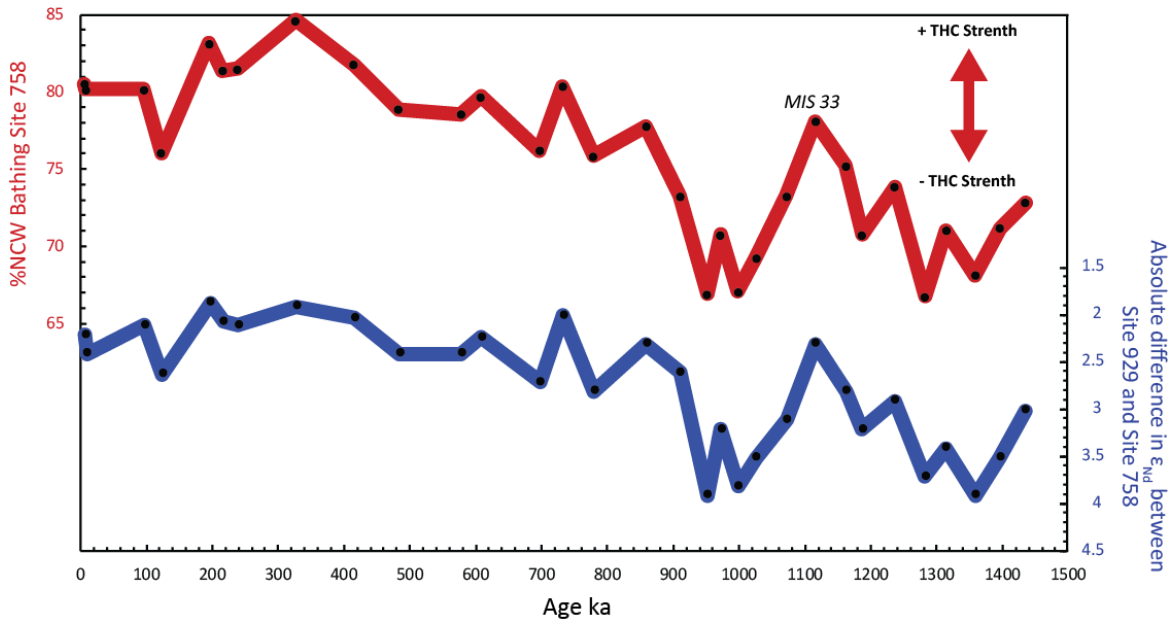

Fig. 4.14 Unradiogenic interglacial peaks in the ε_{Nd} record of Site 929 (Ceara Rise, equatorial Atlantic, 4897 m. water depth, Howe et al., unpublished) have been correlated with unradiogenic interglacial peaks in the ε_{Nd} record of Site 758, and a mixing calculation performed as discussed in the text above, to assess the proportion of NCW bathing site Site 929 that reaches Site 758 (red curve, upper panel). Also shown are the absolute difference in ε_{Nd} between peaks (blue curve, lower panel).

low in preformed nutrients – propagated through the global THC system and into the Pacific Ocean, augments the efficiency of the global biological pump. This greater efficiency in the biological pump may go some way to explaining the decrease in pCO_2^{atm} and expansion of ice sheets reconstructed to occur across the MPT (Elderfield et al., 2012; Hönisch et al., 2009; Tripati et al., 2009).

The reduced advection of NCW from the Atlantic basin (Site 929) through the ocean conveyor (and thence to Site 758) prior to 936 ka may go some way to reconciling the apparent difference in $\delta^{18}O_{palaeoSW}$ recorded at Site 1123 (SW Pacific, Elderfield et al. (2012)) and Site 607 (North Atlantic, Ford et al. (2016); Sosdian and Rosenthal (2009)) across the MPT. $\delta^{18}O_{palaeoSW}$ at Site 607 shows a gradual increase through the MPT, reflecting the gradual increase in $\delta^{18}O_b$ of the LR04 global stack between c. 1200-750 ka, while Site 1123 shows a step-change in $\delta^{18}O_{palaeoSW}$ between c. 936-866 ka (across MIS 24-22). This difference in $\delta^{18}O_{palaeoSW}$ between the deep North Atlantic and SW Pacific may be symptomatic of the reduced transfer of deep waters between the Atlantic and Pacific prior to 900 ka, owing to a weaker THC compared with the time after 866 ka. The LR04 $\delta^{18}O_b$ stack (Lisiecki and Raymo, 2005) is heavily weighted toward the Atlantic basin (n= 40 of 57) and shows the

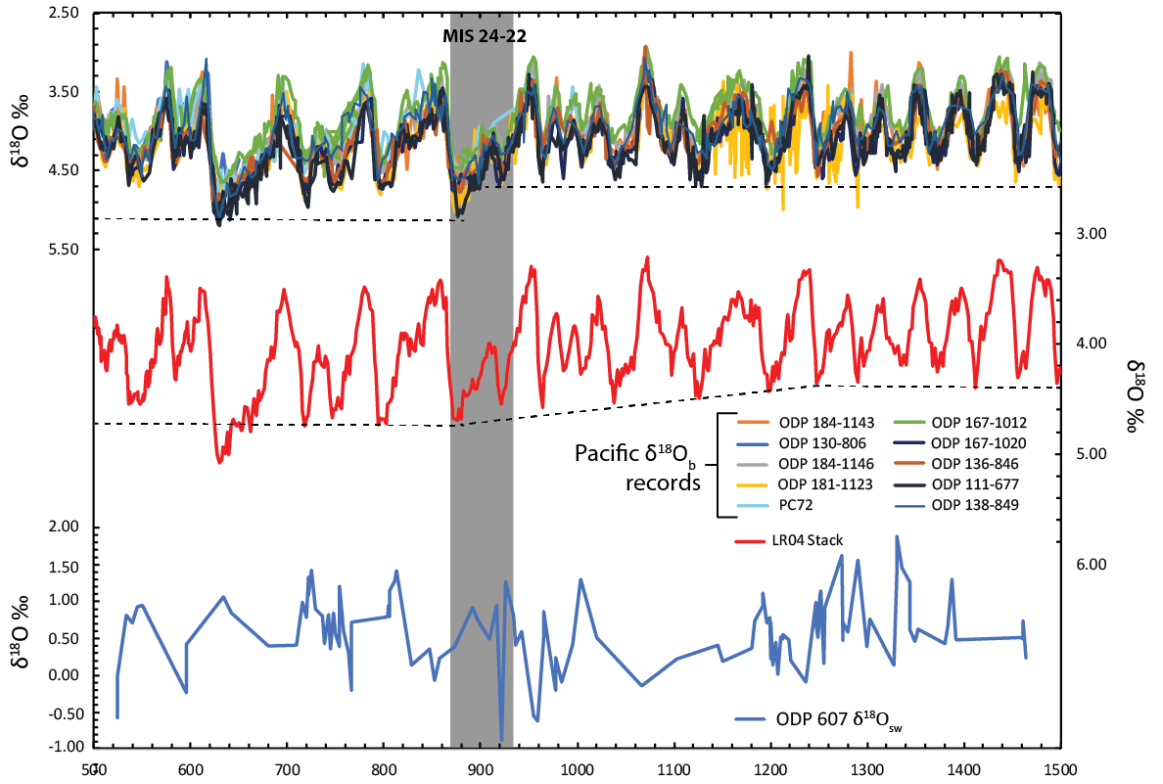

Fig. 4.15 Pacific records of $\delta^{18}O_b$ covering the MPT, compared with the LR04 stack of $\delta^{18}O_b$ records and $\delta^{18}O_b$ at ODP Site 607 in the North Atlantic. $\delta^{18}O_{sw}$ at Site 607 and the LR04 stack, which is heavily weighted towards the Atlantic basin, shows a gradual decrease in $\delta^{18}O_b$ across c. 1250-866 ka (dashed line lower curve), whereas the $\delta^{18}O_b$ records from cores located in the Pacific show a more abrupt shift across MIS 24-23 (dashed line upper curve and grey bar).

same gradual decrease in $\delta^{18}O_b$ across the MPT (1250-750 ka; Fig. 4.15) as observed in the $\delta^{18}O_{palaeoSW}$ record of Site 607. However, when $\delta^{18}O_b$ records from the Pacific are taken in isolation, they in fact show an abrupt rise across c. 936-866 ka (MIS 24-22) rather than the gradual increase across c. 1250-750 ka observed in the LR04 stack (Fig. 4.15).

Reconciling the $\delta^{18}O_{palaeoSW}$ records of Site 607 and Site 1123 requires a decoupling of deep water $\delta^{18}O_{palaeoSW}$ via processes operating in the SO, such that $\delta^{18}O_{palaeoSW}$ is reduced (i.e. depleted in ^{18}O/enriched in ^{16}O) in the Pacific compared to the Atlantic. This could be achieved by bottom waters reaching Site 1123 containing a large fraction of meteoric water (depleted in ^{18}O/enriched in ^{16}O), or formed via brines rejected during sea ice formation (as ^{18}O is preferentially incorporated into sea ice (Toyota et al., 2013), although this affect is relatively small). A decrease in the supply of meteoric water to AABW and/or decreased sea ice formation in AABW precursor water masses, coupled with an increase in the advection of NCW from the Atlantic into the Pacific basin following 866 ka. (i.e. after MIS 24-22)

could therefore go some way to explaining i) the discrepancy between the two $\delta^{18}O_{palaeoSW}$ records of sites 607 and 1123 – which are largest prior to 936 ka –, and ii) the discrepancy between $\delta^{18}O_b$ records in the Pacific basin and the LR04 stack across the MPT (i.e. between c. 1250-866 ka, Fig. 4.15).

4.4.4 Coupling of Neodymium and carbon isotopes at Site 758

By making coupled $\delta^{13}C_b$ and authigenic ε_{Nd} measurements on a sediment sample, it is possible to isolate changes in $\delta^{13}C_b$ related to the physical circulation and mixing of water masses from $\delta^{13}C_b$ changes driven by variations in nutrient content and ventilation (e.g. Piotrowski et al. (2009); Wilson et al. (2015b). As there is a slight offset between sample depths measured for ε_{Nd} and the previously published stable carbon and oxygen isotopes measured on *Cibicidoides wuellerstorfi* (Farrell and Janecek, 1991), only $\delta^{13}C_b$ data which fall within 2 kyr of ε_{Nd} measurements have been collated as coupled samples here. Although this 2 kyr window is longer than the whole-ocean mixing time of the modern ocean, and therefore likely to cause a greater scatter in these paired ε_{Nd} / $\delta^{13}C_b$ data, this approach was preferred to an artificial interpolation of either the $\delta^{13}C_b$ or ε_{Nd} datasets, as this could lead to spuriously high or low ε_{Nd} or $\delta^{13}C_b$ values. The 2 kyr window used here bin ε_{Nd} and $\delta^{13}C_b$ data is a higher resolution than the ε_{Nd} record (mean resolution = 5.8 kyr), and still captures the salient features at orbital time-scales. The trend in glacial-interglacial $\delta^{13}C_b$ vs percentage of NCW bathing Site 758 is similar both before and after the intense glacial conditions of MIS 22-24 (Fig 4.16). This suggests that most of the pre- and post-MPT glacial-interglacial variability in $\delta^{13}C_b$ at Site 758 can be explained in terms of the proportion of high-$\delta^{13}C_{palaeoSW}$ NCW admixing into CDW and circulating to Site 758. These data illustrate that water masses are the dominant control on $\delta^{13}C_b$ and provide additional assurance that applying the simple binary mixing calculation (section 4.4.4) was appropriate.

Samples from the interval spanning 927-865 ka (MIS 24-22, n= 7, orange dots in Figs. 4.16 and 14.17) are characterised by negative $\delta^{13}C_b$ and low % NCW, indicative of a prolonged period of intense glacial conditions at this time. These MIS 24-22 samples fall outside the statistical Predictive Interval (95% confidence)of the preceding glacial-interglacial cycles of 1496-972 ka (MIS 50-26, data coverage 1496-972 ka, n= 62, green dots in Fig 4.16), and instead fall within the range of the glacial-interglacial variability across 858-5 ka (MIS 21-1, n= 68, blue dots in Fig 4.16). Following the period from 927-865 (MIS 24-22), the 858-5 ka interval is characterized by an increase in the range of $\delta^{13}C_b$ relative to the period from 1496-972 ka (see table 4.3), independent of changes to the proportion of NCW admixing to Site 758 across the same time period. This increase in the range of

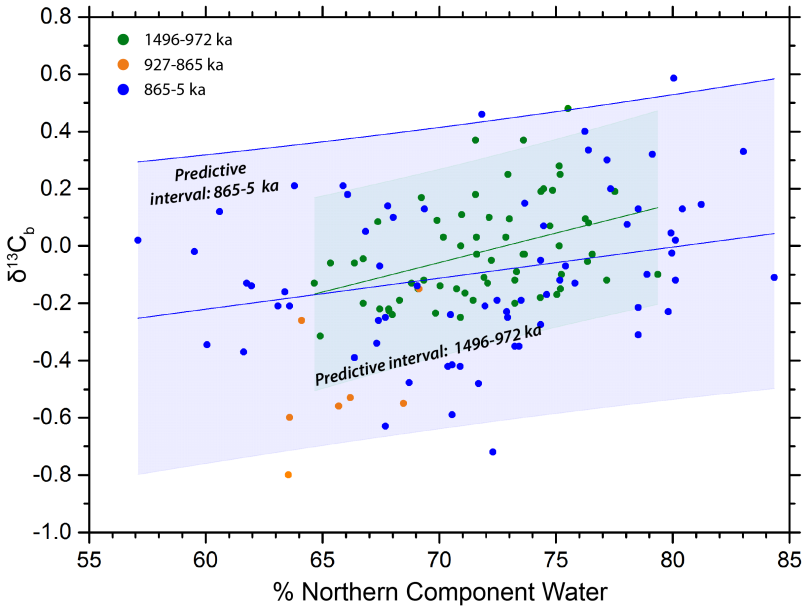

Fig. 4.16 Coupled $\delta^{13}C_b$ measured at Site 758 and percentage of NCW bathing Site 758, as calculated using ε_{Nd} (see section 4.4.4.) between 1496-972 ka (i.e. pre-MIS 24, green dots) and 865-5 ka (i.e. post MIS-22, blue dots) with the respective predictive intervals (95% confidence; PI) and slope of data for the 1496-972 ka; (pre MIS 24, green shading, green line) and 858-5 ka; (post MIS 22, blue shading, blue line). Orange dots are data from the interval between 927-865 ka (MIS 24-22).

$\delta^{13}C_b$ is driven by a decrease in glacial $\delta^{13}C_b$ minima, and indicates a lowering of the glacial $\delta^{13}C_{palaeoSW}$ of CDW/NCW which is, in turn, transferred to waters at Site 758.

Intervals of decreased $\delta^{13}C_b$ during glacial periods at Site 758 coincide with episodes of intermediate percentage NCW: all $\delta^{13}C_b$ values <-0.4‰ occur when Site 758 is bathed in approximately 64-72% NCW (n= 13, mean= 68% NCW). The fact that these $\delta^{13}C_b$ (<-0.4‰) minima do not occur during NCW minima suggests they are related to changing $\delta^{13}C_{sw}$ of CDW and/or NCW, rather than changes in the proportion of NCW entrained within the mCDW bathing Site 758. All $\delta^{13}C_b$ values <0.4‰ at Site 758 throughout the last 1.5 Ma occur after 972 ka, that is during or following the intensification of glacial-interglacial variability associated with the glacial conditions between c. 972-865 ka.

Following c. 430 ka, there is a marked increase in the glacial-interglacial variability in percentage NCW bathing Site 758, ranging from 57-84% (red dots in Fig. 4.17; table 4.3), driven by an increase in both maximum %NCW (i.e. interglacial maxima) and minimum %NCW (i.e. glacial minima). The timing of this change coincides with an increase in the amplitude of 100 kyr glacial-interglacial cycles observed in a range of palaeoclimatic archives following the MBE. The glacial-interglacial $\delta^{13}C_b$ variability following the MBE (-0.69 to

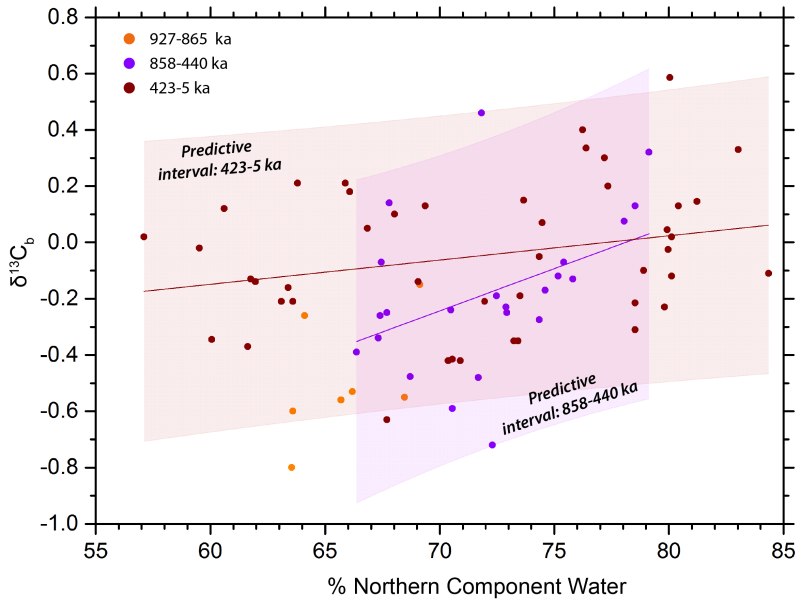

Fig. 4.17 Coupled $\delta^{13}C_b$ measured at Site 758 and percentage of NCW bathing Site 758, as calculated using ε_{Nd} (see section 4.4.4.) between 858-440 ka data, PI and slope of data, (purple dots, purple shading and purple line) and from 423-5 ka data, PI and slope of data (red dots, red shading and red line). Data from between 827-865 ka (MIS 24-22, orange dots) fall outside the PI of glacial-interglacial variability of data immediately following the MPT (858-440 ka), highlighting the severity of this glacial-like interval.

0.59 ‰) is more or less unchanged compared with before the MBE (858-440 ka; -0.72 to 0.46 ‰). There is a slightly higher average $\delta^{13}C_b$ from 440 ka onwards (i.e. following to the MBE) which cannot entirely be explained by the more modest increase in average %NCW. This discrepancy manifests as an increase in the slope of $\delta^{13}C_b$ vs percentage NCW between 858-440 ka compared with MIS 440-5 ka in Fig. 4.17, and likely reflects a long-term drift in global $\delta^{13}C_{palaeoSW}$ over this time period. An Analysis of Covariance Test (ANCOVA) was performed on these two slopes, and the change is found to be statistically significant(95% confidence level). This long-term drift in global $\delta^{13}C_b$ values is thought to occur due to broader changes in the global carbon cycle, assumed to be paced by the 413 kyr eccentricity cycle. However, the exact causes of this drift and of the difference between the wavelength of proposed forcing and of the climatic response (413 kyr vs c. 500 kyr) during the Pleistocene remains unclear (Hoogakker et al., 2006; Russon et al., 2010).

Table 4.2 Characterisation of $\delta^{13}C_b$ values and percentage of NCW bathing Site 758 across discrete intervals of the last 1.5 myr

	MIS 1-11 5-423 ka	MIS 12-21 440-858 ka	MIS 22-24 865-927 ka	MIS 25-50 927-1496 ka
No. Samples	*45*	*23*	*7*	*62*
$\delta^{13}C_b$ Max ‰	*0.59*	*0.46*	*-0.15*	*0.48*
$\delta^{13}C_b$ Min ‰	*-0.69*	*-0.72*	*-0.8*	*-0.32*
$\delta^{13}C_b$ Range ‰	*1.28*	*1.18*	*0.65*	*0.18*
$\delta^{13}C_b$ Mean ‰	*-0.05*	*-0.18*	*-0.49*	*-0.02*
$\delta^{13}C_b$ σ ‰	*0.26*	*0.28*	*0.22*	*0.18*
%NCW Max	*84%*	*79%*	*69%*	*79%*
%NCW Min	*57%*	*66%*	*64%*	*65%*
%NCW Range	*27%*	*13%*	*5%*	*14%*
%NCW Mean	*75%*	*72%*	*3%*	*72%*
%NCW σ	*7%*	*4%*	*3%*	*3%*

4.5 Conclusions

In this chapter, I have presented an authigenic ε_{Nd} record covering the last 1500 ka measured on sediments from Site 758, located in the equatorial Indian Ocean, incorporating and building upon the previously published work of Burton and Vance (2000) and Gourlan et al. (2010). ε_{Nd} at Site 758 is sensitive to changes in the flow of NCW into the SO and its entrainment within CDW, and records persistent orbital-scale cycles of reduced NCW advection into the SO during past glacial periods. Past changes in the advection of NCW to Site 758 reflect both changes in deep water production in the North Atlantic, and the entrainment of this NCW within CDW of the SO.

In the middle Pleistocene, between c. 1500-931 ka, repeated cycles of changing ε_{Nd} are ascribed to the 41 kyr orbital obliquity cycle. During the early stages of the MPT between 1043-936 ka, the amplitude of this cyclicity is reduced, with continued advection of NCW to Site 758 during glacial periods, but slightly lower proportions of NCW during interglacials. This interval is interpreted as a prolonged period of stable but reduced THC flow, whereby conditions never reach those typical for peak glacial or interglacial periods recorded before and after this time interval. This period of THC stability is followed by a greatly reduced proportion of NCW in the waters bathing Site 758, reflecting a crash in the circulation of NCW previously identified in the ε_{Nd} signal of cores from the Atlantic sector of the SO (Pena and Goldstein, 2014). This greatly reduced NCW flow to the SO spans the interval between 936-866 ka (MIS 24-22), effectively marking the first prolonged glacial-interglacial cycle of the Pleistocene. The timing of this interval (936-866 ka) coincides with

an expansion in global ice volume (Elderfield et al., 2012) and a drop in baseline glacial and interglacial pCO_2^{atm} values (Hönisch et al., 2009; Tripati et al., 2009). By calculating the mixing proportions of NCW and PDW in waters bathing Site 758, Site 929 on the Ceara Rise in the Equatorial Atlantic (Howe et al., unpublished) and Site 1123 in the SW Pacific (Piotrowski et al., unpublished), it is demonstrated that during MIS 23 (917-900 ka) the advection of NCW into the SO is greatly reduced despite evidence for consistent NCW production in the Atlantic. Following 866 ka, there is a marked strengthening of THC, as demonstrated by an increase in the proportion of NCW bathing Site 758. It is suggested that the reduced THC prior to 866 ka may go some way to reconciling differences in $\delta^{18}O_b$ and $\delta^{18}O_{palaeosw}$ records between the Atlantic and Pacific basins at this time.

Following the MPT, the periodicity of glacial-interglacial cycles in ε_{Nd} at Site 758 increased from 41 kyr to c. 100 kyr. After c. 430 ka (i.e. following the MBE), NCW flow into the SO increased during interglacial periods. It has previously been suggested that a southward shift in southern hemisphere westerlies during interglacials following the MBE may have resulted in a larger proportion of NCW being entrained within CDW (Oke and England, 2004; Santoso et al., 2006; Toggweiler and Samuels, 1995), which may explain the slightly less radiogenic ε_{Nd} values recorded during peak interglacials at Site 758 from c. 430 ka onwards. A southward shift in southern hemisphere westerlies during interglacials following the MBE is supported by warmer SST recorded at core Site 1090 in the Atlantic sector of the SO following the MBE, which may relate to a southward shift in the location of ACC frontal positions, which are in turn expected to closely track southern hemisphere westerlies (Orsi et al., 1995).

Finally, by assessing changes in the previously published $\delta^{13}C_b$ record of Site 758 (Farrell and Janecek, 1991), it is demonstrated that, despite a high degree of scatter and the influence of long-term changes in the carbon cycle, the glacial-interglacial cyclicity in $\delta^{13}C_b$ at this site can largely be explained by the proportion of NCW bathing the core site. By examining how much changes in $\delta^{13}C_b$ at Site 758 can be explained by the percentage of NCW in mCDW bathing the core site, it is demonstrated that the most depleted $\delta^{13}C_b$ values at Site 758 (=< -0.4 ‰) require a lowering of $\delta^{13}C_{palaeosw}$ of CDW and/or NCW. This highlights the importance of NCW in setting the $\delta^{13}C_b$ of CDW, and demonstrates that $\delta^{13}C_b$ can be an important tool in assessing palaeocirculation changes within the SO, as discussed in chapter 3.

Chapter 5

Deep water formation and palaeocirculation in the western Pacific sector of the Southern Ocean during the last 540 ka

5.1 Introduction

In chapters 3 and 4 I examined how circulation from the Atlantic to the Pacific sectors of the Southern Ocean (SO) changed throughout the middle to late Quaternary, and in particular highlighted the heterogeneity in deep and bottom water masses of the SO during glacial periods. Several studies have examined the palaeocirculation history of the Atlantic sector of the SO and Atlantic basin, including studies utilising neodymium isotopes (ε_{Nd}) to reconstruct past changes in physical circulation (Howe et al., 2016b; Pena and Goldstein, 2014; Piotrowski, 2005; Piotrowski et al., 2012, 2008; Wei et al., 2016), and nutrient proxies, such as the Cd/Ca ratio (Boyle and Keigwin, 1987; Marchitto and Broecker, 2006; Rickaby and Elderfield, 2005) and the $\delta^{13}C$ (Charles and Fairbanks, 1992; Curry and Oppo, 2005; Hodell et al., 2003) of benthic foraminifera tests, which contain information about physical circulation, biological processes, and air-sea gas exchange. ε_{Nd} studies in the Atlantic and Atlantic sector of the SO have shown an expanded contribution of Antarctic Bottom Water (AABW) to sites in the deep Cape Basin during past glacial periods (e.g. Pena and Goldstein (2014); Piotrowski et al. (2012)); however, studies of the physical circulation of the southern Pacific and Pacific sector of the SO utilising ε_{Nd} are more limited. Previous reconstructions of past circulation employing ε_{Nd} in the Pacific and Pacific sector of the SO have focused

on the region around Chatham Rise (c.40 - 45°S) (Elderfield et al., 2012; Hu et al., 2016a,b; Noble et al., 2013), and locations on the southern East Pacific Rise (c. 45 - 50°S) (Hu et al., 2016b; Molina-Kescher et al., 2016). These studies have shown an increase in the influence of Pacific-sourced waters at core sites during past glacial periods, with a reduced contribution of waters sourced in the Atlantic (see chapter 4). However, to date little work has been done to characterise changes in the production and advection of deep and bottom waters in the Pacific sector of the SO, and whether the end member ε_{Nd} values of deep waters formed in the Pacific sector have remained constant through time. This chapter will focus on using ε_{Nd} recorded in Fe-Mn coatings of planktic foraminifera ($\varepsilon_{Nd}{}^{foram}$) and leached from the Fe-Mn coatings of the <125 μm size fraction of sediments ($\varepsilon_{Nd}{}^{leachate}$), alongside measurements of rare earth element (REE) concentrations made on the Fe-Mn sediment leachates, to reconstruct the palaeocirculation history of the western Pacific sector of the SO. I will first explore the possible sources of the ε_{Nd} signatures recorded in the sedimentary leachate data, using REE profiles to examine the possibility of a hydrothermal contamination of the bottom water ε_{Nd} signal. I will then use the $\varepsilon_{Nd}{}^{foram}$ and $\varepsilon_{Nd}{}^{leachate}$ data to examine the varying contribution of deep waters sourced in the Ross Sea to the western Pacific sector of the SO, and finally to explore the relationship between deep water formation in the Ross Sea and ice dynamics throughout the last 550 ka.

5.2 Core locations and chronology

5.2.1 Core location

Core sites NBP9802-04PC1 (64°11'74" S, 170°04'77" W, 2696 m. water depth; hereafter NBP-04) and NBP9802-06PC1 (61°52'00" S, 169°58'00" W, 3245 m. water depth; hereafter NBP-06) are both situated on the northern flank of the Pacific-Antarctic Ridge in the western Pacific sector of the SO. Site NBP-04 lies c. 4° south of the modern Polar Front (PF), c. 0.5° north of the southern boundary of the Antarctic Circumpolar Current (SBACC) and c. 2° South of the maximum extent of winter sea ice (WSI; >15% September sea ice concentration average 1979-1999). Site NBP-06 lies c. 0.5° south of the PF, c. 3° north of the SBACC and c. 1° north of maximum WSI extent (Comiso, 2003; Orsi et al., 1995). Both piston cores were collected by the R/V Nathaniel B. Palmer as part of the United States Joint Global Ocean Flux: Antarctic Environment and Southern Ocean Process Study between February and April 1998. These core sites are today bathed in lower Lower Circumpolar Deep Water (lLCDW), and are situated close to the inflow of Ross Sea Bottom Water (RSBW) to the Antarctic Circumpolar Current (ACC) (Fig. 5.1). Although not today bathed in pure RSBW,

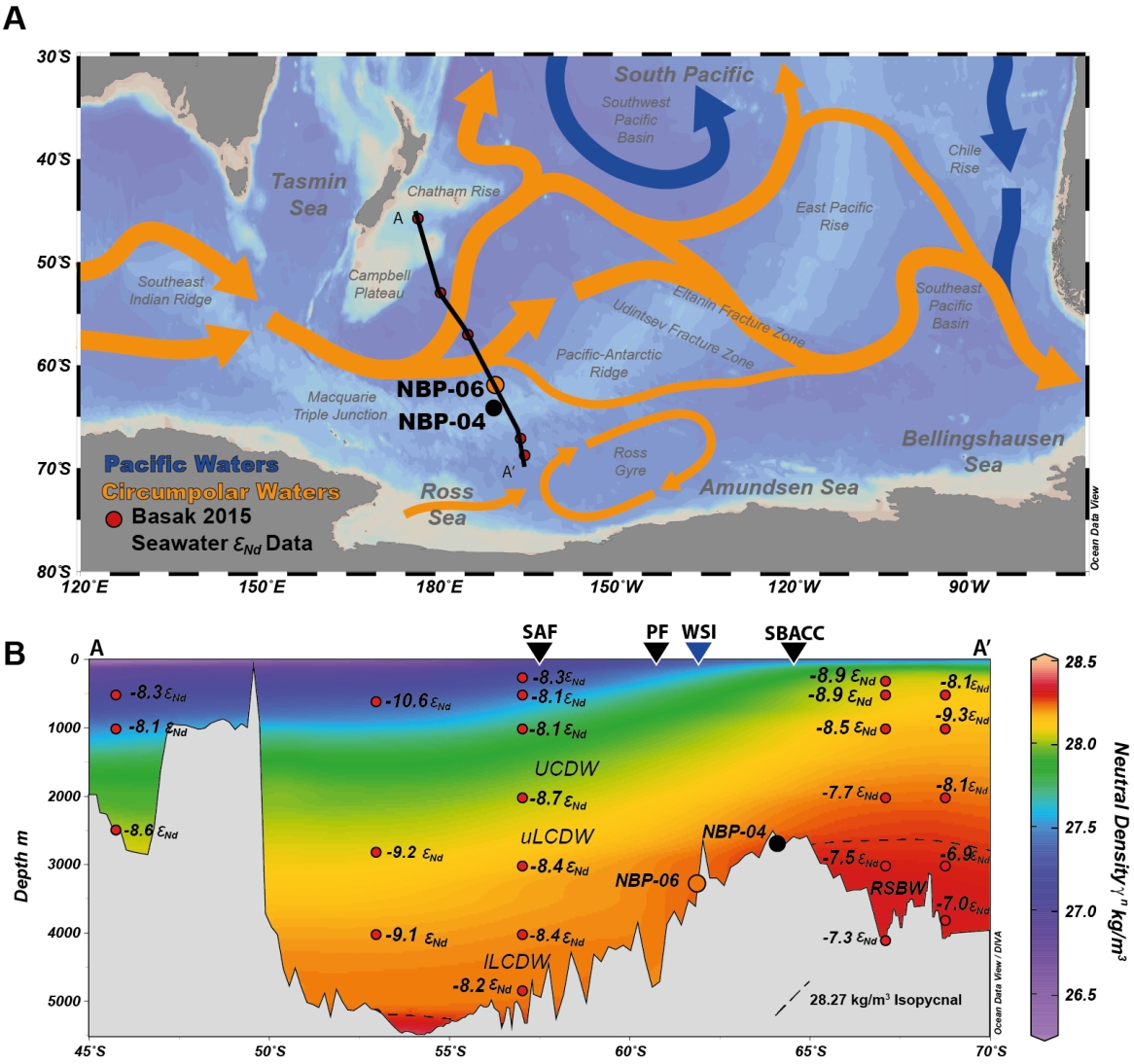

Fig. 5.1 Map of study area showing location of core sites NBP-04 (2696 m. water depth) and NBP-06 (3245 m. water depth), and the location of nearby $\varepsilon_{Nd}{}^{seawater}$ measurements (Basak et al., 2015). Orange and blue arrows show schematic flow paths of deep water masses at 3000 m. water depth (Reid, 1986). B: $\varepsilon_{Nd}{}^{seawater}$ (red dots) and neutral density across line A-A' in the upper panel. Antarctic Bottom Water (AABW) and Ross Sea Bottom Water (RSBW) with neutral densities greater than >28.27 γ^n (Orsi et al., 1999) are highlighted, as are the positions of the Subantarctic Front (SAF), Polar Front (PF), the Southern Boundary of the ACC (SBACC) after Orsi et al. (1995) and the maximum extent of winter sea ice (WSI; =>15% September sea ice concentration average 1979-1999, after Comiso (2003). Both panels reated using Ocean Data View (Schlitzer, 2015)

core sites NBP-04 and NBP-06 lie just north of the boundary between RSBW and lLCDW, and any expansion in the RSBW across the Pacific-Antarctic Ridge would lead to RSBW making its way to the core sites (Fig. 5.1.). Cores NBP-04 and NBP-06 are therefore well

placed to record past increases in the advection of deep and bottom waters formed in the Ross Sea into the Pacific sector of the SO.

5.2.2 Chronology

5.2.2.1 Radiocarbon Dates

Nine radiocarbon dates measured on bulk sedimentary carbonate have previously been published from core NBP-06, and suggest an age of Marine Isotope Stages (MIS) 1 and MIS 2 for its upper core sections (Chase et al., 2003). An additional five radiocarbon dates from core NBP-06, and seven from core NBP-04 measured on mixed planktic foraminifera (mostly *N. pachyderma* sin., with a minor contribution from *Globigerina bulloides*) were obtained as part of this thesis. These radiocarbon dates were funded by the Natural Environment Research Council (NERC) and measured at the ^{14}Chrono Centre at Queens University, Belfast. Where the bulk carbonate and foraminifera radiocarbon dates from similar depths are in conflict, those measured on foraminifera are preferred for constructing the age model, due to the possibility of contamination of bulk radiocarbon by detrital carbonate. All radiocarbon dates were converted to calendar years using the Calib software (Stuiver and Reimer, 1993), and are presented as years before present (B.P., years before 1950). The Marine13 radiocarbon calibration curve was used (Reimer et al., 2013) and a delta-R (ΔR) offset of 857$\pm$81 yrs applied. A ΔR is required to describe the local deviation in radiocarbon reservoir age from the global average. The ΔR used here is based on the extrapolated surface ΔR based on radiocarbon measurements made at 1-6 cm and 20-21 cm in core NBP-06, which yields a surface ΔR of 857$\pm$81 yrs. This is in good agreement with published pre-bomb estimates made on marine molluscs collected from the Antarctic peninsula and the Bellingshausen and Ross seas (ΔR of 900$\pm$100, Berkman and Forman (1996) and solitary corals collected from the Ross Sea (ΔR of 744$\pm$120 yrs , Hall et al. (2010)). The same ΔR offset is applied to all radiocarbon samples presented in this chapter. Although there is evidence that the marine reservoir effect in this region remained constant throughout at least the past 6000 years (Hall et al., 2010), it is acknowledged that ΔR may have been higher during MIS 2 (Sikes et al., 2016). All radiocarbon dates are provided in Table 5.1 below (data with UBA laboratory codes were produced as part of this thesis; data with no laboratory code from Chase et al. (2003)).

Table 5.1 Radiocarbon measurements made on the sediments of cores NBP-04 and NBP-06

Laboratory Code	**Core**	**Core Depth cm**	**Radiocarbon Age years**	**Delta R**	**Calendar Age ka**	**Material Measured**	**Comments**
UBA-32997	NBP-06	1-6	1574±24	857±81	0.35±0.16	Mixed planktic foram.	
Non provided	NBP-06	20-21	2750±45	857±81	1.47±0.20	Bulk carbonate	
Non provided	NBP-06	55-56	4540±70	857±81	3.61±0.26	Bulk carbonate	
UBA-32998	NBP-06	108.5-111.5	10323±44	857±81	10.35±0.20	Mixed planktic foram.	
Non provided	NBP-06	110-111	10400±130	857±81	10.43±0.40	Bulk carbonate	
Non provided	NBP-06	120-121	10700±60	857±81	10.81±0.27	Bulk carbonate	Not used in age model
Non provided	NBP-06	130-130	10650±55	857±81	10.76±0.27	Bulk carbonate	Not used in age model
Non provided	NBP-06	130-130	10750±55	857±81	10.85±0.26	Bulk carbonate	Not used in age model
UBA-32999	NBP-06	138.5-142.5	10393±45	857±81	10.40±0.21	Mixed planktic foram.	
Non provided	NBP-06	200-201	20400±100	857±81	23.07±0.38	Bulk carbonate	Not used in age model
UBA-33000	NBP-06	205-210	20192±118	857±81	22.81±0.36	Mixed planktic foram.	
Non provided	NBP-06	208-209	22800±120	857±81	25.82±0.25	Bulk carbonate	Not used in age model
Non provided	NBP-06	210-211	22800±500	857±81	25.78±1.19	Bulk carbonate	Not used in age model
UBA-33001	NBP-06	211.5-214.5	19754±112	857±81	22.30±0.34	Mixed planktic foram.	
UBA-33002	NBP-04	1-6	10223±43	857±81	10.18±0.26	Mixed planktic foram.	
UBA-33003	NBP-04	22.5-27.5	17256±88	857±81	19.28±0.31	Mixed planktic foram.	Not used in age model
UBA-33004	NBP-04	35-40	24550±185	857±81	27.51±0.30	Mixed planktic foram.	Not used in age model
UBA-33005	NBP-04	45-50	22988±153	857±81	26.00±0.34	Mixed planktic foram.	
UBA-33006	NBP-04	51-54	23081±154	857±81	26.10±0.35	Mixed planktic foram.	
UBA-33007	NBP-04	61-64	23848±181	857±81	26.87±0.49	Mixed planktic foram.	
UBA-33008	NBP-04	79-82	30256±355	857±81	32.94±0.93	Mixed planktic foram.	

Four radiocarbon dates measured on bulk sedimentary carbonate and two measured on mixed planktic foraminifera between 108.5 and 142.5 cm depth in core NBP-06 yielded ages of 10.35±0.20 to 10.85±0.26 cal. ka BP , leading to a drastic increase in sedimentation rates from c. 8.0 cm/ka to c. 380 cm/ka in this core section, followed by a major drop down to c. 5.6 cm/ka in the overlying section. Estimates of surface water radiocarbon reservoir ages from the eastern equatorial Pacific (de la Fuente et al., 2015), southern Chilean margin (Siani et al., 2013) and Southwest Pacific (Sikes et al., 2016; Skinner et al., 2015) suggest that at around 10.5 ka Subtropical and Subpolar surface water ventilation ages were similar to today, i.e. the ΔR value was similar to modern. Considerable fluctuations in the radiocarbon reservoir age of Antarctic Surface Water above site NBP-06 are therefore deemed unlikely, though cannot be ruled out entirely, as an explanation for the similar radiocarbon ages across this depth interval. The similar radiocarbon ages obtained from 108.5 to 142.5 cm depth in core NBP-06 most likely result from sediment mixing and/or a substantial increase in sediment deposition, for example due to a turbidity current or bioturbation. Core descriptions for core NBP-06 are unavailable.

5.2.2.2 Litho- and Biostratigraphy

The age models of cores NBP-06 and NBP-04 are also constrained by visual correlation between the magnetic susceptibility (MS) measured on the sediment cores and the record of dust flux to the EPICA Dome C ice core site in East Antarctica (Pugh et al. (2009); Fig. 5.2). The striking correlation between the MS of SO sediments and dust flux to Antarctic ice cores is well documented across multiple glacial cycles in sediment cores from throughout the SO (e.g. Pugh et al. (2009); Weber et al. (2012)), with both sediment MS and ice core dust flux showing marked increases during past glacial periods. However, a mechanistic understanding of this relationship is yet to be fully established (Pugh et al., 2009). Increased dust transport to Antarctica during glacial periods has been linked to a reduced hydrological cycle and the availability of dust in source regions (Lambert et al., 2008). The Nd and Sr isotopic composition of dust in both Antarctic ice cores and marine core sites located in the Scotia Sea implicates South America as the dominant glacial source region (Delmonte et al., 2004; Walter et al., 2000), possibly due to increased availability of Patagonian glacial outwash as sea levels dropped (Sugden et al., 2009) and increased aridity and wind strength (Fischer et al., 2007). The Nd and Sr isotopic composition of dust in Antarctic ice cores suggest the dominant source during interglacial periods is eastern Australia, with Australian dust likely making up a proportion of dust reaching Antarctica during glacial periods as well (Revel-Rolland et al., 2006), and it is this eastern Australian source which likely dominates the supply of aeolian dust to core sites NBP9802-04PC1 and NBP9802-06PC1 (Jaeschke

et al., 2017). How the MS of marine sediments is related to the dust flux to Antarctic ice is less clear, and may not in fact be directly related to aeolian dust supply to these sediments (Diekmann et al., 2000; Walter et al., 2000). It has been suggested that increases in MS reflects reduced flow of the Antarctic Circumpolar Current during glacial periods (Mazaud et al., 2010), although this is contradicted by sortable silt data suggesting flow speeds during past glacial periods was similar to today (McCave et al., 2013). Other studies suggest the magnetic susceptibility of SO sediments is dominated by biogenic magnetite and thus reflects biological productivity changes, modulated by iron fertilization through dust supply (Yamazaki and Ikehara, 2012). Although the exact reason for the striking correlation between the MS record of some marine sediment cores from the SO and dust flux in East Antarctica is still unresolved, these mechanisms all imply that the MS peak during the last glacial period should either coincide with the peak in Antarctic dust flux at c. 26 ka, or slightly lag it.

The radiocarbon and magnetic susceptibility data from site NBP-06 are supplemented by a previously unpublished relative abundance stratigraphy of the polar diatom *Eucampia antarctica*, expressed as a percentage of the total diatom assemblage (R.F. Anderson, unpublished). Increased *E. antarctica* abundances in Quaternary sediments from the SO reflect glacial conditions, with abundance peaks correlating with increased sea ice extent and maxima in oxygen isotope data (Burckle and Burak, 1996; Burckle and Cooke, 1983). *E. antarctica* abundance data from core NBP-06 are not used as a direct chronostratigraphic marker, but provide additional confidence in the correct identification of the Last Glacial Maximum (LGM; defined here as 18-24 ka (Mix, 2001) in the MS record (dated to c. 26 ka; Fig. 5.2b).

The upper c. 20 cm of core NBP-04 were lost during coring (R.F. Anderson, pers. comm.), leading to a core-top radiocarbon age of 10.18 cal. ka BP. The MS record from this core suggests its sediments date back to MIS 14 (533-563 ka). To test the robustness of its age model, six samples of sediment from the <125 μm size fraction of core NBP-04 were screened for the presence or absence of the diatom species *Hemidiscus karstenii*. This species is known to become extinct in SO sediments during MIS 6 (130-191 ka; Burckle et al. (1978), and the disappearance of *H. karstenii* between 345-348 cm and 226-229 cm is consistent with the modelled sediment ages of late MIS 7 and MIS 5 for these core depths (Fig 5.2d).

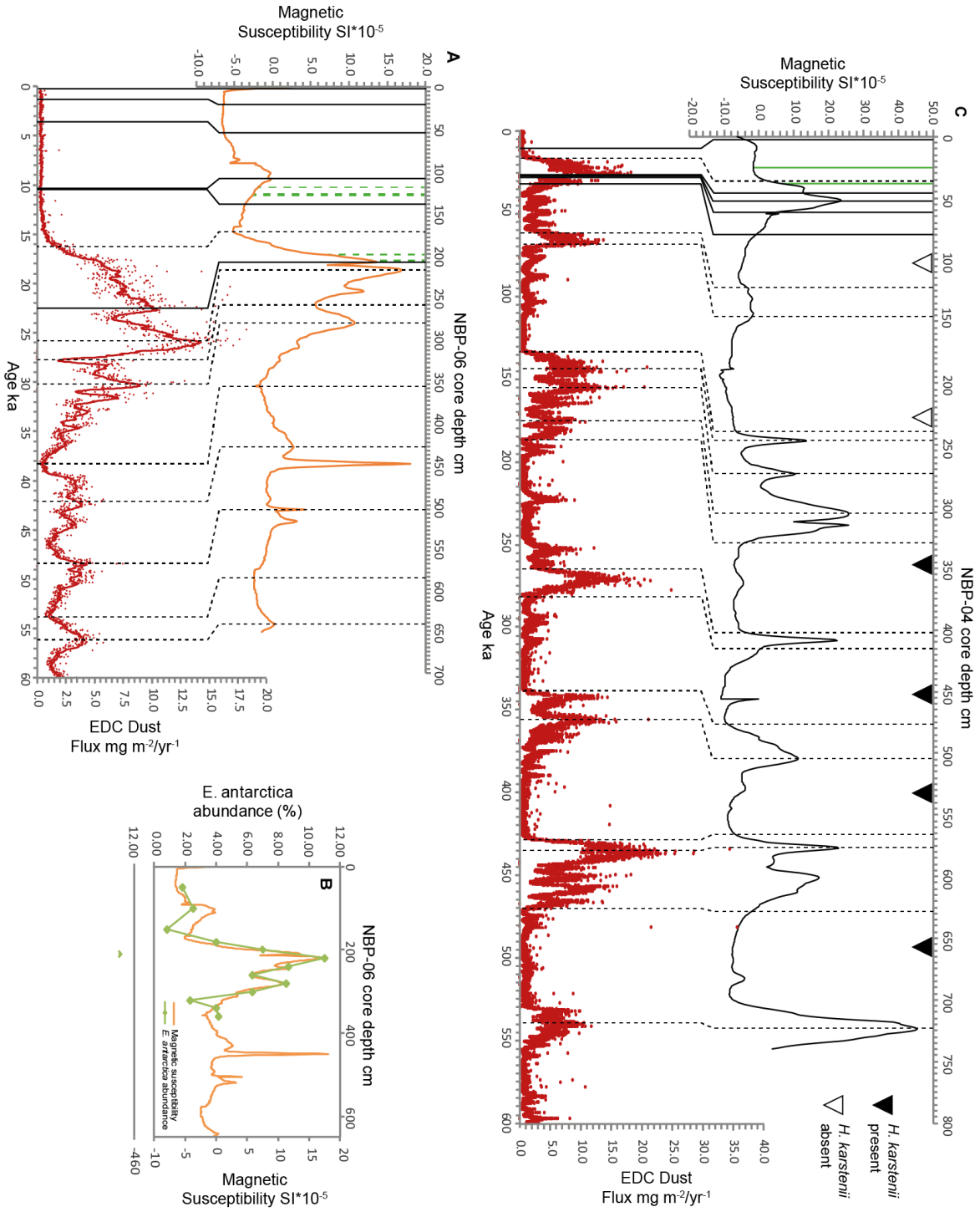

Fig. 5.2 A: Magnetic susceptibility record of NBP-06 (orange) alongside the record of dust flux to the EPICA Dome C ice core (Lambert et al., 2008) (red dots, and 24-point running mean shown with red line). Dashed black lines mark tie points between these two records, while thick black lines highlight radiocarbon dates used for constructing the age model and dashed green line denotes radiocarbon measurements made on bulk sedimentary carbonate which have been excluded from the age model. B: NBP-06 *E. antarctica* abundance record (R.F. Anderson, unpublished) and magnetic susceptibility. C: Magnetic susceptibility record of NBP-04 (black) alongside dust flux at the EPICA Dome C ice core site. Dashed black lines mark tie points between the two records and thick black lines mark the radiocarbon data used for constructing the age model, while thick green lines denote radiocarbon measurments made on planktic foraminifera which are excluded. The presence/absence of the diatom *H. karstenii* in core NBP-04 is visualised by filled/empty triangles.

Two radiocarbon dates obtained from planktic foraminifera from 22.5-27.5 cm and 35-40 cm depth in core NBP-04 yielded ages of 19.28±0.31 cal. ka BP and 27.51±30 cal. ka BP, respectively. These two radiocarbon dates are in poor agreement with both the MS-based age model and three other radiocarbon dates on planktic foraminifera (Table 5.1), and incorporating them into the age model would shift the timing of the LGM in this core to a shallower depth than suggested by these other data. Quantitative diatom slides of the <125 μm size fraction were prepared from these two depths and from 45-48 cm and 51-54 cm depth, where planktic foraminifera gave radiocarbon dates of 26.00±0.34 cal. Ka BP and 26.10±0.35 cal. Ka BP, respectively. The abundance of E. antarctica, was considerably lower in the samples from 22.5-27.5 cm and 35-40 cm when compared to that in the two deeper samples, but broadly indistinguishable from a late Holocene sample of core NBP-06 (pers. comm. C.S. Allen). The *E. antarctica* data therefore suggest that sediments deposited during peak glacial conditions lie below the samples from 22.5-27.5 cm and 35-40 cm which, however, provided radiocarbon ages spanning the LGM. As these two radiocarbon dates are not compatible with i) the MS-based age model, ii) three other radiocarbon dates from planktic foraminifera, and iii) the down-core abundance pattern of *E. antarctica*, they were excluded from the construction of the age model for core NBP-04. A core description for core NBP-04 was provided by the Lamont-Doherty Earth Observatory Core Repository, and shows no change in sediment facies between 0-33.5 cm depth; a shift in facies from diatomaceous ooze to foraminferal diatomaceous ooze is recorded at 38.5 cm depth, with a distinct change in colour at the contact, with no evidence for the presence turbidites at the contact, or in the units above and below the contact. The excluded radiocarbon dates may not fit with the rest of the age model due to bioturbation, although this would require a size-dependence to the bioturbation, such that foraminifera were preferentially bioturbated from deeper within the core, while the smaller *E. antarctica* frustules and the magnetic minerals within the sediment (presumed to be particles smaller than foraminifera) were unaffected. A list of radiocarbon dates and MS age-depth tie points is provided in Appendix Table B.6, while correlations with tie points and age-depth plots are shown in Figs. 5.2 and 5.3.

5.3 Results

To maximise the yield of foraminifera from the predominantly biosiliceous but carbonate-poor sediments, cores NBP-04 and NBP-06 were sampled across 3 cm and 5 cm depth intervals, which inevitably limited the resolution of the records presented in this chapter. To acknowledge this effect, all figures showing $\varepsilon_{Nd}{}^{leachate}$ from sites NBP-04 and NBP-06

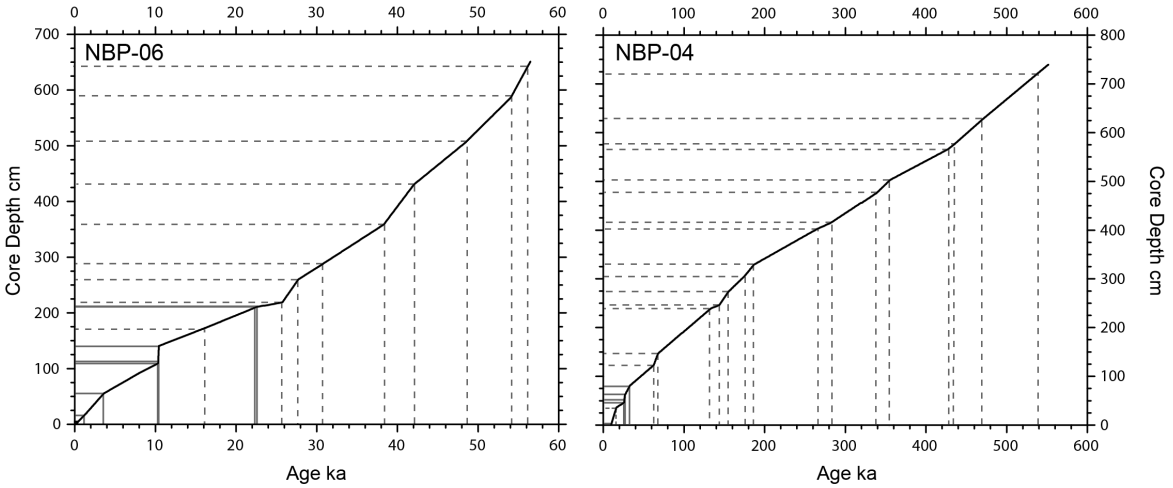

Fig. 5.3 Age-depth plots for cores NBP-06 and NBP-04. Age-depth tie points used in constructing the age models are shown as thick (radiocarbon data) and dashed (MS-dust correlation) grey lines.

include an uncertainty envelope illustrating the age range of the analysed depth intervals, as well as analytical error. Age model uncertainties for ε_{Nd} and $REE^{leachate}$ data are quoted in the text where appropriate, and the maximum and minimum sample ages are also included in appendices data tables A5.2 - A5.9.

Siliceous microfossils from core NBP-06 were isolated and leached to determine whether biogenic opal acts as a carrier phase for authentic Fe-Mn, from which Nd could be extracted for isotopic analyses. Unfortunately, concentrations of Nd within these samples were bellow detection limits, indicating samples of biogenic opal are not potential archives for past seawater ε_{Nd}.

5.3.1 Neodymium isotope composition of foraminifera Fe-Mn coatings, sediment leachates and terrigenous detritus

In both studied cores, the $\varepsilon_{Nd}{}^{foram}$ values are in very good agreement with the $\varepsilon_{Nd}{}^{leachate}$ values from the same sample depths (Fig. 5.4a; R^2=0.96). In contrast, $\varepsilon_{Nd}{}^{detrital}$ and $\varepsilon_{Nd}{}^{leachate}$ values measured on the same samples show no significant correlation (Fig. 5.4b; R^2= 0.16).

Core top $\varepsilon_{Nd}{}^{foram}$ and $\varepsilon_{Nd}{}^{leachate}$ values of -8.50±0.26 and -8.44±0.10 at site NBP-06 are both in agreement with modern $\varepsilon_{Nd}{}^{seawater}$ values of -8.2 to -8.4, measured on lLCDW close to the core site (Basak et al. (2015); Figs. 5.1 and 5.5; Appendix Tables C.4-C.9). The uppermost sediments at site NBP-04 yield an $\varepsilon_{Nd}{}^{leachate}$ value of -6.91±0.13 at 10.18±0.46

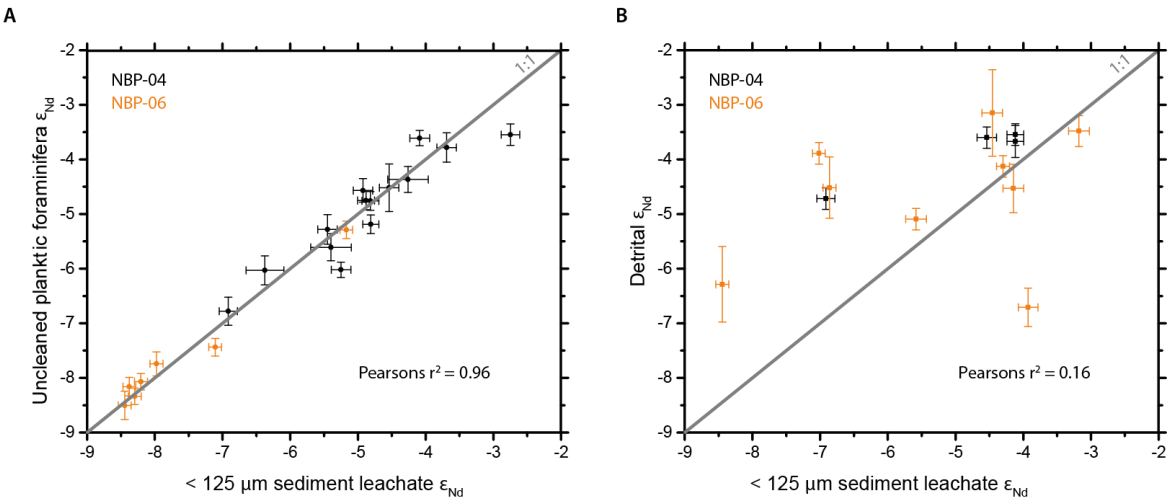

Fig. 5.4 A: ε_{Nd} measured on uncleaned planktic foraminifera and sedimentary leachates from the same core intervals show very good agreement throughout both records. B: There is no significant relationship between detrital ε_{Nd} and sediment leachate ε_{Nd}

ka, matching within error an $\varepsilon_{Nd}{}^{leachate}$ value of -6.86±0.10 measured on a sample of similar age (10.28±0.13 ka) in core NBP-06.

The down-core ε_{Nd} records of the last glacial period at sites NBP-04 and NBP-06 (Fig. 5.5) both show broadly the same features, with $\varepsilon_{Nd}{}^{leachate}$ values becoming more radiogenic with age, peaking at 49.21±0.10 ka (NBP-06, $\varepsilon_{Nd}{}^{leachate}$ = -3.02±0.14) and 63.55±0.34 ka (NBP-04 $\varepsilon_{Nd}{}^{leachate}$ = -2.51±0.14). The absolute values of the two $\varepsilon_{Nd}{}^{leachate}$ records diverge during the last glacial period between 27.03±0.40 ka to 48.20, with more radiogenic $\varepsilon_{Nd}{}^{leachate}$ values recorded at the shallower and more southerly site, NBP-04. Similar deglacial trends towards less radiogenic $\varepsilon_{Nd}{}^{leachate}$ values are apparent in both cores, again with an ε_{Nd} offset of 0.60 to 0.97 epsilon units between the two cores from c.17.7 to c.14.2 ka.

The extended $\varepsilon_{Nd}{}^{leachate}$ record of site NBP-04 shows a degree of cyclicity throughout the last 540 ka, with a tendency towards more radiogenic values during glacial periods and less radiogenic values during interglacials; however, there are exceptions: There is little difference in $\varepsilon_{Nd}{}^{leachate}$ values between glacial MIS 10 and interglacial MIS 9, when values range between -4.33±0.16 to -4.75±0.14, and a shift towards more radiogenic values is observed at 341.57±0.94 ka ($\varepsilon_{Nd}{}^{leachate}$= -3.87±0.15). Glacial-time $\varepsilon_{Nd}{}^{leachate}$ values during early MIS 6 at 181.06±1.21 ka are less radiogenic ($\varepsilon_{Nd}{}^{leachate}$= -5.18±0.30) than at any point during the preceding two interglacials. At no point during the last 550 ka the $\varepsilon_{Nd}{}^{leachate}$ values are as unradiogenic as those during MIS 1 at site NBP-04, with unradiogenic peaks during the interglacials MIS 13 (505.16±1.09 ka), MIS 11 (397.21±1.71 ka) and MIS 9

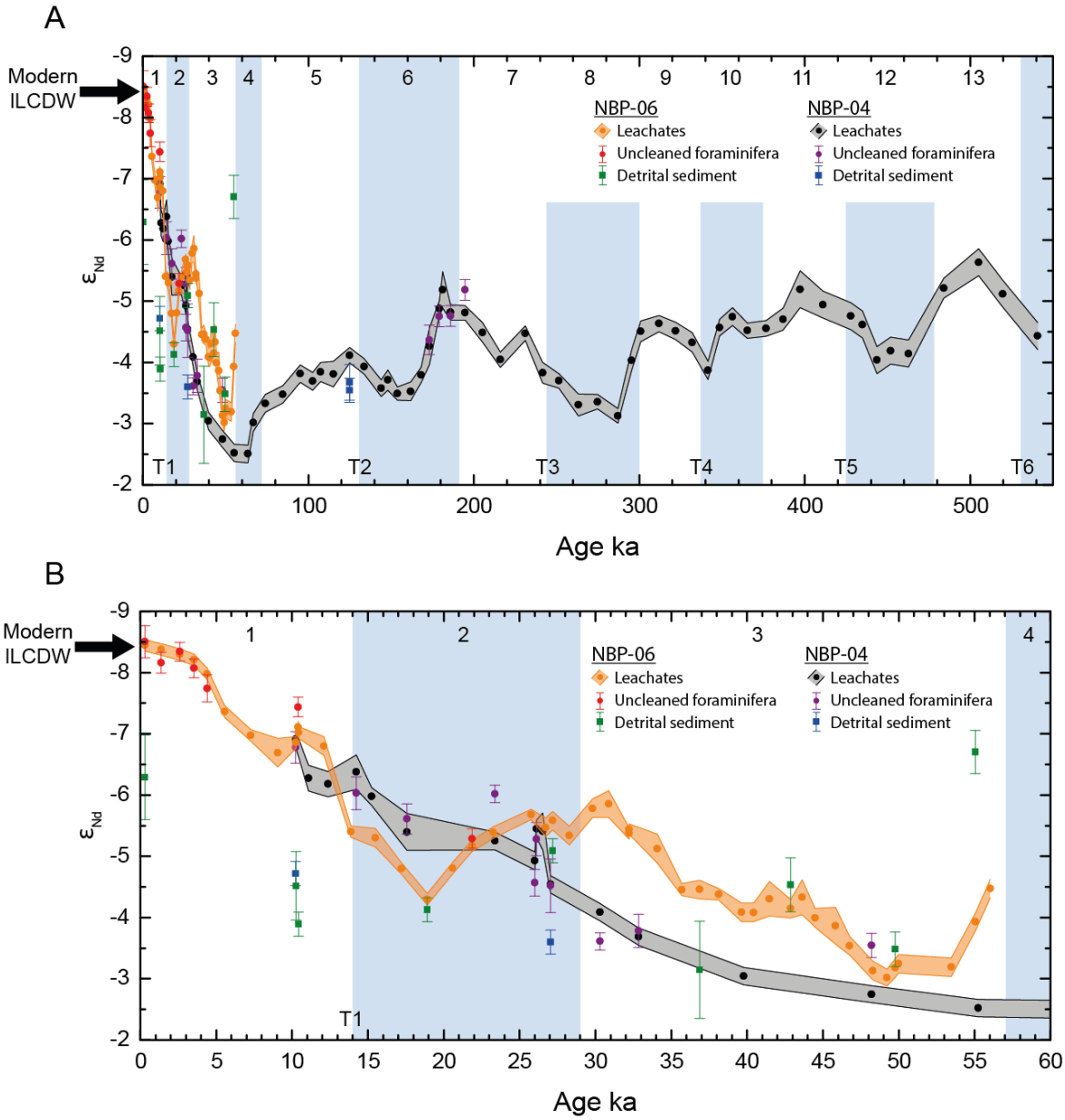

Fig. 5.5 $\varepsilon_{Nd}^{leachate}$, ε_{Nd}^{foram} and $\varepsilon_{Nd}^{detrital}$ records of cores NBP-04 and NBP-06 during the last 540 ka (A) and 60 ka (B). Modern seawater ε_{Nd} value of lLCDW from close to the core sites from Basak et al. (2015). Marine Isotope Stages (MIS) as defined by the LR04 benthic oxygen isotope stack (Lisiecki and Raymo, 2005) are numbered, with glacial MIS highlighted by blue shading. Glacial terminations are also labelled (i.e. T1, T2 etc.).

(311.78±1.37 ka) of -5.63±0.22, -5.19±0.30 and -4.64±0.13, respectively. The penultimate glacial termination (T2) registers only a small shift towards less radiogenic $\varepsilon_{Nd}^{leachate}$ values, from -3.58±0.14 during late MIS 6 (144.03±1.28 ka) to -4.12±0.12 ε_{Nd} during MIS5e (125.04±1.05 ka).

The $\varepsilon_{Nd}{}^{detrital}$ record of site NBP-06 shows a trend towards less radiogenic values from the early to the late Holocene (-3.89±0.20 at 10.43±0.08 ka to -6.29±0.69 at 0.38±0.16 ka), while $\varepsilon_{Nd}{}^{detrital}$ values during the last glacial period ranged from -3.15±0.79 to -5.29±0.20, with one exceptional value of -6.71±0.35 at 55.15±0.35 ka. The $\varepsilon_{Nd}{}^{detrital}$ samples of site NBP-04 show radiogenic early Holocene and last glacial values of -4.72±0.20 (10.18±0.46 ka) and -3.60±0.20 (27.03±0.19 ka). NBP-04 $\varepsilon_{Nd}{}^{detrital}$ values of -3.54±0.20 and -3.67±0.29 (both 125.04 ka) during the last peak interglacial MIS 5e are more radiogenic than the early Holocene values observed at both sites NBP-04 and NBP-06.

5.3.2 Rare Earth Element concentrations of sedimentary leachates

$REE^{leachate}$ profiles were measured on 5% aliquots taken from samples prior to the isolation of Nd via column chromatography (see Chapter 3 "Methods"). Normalised REE data are provided in Appendix Tables C.10 and C.11, and are shown in Appendix Fig. A.5 plotted on a log scale owing to the inter-sample variability in $REE^{leachate}$ concentrations. As plotting on a log scale can obscure trends in lower concentration samples, PAAS normalised data are also shown in Appendix Fig. A.5 normalised to [Lu] = 1. Down-core PAAS normalised $REE^{leachate}$ concentrations and Cerium (Ce/Ce*), Europium (Eu/Eu*) and middle rare earth elements (MREE/MREE*) anomalies are shown Fig. 5.6.

The $REE^{leachate}$ profile at site NBP-06 shows a pronounced increase in element concentrations between 17.21±0.25 and 35.68±0.16 ka (Fig. 5.6), which coincides with an increase in Eu/Eu*. A similar increase in REE concentrations (though not Y) and Eu/Eu* is observed in $REE^{leachate}$ data from 3.38±1.46 to 39.76±1.05 ka at site NBP-04, with further increases at 84.57±1.05 ka and between 179.11±0.78 to 295.32±1.37 ka. Both core sites experience a spike in heavy REE (HREE)/light REE (LREE) during the last deglaciation, at 10.43±0.08ka in NBP-06 and 15.24±0.28 in NBP-04. Particulate absorption within the ocean preferentially effects the LREE (Alido and Nozaki, 1999), while HREE are more readily held in solution by complexing species (Akagi, 2013), leading to seawater REE profiles enriched HREE. Authigenic Fe-Mn oxyhydroxides typically demonstrate an enrichment in MREE (Haley, 2004), and a less steeply enriched (though generally still enriched) HREE pattern than observed in seawater (Bau et al., 2014). The REE patterns observed from the Fe-Mn leachates of cores NBP-04 and NBP-06 are therefore in line with those expected from leaching authigenic Fe-Mn oxyhydroxides precipitated from seawater: moderate enrichment in HREE/LREE for most samples, and enrichment in MREE/MREE* (Fig. 5.6.).

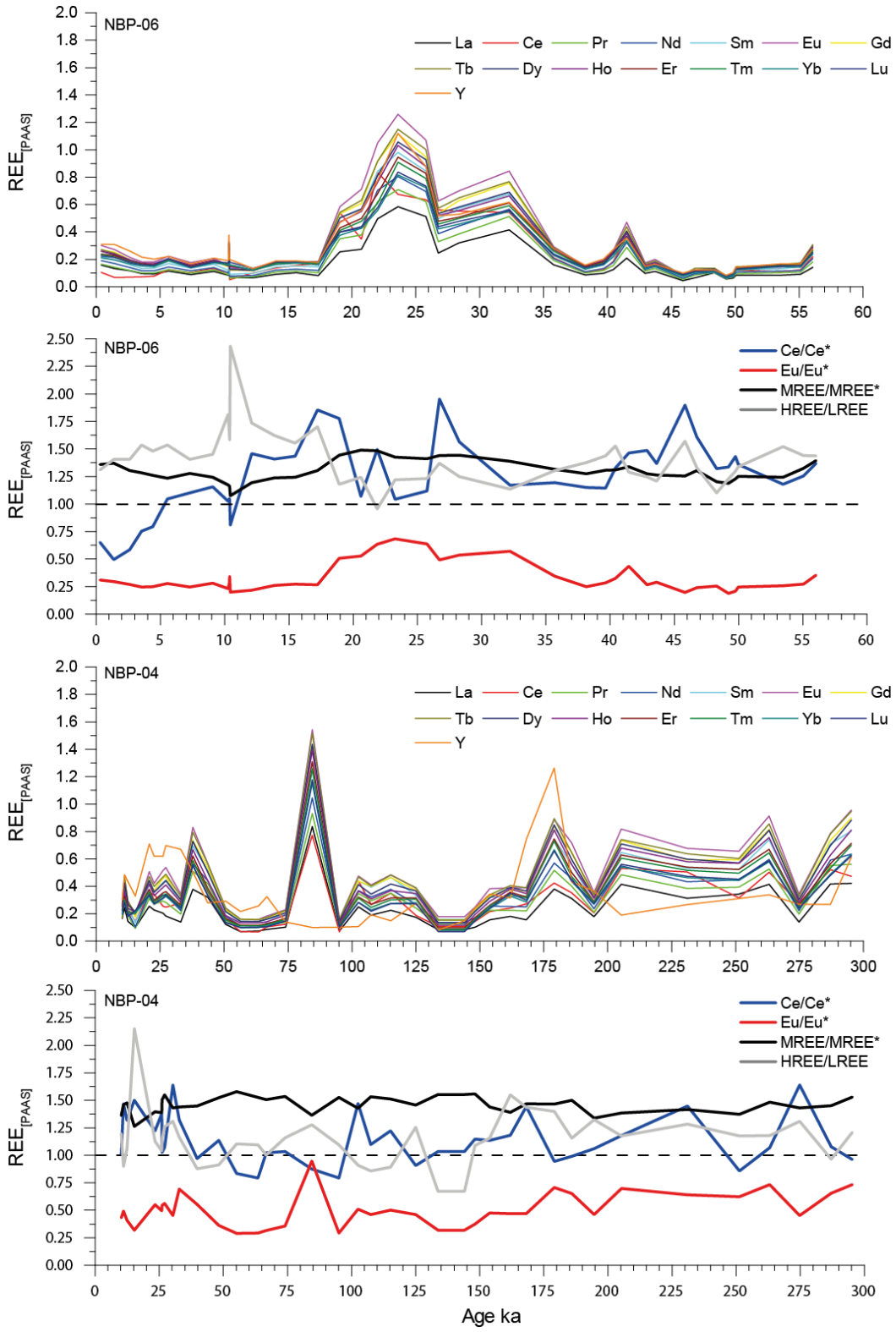

Fig. 5.6 Down-core $REE^{leachate}$ concentrations of cores NBP-06 and NBP-04, alongside Ce/Ce*, Eu/Eu*/ MREE/MREE* and HREE/LREE concentrations. All data plotted vs age.

Table 5.2 Ce/Ce*, Eu/Eu*, MREE/MREE*, and HREE/HREE* averages and standard deviation of measurements made on sediment leachates from cores NBP-06 and NBP-04

	Ce/Ce*	**Eu/Eu***	**MREE/MREE***	**HREE/LREE**
NBP-06	*1.24, σ= 0.34*	*0.33, σ= 0.13*	*1.30, σ= 0.10*	*1.42, σ= 0.25*
NBP-04	*1.14, σ= 0.23*	*0.50, σ= 0.15*	*1.46, σ= 0.07*	*1.15, σ= 0.26*

5.4 Discussion

5.4.1 $\varepsilon_{Nd}{}^{leachate}$ as a recorder of bottom water ε_{Nd}.

The very good agreement between $\varepsilon_{Nd}{}^{leachate}$ and $\varepsilon_{Nd}{}^{foram}$ across a wide range of values (see section 5.3.1, Fig. 5.4) at both core sites provides confidence that $\varepsilon_{Nd}{}^{leachate}$ and $\varepsilon_{Nd}{}^{foram}$ are recording the ε_{Nd} values of the same authigenic Fe-Mn phase. This interpretation is further supported by the lack of agreement between $\varepsilon_{Nd}{}^{detrital}$ and $\varepsilon_{Nd}{}^{leachate}$ values measured from the same core depths, demonstrating that $\varepsilon_{Nd}{}^{leachate}$ measurements faithfully record the ε_{Nd} values of authigenic Fe-Mn phases without being contaminated by detrital Nd during the leaching procedure.

It is possible that the ε_{Nd} values measured on authigenic Fe-Mn phases at sites NBP-04 and NBP-06 do not record the ε_{Nd} value of bottom waters ($\varepsilon_{Nd}{}^{seawater}$) due to alteration of $\varepsilon_{Nd}{}^{seawater}$ in the pore waters of both cores, or that the $\varepsilon_{Nd}{}^{seawater}$ values of bottom waters at both sites were derived from local boundary exchange. If $\varepsilon_{Nd}{}^{seawater}$ recorded a local boundary exchange signature, down-core changes in the ε_{Nd} values of authigenic Fe-Mn at NBP-04 and NBP-06 would represent a mixture of palaeocirculation changes and local boundary exchange.

A potential source of radiogenic Nd to deep-, bottom-, and pore waters at sites NBP-04 and NBP-06 is the Pacific-Antarctic Ridge. Hydrothermal activity is known to occur today along the Pacific-Antarctic Ridge: a plume of mantle-derived ^{3}He in the western Pacific sector of the SO was used to identify the existence of a hydrothermal vent system somewhere along the ridge between 145°W and 175°W (Winckler et al., 2010), i.e. in the region of sites NBP-04 and NBP-06. Hydrothermal solutions in vent systems on the East Pacific Rise show dissolved Nd with a depleted oceanic mantle source signature (end member ε_{Nd} values= +2 to +8, Piepgras and Wasserburg (1985)). Although hydrothermal Nd is quickly removed from seawater as hydrothermal Mn and Fe rapidly oxidise to form a plume of particulate precipitates, these plumes of Fe-Mn precipitates can travel tens of kms from the vent source (Khripounoff and Alberic, 1991), and offer a potential source of radiogenic Nd to Fe-Mn coatings formed at core sites NBP-04 and NBP-06.

Nd and other REE in these hydrothermal Fe-Mn deposits are scavenged from both the vent fluid and surrounding seawater, resulting in precipitates with PAAS-normalised REE concentrations exhibiting a negative Ce/Ce* (imparted by seawater) and a positive Eu/Eu* (imparted by the hydrothermal fluids) (German et al., 1990). The same positive Eu/Eu* would be expected in hydrothermal Fe and Mn deposits precipitated directly within sediments via diffuse flow of hydrothermal fluids through pore spaces (Bemis et al., 2012). $REE^{leachate}$ samples at neither core site show a positive Eu/Eu* (Fig 5.6), indicating that in the samples analysed for this study the Fe-Mn phases extracted during the leaching of the sediments – and by association the composition of the Fe-Mn coatings of uncleaned foraminifera – were not of hydrothermal origin. There are down-core variations in $REE^{leachate}$ Eu/Eu*, but a significant correlation between radiogenic $\varepsilon_{Nd}{}^{leachate}$ values and high Eu/Eu*, which would be expected if hydrothermal precipitates were partially responsible for the $\varepsilon_{Nd}{}^{leachate}$ values at either core site, is lacking (Fig 5.7a).

Further evidence for a lack of contribution from hydrothermal vents to the $\varepsilon_{Nd}{}^{leachate}$ and $\varepsilon_{Nd}{}^{foram}$ values at sites NBP-04 and NBP-06 is provided by the concentrations of Y in leachates from both cores. Y is chemically very similar to the Lanthanides, possessing a similar ionic radius and electronegativity; in particular, Y and Ho share very similar ionic radii, and therefore are geochemically very tightly coupled (Bau and Dulski, 1999). Ho has a higher particle reactivity than Y, and thus is quickly removed by scavenging at hydrothermal vent sites, leading to an enrichment in seawater Y/Ho close to hydrothermal vent openings relative to background seawater (Bau and Dulski, 1999), and in pore waters experiencing diffuse hydrothermal flow. A cross plot of Ce/Ce* against Y/Ho can therefore be used to differentiate between hydrogenetic and early diagenetic Fe-Mn deposits (which tend towards positive Ce/Ce* and minor Y/Ho enrichment) and hydrothermal deposits (which tend towards negative Ce/Ce* and major Y/Ho enrichment) (Bau et al., 2014) (Fig. 5.7d). Using these criteria, the presence of hydrothermal Fe and Mn deposits at sites NBP-04 and NBP-06 can be ruled out – indeed the leachate samples with Ce/Ce* and Y/Ho values closest to that of hydrothermal Fe and Mn deposits are also the most unradiogenic ($\varepsilon_{Nd}{}^{leachate}$ = -8.44 to -8.30), the reverse of what would be expected in $\varepsilon_{Nd}{}^{leachate}$ values were leaching hydrothermal Fe and Mn deposits, with a radiogenic ε_{Nd} signature.

All available evidence from core sites NBP-04 and NBP-06 point towards both sedimentary and foraminiferal authigenic Fe-Mn deposits at these sites as reflecting $\varepsilon_{Nd}{}^{seawater}$, and for no impact of boundary exchange on the $\varepsilon_{Nd}{}^{seawater}$ signature. For the remainder of this chapter, the term $\varepsilon_{Nd}{}^{palaeoSW}$ will therefore be used to describe past variations in $\varepsilon_{Nd}{}^{foram}$ and $\varepsilon_{Nd}{}^{leachate}$ values at sites NBP-04 and NBP-06.

5.4.2 Potential water mass sources for radiogenic ε_{Nd} values recorded at sites NBP-04 and NBP-06

Down core $\varepsilon_{Nd}{}^{palaeoSW}$ values recorded at sites NBP-04 and NBP-06 are at times comparable with – or even more radiogenic than – modern North Pacific end-member values of c. -3 to -4 (Piepgras and Wasserburg, 1980). Such radiogenic $\varepsilon_{Nd}{}^{palaeoSW}$ values are difficult to reconcile with modern circulation pathways and water mass $\varepsilon_{Nd}{}^{seawater}$ end-member values. In this section I will explore the potential source of this radiogenic ε_{Nd} signature.

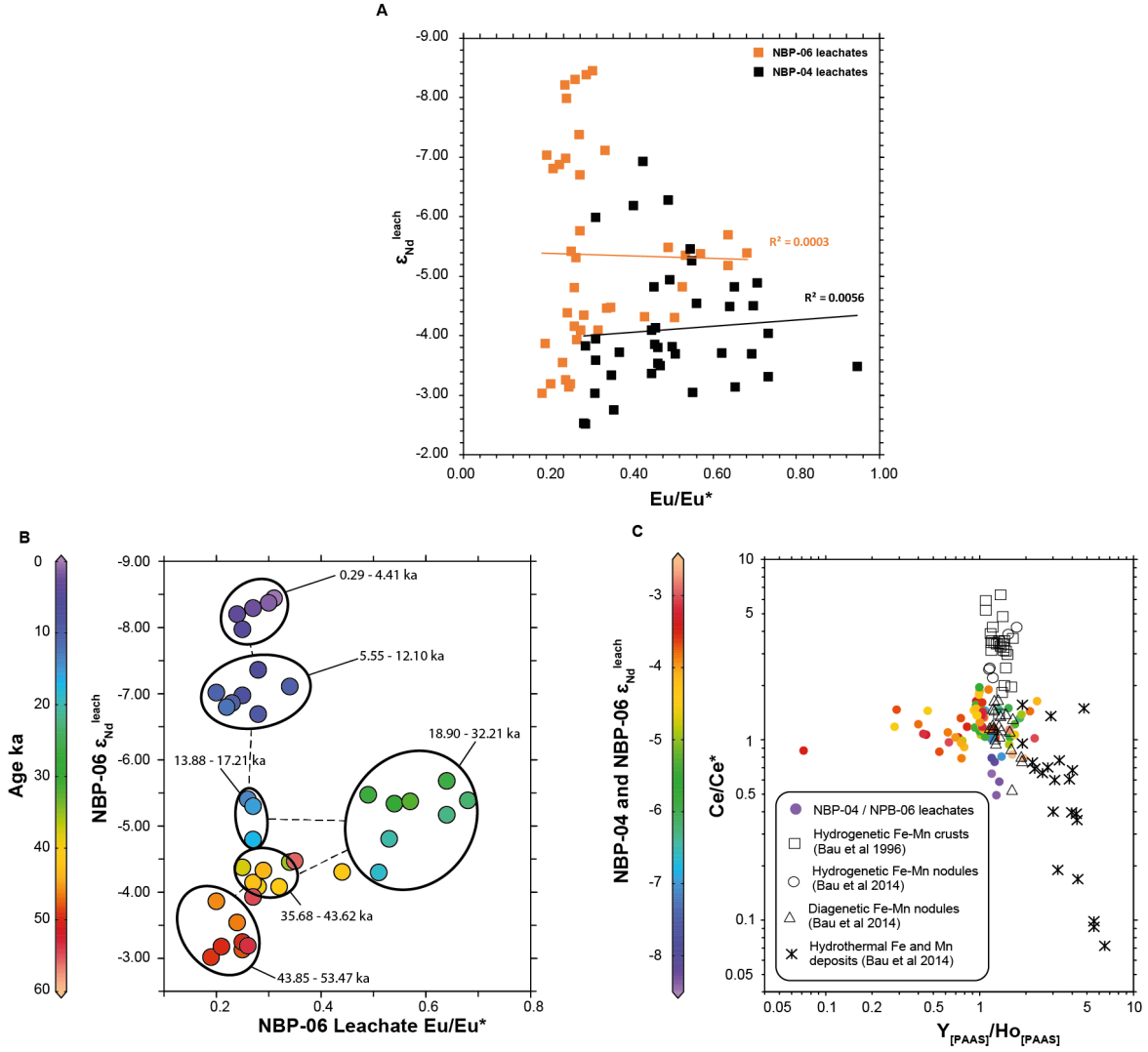

Fig. 5.7 A and B: Cross plots of $\varepsilon_{Nd}{}^{leachate}$ and Eu/Eu* show no relationship between Eu/Eu* and $\varepsilon_{Nd}{}^{leachate}$ at either core site. C: A cross plot of Ce/Ce* and Y/Ho shows no evidence for a hydrothermal influence (high Eu/Eu*; low Ce/Ce* and high Y/Ho) on $\varepsilon_{Nd}{}^{leachate}$.

5.4.2.1 Pacific Deep Water

A possible source for the radiogenic $\varepsilon_{Nd}^{palaeoSW}$ values of cores NBP-04 and NBP-06 is Pacific Deep Water (PDW). PDW ε_{Nd} end member values have remained constant at c. -3 to -4 throughout at least the Holocene and LGM (Hu et al., 2016b), and probably over much longer geological timescales, on the order of millions (Albarède and Goldstein, 1992; Goldstein and O'Nions, 1981; Ling et al., 1997; O'Nions et al., 1978; Piepgras et al., 1979) or even tens of millions (Newkirk and Martin, 2009; Osborne et al., 2014; Thomas, 2004) of years. PDW would therefore be unable to explain $\varepsilon_{Nd}^{palaeoSW}$ values as radiogenic as -2.52±0.14 recorded at site NBP-04 during the last glacial period.

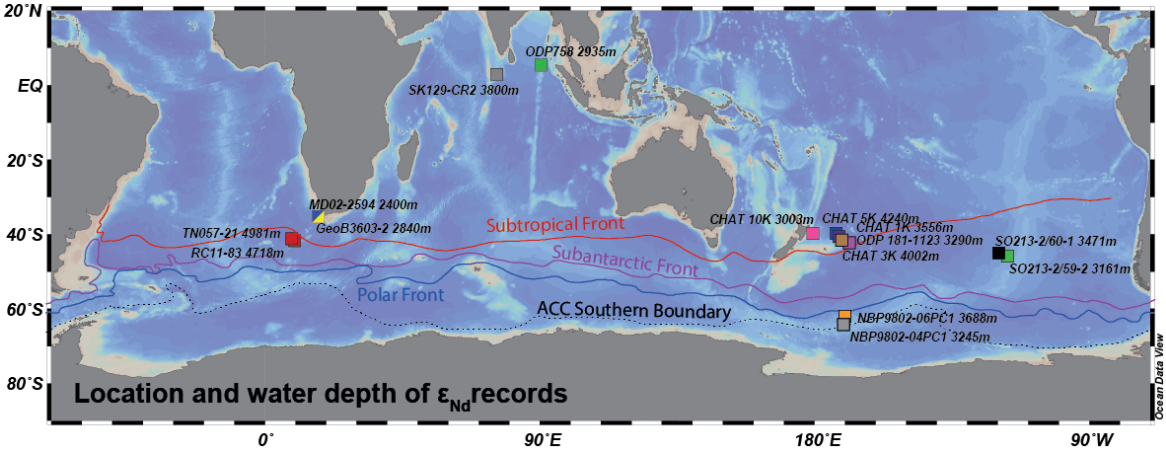

Fig. 5.8 Location of ε_{Nd} records from the South Atlantic, Indian, Pacific and SO shown in Fig. 5.9. References for ε_{Nd} records: RC11-83/TN057-2: (Piotrowski, 2005; Piotrowski et al., 2012); MD02-2594 and GeoB3603: (Wei et al., 2016); SK129-CR2: (Wilson et al., 2015b); ODP 121-758: this study, (Burton and Vance, 2000; Gourlan et al., 2010); CHAT10k and CHAT 3K: (Noble et al., 2013); SO213-2/59-2, SO213-2/60-1: (Molina-Kescher et al., 2016), ODP 1281-1123: Edlerfield et al., (2012); Piotrowski et al., (In Prep); CHAT 1K and CHAT 5K: (Hu et al., 2016a; Noble et al., 2013).

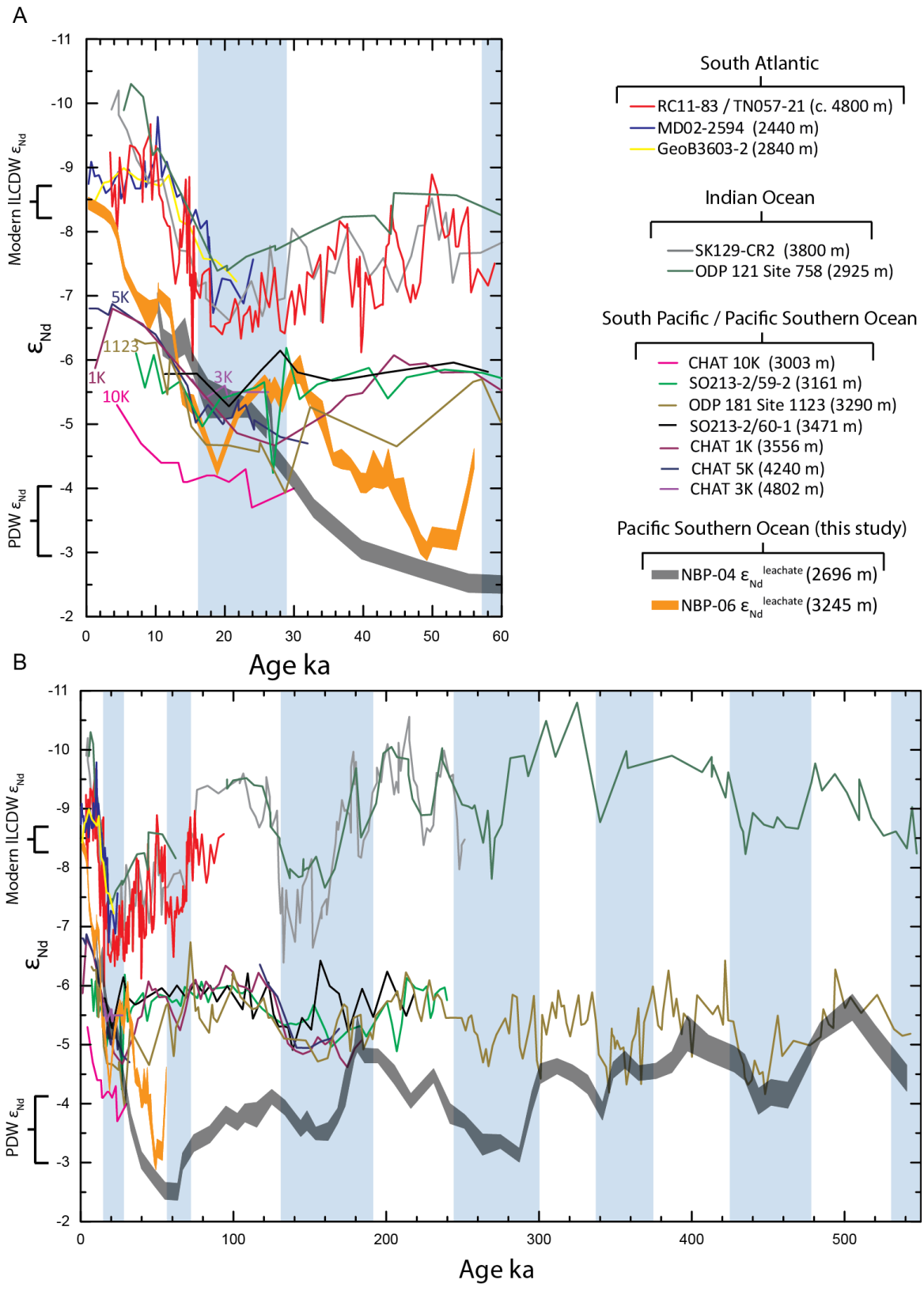

Fig. 5.9 Records of $\varepsilon_{Nd}^{palaeoSW}$ from the South Atlantic, Indian, Pacific and SO. Location of core sites is shown in Fig. 5.8. CHAT and Ocean Drilling Program (ODP) core sites located off Chatham Rise (New Zealand) are individually labelled in A. References given in Fig. 5.8

There is evidence for increased supply of PDW to the Pacific SO during the last glacial period, which could perhaps explain $\varepsilon_{Nd}^{palaeoSW}$ values less radiogenic than -3 recorded at sites NBP-04 and NBP-06: a suite of ε_{Nd} records measured on planktic foraminifera in eight cores located on the Campbell Plateau, Chatham Rise and in the South Fiji Basin around New Zealand in the SW Pacific record LGM $\varepsilon_{Nd}^{palaeoSW}$ values -3.5 and -6, values that are 0.3 to 1.8 more radiogenic than late Holocene values (Elderfield et al., 2012; Hu et al., 2016a; Noble et al., 2013), apparently illustrating a greater influence of PDW at these core sites during the LGM. Radiocarbon evidence from nine core sites located in the same area off New Zealand, and one record from the central Pacific sector of the Southern Ocean (site PS75/059-2; 54°12'54"S, 125° 25' 31.8"W) suggest that between 15 to 24 ka, PDW entered the South Pacific Basin between New Zealand and the East Pacific Rise at a depth of 2,500 to 3,600 m., penetrating the ACC as far as 54°S (Ronge et al., 2016; Sikes et al., 2016, 2000; Skinner et al., 2015). At the same time as this incursion of PDW into the Pacific sector of the SO occurred, radiogenic $\varepsilon_{Nd}^{palaeoSW}$ values of up to -4.30±0.1 are recorded at site NBP-06 (18.90±0.25 ka, see Fig. 5.10). However, for the radiogenic $\varepsilon_{Nd}^{palaeoSW}$ at sites NBP-04 and NBP-06 to be influenced by waters sourced in the Pacific Ocean, PDW would have to have penetrated the clockwise-flowing ACC as far South as 65°S, and remained unmodified by mixing with circumpolar water masses. $\varepsilon_{Nd}^{palaeoSW}$ records from sites located in the SW Pacific off the east coast of New Zealand, and the central Pacific SO on the East Pacific Rise (Fig. 5.8) do show consistently more radiogenic $\varepsilon_{Nd}^{palaeoSW}$ values during glacial periods of the last 550 ka; however, there is no evidence for pure, unmodified PDW reaching these core sites at any point during this time (Fig. 5.9). It therefore seems unlikely that PDW can explain the radiogenic $\varepsilon_{Nd}^{palaeoSW}$ values recorded at sites NBP-06 and NBP-04.

5.4.2.2 Ross Sea Bottom Water

An alternative hypothesis to account for the past radiogenic $\varepsilon_{Nd}^{palaeoSW}$ values recorded at sites NBP-04 and NBP-06 is that both sites were bathed in Ross Sea Bottom Water (RSBW) or lLCDW with more radiogenic ε_{Nd} values than modern deep and bottom waters in this region. Modern bottom water $\varepsilon_{Nd}^{seawater}$ measured by Rickli et al. (2014) at station 116-1 (72°37'S, 164°05'W, 4200 m. water depth, 2 m. from sea bed; Fig. 5.10) only reaches values as radiogenic as -6.55±0.14. Although this represents modified RSBW (mixed with CDW; $\varepsilon_{Nd}^{seawater}$ c. -8.66 to -7.92 at this location, Rickli et al. (2014)), with the modern RSBW end-member therefore being more radiogenic, past RSBW would have to be approximately 3-3.5 epsilon units more radiogenic than modern RSBW to equal the most radiogenic $\varepsilon_{Nd}^{palaeoSW}$ values recorded at sites NBP-04 and NBP-06. If past deep and bottom waters bathing sites NBP-04 and NBP-06 are sourced in the Ross Sea, the fact that RSBW does not significantly

contribute to deep waters north of the Pacific-Antarctic Ridge axis today also implies a greater volume of RSBW filling the deep western Pacific SO in the past, most likely due to an expansion in the production of RSBW.

At present the main region of deep and bottom water formation in the Ross Sea Embayment is located in the western Ross Sea, in Terra Nova Bay (Orsi and Wiederwohl, 2009) (TN in Fig. 5.10). Here, brine rejection during sea ice formation within the Terra Nova Polynya (at c. 75°S, 165°E) converts CDW, Antarctic Surface Water (AASW) and thermocline waters into dense Shelf Water (SW) and dense modified CDW (MCDW), the result of diapycnal mixing between AASW and CDW. The main sources of this SW and MDW are CDW, which enter the Ross Sea Embayment in the east via the clock-wise flowing Ross Gyre. SW is the densest water mass found in the SO, and pools within the Joides and Drygalski troughs in the western Ross Sea Embayment (JT and DT in Fig 5.10), where it constantly mixes with the warmer overlying MCDW to form Modified Shelf Water (MSW), before episodically flowing out across the shelf break to the north as RSBW (Budillon et al., 2002; Gordon et al., 2015; Orsi and Wiederwohl, 2009). A second, smaller region of bottom water production occurs along the front of the Ross Ice Shelf at around 170°E to 178°E, in the Ross Ice Shelf Polynya, where High Salinity Shelf Water (HSSW) produced via brine rejection mixes with Ice Shelf Water (ISW) which has circulated beneath the floating ice shelf and entrained super cooled fresh water from basal melting of the ice shelf (Fig. 5.10).

In the following sections (5.4.2.3 and 5.4.2.4) I will explore the evidence for changes in the $\varepsilon_{Nd}{}^{palaoeSW}$ composition of RSBW linked to i) the availability of radiogenic sediments which, through boundary exchange processes within the Ross Sea Embayment, alter the ε_{Nd} composition of RSBW, and ii) possible changes in the formation regions of RSBW. In section 5.4.3 I will then discuss possible scenarios of RSBW formation which could explain the changes in $\varepsilon_{Nd}{}^{palaeoSW}$ bathing core sites NBP-04 and NBP-06 during the last 540 ka. In section 5.4.4 I will then focus on changes in RSBW production and deep water circulation in the western Pacific SO during the last 55 ka, as recorded at site NBP-06.

5.4.2.3 Past and present sources of radiogenic Nd in the Ross Sea

The geology of the western Ross Sea includes exposures of the McMurdo Volcanic Group (MVG, see Fig. 5.10), comprising basanites to trachybasalts with strongly radiogenic ε_{Nd} values, with onshore exposure ε_{Nd} values between +4.3 to +5.8 (Futa and Le Masurier, 1983; Kyle et al., 1990; Lee et al., 2015b; Nardini et al., 2009; Rocchi et al., 2002; Rocholl et al., 1995; Wegner et al., 2011). Offshore dredging in the south-western Ross Sea has provided samples from the MVG (DR1 and DR2-4, Fig. 5.10) with ε_{Nd} values of +5.0 to +6.5 (Lee et al., 2015b), while dust samples collected from sea ice in McMurdo Sound (see Fig. 5.10)

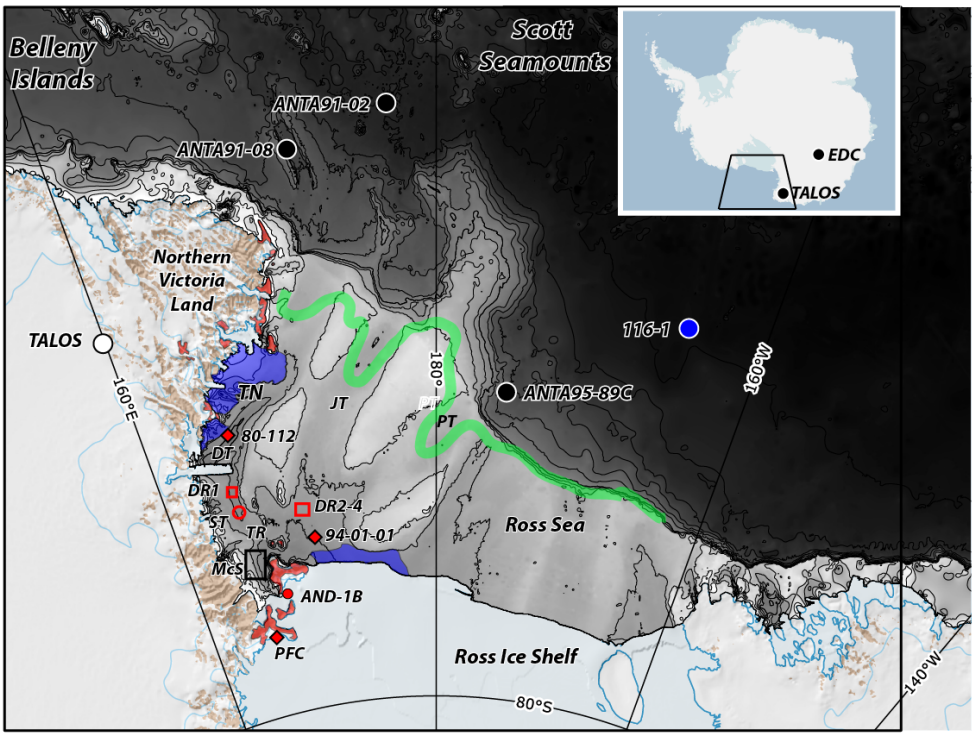

Fig. 5.10 Map of the Ross Sea Embayment showing location of modern deep water formation in Terra Nova Bay (TN, in the region of the Joides, Drygalski and Pennel troughs, JT, DT and PT), and in front of the Ross Ice Shelf (blue shading) alongside exposures of the McMurdo Volcanic Group (MVG, red shading) and the location of Terror Rift (TR). Study locations of till deposits from the last glacial period (red diamonds, Lang Farmer et al. (2006); Licht et al. (2005)), marine sediments and aeolian dust in the McMurdo Sound (McS, black open square, Glasby et al. (1975); Winton et al. (2016)), sediment trap data (ST, red open cycle, Winton et al. (2016)), rock dredges (DR1-4, red open squares, Lee et al. (2015a)), ANDRILL McMurdro Ice Shelf Project site 1B (filled red dot AND-1B, Monien et al. (2012); Naish et al. (2009)) marine sediment cores showing evidence for presence of polynyas during the last glacial period (black dots, Bonaccorsi et al. (2007); Quaia and Cespuglio (2000); Smith et al. (2010)), the location of the TALSO Dome ice core (white dot, Stenni et al. (2002)) and sampling station for seawater chemistry (blue dot, Rickli et al. (2014)) are also shown. The reconstructed position of the grounding line of the Ross Ice Sheet at its maximum extent during the last glacial period is illustrated by the green line (Halberstadt et al., 2016).The loation of the Talos Dome (TALOS) and EPICA Dome C (EDC; Augustin et al. (2004) ice cores are shown in the inset map

mainly possess ε_{Nd} values between -0.94 to +3.45, sourced from the MVG (Winton et al., 2016). Marine sediments deposited close to the MVG in McMurdo Sound consist of coarse,

poorly sorted muddy sands containing a large sediment fraction derived from the surrounding MVG (Glasby et al., 1975), while a sediment trap located in the SW Ross Sea (ST in Fig. 5.10) deployed at 200 m. water depth (630 m. above the sea floor) between December 1997-January 1998 collected bulk sediments with ε_{Nd} values of +3.9 (Winton et al., 2016). Lithogenic Fe fluxes measured on a suite of sediment traps close by (between 165°E to 175°W at c. 76°S) show Fe concentrations increase with increasing water depths, suggesting remobilisation and lateral transport of MVG sediments within the water column (Collier et al., 2000).

The composition of glacimarine sediments deposited at the ANDRILL McMurdro Ice Shelf Project site 1B (site AND-1B in Fig. 5.10) suggests an increase in the proportion of eroded MVG sediments to this site during glacial periods of the late Pliocene and Pleistocene, probably due to the overtopping of MVG outcrops south of Ross Island – which are today subaerially exposed – by glacial ice (Monien et al., 2012). This increased erosion and subsequent deposition is corroborated by the radiogenic ε_{Nd} of tills deposited during the LGM in the western Ross Sea (sites 80-112 and 94-01; <63 μm fraction ε_{Nd} = -3.76 and -6.94, and -4.64 respectively, see Fig. 5.10) and in onshore deposits adjacent to McMurdo Sound (Pyramid Fuel Cache, PFC in Fig. 5.10; <63 μm fraction ε_{Nd}Nd = +1.54) (Lang Farmer et al., 2006), and by observations of increased proportions of basaltic sands and rock fragments within LGM till deposits in the western vs central Ross Sea (Licht et al., 2005).

The evidence presented above demonstrates that MVG rocks and sediments with a strongly radiogenic ε_{Nd} signature (ε_{Nd} = -0.94 to +6.5) are today being eroded and deposited within the SW Ross Sea. Although there are no ε_{Nd} data measured on seawater from within the Ross Sea itself, it is most likely these radiogenic sediments which impart RSBW precursor water masses (i.e. SW and MSW) with the radiogenic the ε_{Nd} values observed in RSBW offshore of the Ross Sea today (Basak et al., 2015; Rickli et al., 2014). Data from LGM till deposits suggest a continued, and most likely increased, contribution of MVG sediments to the western Ross Sea region during past glacial periods. This evidence all points towards a source of MVG sediments for RSBW, which may have isotopically 'labelled' RSBW with a strongly radiogenic ε_{Nd} signature in the past.

5.4.2.4 Past regions of RSBW formation

The ability of MVG rocks to imprint RSBW with a radiogenic ε_{Nd} signature is determined not only by the supply of radiogenic sediments, but also by the location of RSBW production, i.e. the proximity of RSBW formation sites to these sediments. Changes in the region of RSBW formation could therefore lead to more/less radiogenic ε_{Nd} signature.

The location of past deep and bottom water formation in the Ross Sea Embayment was likely closely linked to the past extent of grounded ice. During the LGM, the grounding line of the Ross Ice Sheet extended north, beyond modern regions of deep water formation on the Ross Sea continental shelf (Fig. 5.10), shifting the locus of bottom water production north of its present location. A candidate for the location of bottom water formation during the last glacial period is the northwestern Ross Sea shelf, which remained free of grounded ice even during the LGM, allowing for the formation of ISW beneath the ice shelf which presumably existed in this area (Licht et al., 1996; McKay et al., 2008). Two sediment cores recovered from the western Ross Sea continental slope (ANT91-08 and ANTA91-02, Fig. 5.10) contain planktic foraminifera-bearing sediment layers enriched in ice-rafted debris (IRD) and interpreted as identifying the presence of polynyas above these core sites at that time (Bonaccorsi et al., 2007; Smith et al., 2010). The organic matter from sediment horizons sandwiching these layers was radiocarbon dated to between 26.0 and 14.4 cal. Ka (Bonaccorsi et al., 2007; Quaia and Cespuglio, 2000), but ^{14}C dating of organic matter in Antarctic shelf sediments is problematic because of contamination with reworked fossil organic material (e.g. Domack et al. (1999a); Licht et al. (1998). A third sediment core recovered from the eastern central region of the Ross Sea continental slope (ANT95-89C) contains very similar foraminifera-bearing, IRD-rich layers (Bonaccorsi et al., 2007). Reliable radiocarbon dates obtained from calcareous foraminifera shells of these layers indicate that the layers were deposited between 32.2 and 19.1 cal. ka (Bonaccorsi et al., 2007; Smith et al., 2010), documenting the presence of coastal polynyas above the Ross Sea continental slope during MIS 2 and latest MIS 3. These polynyas would provide a mechanism for the production of HSSW, close to the location of super-cooled, but less saline, ISW sourced from below the Ross Ice Shelf, possibly suitable conditions for RSBW formation.

Given the evidence for highly radiogenic ε_{Nd} sediment input to the likely regions of glacial-time RSBW production in the Ross Sea Embayment, RSBW is a plausible candidate for the source of the highly radiogenic $\varepsilon_{Nd}^{palaeoSW}$ signature recorded at sites NBP-04 and NBP-06 during the last glacial period.

5.4.3 Changes in Bottom Water production in the Ross Sea over the last 540 ka

The timing of the radiogenic peak in ε_{Nd} of bottom waters bathing sites NBP-04 and NBP-06 during the last glacial period between 49.21$\pm$0.10 ka and 63.55$\pm$0.34 ka would indicate that this time interval represents the peak in bottom water production in the Ross Sea during the last glacial period, and/or a shift in the $\varepsilon_{Nd}^{palaeoSW}$ value of RSBW towards a more

radiogenic end member. The location – and the mechanism – of the production of pre-cursor water masses for RSBW in the Ross Sea Embayment is likely to be crucial to both these factors. Based on the timing of export of RSBW with radiogenic $\varepsilon_{Nd}^{palaeoSW}$ values to sites NBP-04 and NBP-06, three regimes of bottom water production in the Ross Sea are proposed here.

In the 'modern interglacial' regime, SW and MSW are mostly formed due to winter buoyancy loss from AASW and MCDW in the western Ross Sea, in the region of Terra Nova Bay (Orsi and Wiederwohl, 2009). The precursor waters for this these water mass for MCDW ultimately derived from CDW which flows onto the Ross Sea shelf to the east, which above the central Ross Sea continental slope has $\varepsilon_{Nd}^{seawater}$ values of between -8.66 to -7.92 (1400 m. to 2800 m. water depth, Rickli et al. (2014) station 116-1), while AASW in this region has $\varepsilon_{Nd}^{seawater}$ values of -8.82 to -8.84 (10 m to 100 m. water depth, Rickli et al. (2014) station 116-1). The dense MCDW and SW which result from deep water formation in Terra Nova Bay pool within the troughs of the western Ross Sea, where the presence of MVG sediments with radiogenic ε_{Nd} values lead to modification of the $\varepsilon_{Nd}^{seawater}$ value bottom waters via boundary exchange. Further mixing occurs between CDW, MCDW and SW, leading to MSW which is eventually exported across sills at the continental shelf edge as RSBW (Orsi and Wiederwohl, 2009).

The second regime of bottom water production occurs during 'peak glacial' conditions, as exemplified by conditions during the LGM, when grounded ice extended across much of the Ross Sea continental shelf, reaching the shelf edge in the central and eastern Ross Sea (green line in Fig. 5.10 Under this scenario, production of super cooled ISW continues under the floating ice shelf which presumably existed in the NW Ross Sea (Licht et al., 1996; McKay et al., 2008), which remained free of grounded ice. It has been demonstrated that erosion and transport of MVG-derived glacial sediments to the grounding line likely continued, or even increased, at the LGM, and provided a source for the radiogenic ε_{Nd} signature to the ISW. The presence of polynyas over the Ross Sea continental slope likely led to bottom water production via sea-ice formation in this region, as occurs today in Terra Nova Bay and at sites along the Adelie and George V Land coasts (Williams et al., 2010). It is unlikely that bottom waters produced in these polynyas would possess significantly more radiogenic $\varepsilon_{Nd}^{palaeoSW}$ values than CDW at that time, as they were not forming in close proximity to radiogenic MVG sediments. Mixing between ISW, which presumably would have had a radiogenic $\varepsilon_{Nd}^{palaeoSW}$ signature due to its proximity to MVG sediments, and bottom waters produced along the continental slope with a less radiogenic $\varepsilon_{Nd}^{leachate}$ signature, would still result in the export of RSBW with $\varepsilon_{Nd}^{leachate}$ values more radiogenic than CDW at that time.

The third proposed regime of RSBW production is an 'intermediate glacial' scenario that occurred during the transition from interglacial to full glacial conditions. Advance of the Ross Ice Sheet and the Ross Ice Shelf during the onset of glaciation led to a continued production of ISW, however the location of HSSW production would shift to the north of Terra Nova Bay, towards the MVG outcrops located in northern Victoria Land (Fig. 5.10). In section 5.4.2.3 I presented evidence that a large proportion of marine sediments deposited within McMurdo Sound, which is located in close proximity to MVG outcrops, comprises volcanogenic detritus with very radiogenic ε_{Nd} values. It therefore seems likely that marine sediments eroded and deposited off the eastern coast of northern Victoria Land – the location of many MVG outcrops (Fig. 5.10) – are similarly enriched in volcanogenic detritus. The potential for increased erosion and deposition of MVG-derived sediments during past glacial periods, coupled with a more northerly formation region of RSBW precursor water masses within the Ross Sea, closer to MVG sources in northern Victoria Land, would lead to RSBW with more radiogenic $\varepsilon_{Nd}{}^{palaeoSW}$ values than observed in both the modern and glacial regimes.

Although the position of the maximum extent of grounded ice in the Ross Sea during the LGM, and the timing of its retreat, is reasonably well constrained (see Anderson et al. (2014) and Halberstadt et al. (2016) for recent reviews), the timing of ice sheet advance during the inception of the last glacial period, and the ice-sheet extent during previous glacial and interglacial periods, is not well known (Naish et al., 2009). Nonetheless, there is some evidence supporting the three proposed scenarios. A comparison between the $\varepsilon_{Nd}{}^{palaeoSW}$ recorded at sites NBP-04 and NBP-06 and a model of Antarctic ice volume changes during the climatic cycles of the Quaternary and Pliocene (Pollard and DeConto, 2009; Pollard and Deconto, 2012) shows that peaks in radiogenic $\varepsilon_{Nd}{}^{leachate}$ values at these core sites coincide with periods of increasing Antarctic ice volume (blue shading in Fig 5.11), with trends towards more radiogenic $\varepsilon_{Nd}{}^{leachate}$ values during periods of ice sheet advance (arrows in Fig. 5.11) as proposed in the scenario for the 'intermediate' regime of RSBW formation. This scenario appears to occur during periods of ice expansion during the transition from interglacial to full glacial conditions, but does not appear to be prevalent during glacial terminations: This may be a result of the saw-tooth pattern of ice expansion (which may occur over tens of thousands of years) and retreat (which may occur much more rapidly).

Evidence for rapid deglacial retreat of ice in the western Ross Sea is observed in the well preserved mega-scale glacial lineations located in the Drygalski Trough which have not been overprinted by ice-marginal deposits, suggesting rapid detachment of grounded ice from the seafloor followed by a rapid retreat. However, deposition of recessional geomorphological features suggest deglaciation was more of a step-wise process in the JOIDES and Pennell

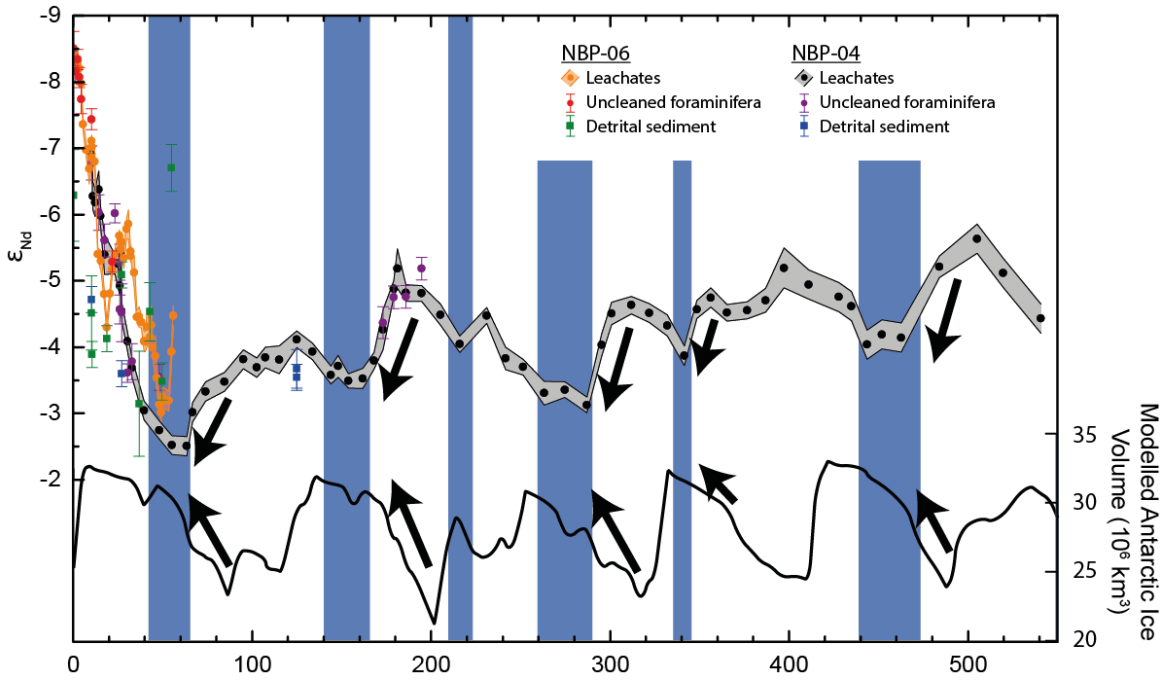

Fig. 5.11 ε_{Nd} records from sites NBP-04 and NBP-06 suggest peaks in radiogenic $\varepsilon_{Nd}^{palaeoSW}$ bathing these core sites coincide with periods of modelled increases in Antarctic ice volume (Pollard and DeConto, 2009; Pollard and Deconto, 2012). Peaks in $\varepsilon_{Nd}^{palaeoSW}$ tend to occur within glacial intervals prior to maximum ice extent (blue shading). Periods of increasing ice volume around Antarctica coincide with trends towards more radiogenic $\varepsilon_{Nd}^{palaoeSW}$ (arrows).

Troughs (Halberstadt et al., 2016). The lack of recessional geomorphological features, along with the presence of mega-scale glacial lineations suggest detachment and retreat of grounded ice during deglaciation occurred rapidly in the eastern Ross Sea Embayment, punctuated by grounding line stabilisation and the development of grounding zone wedges (Bart and Cone, 2012). The sediment core drilled at site ANDRILL AND-1b in McMurdo Sound showed that, in general, the phases of ice sheet and ice shelf advance and retreat over the last 5 Ma as predicted in the model by Pollard and DeConto (2009); Pollard and Deconto (2012) are matched by corresponding facies changes (Naish et al., 2009). Clearly the interplay between the availability of sediment with radiogenic ε_{Nd} values, extent of grounded and floating ice, the location of the formation of precursor water masses for RSBW and the volume of RSBW export from the Ross Sea is more complex than given in the three scenarios outlined above. However, it seems that the long-term variations in RSBW $\varepsilon_{Nd}^{palaeoSW}$ reaching sites NBP-04 and NBP-06 can, at least in part, be explained by these simplified scenarios.

To further investigate the relationship between ice sheet and ice shelf extent, RSBW production, and changes in the end-member $\varepsilon_{Nd}^{palaeoSW}$ values of RSBW, further work is

needed to better characterise the modern seawater ε_{Nd} values of the precursor water masses to RSBW, and to better constrain the position of grounded and floating ice within the Ross Sea during the past. A better understanding of the history of erosion and transport of MVG-derived detritus within the Ross Sea Embayment and studies of the magmatic history of MVG within the Ross Sea are required (i.e. both eruptive volcanism and the generation and advection of any hydrothermal fluids within the Ross Sea embayment). In particular, a better understanding of the eruptive history of the MVG submarine volcanoes which are known from the Ross Sea shelf and may have implications for the deposition of lithologies with radiogenic ε_{Nd} values proximal to regions of deep water formation: To date at least three magmatic episodes of the MVG have been identified, including submarine volcanism with extremely radiogenic ε_{Nd} values (ε_{Nd} = +5.0 to +6.5) within the Terror Rift region between 460-570 ka (Lee et al., 2015a). More work is also required to better constrain the past ε_{Nd} of CDW and AASW as they flow into the Ross Sea Embayment, prior to modification via boundary exchange during production of RSBW: sediment cores around New Zealand and the East Pacific Rise (Fig. 5.9) all show an increased contribution from a radiogenic $\varepsilon_{Nd}{}^{palaeoSW}$ source during the last glacial period, in part due to reduced inflow of deep waters from the North Atlantic region to the SO and increased inflow of deep waters sourced in the Pacific basin. If CDW and AASW had more radiogenic $\varepsilon_{Nd}{}^{palaeoSW}$ values during past glacial periods, this would clearly influence the final $\varepsilon_{Nd}{}^{palaeoSW}$ value of RSBW.

5.4.4 Changes in deep water circulation and RSBW production in the SW Pacific Sector of the Southern Ocean during the last 55 ka.

Examining the $\varepsilon_{Nd}{}^{palaeoSW}$ of RSBW recorded at the higher resolution core site NBP-06 through the last glacial period and into the Holocene allows for a better understanding of the interplay between past circulation changes, ice sheet extent, and the production and $\varepsilon_{Nd}{}^{palaeoSW}$ of RSBW during this time period (Fig. 5.12).

5.4.4.1 55 to 33.5 ka: From 'Intermediate Glacial' towards 'Peak Glacial' RSBW production

The early phases of MIS 3 between c. 55.5–45.5 ka are characterised by relatively warm intervals during Antarctic Isotope Maxima (AIM) 12 and 14, when both pCO_2^{atm} and the $\delta^{18}O$ values of ice at the Talos Dome ice core (located in northern Victoria Land, 159°11'E 72°49'S; 2315 m. above sea level, see Fig. 5.10) were elevated (red shaded interval in Fig. 5.12). This time period also sees the most radiogenic $\varepsilon_{Nd}{}^{palaeoSW}$ values (-3.02±0.14 and -3.25±0.15) recorded at site NBP-06, consistent with the scenario of RSBW formation during

'intermediate glacial' conditions (section 5.4.3). This is followed by a lowering of pCO_2^{atm}, with a cooling and possible expansion of ice sheets and floating ice shelves, reflected in the decreasing $\delta^{18}O$ of the Talos Dome ice core between c. 45.5–33.5 ka (white period in Fig. 5.12). This cooling may have led to a gradual expansion of grounded and floating ice on the Ross Sea shelf, and a shift towards a more northerly production of RSBW, leading to a gradual change towards less radiogenic ${\varepsilon_{Nd}}^{palaeoSW}$ values at site NBP-06. This shift in ${\varepsilon_{Nd}}^{palaeoSW}$ values at site NBP-06 occurred either due to a reduction in RSBW production or a shift towards a less radiogenic ε_{Nd} end-member value of RSBW as the region of bottom water production shifted north of MVG outcrops in Northern Victoria Land: i.e. towards the 'peak glacial' scenario (section 5.4.3). Throughout the period of cooling between c. 45.5 and 33.5 ka, while bottom water ${\varepsilon_{Nd}}^{palaeoSW}$ recorded at site NBP-06 are shifting towards less radiogenic ε_{Nd} values, ${\varepsilon_{Nd}}^{palaeoSW}$ recorded at deep sites in the Cape Basin (TN057-21/RC11-83 composite record, Fig. 5.12) and in the Indian Ocean (SK129-CR2, Fig. 5.12), which during the last glacial period were bathed predominantly in SCW sourced in the Atlantic sector of the SO, are shifting towards more radiogenic values, reflecting the heterogeneity of deep water masses within the SO during this period.

Transient simulations of ocean circulation during MIS 3 suggest that the increase in pCO_2^{atm} recorded in Antarctic ice cores during the AIM 8 and 12 events (Fig. 5.12) are linked to increased production of AABW, which ultimately led to the increased ventilation of the deep Pacific, and a release of the remineralised carbon stored there (Menviel et al., 2015). A trend towards less radiogenic ${\varepsilon_{Nd}}^{palaeoSW}$ values recorded at site NBP-06 during AIM 12 and 8 suggests a gradual decrease in RSBW influence during this interval, which is inconsistent with this scenario. Assuming the 1.7 epsilon shift in ${\varepsilon_{Nd}}^{palaeoSW}$ towards more radiogenic values recorded at site NBP-06 between 56.03$\pm$0.06 ka and 53.47$\pm$0.10 ka reflects – at least in part – an increase in RSBW export to the core site, the mechanism proposed by Menviel et al. (2015) might account for some of the increase in pCO_2^{atm} during AIM 14. However, a transfer of carbon between the deep Pacific and the atmosphere related to increased RSBW production is also inconsistent with the gradual decrease in $\delta^{13}C^{atm}$ across AIM 14 (Fig. 5.12).

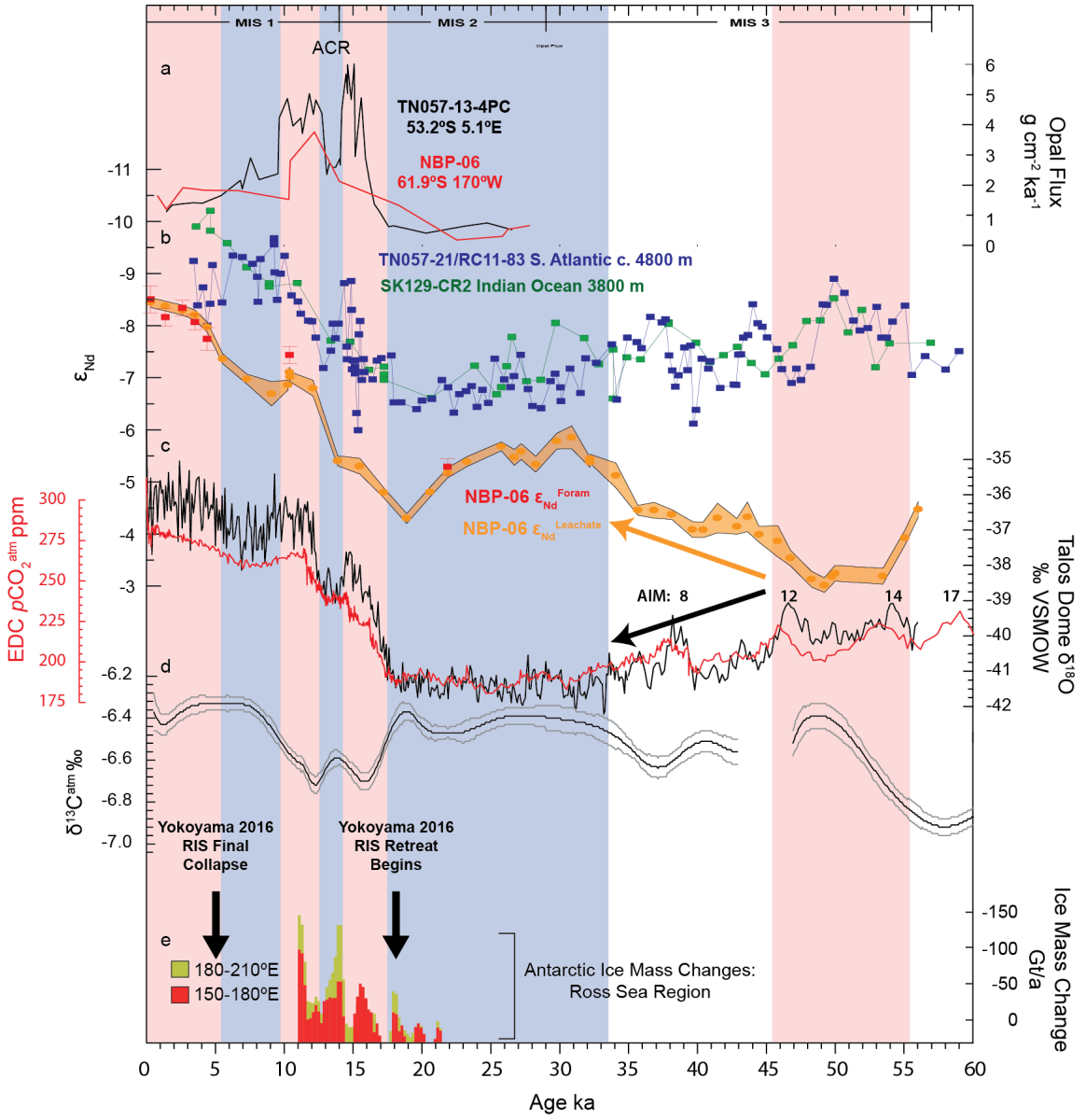

Fig. 5.12 a)Opal flux in the Atlantic (black, Anderson et al. (2009) and Pacific (red, Chase et al. (2003) sectors of the SO. b) $\varepsilon_{Nd}{}^{palaeoSW}$ in the deep South Atlantic (Piotrowski, 2005; Piotrowski et al., 2012), Indian Ocean (Piotrowski et al., 2009; Wilson et al., 2015a) and western Pacific sector of the SO (this study). c) $\delta^{18}O$ measured on ice from the Talos Dome ice core (Bazin et al., 2013) and atmospheric pCO_2 from the EPICA Dome C ice core (Augustin et al., 2004) (both locations shown in Fig. 5.10; records are on AICC2012 timescale of Bazin et al. (2013)). d) A composite record of atmospheric $\delta^{13}C$ from Antarctic ice cores (Eggleston et al., 2016). e) Modelled ice mass changes between 24 to 11 ka from the Ross Sea region of Antarctica (Golledge et al., 2014) with arrows denoting beginning of Ross Ice Shelf retreat (c. 18 ka) and collapse (c. 5 ka) according to Yokoyama et al. (2016). Red shading denotes periods of elevated $\delta^{18}O$ values (= warm phases) within the Talos Dome ice core, wihile blue shading illustrates relatively low $\delta^{18}O$ values (= cool phases).

5.4.4.2 33.5 to 13.9 ka : 'Peak Glacial' RSBW production

The cooling recorded in the Talos Dome ice core from c. 45.5 to 33.5 ka ended during late MIS 3, with full glacial conditions recorded in the Talos Dome δ^{18}O between c. 33.5 - 18 ka. Less radiogenic $\varepsilon_{Nd}{}^{palaeoSW}$ values are recorded at site NBP-06 during that time (blue shaded interval in Fig. 5.12), when compared to the preceding, relatively warm interval, suggesting the 'peak glacial' RSBW production scenario was operating at this time. The onset of 'peak glacial' RSBW production at c. 33.5 ka, is followed by the creation of ice-dammed lakes within the dry valleys of the Transantarctic Mountains (TAM), which document the thickening of ice within the TAM by c. 28.5 ka (Hall et al., 2015). The timing of maximum ice extent within the Ross Sea Embayment hinterland appears to have been asynchronous, with terrestrial evidence for the timing of maximum ice thicknesses at the head of outlet glaciers surrounding the western Ross Sea Embayment and McMurdo Sound suggesting maximum ice thicknesses were reached between 19-13 ka (Hall and Denton, 2000; Hall et al., 2015; Todd et al., 2010), and propagated up-glacier. This timing of maximum ice thickness in the Ross Sea hinterland between 19-13 ka is attributed to an increase in accumulation, leading to the build-up of ice despite rising temperatures (Members, 2013), while the earlier thickening of ice by c. 28.5 ka within the TAM suggests the grounding line of ice within the Ross Sea Embayment may have stabilised, buttressing outflow glaciers and allowing the build-up of ice prior to c. 28.5 ka.

An ice-proximal grounding zone wedge, which formed during a pause in ice sheet retreat on the eastern middle Ross Sea shelf during the last glacial period, contained foraminifera radiocarbon dated to c. 30.8 cal. ka BP (Bart and Cone, 2012), indicating that the maximum ice extent within the eastern Ross Sea Embayment reached its peak prior to this time, and had begun retreating by c. 31 ka. Radiocarbon measurements made on the acid insoluble organic (AIO) component of sediments and the identification of tephra layers in the western Ross Sea equatorward of c. 74°S suggest open marine conditions of the western outer shelf between 22-26 cal. ka BP (Licht et al., 1999, 1996), although another suite of AIO-dated deposits from the western Ross Sea Embayment suggest maximum ice extent occurred north of this between c. 26.5 to 19.5 cal. ka BP, with the grounding line retreating south of 74°S in the Drygalski Trough by c. 9.5 cal. ka BP. This discrepancy highlights the difficulty of obtaining reliable radiocarbon dates from the Antarctic continental shelf, which are low in carbonate material, often leading to a reliance on AIO radiocarbon dating, which is prone to reworking of old carbon (Andrews et al., 1999; Licht et al., 1998). A single radiocarbon date measured on foraminifera obtained from sediments located in the northern JOIDES Trough constrains the timing of ice shelf retreat and initiation of open marine conditions in this region as occurring prior to 18 ka (Yokoyama et al., 2016); arrow in Fig. 5.12), in

agreement with a modelled loss of ice volume from the Ross Sea region of Antarctica around c.18 ka (Fig. 5.12e) (Golledge et al., 2014). This coincides with a slight shift in $\varepsilon_{Nd}{}^{palaeoSW}$ values towards more radiogenic values, from -5.17±0.10 at 21.86±0.42 ka to -4.30±0.10 at 18.90±0.25 ka, perhaps reflecting a slight southward shift in the location of RSBW formation, or an increase in RSBW production at this time. However, this single date is in conflict with the findings of Hall et al. (2015), who date the greatest thickness of grounded ice in western Ross Sea to between 18.7 and 12.8 ka, based on radiocarbon analyses of terminal moraines from the hinterland surrounding McMcurdo sound, suggesting changes in ice shelf extent in northern JOIDES Trough at this time may have been localised rather than part of a larger retreat of ice shelves.

Aside from the radiogenic peak centred on c. 18 ka, $\varepsilon_{Nd}{}^{palaeoSW}$ values recorded at site NBP-06 between 33.5-13.9 ka were relatively stable, and RSBW production at this time can be attributed to the 'peak glacial' scenario throughout this interval. This is broadly in agreement with the reconstructed glacial history of the western Ross Sea Embayment, which indicate that although the extent of grounded and floating ice was variable through this period, with discrepancies in the timing of peak glacial conditions, the main portion of deglaciation followed the interval of 33.5-13.9 ka.

At c. 18 ka, $\varepsilon_{Nd}{}^{palaeoSW}$ values recorded at site NBP-06 shifted slightly towards less radiogenic values, from -4.30±0.10 at 18.90±0.25 ka, to -5.30±0.15 at 15.48±0.27 ka, and remained unchanged until 13.88±0.44 ka. During this period, the deep South Atlantic and Indian Ocean experienced rapid fluctuations in $\varepsilon_{Nd}{}^{palaeoSW}$ values (Fig 5.12b), due to changes in the relative contribution of northern Atlantic-sourced waters with a less radiogenic ε_{Nd} signature vs SO-sourced deep waters with a more radiogenic ε_{Nd} signature. The first shift towards less radiogenic (North Atlantic sourced) values in the Cape Basin occurred at 17.78 ka (a shift of 0.90 epsilon units within the TN057-21/RC11-83 composite record of Fig. 5.12b), and was followed by a rapid shift of 1.84 epsilon units towards more radiogenic (SO sourced) values following a reduction in Atlantic Meridional Overturning Circulation (AMOC) during Heinrich Stadial 1 at c. 16 ka. Heinrich Stadial 1 was followed by a shift towards less radiogenic $\varepsilon_{Nd}{}^{palaeoSW}$ values at the onset of the Bølling-Allerød at 14.87 ka in the TN057-21/RC11-83 composite record (a shift of 1.70 epsilon units, Fig. 5.12). These events coincided with an early breakdown in the stratification of the deep Atlantic, which led to an increase in primary productivity within the SO, due to upwelling of old, nutrient rich water masses (e.g. the increase in opal flux at site TN057-13-4C in Fig. 5.12a) (Anderson et al., 2009), and also a drop in atmospheric $\delta^{13}C$ (Fig. 5.12). These events also coincided with an increase in IRD deposition within 'Iceberg Alley' in the Scotia Sea, attributed by Weber et al. (2014) to an increase in iceberg calving around Antarctica. However, the lack

of variability in $\varepsilon_{Nd}^{palaeoSW}$ at site NBP-06 suggests that the early deglacial breakdown in Atlantic Ocean stratification did not impact the deep water circulation in the western Pacific sector of the SO, and any instabilities in grounded ice or ice shelves in the Ross Sea region during that time interval did not lead to a modification in RSBW production or its $\varepsilon_{Nd}^{palaeoSW}$.

The adjustment of the age model of core NBP-06 from that previously published by Chase et al. (2003) performed as part of this thesis impacts the timing of increased opal fluxes at NBP-06, such that the peak in opal flux to the sediments of NBP-06 now occurs at c.12.2 ka, rather than 16 ka as proposed previously. This has important implications for the findings of Anderson et al. (2009), who claim that the increase in opal flux identified in the Atlantic SO between 15.6 and 14.5 ka (exemplified by core TN057-13-4 PC in Fig. 5.12) and attributed to increased upwelling, is circum-Antarctic, which may not in fact be the case. However, it could equally be the case that the opal flux record of NBP-06 is unable to resolve this early peak in opal deposition, as there is a gap in sampling between 18.3 and 14 ka (Fig. 5.12; the opal record of NBP-06 in this figure has been recalculated based in the updated chronology for NBP-06 presented in this thesis).

5.4.4.3 13.9to 0 ka: Onset of 'Modern Interglacial' RSBW production

A shift in $\varepsilon_{Nd}^{palaeoSW}$ values at site NBP-06 of 0.80 epsilon units towards less radiogenic values occurred between 13.88±0.44 ka and 12.10±0.44 ka, during the Antarctic Cold Reversal (ACR, Fig. 5.12). Despite this time interval being a period of cooling in Antarctica, elevation changes reconstructed from the Patriot Hills blue ice area in the Weddell Sea region of the West Antarctic Ice Sheet suggest significant thinning of c. 600 m. across the ACR in this region (Fogwill et al., 2017). Model simulations further suggest the ice mass loss during the ACR was possibly Antarctic-wide and also affected the Ross Sea region (Fogwill et al. (2017), Fig. 5.12e). The shift towards less radiogenic $\varepsilon_{Nd}^{palaeoSW}$ values recorded at site NBP-06 during the ACR may reflect a rapid retreat of both grounded and floating ice within the western Ross Sea Embayment, leading to a shift in RSBW formation towards its modern day position. This is in agreement with terrestrial evidence for ice sheet retreat from radiocarbon dating of terminal moraines in the region of McMurdo Sound at c.12.7 cal. ka BP (Hall et al., 2015, 2013) and ^{10}Be exposure dating suggesting thinning of ice south of McMurdo Sound from c. 14 ka onwards, and accelerating between 10.3 and 8.3 ka (Anderson et al., 2017). This terrestrial evidence is also in agreement with marine geological evidence for the presence of floating ice shelves in the region of the outer Drygalski Trough by least 11 ka, and for the retreat of these ice shelves by 9.5 ka (Domack et al., 1999b), as well as evidence that the Ross Ice Shelf reached its current position around McMurdo Sound

by c. 7 ka (Licht et al., 1996). McKay et al. (2016) suggest the retreat of ice sheets and initiation of open marine conditions to the east of Ross Island occurred by 8.6 cal. ka BP, as indicated by radiocarbon dating of benthic and planktic foraminifera, although radiocarbon dating of raised beaches suggests the retreat of grounded ice from Terra Nova Bay occurred no earlier than c. 7.2 cal. ka BP (Hall et al., 2004).

$\varepsilon_{Nd}{}^{palaeoSW}$ values recorded at site NBP-06 remained largely unchanged during the early to mid-Holocene (11.7–5.5 ka), with $\varepsilon_{Nd}{}^{palaeoSW}$ values at site NBP-06 varying between -6.69±0.23 and -7.36±0.10 throughout this interval (Fig 5.12). This was followed by a rapid shift from -7.36±0.10 to -8.20±0.10 between 5.5±0.30 and 3.53±0.09 ka. This shift indicates a change in bottom water formation in the Ross Sea from the mid to late Holocene, to the 'modern interglacial' scenario (section 5.4.3) with little or no advection of RSBW to site NBP-06 after this time. The timing of this change suggests the final retreat of ice within the Ross Sea towards its modern location occurred sometime between c. 5.5 to 3.5 ka. According toYokoyama et al. (2016), the final breakup of the Ross Ice Shelf occurred after the main retreat of grounded ice, between c. 5 and 1.5 ka, and saw ice shelves retreat across an area of c. 280,000 km^2. The initiation of this disintegration of the Ross Ice Shelf coincides with the change in bottom water formation occurring in the Ross Sea in the mid- to late-Holocene, as inferred by the $\varepsilon_{Nd}{}^{palaeoSW}$ record of NBP-06, and resulted in a reduction in RSBW export to the core site. However, the timing of ice shelf retreat identified by Yokoyama et al. (2016) is in conflict with the findings of McKay et al. (2016), who date the onset of open marine conditions to the east of Ross Island to before c. 8.6 cal. ka BP. $\varepsilon_{Nd}{}^{palaeoSW}$ values at site NBP-06 remained between -8.44±0.10 and -8.20±0.10 since 3.53±0.09 ka: assuming that the production in RSBW is linked to the extent of ice shelves within the Ross Sea Embayment, the low RSBW production during the last 5 ka would suggest the current extent of the Ross Ice Shelf is smaller than at any point during the last 550 ka.

5.5 Conclusions

In this chapter, I have presented ε_{Nd} records measured on the detrital sediments, uncleaned foraminifera and leachates of the <125 μm sediment size fraction of the two marine sediment cores NBP-04 and NBP-06 located at 2696 m. and 3245 m. water depths on the Pacific-Antarctic Ridge in the western Pacific sector of the SO. Recent (0.38±0.16 ka) $\varepsilon_{Nd}{}^{leachate}$ (-8.44±0.10) and $\varepsilon_{Nd}{}^{foram}$ (-8.50±0.26) values measured on core NBP-06 are in very good agreement with modern $\varepsilon_{Nd}{}^{leachate}$ values of lLCDW measured close to the core site (-8.2 to -8.4, (Basak et al., 2015). $\varepsilon_{Nd}{}^{leachate}$ and $\varepsilon_{Nd}{}^{foram}$ are in very good agreement (R^2= 0.96) with one another at both core sites, giving confidence that Fe-Mn phases in authigenic coatings of

both foraminifera and terrigenous sedimentary particles are recording the same ε_{Nd} signature. Comparisons between $\varepsilon_{Nd}{}^{leachate}$ and $\varepsilon_{Nd}{}^{detrital}$ of terrigenous particles ($R^2 = 0.16$) suggest no contamination of $\varepsilon_{Nd}{}^{leachate}$ via leaching of detrital sediment at either core site. REE profiles measured on leachate samples at both core sites show that the $\varepsilon_{Nd}{}^{leachate}$ is recording $\varepsilon_{Nd}{}^{palaeoSW}$, and rule out any contamination from local hydrothermal Nd.

Between c. 5 ka and 550 ka, $\varepsilon_{Nd}{}^{palaeoSW}$ at sites NBP-04 and NBP-06 both record a contribution of bottom waters sourced in the Ross Sea (RSBW) to the core sites, with characteristically radiogenic $\varepsilon_{Nd}{}^{palaeoSW}$ values. The end member $\varepsilon_{Nd}{}^{palaeoSW}$ value of RSBW – and most likely the contribution of RSBW to bottom waters at sites NBP-04 and NBP-06 – has fluctuated in the past, with the timing of these fluctuations linked to the extent of grounded and floating ice on the Ross Sea continental shelf, the region of RSBW formation, and the supply of lithogenic sediments with strongly radiogenic ε_{Nd} signature to the location of RSBW formation. During periods when grounded ice was located north of its current location, but prior to peak glacial conditions, production of RSBW with a radiogenic ε_{Nd} signature was at its maximum and characterised by $\varepsilon_{Nd}{}^{palaeoSW}$ values more radiogenic than modern RSBW (modern $\varepsilon_{Nd}{}^{seawater}$ = c. -6.5, Rickli et al. (2014), at times up to c. -2.5. Throughout periods of maximum grounded ice extent within the Ross Sea (i.e. during peak glacial conditions), production of RSBW with a radiogenic signature was curtailed relative to the intervening periods of intermediate ice extent, but still greater than today. RSBW export to sites NBP-04 and NBP-06 – and therefore by inference the production of RSBW – is less today than at any point over the last 550 ka. The drop in RSBW advection to these core sites followed the final breakup of the Ross Ice Shelf during the late Holocene at c. 5 ka, which suggests the current ice-shelf cover within the Ross Sea Embayment is at its minimum during the last 540 ka, although the timing of the final breakup of the Ross Ice Shelf following the LGM is still debated.

The possibility of changes in production rate and $\varepsilon_{Nd}{}^{palaeoSW}$ values of bottom waters formed in the Ross Sea over the last 550 ka must be taken into account when interpreting ε_{Nd} records of bottom water palaeocirculation the Pacific sector of the SO. Records of past $\varepsilon_{Nd}{}^{palaeoSW}$ of CDW from depths <4240 m. water depth located at Chatham Rise (CHAT 10k, Ocean Drilling Program Leg 181 Site 1123, CHAT 1k and CHAT 5K) and the southern East Pacific Rise (SO213-2/59-2 and SO213-2/60-1) do not show radiogenic peaks in $\varepsilon_{Nd}{}^{palaeoSW}$ values coinciding with those observed at sites NBP-04 and NBP-06, and are instead consistent with an interpretation of variable mixing between Pacific- and Atlantic-derived deep waters, and any contribution of bottom waters sourced in the Ross Sea are minimal (Fig. 5.9). However, future studies of $\varepsilon_{Nd}{}^{palaeoSW}$ from core sites located in the Pacific sector of the SO which are likely to have been bathed in RSBW, need to take into account the contribution

of the previously unrecognised, extremely radiogenic $\varepsilon_{Nd}{}^{palaeoSW}$ values of bottom waters sourced in the Ross Sea region.

Finally, more work is required to better constrain the end-member ε_{Nd} values of RSBW and its precursor water masses, both today and in the past. Changes in past $\varepsilon_{Nd}{}^{palaeoSW}$ values at sites NBP-04 and NBP-06 can be explained by changes in either the end member $\varepsilon_{Nd}{}^{palaeoSW}$ value of RSBW or the location of its production; however it is not possible to distinguish between the two. Further work is needed to understand the mechanisms of boundary exchange which isotopically 'label' bottom waters within the Ross Sea, including better constraining i) the modern end member $\varepsilon_{Nd}{}^{seawater}$ values of RSBW and its precurser water masses, and ii) the outcrop locations and erosional pathways of the MVG, both onshore and offshore within the Ross Sea Embayment.

Chapter 6

Synthesis of results

This thesis aimed to reconstruct past changes in deep and bottom water circulation of Southern Ocean (SO) water masses using measurements of stable carbon isotopes on the benthic foraminifer *Cibicidoides* ($\delta^{13}C_b$) and of neodymium isotopes (ε_{Nd}) on the authigenic fraction of marine sediments. Specifically, the thesis objectives were threefold: First, to characterise the past $\delta^{13}C$ and ε_{Nd} values of the deep and bottom water masses within the SO, and, in doing so, investigate any changes in the mode of bottom water formation. Second, to reconstruct the palaeocirculation pathways of deep and bottom water masses sourced within the SO at various timescales across the last 1.5 Ma. Third, to investigate the role of deep and bottom water circulation changes in wider palaeoclimatic changes and their response to these wider climatic changes across this time period. This chapter will synthesise conclusions drawn throughout this work, and identify future research areas which will build upon the findings presented here.

6.1 Formation and palaeocirculation of Antarctic Bottom Water

A persistent theme throughout this thesis has been the cirum-Antarctic connectivity of deep and bottom water masses, and how this changed across the glacial-interglacial cycles of the Middle to Late Quaternary. During glacial periods of the last 800 ka, bottom waters formed in the Pacific sector of the SO were enriched in ^{13}C relative to bottom waters in the Atlantic and Indian sectors of the SO, which had much lower $\delta^{13}C$ values. This increased spatial heterogeneity in glacial SO deep and bottom water chemistry suggests bathymetric controls on deep water circulation within the SO were more pronounced during these periods, reflecting the increased density of these water masses. The higher density of deep and

bottom waters in part stems from the increase in salinity due to an expansion of grounded and floating ice, as well as increased storage of fresh water within groundwater reservoirs (Adkins et al., 2002). However, the extremely high salinity of reconstructed deep and bottom water masses within the Atlantic sector of the SO during the Last Glacial Maximum (LGM; c. 18-24 ka) requires additional salinity increases during bottom water formation (Adkins et al., 2002; Roberts et al., 2016). This could be achieved by increasing the proportion of Antarctic Bottom Water (AABW) produced via brine rejection during sea ice formation. This would impart newly formed AABW with elevated δ^{13}C values, owing to thermodynamic fractionation during air-sea gas exchange. The low δ^{13}C values observed in the deep Atlantic sector of the SO, however, suggests the opposite: that in fact air-sea gas exchange was reduced during bottom water formation, leading to a poorly ventilated abyssal Atlantic sector of the SO, with waters high in remineralised carbon. Relative ^{13}C depletion within the Atlantic sector of the SO may be a symptom of reduced AABW formation during glacial periods, leading to a longer residence time of deep waters and more time to build up large reservoirs of ^{13}C-depleted remineralised carbon. However, this is difficult to reconcile with the observed glacial expansion of AABW within the abyssal Atlantic Ocean and greatly increased salinity of deep waters, which imply greater production of AABW.

Continued, and most likely enhanced, Ross Sea Bottom Water (RSBW) production during periods of ice advancement within the Ross Sea Embayment have been identified based on rare earth element and authigenic ε_{Nd} records measured on sediments from the Pacific-Antarctic Ridge. This data suggests RSBW formation shifted to the NW Ross Sea Embayment – most likely northward on the continental shelf and within polynyas above the continental slope – when current-day regions of deep and bottom water formation were covered by grounded ice. The production of RSBW within polynyas is consistent with the elevated δ^{13}C values, and presumably a low remineralised nutrient inventory, of AABW in the Pacific sector of the SO, compared to those of the Atlantic SO during past glacials. The continued advection of RSBW to core sites on the Pacific-Antarctic Ridge, which is today bathed in little or only modified RSBW, suggests an expansion of RSBW within the Pacific sector of the SO from 540 ka to 5 ka, compared with today. This data indicates the proportion of RSBW reaching the Pacific-Antarctic Ridge from 5 ka until today is anomalously low. The timing of changes in authigenic ε_{Nd} values recorded at these sites does not follow the classical 'saw-tooth' pattern of glacial-interglacial cycles. However, ε_{Nd} values generally shift towards more radiogenic values during interglacial periods. Past changes in RSBW production are linked to changes in the extent of grounded and floating ice within the Ross Sea Embayment, which influence the region – and most likely rate – of RSBW production.

Proxies for surface water nutrient content and utilisation within the Pacific sector of the SO suggest a more complete consumption of surface nutrients by primary producers during past glacial periods compared to today (Robinson and Sigman, 2008; Wang et al., 2017). This suggests that any deep or bottom water formation occurring within these surface waters likely had a lower preformed nutrient content compared to modern waters in the Pacific sector of the SO. Restricting the advection of dense AABW high in remineralised nutrients out of the Atlantic sector of the SO and into the Pacific basin at the expense of deep waters formed in the Pacific sector (which were potentially lower in preformed nutrients), may have increased the efficiency of the global biological pump during past glacial periods, acting to lower pCO_2^{atm}. Coupled with the increased isolation, reduced ventilation, and build-up of respired carbon within the abyssal Atlantic sector of the SO, changes in the nature of deep water production within the Atlantic sector of the SO could have acted to lower pCO_2^{atm} during past glacials.

6.2 Middle- to Late-Quaternary palaeocirculation history of modified Circumpolar Deep Water in the Indian Ocean

An authigenic ε_{Nd} record of palaeocirculation from Ocean Drilling Program Leg 121 Site 758 in the deep equatorial Indian Ocean reveals varying contributions of unradiogenic deep waters formed in the North Atlantic (Northern Component Water, NCW) to modified Circumpolar Deep Water (mCDW) that bathed the core site throughout the last 1.5 million years. Glacial shifts towards more radiogenic ε_{Nd} values reflect a reduction in NCW ε_{Nd} within the SO, and the subsequent advection of its radiogenic ε_{Nd} signature to Site 758. This observation is consistent with nutrient and radiogenic isotope reconstructions of palaeocirculation suggesting a reduced flow of NCW entering the SO during glacial periods across the same period (e.g. Hodell et al. (2003); Pena and Goldstein (2014)). Calculations of the percentage of NCW within mCDW bathing Site 758 show remarkable coherence with equivalent analyses performed on ε_{Nd} records from the deep equatorial Atlantic and SW Pacific oceans (Howe, unpublished; Piotrowski, unpublished). The coherence of the calculated mixing demonstrates that past changes in ε_{Nd} share a common driver, and reflect mixing between NCW and other deep water masses along the flow path of the 'conveyor belt' of ocean circulation. There is no evidence that ε_{Nd} values at Site 758 are responding to changes in the proportion of Himalayan river waters entering the Bay of Bengal, as previously reported (Burton and Vance, 2000; Gourlan et al., 2010).

During the early stages of the Mid Pleistocene Transition, between c. 1043 and 936 ka, the amplitude of glacial-interglacial cyclicity in ε_{Nd} at Site 758 is greatly reduced. This reduction

in variability is largely driven by an increase in the advection of NCW with an unradiogenic ε_{Nd} signal to the core site during glacial periods. This is interpreted as a prolonged period of stability in global thermohaline circulation (THC), with the export of NCW during glacial periods at a similar level to interglacial periods. Immediately following this interval, between 931 and 866 ka, mCDW waters bathing Site 758 record a prolonged shift towards more radiogenic values, representing a reduction in the advection of NCW into the SO, consistent with previously published low resolution ε_{Nd} records spanning this interval from the Atlantic sector of the SO (Pena and Goldstein, 2014). After 866 ka, mixing calculation suggest that during interglacial periods the advection of NCW from the Atlantic basin into the SO and to Site 758 was increased compared to the interglacials of the preceding 634 ka. This increased propagation of a NCW signal through the 'conveyor' of ocean circulation is interpreted as a THC strengthening during interglacial periods.

6.3 Targeting strategies for future work

The authigenic ε_{Nd} records measured as part of this thesis on sediments from cores NBP-06 and NBP-04 on the Pacific-Antarctic Ridge provide minimum values for the past ε_{Nd} end member values of RSBW. It is possible that the true ε_{Nd} end member values of RSBW exported from the Ross Sea Embayment was more radiogenic. It is therefore not possible to determine whether shifts towards more radiogenic ε_{Nd} values at sites NBP-04 and NBP-06 reflect an increased production/advection of RSBW to these core sites, or changes in the end-member ε_{Nd} values of RSBW. A better characterisation of the past RSBW ε_{Nd} end member values would therefore allow for reconstructions of changes in the production and export of RSBW from the Ross Sea. Marine sediments deposited on the continental slope of the Ross Sea, or on the flanks of the Balleny Islands and/or Scott Seamounts, located closer to the Ross Sea Embayment (locations provided in Fig. 5.11), are suitable targets for studies of past RSBW end member values. However, attempts to produce authigenic ε_{Nd} records at sites on flanks of the Balleny Islands/Scott Seamounts may be hampered by the presence of volcanogenic sediments, as proved to be the case for site PC493 recovered from a seamount on the continental slope in the Amundsen Sea (see Chapter 3).

Our knowledge of modern day RSBW ε_{Nd} is limited by a lack of ε_{Nd} measurements on seawater samples from locations on the Ross Sea continental shelf. These samples would provide much needed constraints on the ε_{Nd} values of RSBW precursor water masses. A better understanding of the sources and the ε_{Nd} values of sedimentary and volcanic inputs to different regions of the Ross Sea Embayment, both today and in the past, would allow for a

better mechanistic understanding of how deep and bottom waters in the Ross Sea acquire their radiogenic ε_{Nd} signature.

Finally, the discovery of an expanded RSBW within the Pacific sector of the SO in the past with strongly radiogenic ε_{Nd} values highlights the importance of identifying changes in the ε_{Nd} values of AABW in the past. In particular, studies of deep water circulation within the Pacific sector of the SO using Nd isotopes must take into account past changes in the ε_{Nd} end member value of RSBW. To constrain the past advection of RSBW with radiogenic ε_{Nd} values into the Pacific Ocean, deep core sites located at Chatham Rise off New Zealand may be suitable targets for future ε_{Nd} reconstructions. Authigenic ε_{Nd} measurements made at two core sites at this location, Chat 5k (4240 m. water depth) and Chat 3K (4802 m. water depth) both exhibit similar ε_{Nd} values as core site NBP-04 on the Pacific-Antarctic Ridge (Hu et al., 2016b; Noble et al., 2013). However, these records go back to only 31 ka (CHAT 5K) and 16.5 ka (CHAT 3K). Future work should aim at investigating the period between 64 and 50 ka, when RSBW recorded at the Pacific-Antarctic Ridge reached its radiogenic ε_{Nd} peak.

References

Abe-Ouchi, A., Saito, F., Kawamura, K., Raymo, M. E., Okuno, J., Takahashi, K., and Blatter, H. (2013). Insolation-driven 100,000-year glacial cycles and hysteresis of ice-sheet volume. *Nature*, 500(7461):190–193.

Adkins, J. F. (2013). The role of deep ocean circulation in setting glacial climates. *Paleoceanography*, 28(3):539–561.

Adkins, J. F., McIntyre, K., and Schrag, D. (2002). The salinity, temperature, and δ^{18}O of the glacial deep ocean. *Science*, 298(November):1769–1773.

Albarède, F. and Goldstein, S. L. (1992). Nd isotopes in sea-floor ferromanganese deposits. *Geology*, 20(8):8–11.

Allen, C. S., Pike, J., and Pudsey, C. J. (2011). Last glacial–interglacial sea-ice cover in the SW Atlantic and its potential role in global deglaciation. *Quaternary Science Reviews*, 30(19-20):2446–2458.

Amakawa, H., Sasaki, K., and Ebihara, M. (2009). Nd isotopic composition in the central North Pacific. *Geochimica et Cosmochimica Acta*, 73(16):4705–4719.

Anderson, J. B., Conway, H., Bart, P. J., Witus, A. E., Greenwood, S. L., McKay, R. M., Hall, B. L., Ackert, R. P., Licht, K. J., Jakobsson, M., and Stone, J. O. (2014). Ross Sea paleo-ice sheet drainage and deglacial history during and since the LGM. *Quaternary Science Reviews*, 100:31–54.

Anderson, J. T., Wilson, G. S., Fink, D., Lilly, K., Levy, R. H., and Townsend, D. (2017). Reconciling marine and terrestrial evidence for post LGM ice sheet retreat in southern McMurdo Sound, Antarctica. *Quaternary Science Reviews*, 157:1–13.

Anderson, R. F., Ali, S., Bradtmiller, L. I., Nielsen, S. H. H., Fleisher, M. Q., Anderson, B. E., and Burckle, L. H. (2009). Wind-driven upwelling in the Southern Ocean and the deglacial rise in atmospheric CO_2. *Science*, 323(5920):1443–1448.

Andrews, J. T., Domack, E. W., Cunningham, W. L., Leventer, A., Licht, K. J., Jull, A. J. T., DeMaster, D. J., and Jennings, A. E. (1999). Problems and Possible Solutions Concerning Radiocarbon Dating of Surface Marine Sediments, Ross Sea, Antarctica. *Quaternary Research*, 52(2):206–216.

Augustin, L., Barbante, C., Barnes, P. R. F., Barnola, J. M., Bigler, M., Castellano, E., Cattani, O., Chappellaz, J., Dahl-Jensen, D., Delmonte, B., Dreyfus, G., Durand, G., Falourd, S., Fischer, H., Flückiger, J., Hansson, M. E., Huybrechts, P., Jugie, G., Johnsen, S. J., Jouzel,

J., Kaufmann, P., Kipfstuhl, J., Lambert, F., Lipenkov, V. Y., Littot, G. C., Longinelli, A., Lorrain, R., Maggi, V., Masson-Delmotte, V., Miller, H., Mulvaney, R., Oerlemans, J., Oerter, H., Orombelli, G., Parrenin, F., Peel, D. a., Petit, J.-R., Raynaud, D., Ritz, C., Ruth, U., Schwander, J., Siegenthaler, U., Souchez, R., Stauffer, B., Steffensen, J. P., Stenni, B., Stocker, T. F., Tabacco, I. E., Udisti, R., Van De Wal, R. S. W., Van Den Broeke, M., Weiss, J., Wilhelms, F., Winther, J.-G., Wolff, E. W., and Zucchelli, M. (2004). Eight glacial cycles from an Antarctic ice core. *Nature*, 429(6992):623–8.

Bart, P. J. and Cone, A. N. (2012). Early stall of West Antarctic Ice Sheet advance on the eastern Ross Sea middle shelf followed by retreat at 27,500 ^{14}C yr BP. *Palaeogeography, Palaeoclimatology, Palaeoecology*, 335-336:52–60.

Basak, C., Pahnke, K., Frank, M., Lamy, F., and Gersonde, R. (2015). Neodymium isotopic characterization of Ross Sea Bottom Water and its advection through the southern South Pacific. *Earth and Planetary Science Letters*, 419:211–221.

Bau, M. and Dulski, P. (1999). Comparing yttrium and rare earths in hydrothermal fluids from the Mid-Atlantic Ridge: Implications for Y and REE behaviour during near-vent mixing and for the Y/Ho ratio of proterozoic seawater. *Chemical Geology*, 155(1-2):77–90.

Bau, M., Schmidt, K., Koschinsky, A., Hein, J., Kuhn, T., and Usui, A. (2014). Discriminating between different genetic types of marine ferro-manganese crusts and nodules based on rare earth elements and yttrium. *Chemical Geology*, 381:1–9.

Bazin, L., Landais, A., Lemieux-Dudon, B., Toyé Mahamadou Kele, H., Veres, D., Parrenin, F., Martinerie, P., Ritz, C., Capron, E., Lipenkov, V., Loutre, M.-F., Raynaud, D., Vinther, B., Svensson, A., Rasmussen, S. O., Severi, M., Blunier, T., Leuenberger, M., Fischer, H., Masson-Delmotte, V., Chappellaz, J., and Wolff, E. W. (2013). An optimized multi-proxy, multi-site Antarctic ice and gas orbital chronology (AICC2012): 120-800 ka. *Climate of the Past*, 9(4):1715–1731.

Belanger, P. E., Curry, W. B., and Matthews, R. K. (1981). Core-top evaluation of benthic foraminiferal isotopic ratios for paleo-oceanographic interpretations. *Palaeogeography, Palaeoclimatology, Palaeoecology*, 33:205–220.

Bemis, K., Lowell, R., and Farough, A. (2012). Diffuse flow on and around hydrothermal vents at mid-ocean ridges. *Oceanography*, 25(1):182–191.

Bentley, M. J. (2010). The Antarctic palaeo record and its role in improving predictions of future Antarctic Ice Sheet change. *Journal of Quaternary Science*, 25(June 2009):5–18.

Benz, V., Esper, O., Gersonde, R., Lamy, F., and Tiedemann, R. (2016). Last Glacial Maximum sea surface temperature and sea-ice extent in the Pacific sector of the Southern Ocean. *Quaternary Science Reviews*, 146:216–237.

Bereiter, B., Eggleston, S., Schmitt, J., Nehrbass-Ahles, C., Stocker, T. F., Fischer, H., Kipfstuhl, S., and Chappellaz, J. (2015). Revision of the EPICA Dome C CO_2 record from 800 to 600 kyr before present. *Geophysical Research Letters*, 42(2):542–549.

Berkman, P. A. and Forman, S. L. (1996). Pre-bomb radiocarbon and the reservoir correction for calcareous marine species in the Southern Ocean. *Geophysical Research Letters*, 23(4):363–366.

Bersch, M., Becker, G. a., Frey, H., and Koltermann, K. P. (1992). Topographic effects of the Maud Rise on the stratification and circulation of the Weddell Gyre. *Deep Sea Research Part A. Oceanographic Research Papers*, 39(2):303–331.

Bickert, T., Curry, W. B., and Wefer, G. (1997). Late Pliocene to Holocene (2.6-0 Ma) western equatorial Atlantic deep-water circulation: Inferences from benthic stable isotopes. *Proceedings of the Ocean Drilling Program, Scientific Results*, 154:239–254.

Blaser, P., Lippold, J., Gutjahr, M., Frank, N., Link, J. M., and Frank, M. (2016). Extracting foraminiferal seawater Nd isotope signatures from bulk deep sea sediment by chemical leaching. *Chemical Geology*, 439:189–204.

Böhm, E., Lippold, J., Gutjahr, M., Frank, M., Blaser, P., Antz, B., Fohlmeister, J., Frank, N., Andersen, M. B., and Deininger, M. (2014). Strong and deep Atlantic meridional overturning circulation during the last glacial cycle. *Nature*, 517(7532):73–76.

Bonaccorsi, R., Quaia, T., Burckle, L. H., Anderson, R. F., Melis, R., and Brambati, A. (2007). C-14 age control of pre- and post-LGM events using *N. pachyderma* preserved in deep-sea sediments (Ross Sea , Antarctica). In Cooper, A. and Raymond, C., editors, *A Keystone in a Changing World—Online Proceedings of the 10th ISAES X USGS Open-File Report 2007. Extended Abstract*, pages 1995–1998.

Böning, C. W., Dispert, A., Visbeck, M., Rintoul, S. R., and Schwarzkopf, F. U. (2008). The response of the Antarctic Circumpolar Current to recent climate change. *Nature Geoscience*, 1(December):864–869.

Bonn, W. J., Gingele, F. X., Grobe, H., and Fütterer, D. K. (1998). Palaeoproductivity at the Antarctic continental margin: opal and barium records for the last 400 ka. *Palaeogeography, Palaeoclimatology, Palaeoecology*, 139(3-4):195–211.

Bostock, H. C., Barrows, T., Carter, L., Chase, Z., Cortese, G., Dunbar, G., Ellwood, M. J., Hayward, B., Howard, W., Neil, H., Noble, T. L., Mackintosh, A., Moss, P., Moy, A. D., White, D., Williams, M., and Armand, L. (2013). A review of the Australian–New Zealand sector of the Southern Ocean over the last 30 ka (Aus-INTIMATE project). *Quaternary Science Reviews*, 74:35–57.

Bouttes, N., Paillard, D., and Roche, D. M. (2010). Impact of brine-induced stratification on the glacial carbon cycle. *Climate of the Past*, 6(5):575–589.

Boyle, E. A. (1983). Manganese carbonate overgrowths on foraminifera tests. *Geochimica et Cosmochimica Acta*, 47(10):1815–1819.

Boyle, E. A. and Keigwin, L. D. (1987). North Atlantic thermohaline circulation during the past 20,000 years linked to high-latitude surface temperature. *Nature*, 330(6143):35–40.

Bradtmiller, L. I., Anderson, R. F., Fleisher, M. Q., and Burckle, L. H. (2009). Comparing glacial and Holocene opal fluxes in the Pacific sector of the Southern Ocean. *Paleoceanography*, 24(2).

Broecker, W. S. (1982). Glacial to interglacial changes in ocean chemistry. *Progress in Oceanography*, 11(2):151–197.

Broecker, W. S. (1991). The Great Ocean Conveyor. *Oceanography*, 4(2):79–89.

Budillon, G., Gremes Cordero, S., and Salusti, E. (2002). On the dense water spreading off the Ross Sea shelf (Southern Ocean). *Journal of Marine Systems*, 35(3-4):207–227.

Burckle, L. H. and Burak, R. (1996). Relative abundance of *Eucampia antarctica* as a proxy to δ^{18}O in upper Quaternary sediments of the Southern Ocean. *PACT*, 50:15–22.

Burckle, L. H., Clarke, D. B., and Shackleton, N. J. (1978). Isochronous last-abundant-appearance datum (LAAD) of the diatom hemidiscus karstenii in the sub-antarctic. *Geology*, 6(4):243–246.

Burckle, L. H. and Cooke, D. W. (1983). Late Pleistocene *Eucampia antarctica* abundance stratigraphy in the Atlantic sector of the Southern Ocean. *Micropaleontology*, 29(1):6–10.

Burton, K. W., Lee, D.-C., Christensen, J. N., Halliday, A. N., and Hein, J. R. (1999). Actual timing of neodymium isotopic variations recorded by FeMn crusts in the western North Atlantic. *Earth and Planetary Science Letters*, 171(1):149–156.

Burton, K. W. and Vance, D. (2000). Glacial–interglacial variations in the neodymium isotope composition of seawater in the Bay of Bengal recorded by planktonic foraminifera. *Earth and Planetary Science Letters*, 176(3-4):425–441.

Candy, I. and McClymont, E. L. (2013). Interglacial intensity in the North Atlantic over the last 800 000 years: investigating the complexity of the mid-Brunhes Event. *Journal of Quaternary Science*, 28(4):343–348.

Carroll, J. J., Slupsky, J. D., and Mather, A. E. (1991). The solubility of carbon dioxide in water at low pressure. *Journal of Physical and Chemical Reference Data*, 20(6):1201.

Carter, L., McCave, I. N., Williams, M. J. M., Siegert, M. J., and Florindo, F. (2008). Circulation and Water Masses of the Southern Oean: A Reveiw. In *Antarctic Climate Evolution*, volume 8 of *Developments in Earth and Environmental Sciences*, pages 85–114. Elsevier.

Carter, P., Vance, D., Hillenbrand, C.-D., Smith, J. A., and Shoosmith, D. (2012). The neodymium isotopic composition of waters masses in the eastern Pacific sector of the Southern Ocean. *Geochimica et Cosmochimica Acta*, 79:41–59.

Charles, C. D. and Fairbanks, R. G. (1990). Glacial to interglacial changes in the isotopic gradients of southern ocean surface water. In Bleil, U. and Thiede, J., editors, *Charles, CD, Fairbanks R. 1990. Glacial to interglacial changes in the isotopic gradients of southern ocean surface water. The Geologic History of Polar oceans: Arctic Vs Antarctic NATO/ASI series*.

Charles, C. D. and Fairbanks, R. G. (1992). Evidence from Southern Ocean sediments for the effect of North Atlantic deep-water flux on climate. *Nature*, 355(6359):416–419.

Chase, Z., Anderson, R. F., Fleisher, M. Q., and Kubik, P. W. (2003). Scavenging of ^{230}Th, ^{231}Pa and ^{10}Be in the Southern Ocean (SW Pacific sector): The importance of particle flux, particle composition and advection. *Deep-Sea Research Part II: Topical Studies in Oceanography*, 50(3-4):739–768.

Chen, J., Farrell, J. W., Murray, D. W., and Prell, W. L. (1995). Timescale and paleoceanographic implications of a 3.6 m.y. oxygen isotope record from the northeast Indian Ocean (Ocean Drilling Program Site 758). *Paleoceanography*, 10(1):21–47.

Chester, R. and Hughes, M. J. (1967). A chemical technique for the separation of ferromanganese minerals, carbonate minerals and absorbed trace elements from pelagic sediments. *Chemical Geology*, 2:249–262.

Clark, P. U., Archer, D. E., Pollard, D., Blum, J. D., Rial, J. a., Brovkin, V., Mix, A. C., Pisias, N. G., and Roy, M. (2006). The middle Pleistocene transition: characteristics, mechanisms, and implications for long-term changes in atmospheric pCO_2. *Quaternary Science Reviews*, 25(23-24):3150–3184.

Clark, P. U. and Pollard, D. (1998). Origin of the middle Pleistocene transition by ice sheet erosion of regolith. *Paleoceanography*, 13(1):1–9.

Collier, R., Dymond, J., Honjo, S., Manganini, S., Francois, R., and Dunbar, R. (2000). The vertical flux of biogenic and lithogenic material in the Ross Sea: Moored sediment trap observations 1996-1998. *Deep-Sea Research Part II: Topical Studies in Oceanography*, 47(15-16):3491–3520.

Collins, L. G., Pike, J., Allen, C. S., and Hodgson, D. a. (2012). High-resolution reconstruction of southwest Atlantic sea-ice and its role in the carbon cycle during marine isotope stages 3 and 2. *Paleoceanography*, 27(3):PA3217.

Comiso, J. C. (2003). Large-scale Characteristics and Variability of the Global Sea Ice Cover. *Sea Ice: An Introduction to its Physics, Chemistry, Biology and Geology*, pages 1–31.

Crowley, T. J. and Hyde, W. T. (2008). Transient nature of late Pleistocene climate variability. *Nature*, 456(7219):226–230.

Curry, W. B. and Oppo, D. W. (2005). Glacial water mass geometry and the distribution of $\delta^{13}C$ of ΣCO_2 the western Atlantic Ocean. *Paleoceanography*, 20(1):1–12.

Curry, W. B., Shackleton, N. J., Richter, C., and Shipboard Scientific Party (1995). Site 929. In *Proceedings of the Ocean Drilling Program, 154 Initial Reports*, volume 154. Ocean Drilling Program.

de la Fuente, M., Skinner, L. C., Calvo, E., Pelejero, C., and Cacho, I. (2015). Increased reservoir ages and poorly ventilated deep waters inferred in the glacial Eastern Equatorial Pacific. *Nature Communications*, 6(May):7420.

Delmonte, B., Petit, J., Andersen, K., Basile-Doelsch, I., Maggi, V., and Ya Lipenkov, V. (2004). Dust size evidence for opposite regional atmospheric circulation changes over east Antarctica during the last climatic transition. *Climate Dynamics*, 23(3-4):427–438.

DeMaster, D. J. and Ragueneau, O. (1996). Preservation efficiencies and accumulation rates fo biogenic silica and organic C, N, and P in high-latitude sediments: The Ross Sea. *Journal of Geophysical Research*, 101(C8):18501–18518.

DePaolo, D. J. and Wasserburg, G. (1976). Nd isotopic variations and petrogenetic models. *Geophysical Research Letters*, 3(5):249–252.

Diekmann, B., Fütterer, D. K., Grobe, H., Hillenbrand, C.-D., Kuhn, G., Michels, K., Petschick, R., and Pirrung, M. (2003). *The South Atlantic in the Late Quaternary*. Springer Berlin Heidelberg, Berlin, Heidelberg.

Diekmann, B. and Kuhn, G. (2002). Sedimentary record of the mid-Pleistocene climate transition in the southeastern South Atlantic (ODP Site 1090). *Palaeogeography, Palaeoclimatology, Paleocology*, 182:241–258.

Diekmann, B., Kuhn, G., Rachold, V., Abelmann, A., Brathauer, U., Fütterer, D. K., Gersonde, R., and Grobe, H. (2000). Terrigenous sediment supply in the Scotia Sea (Southern Ocean): response to Late Quaternary ice dynamics in Patagonia and on the Antarctic Peninsula. *Palaeogeography, Palaeoclimatology, Palaeoecology*, 162(3-4):357–387.

Domack, E. W., Hall, B. L., and Hayes, J. M. (1999a). Accurate Antarctic dating technique sought by Quaternary community. *Eos, Transactions American Geophysical Union*, 80(49):591.

Domack, E. W., Jacobson, E. A., Ship, S., and Anderson, J. (1999b). Late Pleistocene–Holocene retreat of the West Antarctic Ice-Sheet system in the Ross Sea: Part 2—Sedimentologic and stratigraphic signature. *Geological Society of America Bulletin*, 111(10):1486.

Duplessy, J.-C., Shackleton, N. J., Matthews, R. K., Prell, W., Ruddiman, W. F., Caralp, M., and Hendy, C. H. (1984). ^{13}C Record of benthic foraminifera in the last interglacial ocean: Implications for the carbon cycle and the global deep water circulation. *Quaternary Research*, 21(2):225–243.

Eggleston, S., Schmitt, J., Bereiter, B., Schneider, R., and Fischer, H. (2016). Evolution of the stable carbon isotope composition of atmospheric CO_2 over the last glacial cycle. *Paleoceanography*.

Elderfield, H., Ferretti, P., Greaves, M., Crowhurst, S. J., McCave, I. N., Hodell, D. A., and Piotrowski, A. M. (2012). Evolution of Ocean Temperature. *Science*, 337:704–709.

Elmore, A. C., Piotrowski, A. M., Wright, J. D., and Scrivner, A. E. (2011). Testing the extraction of past seawater Nd isotopic composition from North Atlantic deep sea sediments and foraminifera. *Geochemistry, Geophysics, Geosystems*, 12(9).

Farrell, J. W. and Janecek, T. R. (1991). Late Neogene paleoceanography and paleoclimatology of the northern Indian Ocean (Site 758). *Proceedings of the Ocean Drilling Program, Scientific results*, 121:297–355.

Ferrari, R., Jansen, M. F., Adkins, J. F., Burke, A., Stewart, A. L., and Thompson, A. F. (2014). Antarctic sea ice control on ocean circulation in present and glacial climates. *Proceedings of the National Academy of Sciences*, 111(24):8753–8758.

Fischer, H., Fundel, F., Ruth, U., Twarloh, B., Wegner, A., Udisti, R., Becagli, S., Castellano, E., Morganti, A., Severi, M., Wolff, E. W., Littot, G., Röthlisberger, R., Mulvaney, R., Hutterli, M. A., Kaufmann, P., Federer, U., Lambert, F., Bigler, M., Hansson, M., Jonsell, U., de Angelis, M., Boutron, C., Siggaard-Andersen, M.-L., Steffensen, J. P., Barbante, C., Gaspari, V., Gabrielli, P., and Wagenbach, D. (2007). Reconstruction of millennial

changes in dust emission, transport and regional sea ice coverage using the deep EPICA ice cores from the Atlantic and Indian Ocean sector of Antarctica. *Earth and Planetary Science Letters*, 260(1-2):340–354.

Fogwill, C. J., Turney, C. S. M., Golledge, N. R., Etheridge, D. M., Rubino, M., Thornton, D. P., Baker, A., Woodward, J., Winter, K., van Ommen, T. D., Moy, A. D., Curran, M. A. J., Davies, S. M., Weber, M. E., Bird, M. I., Munksgaard, N. C., Menviel, L., Rootes, C. M., Ellis, B., Millman, H., Vohra, J., Rivera, A., Cooper, A., Joughin, I., Smith, B. E., Medley, B., van Wijk, E. M., Rintoul, S. R., Jones, J. M., Anderson, R. F., Marcott, S. A., Pedro, J. B., Hogg, A., Deschamps, P., Liu, J., Milne, G. A., Kopp, R. E., Clark, P. U., Shennan, I., Hillenbrand, C.-D., Mitrovica, J. X., Tamisiea, M. E., Timmermann, A., Timm, O. E., Mouchet, A., Hein, A. S., Mulvaney, R., Jouzel, J., Bentley, M. J., Jacobs, S. S., Jenkins, A., Giulivi, C. F., Dutrieux, P., Fabel, D., Hein, A., Bradley, S. L., Lüthi, D., Monnin, E., Haran, T., Bohlander, J., Scambos, T., Painter, T., Fahnestock, M., Rodionov, S. N., Rasmussen, S. O., and Blunier, T. (2017). Antarctic ice sheet discharge driven by atmosphere-ocean feedbacks at the Last Glacial Termination. *Scientific Reports*, 7(October 2016):39979.

Fontanier, C., Mackensen, A., Jorissen, F. J., Anschutz, P., Licari, L., and Griveaud, C. (2006). Stable oxygen and carbon isotopes of live benthic foraminifera from the Bay of Biscay: Microhabitat impact and seasonal variability. *Marine Micropaleontology*, 58(3):159–183.

Ford, H. L., Sosdian, S. M., Rosenthal, Y., and Raymo, M. E. (2016). Gradual and abrupt changes during the Mid-Pleistocene Transition. *Quaternary Science Reviews*, 148:222–233.

Foster, G. L., Vance, D., and Prytulak, J. (2007). No change in the neodymium isotope composition of deep water exported from the North Atlantic on glacial-interglacial time scales. *Geology*, 35(1):37–40.

Frank, M. (2002). Radiogenic isotopes: Tracers of past ocean circulation and erosional input. *Reviews of Geophysics*, 40(1):1001.

Futa, K. and Le Masurier, W. E. (1983). Nd and Sr isotopic studies on cenozoic mafic lavas from West Antarctica: Another source for continental alkali basalts. *Contributions to Mineralogy and Petrology*, 83(1-2):38–44.

Garcia, H. E., Locarnini, R. A., Boyer, T. P., Antonov, J. I., Baranova, O., Zweng, M., Reagan, J., and Johnson, D. (2014). *World Ocean Atlas 2013, Volume 3: Dissolved Oxygen, Apparent Oxygen Utilization, and Oxygen Saturation*.

Gebbie, G. (2014). How much did Glacial North Atlantic Water shoal? *Paleoceanography*, 29(3):190–209.

Gebbie, G. and Huybers, P. (2011). How is the ocean filled? *Geophysical Research Letters*, 38(6).

German, C. R., Klinkhammer, G. P., Edmond, J. M., Mitra, A., and Elderfield, H. (1990). Hydrothermal scavenging of rare-earth elements in the ocean. *Nature*, 345:516–518.

Gersonde, R., Crosta, X., Abelmann, A., and Armand, L. (2005). Sea-surface temperature and sea ice distribution of the Southern Ocean at the EPILOG Last Glacial Maximum—a circum-Antarctic view based on siliceous microfossil records. *Quaternary Science Reviews*, 24(7-9):869–896.

Glasby, G., Barrett, P. J., McDougall, J., and McKnight, D. (1975). Localised variations in sedimentation characteristics in the Ross Sea and McMurdo Sound regions, Antarctica. *New Zealand Journal of Geology and Geophysics*, 18(4):605–612.

Goldstein, S. L. and O'Nions, R. (1981). Nd and Sr isotopic relationships in pelagic clays and ferromanganese deposits. *Nature*, 292(5821):324–327.

Golledge, N. R., Menviel, L., Carter, L., Fogwill, C. J., England, M. H., Cortese, G., and Levy, R. H. (2014). Antarctic contribution to meltwater pulse 1A from reduced Southern Ocean overturning. *Nature Communications*, 5:5107.

Gordon, A. L., Huber, B. A., and Busecke, J. (2015). Bottom water export from the western Ross Sea, 2007 through 2010. *Geophysical Research Letters*, 42(13):5387–5394.

Gourlan, A. T., Meynadier, L., Allègre, C. J., Tapponnier, P., Birck, J.-L., and Joron, J.-L. (2010). Northern Hemisphere climate control of the Bengali rivers discharge during the past 4 Ma. *Quaternary Science Reviews*, 29(19-20):2484–2498.

Govin, A., Michel, E., Labeyrie, L., Waelbroeck, C., Dewilde, F., and Jansen, E. (2009). Evidence for northward expansion of Antarctic Bottom Water mass in the Southern Ocean during the last glacial inception. *Paleoceanography*, 24(PA1202).

Graham, D., Corliss, B., Bender, M. L., and Keigwin, L. D. (1981). Carbon and oxygen isotopic disequilibria of recent deep-sea benthic foraminifera. *Marine Micropaleontology*, 6:483–497.

Gutjahr, M., Frank, M., Stirling, C. H., Klemm, V., van de Flierdt, T. V. D., and Halliday, A. N. (2007). Reliable extraction of a deepwater trace metal isotope signal from Fe-Mn oxyhydroxide coatings of marine sediments. *Chemical Geology*, 242(3-4):351–370.

Hain, M. P., Sigman, D. M., and Haug, G. H. (2010). Carbon dioxide effects of Antarctic stratification , North Atlantic Intermediate Water formation , and subantarctic nutrient drawdown during the last ice age : Diagnosis and synthesis in a geochemical box model. *Global Biogeochemical Cycles*, 24:1–19.

Hain, M. P., Sigman, D. M., and Haug, G. H. (2014). The Biological Pump in the Past. In *Treatise on Geochemistry (Second Edition) Volume 8:The Oceans and Marine Geochemistry*, volume 8, chapter 18, pages 373–397. Elsevier Ltd., Amsterdamn NL, 2 edition.

Halberstadt, A. R. W., Simkins, L. M., Greenwood, S. L., and Anderson, J. B. (2016). Past ice-sheet behaviour: Retreat scenarios and changing controls in the Ross Sea, Antarctica. *Cryosphere*, 10(3):1003–1020.

Hall, B. L., Baroni, C., and Denton, G. H. (2004). Holocene relative sea-level history of the Southern Victoria Land Coast, Antarctica. *Global and Planetary Change*, 42(1-4):241–263.

Hall, B. L. and Denton, G. H. (2000). Radiocarbon chronology of Ross Sea Drift, eastern Taylor Valley, Antarctica: evidence for a grounded ice Sheet in the Ross Sea at the Last Glacial Maximum. *Geografiska Annaler, Series A: Physical Geography*, 82(2-3):305–336.

Hall, B. L., Denton, G. H., Heath, S. L., Jackson, M. S., and Koffman, T. N. B. (2015). Accumulation and marine forcing of ice dynamics in the western Ross Sea during the last deglaciation. *Nature Geoscience*, 8(8):625–628.

Hall, B. L., Denton, G. H., Stone, J. O., and Conway, H. (2013). History of the grounded ice sheet in the Ross Sea sector of Antarctica during the Last Glacial Maximum and the last termination. *Geological Society, London, Special Publications*, 381(1):167–181.

Hall, B. L., Henderson, G. M., Baroni, C., and Kellogg, T. B. (2010). Constant Holocene Southern-Ocean ^{14}C reservoir ages and ice-shelf flow rates. *Earth and Planetary Science Letters*, 296(1-2):115–123.

Hall, I. R., McCave, I. N., Shackleton, N. J., Weedon, G. P., and Harris, S. E. (2001). Intensified deep Pacific inflow and ventilation in Pleisctocene glacial times. *Nature*, 412:809–812.

Hays, J. D., Imbrie, J., and Shackleton, N. J. (1976). Variations in the Earth's Orbit: Pacemaker of the Ice Ages. *Science*, 194(4270):1121–1132.

Hein, A. S., Fogwill, C. J., Sugden, D. E., and Xu, S. (2011). Glacial/interglacial ice-stream stability in the Weddell Sea embayment, Antarctica. *Earth and Planetary Science Letters*, 307(1-2):211–221.

Hendry, K. R., Rickaby, R. E., Meredith, M. P., and Elderfield, H. (2009). Controls on stable isotope and trace metal uptake in *Neogloboquadrina pachyderma* (sinistral) from an Antarctic sea-ice environment. *Earth and Planetary Science Letters*, 278(1-2):67–77.

Heywood, K. J., Naveira Garabato, A. C., and Stevens, D. P. (2002). High mixing rates in the abyssal Southern Ocean. *Nature*, 415(6875):1011–1014.

Hillenbrand, C.-D., Bentley, M. J., Stolldorf, T. D., Hein, a. S., Kuhn, G., Graham, A. G., Fogwill, C. J., Kristoffersen, Y., Smith, J. A., Anderson, J. B., Larter, R. D., Melles, M., Hodgson, D. a., Mulvaney, R., and Sugden, D. E. (2014). Reconstruction of changes in the Weddell Sea sector of the Antarctic Ice Sheet since the Last Glacial Maximum. *Quaternary Science Reviews*, 100:111–136.

Hillenbrand, C.-D. and Cortese, G. (2006). Polar stratification: A critical view from the Southern Ocean. *Palaeogeography, Palaeoclimatology, Palaeoecology*, 242(3-4):240–252.

Hillenbrand, C.-D., Ehrmann, W., Larter, R. D., Benetti, S., Dowdeswell, J. A., Ó Cofaigh, C., Graham, A. G., and Grobe, H. (2009). Clay mineral provenance of sediments in the southern Bellingshausen Sea reveals drainage changes of the West Antarctic Ice Sheet during the Late Quaternary. *Marine Geology*, 265(1-2):1–18.

Hillenbrand, C.-D., Fütterer, D., Grobe, H., and Frederichs, T. (2002). No evidence for a Pleistocene collapse of the West Antarctic Ice Sheet from continental margin sediments recovered in the Amundsen Sea. *Geo-Marine Letters*, 22(2):51–59.

Hillenbrand, C.-D., Melles, M., Kuhn, G., and Larter, R. D. (2012). Marine geological constraints for the grounding-line position of the Antarctic Ice Sheet on the southern Weddell Sea shelf at the Last Glacial Maximum. *Quaternary Science Reviews*, 32:25–47.

Hodell, D. A., Kanfoush, S. L., Venz, K. A., Charles, C. D., and Sierro, F. J. (2003). The Mid-Brunhes Transition in ODP Sites 1089 and 1090 (Subantarctic South Atlantic). In Droxler, A., Poore, R., and Burckle, L., editors, *Earth's Climate and Orbital Eccentricity: The Marine Isotope Stage 11 Question*, volume 1090, pages 113–129. American Geophysical Union Geophysical Monograph 137.

Hönisch, B., Hemming, N. G., Archer, D., Siddall, M., and McManus, J. F. (2009). Atmospheric carbon dioxide concentration across the mid-Pleistocene transition. *Science*, 324(5934):1551–4.

Hoogakker, B. A. A., Elderfield, H., Schmiedl, G., McCave, I. N., and Rickaby, R. E. (2015). Glacial – interglacial changes in bottom-water oxygen content on the Portuguese margin. *Nature Geoscience*, 8(January):2–5.

Hoogakker, B. A. A., Rohling, E. J., Palmer, M., Tyrrell, T., and Rothwell, R. (2006). Underlying causes for long-term global ocean δ^{13}C fluctuations over the last 1.20 Myr. *Earth and Planetary Science Letters*, 248(1-2):15–29.

Howe, J. N., Piotrowski, A. M., Hu, R., and Bory, A. (2016a). Reconstruction of east–west deep water exchange in the low latitude Atlantic Ocean over the past 25,000 years. *Earth and Planetary Science Letters*, 1:1–10.

Howe, J. N., Piotrowski, A. M., Noble, T. L., Mulitza, S., Chiessi, C. M., and Bayon, G. (2016b). North Atlantic Deep Water Production during the Last Glacial Maximum. *Nature Communications*, 7:11765.

Howe, J. N., Piotrowski, A. M., and Rennie, V. C. (2016c). Abyssal origin for the early Holocene pulse of unradiogenic neodymium isotopes in Atlantic seawater. *Geology*, 1(10):G38155.1.

Hu, R., Noble, T. L., Piotrowski, A. M., McCave, I. N., Bostock, H. C., and Neil, H. L. (2016a). Neodymium isotopic evidence for linked changes in Southeast Atlantic and Southwest Pacific circulation over the last 200 kyr. *Earth and Planetary Science Letters*, 1:1–9.

Hu, R., Piotrowski, A. M., Bostock, H. C., Crowhurst, S., and Rennie, V. (2016b). Variability of neodymium isotopes associated with planktonic foraminifera in the Pacific Ocean during the Holocene and Last Glacial Maximum. *Earth and Planetary Science Letters*, 447:130–138.

Imbrie, J., Hays, J. D., Martinson, D. G., McIntyre, A., Mix, A. C., Morley, J. J., Pisias, N. G., Prell, W. L., and Shackleton, N. J. (1984). The orbital theory of Pleistocene climate: Support from a revised chronology of the marine δ^{18}O record. *Milankovitch and Climate: Understanding the Response to Astronomical Forcing*, (November 2015):269–305.

Jaccard, S. L., Galbraith, E. D., Martínez-García, A., and Anderson, R. F. (2016). Covariation of deep Southern Ocean oxygenation and atmospheric CO_2 through the last ice age. *Nature*, 530(7589):207–210.

Jaccard, S. L., Hayes, C. T., Martinez-Garcia, A., Hodell, D. A., Anderson, R. F., Sigman, D. M., and Haug, G. H. (2013). Two modes of change in Southern Ocean productivity over the past million years. *Science*, 339(6126):1419–1423.

Jacka, T. A. (1997). Antarctic CRC and Australian Antarctic Division Climate Data Sets.

Jacobsen, S. B. and Wasserburg, G. (1980). Sm-Nd isotopic evolution of chondrites. *Earth and Planetary Science Letters*, 50(1):139–155.

Jaeschke, A., Wengler, M., Hefter, J., Ronge, T. A., Geibert, W., Mollenhauer, G., Gersonde, R., and Lamy, F. (2017). A biomarker perspective on dust, productivity, and sea surface temperature in the Pacific sector of the Southern Ocean. *Geochimica et Cosmochimica Acta*, 204:120–139.

Jeandel, C., Arsouze, T., Lacan, F., Techine, P., and Dutay, J. (2007). Isotopic Nd compositions and concentrations of the lithogenic inputs into the ocean: A compilation, with an emphasis on the margins. *Chemical Geology*, 239(1-2):156–164.

Jenkins, A., Dutrieux, P., Jacobs, S., Steig, E., Gudmundsson, H., Smith, J. A., and Heywood, K. (2016). Decadal Ocean Forcing and Antarctic Ice Sheet Response: Lessons from the Amundsen Sea. *Oceanography*, 29(4):106–117.

Jouzel, J., Masson-Delmotte, V., Cattani, O., Dreyfus, G., Falourd, S., Hoffmann, G., Minster, B., Nouet, J., Barnola, J. M., Chappellaz, J., Fischer, H., Gallet, J. C., Johnsen, S., Leuenberger, M., Loulergue, L., Luethi, D., Oerter, H., Parrenin, F., Raisbeck, G., Raynaud, D., Schilt, A., Schwander, J., Selmo, E., Souchez, R., Spahni, R., Stauffer, B., Steffensen, J. P., Stenni, B., Stocker, T. F., Tison, J. L., Werner, M., and Wolff, E. W. (2007). Orbital and millennial Antarctic climate variability over the past 800,000 years. *Science*, 317(5839):793–796.

Keigwin, L. D. (1998). Glacial-age hydrography of the far northwest Pacific Ocean. *Paleoceanography*, 13(4):323–339.

Khripounoff, A. and Alberic, P. (1991). Settling of particles in a hydrothermal vent field (East Pacific Rise 13°N) measured with sediment traps. *Deep Sea Research Part A. Oceanographic Research Papers*, 38(6):729–744.

Kim, M., Hwang, J., Kim, H. J., Kim, D., Yang, E. J., Ducklow, H. W., Hyoung, S. L., Lee, S. H., Park, J., and Lee, S. (2015). Sinking particle flux in the sea ice zone of the Amundsen Shelf, Antarctica. *Deep Sea Research Part I: Oceanographic Research Papers*, 101:110–117.

Knox, F. and McElroy, M. B. (1984). Changes in atmospheric CO_2: Influence of the marine biota at high latitude. *Journal of Geophysical Research*, 89(D3):4629.

Kobayashi, H., Abe-Ouchi, A., and Oka, A. (2015). Role of Southern Ocean stratification in glacial atmospheric CO_2 reduction evaluated by a three-dimensional ocean general circulation model. *Paleoceanography*, 30(9):1202–1216.

Kohfeld, K. E., Anderson, R. F., and Lynch-Stieglitz, J. (2000). Carbon isotopic disequilibrium in polar planktonic foraminifera and its impact on modern and Last Glacial Maximum reconstructions. *Paleoceanography*, 15(1):53–64.

Kohfeld, K. E., Fairbanks, R. G., Smith, S. L., and Walsh, I. D. (1996). *Neogloboquadrina Pachyderma* (sinistral coiling) as paleoceanographic tracers in polar oceans: Evidence from northeast water polynya plankton tows, sediment traps, and surface sediments. *Paleoceanography*, 11(6):679–699.

Kohfeld, K. E., Le Quéré, C., Harrison, S. P., and Anderson, R. F. (2005). Role of marine biology in glacial-interglacial CO_2 cycles. *Science*, 308(5718):74–8.

Kroopnick, P. (1985). The distribution of ^{13}C of ΣCO_2 in the world oceans. *Deep-Sea Research*, 32(I):57–84.

Krueger, S., Leuschner, D., Ehrmann, W., Schmiedl, G., and Mackensen, A. (2012). North Atlantic Deep Water and Antarctic Bottom Water variability during the last 200ka recorded in an abyssal sediment core off South Africa. *Global and Planetary Change*, 80-81:180–189.

Kusahara, K., Williams, G. D., Tamura, T., Massom, R., and Hasumi, H. (2017). Dense Shelf Water spreading from Antarctic coastal polynyas to the deep Southern Ocean: A regional circumpolar model study. *Journal of Geophysical Research: Oceans*, 122:6238–6253.

Kyle, P., McIntosh, W., Schmidt-Thomé, M., Mueller, P., Tessensohn, F., Noll, M., Wörner, G., Wörner, G., Viereck, L., Behrendt, J., Ellerman, P., Wright, A., Moore, J., Stump, E., Borg, S., and Sheridan, M. (1990). A. McMurdo Volcanic Group Western Ross embayment. In *Volcanoes of the Antarctic Plate and Southern Oceans*, pages 18–145.

Lambelet, M., van de Flierdt, T. V. D., Crocket, K., Rehkamper, M., Kreissig, K., Coles, B., Rijkenberg, M. J., Gerringa, L. J., de Baar, H. J., and Steinfeldt, R. (2016). Neodymium isotopic composition and concentration in the western North Atlantic Ocean: Results from the GEOTRACES GA02 section. *Geochimica et Cosmochimica Acta*, 177:1–29.

Lambert, F., Delmonte, B., Petit, J. R., Bigler, M., Kaufmann, P. R., Hutterli, M. a., Stocker, T. F., Ruth, U., Steffensen, J. P., and Maggi, V. (2008). Dust-climate couplings over the past 800,000 years from the EPICA Dome C ice core. *Nature*, 452(7187):616–9.

Lamy, F., Gersonde, R., Winckler, G., Esper, O., Jaeschke, A., Kuhn, G., Ullermann, J., Martínez-García, A., Lambert, F., and Kilian, R. (2014). Increased Dust Deposition in the Pacific Southern Ocean During Glacial Periods. *Science*, 343(6169):403–407.

Lang, N. and Wolff, E. W. (2011). Interglacial and glacial variability from the last 800 ka in marine, ice and terrestrial archives. *Climate of the Past*, 7(2):361–380.

Lang Farmer, G., Licht, K. J., Swope, R. J., and Andrews, J. (2006). Isotopic constraints on the provenance of fine-grained sediment in LGM tills from the Ross Embayment, Antarctica. *Earth and Planetary Science Letters*, 249(1-2):90–107.

Lee, J.-M., Boyle, E. A., Gamo, T., Obata, H., Norisuye, K., and Echegoyen, Y. (2015a). Impact of anthropogenic Pb and ocean circulation on the recent distribution of Pb isotopes in the Indian Ocean. *Geochimica et Cosmochimica Acta*, 170:126–144.

Lee, M. J., Lee, J. I., Kim, T. H., Lee, J., and Nagao, K. (2015b). Age, geochemistry and Sr-Nd-Pb isotopic compositions of alkali volcanic rocks from Mt. Melbourne and the western Ross Sea, Antarctica. *Geosciences Journal*, 19(4):681–695.

Licht, K. J., Cunningham, W., Andrews, J. T., Domack, E. W., and Jennings, A. (1998). Establishing chronologies from acid-insoluble organic ^{14}C dates on Antarctic (Ross Sea) and Arctic (North Atlantic) marine sediments. *Polar Research*, 17(2):203–216.

Licht, K. J., Dunbar, N. W., Andrews, J. T., and Jennings, A. E. (1999). Distinguishing subglacial till and glacial marine diamictons in the western Ross Sea, Antarctica: Implications for a last glacial maximum grounding line. *Bulletin of the Geological Society of America*, 111(1):91–103.

Licht, K. J., Jennings, A. E., Andrews, J. T., and Williams, K. M. (1996). Chronology of late Wisconsin ice retreat from the western Ross Sea, Antarctica. *Geology*, 24(3):223–226.

Licht, K. J., Lederer, J. R., and Swope, R. J. (2005). Provenance of LGM glacial till (sand fraction) across the Ross embayment, Antarctica. *Quaternary Science Reviews*, 24(12-13):1499–1520.

Ling, H., Burton, K., O'Nions, R., Kamber, B., von Blanckenburg, F., Gibb, A., and Hein, J. (1997). Evolution of Nd and Pb isotopes in Central Pacific seawater from ferromanganese crusts. *Earth and Planetary Science Letters*, 146(1-2):1–12.

Lippold, J., Gutjahr, M., Blaser, P., Christner, E., Ferreira, M. L. d. C., Mulitza, S., Christl, M., Wombacher, F., Böhm, E., Antz, B., Cartapanis, O., Vogel, H., and Jaccard, S. L. (2016). Deep water provenience and dynamics of the (de)glacial Atlantic meridional overturning circulation. *Earth and Planetary Science Letters*, 445:68–78.

Lisiecki, L. E. (2010). Links between eccentricity forcing and the 100,000-year glacial cycle. *Nature Geoscience*, 3(5):349–352.

Lisiecki, L. E. (2014). Atlantic overturning responses to obliquity and precession over the last 3 Myr. *Paleoceanography*, 29(2):71–86.

Lisiecki, L. E. and Raymo, M. E. (2005). A Pliocene-Pleistocene stack of 57 globally distributed benthic ^{18}O records. *Paleoceanography*, 20(1):1–17.

Loubere, P. (1987). Late Pliocene variations in the carbon isotope values of North Atlantic benthic Foraminifera: Biotic control of the isotopic record? *Marine Geology*, 76(C):45–56.

Lu, Z., Hoogakker, B. A. A., Hillenbrand, C.-d., Zhou, X., Thomas, E., Gutchess, K. M., Lu, W., Jones, L., and Rickaby, R. E. (2016). Oxygen depletion recorded in upper waters of the glacial Southern Ocean. *Nature Communications*, (May 2015):1–8.

Lumpkin, R. and Speer, K. G. (2007). Global Ocean Meridional Overturning. *Journal of Physical Oceanography*, 37(10):2550–2562.

Lutze, G. and Coulbourn, W. (1984). Recent benthic foraminifera from the continental margin of northwest Africa: Community structure and distribution. *Marine Micropaleontology*, 8(5):361–401.

Lynch-Stieglitz, J., Stocker, T. F., Broecker, W. S., and Fairbanks, R. G. (1995). The influence of air-sea exchange on the isotopic composition of oceanic carbon: Observations and modeling. *Global Biogeochemical Cycles*, 9(4):653–665.

Mackensen, A., Hubberten, H.-W., Bickert, T., and Futterer, D. (1993). The δ^{13}C in benthic foraminiferal tests of *Fontbotia Wuellerstorfi* (Scwager) relative to the δ^{13}C of dissolved inorganic carbon in the Southern Ocean deep water: Implications for Glacial ocean circulation models. *Paleoceanography*, 8(5):587–610.

Mackensen, A., Hubberten, H.-W., Scheele, N., and Schlitzer, R. (1996). Decoupling of δ^{13}C ΣCO_2 and phosphate in Recent Weddell Sea deep and bottom water: Implications for glacial Southern Ocean paleoceanography. *Paleoceanography*, 11(2):203–215.

Mackensen, A. and Licari, L. (2004). *Carbon Isotopes of Live Benthic Foraminifera from the South Atlantic: Sensitivity to Bottom Water Carbonate Saturation State and Organic Matter Rain Rates*, pages 623–644. Springer Berlin Heidelberg, Berlin, Heidelberg.

Mackensen, A., Rudolph, M., and Kuhn, G. (2001). Late Pleistocene deep-water circulation in the subantarctic eastern Atlantic. *Global and Planetary Change*, pages 197–229.

Marchitto, T. M. and Broecker, W. S. (2006). Deep water mass geometry in the glacial Atlantic Ocean: A review of constraints from the paleonutrient proxy Cd/Ca. *Geochemistry, Geophysics, Geosystems*, 7(Q12003).

Marchitto, T. M., Curry, W. B., Lynch-Stieglitz, J., Bryan, S. P., Cobb, K. M., and Lund, D. C. (2014). Improved oxygen isotope temperature calibrations for cosmopolitan benthic foraminifera. *Geochimica et Cosmochimica Acta*, 130:1–11.

Marino, M., Maiorano, P., Lirer, F., and Pelosi, N. (2009). Response of calcareous nannofossil assemblages to paleoenvironmental changes through the mid-Pleistocene revolution at Site 1090 (Southern Ocean). *Palaeogeography, Palaeoclimatology, Palaeoecology*, 280(3-4):333–349.

Martin, E. E. and Haley, B. A. (2000). Fossil fish teeth as proxies for seawater Sr and Nd isotopes. *Geochimica et Cosmochimica Acta Cosmochim. Acta*, 64(5):835–847.

Martin, J. H. (1990). Glacial-Interglacial CO_2 change: The Iron Hypothesis. *Paleoceanography*, 5(1):1–13.

Martínez-García, A., Rosell-Melé, A., Geibert, W., Gersonde, R., Masqué, P., Gaspari, V., and Barbante, C. (2009). Links between iron supply, marine productivity, sea surface temperature, and CO_2 over the last 1.1 Ma. *Paleoceanography*, 24(1).

Martínez-García, A., Rosell-Melé, A., Jaccard, S. L., Geibert, W., Sigman, D. M., and Haug, G. H. (2011). Southern Ocean dust–climate coupling over the past four million years. *Nature*, 476(7360):312–315.

Martínez-García, A., Sigman, D. M., Ren, H., Anderson, R. F., Straub, M., Hodell, D. A., Jaccard, S. L., Eglinton, T. I., and Haug, G. H. (2014). Iron fertilization of the Subantarctic ocean during the last ice age. *Science*, 343(6177):1347–50.

Matsumoto, K. and Lynch-stieglitz, J. (1999). Similar glacial and Holocene deep water circulation inferred from southeast Pacific benthic foraminiferal carbon isotope composition. *Paleoceanography*, 14(2):149–163.

Matsumoto, K., Lynch-Stieglitz, J., and Anderson, R. F. (2001). Similar glacial and Holocene Southern Ocean hydrography. *Paleoceanography*, 16(5):445–454.

Mazaud, A., Michel, E., Dewilde, F., and Turon, J. L. (2010). Variations of the Antarctic Circumpolar Current intensity during the past 500 ka. *Geochemistry, Geophysics, Geosystems*, 11(8):1–10.

McCave, I. N., Carter, L., and Hall, I. R. (2008). Glacial–interglacial changes in water mass structure and flow in the SW Pacific Ocean. *Quaternary Science Reviews*, 27(19-20):1886–1908.

McCave, I. N., Crowhurst, S. J., Kuhn, G., Hillenbrand, C.-D., and Meredith, M. P. (2013). Minimal change in Antarctic Circumpolar Current flow speed between the last glacial and Holocene. *Nature Geoscience*, 7(2):113–116.

McClymont, E. L. and Rosell-Melé, A. (2005). Links between the onset of modern Walker circulation and the mid-Pleistocene climate transition. *Geology*, 33(5):389.

McClymont, E. L., Rosell-Melé, A., Haug, G. H., and Lloyd, J. M. (2008). Expansion of subarctic water masses in the North Atlantic and Pacific oceans and implications for mid-Pleistocene ice sheet growth. *Paleoceanography*, 23(4):1–12.

McClymont, E. L., Sosdian, S. M., Rosell-Melé, A., and Rosenthal, Y. (2013). Pleistocene sea-surface temperature evolution: Early cooling, delayed glacial intensification, and implications for the mid-Pleistocene climate transition. *Earth-Science Reviews*, 123:173–193.

McCorkle, D. C., Keigwin, L. D., Corliss, B. H., and Emerson, S. R. (1990). The influence of microhabitats on the carbon isotopic composition of deep-sea benthic foraminifera. *Paleoceanography*, 5(2):161–185.

McCorkle, D. C., Martin, P. a., Lea, D. W., and Klinkhammer, G. P. (1995). Evidence of a dissolution effect on benthic foraminiferal shell chemistry: δ^{13}C, Cd/Ca, Ba/Ca, and Sr/Ca results from the Ontong Java Plateau. *Paleoceanography*, 10(4):699–714.

McKay, R. M., Barrett, P. J., Levy, R. S., Naish, T. R., Golledge, N. R., and Pyne, A. (2016). Antarctic Cenozoic climate history from sedimentary records: ANDRILL and beyond. *Philosophical Transactions of the Royal Society A*, (374).

McKay, R. M., Dunbar, G. B., Naish, T. R., Barrett, P. J., Carter, L., and Harper, M. (2008). Retreat history of the Ross Ice Sheet (Shelf) since the Last Glacial Maximum from deep-basin sediment cores around Ross Island. *Palaeogeography, Palaeoclimatology, Palaeoecology*, 260(1-2):245–261.

Members, W. D. P. (2013). Onset of deglacial warming in West Antarctica driven by local orbital forcing. *Nature*, 500(7463):440–444.

Menviel, L., Spence, P., and England, M. H. (2015). Contribution of enhanced Antarctic Bottom Water formation to Antarctic warm events and millennial-scale atmospheric CO^2 increase. *Earth and Planetary Science Letters*, 413:37–50.

Milankovich, M. (1941). Canon of insolation and the ice-age problem : (Kanon der Erdbestrahlung und seine Anwendung auf das Eiszeitenproblem) Belgrade, 1941. Israel Program for Scientific Translations. *K. Serb. Akad. Beogr. Spec. Publ.*, 132.

Miller, K. G. and Lohmann, G. P. (1982). Experimental distribution of recent benthic foraminifera on the northeast United State Continental Slope. *Geological Society of America Bulletin*, 93(November 1980):200–206.

Mix, A. (2001). Environmental processes of the ice age: land, oceans, glaciers (EPILOG). *Quaternary Science Reviews*, 20(4):627–657.

Mix, A. C., Le, J., and Shackleton, N. J. (1995). Benthic foraminiferal stable isotope stratigraphy of Site 846: 0-1.8 Ma. *Proceedings of the Ocean Drilling Program, Scientific Results*, 138(1991):839–854.

Molina-Kescher, M., Frank, M., Tapia, R., Ronge, T. A., Nürnberg, D., and Tiedemann, R. (2016). Reduced admixture of North Atlantic Deep Water to the deep central South Pacific during the last two glacial periods. *Paleoceanography*, 31:651–668.

Monien, D., Kuhn, G., von Eynatten, H., and Talarico, F. M. (2012). Geochemical provenance analysis of fine-grained sediment revealing Late Miocene to recent Paleo-Environmental changes in the Western Ross Sea, Antarctica. *Global and Planetary Change*, 96-97:41–58.

Moy, A. D., Howard, W. R., and Gagan, M. K. (2006). Late Quaternary palaeoceanography of the Circumpolar Deep Water from the South Tasman Rise. *Journal of Quaternary Science*, 21(7):763–777.

Naish, T. R., Powell, R. D., Levy, R., Wilson, G. S., Scherer, R. P., Talarico, F., Krissek, L. A., Niessen, F., Pompilio, M., Wilson, T., Carter, L., DeConto, R. M., Huybers, P., McKay, R. M., Pollard, D., Ross, J., Winter, D., Barrett, P., Browne, G., Cody, R., Cowan, E. A., Crampton, J., Dunbar, G., Dunbar, N., Florindo, F., Gebhardt, C., Graham, I., Hannah, M., Hansaraj, D., Harwood, D. M., Helling, D., Henrys, S., Hinnov, L. A., Kuhn, G., Kyle, P., Läufer, A., Maffioli, P., Magens, D., Mandernack, K., McIntosh, W., Millan, C., Morin, R., Ohneiser, C., Paulsen, T., Persico, D., Raine, I., Reed, J., Riesselman, C. R., Sagnotti, L., Schmitt, D., Sjunneskog, C., Strong, P., Taviani, M., Vogel, S., Wilch, T., Williams, T., Barrett, A. P., Browne, G., Cody, R., Cowan, E. A., Crampton, J., Dunbar, G., Dunbar, N., Florindo, F., Gebhardt, C., Graham, I., Hannah, M., Hansaraj, D., Harwood, D. M., Helling, D., Henrys, S., Hinnov, L. A., Kuhn, G., Kyle, P., Läufer, A., Maffioli, P., Magens, D., Mandernack, K., McIntosh, W., Millan, C., Morin, R., Ohneiser, C., Paulsen, T., Persico, D., Raine, I., Reed, J., Riesselman, C. R., Sagnotti, L., Schmitt, D., Sjunneskog, C., Strong, P., Taviani, M., Vogel, S., Wilch, T., and Williams, T. (2009). Obliquity-paced Pliocene West Antarctic ice sheet oscillations. *Nature*, 458(7236):322–328.

Nardini, I., Armienti, P., Rocchi, S., Dallai, L., and Harrison, D. (2009). Sr-Nd-Pb-H-O isotope and geochemical constraints on the genesis of cenozoic magmas from the West Antarctic Rift. *Journal of Petrology*, 50(7):1359–1375.

Newkirk, D. R. and Martin, E. E. (2009). Circulation through the Central American Seaway during the Miocene carbonate crash. *Geology*, 37(1):87–90.

Ninnemann, U. S. and Charles, C. D. (1997). Regional differences in Quaternary Subantarctic nutrient cycling: Link to intermediate and deep water ventilation. *Paleoceanography*, 12(4):560–567.

Ninnemann, U. S. and Charles, C. D. (2002). Changes in the mode of Southern Ocean circulation over the last glacial cycle revealed by foraminiferal stable isotopic variability. *Earth and Planetary Science Letters*, 201(2):383–396.

Noble, T. L., Piotrowski, A. M., and McCave, I. N. (2013). Neodymium isotopic composition of intermediate and deep waters in the glacial southwest Pacific. *Earth and Planetary Science Letters*, 384:27–36.

Nürnberg, C. C., Bohrmann, G., and Schltiter, M. (1997). Barium accumulation in the Atlantic sector of the Southern Ocean: Results from 190,000-year records. *Paleoceanography*, 12(4):594–603.

Oke, P. R. and England, M. H. (2004). Oceanic response to changes in the latitude of the Southern Hemisphere subpolar westerly winds. *Journal of Climate*, 17(5):1040–1054.

Olbers, D., Gouretski, V., Seiß, G., and Schröter, J. (1992). *Hydrographic Atlas of the Southern Ocean*. Alfred Wegener Institute, Bremerhaven.

Oliver, K., Hoogakker, B. A. A., Crowhurst, S., Henderson, G. M., Rickaby, R. E., Edwards, N. R., and Elderfield, H. (2010). A synthesis of marine sediment core δ^{13}C data over the last 150 000 years. *Climate of the Past*, 6(5):645–673.

O'Nions, R. K., Carter, S. R., Cohen, R. S., Evensen, N. M., and Hamilton, P. J. (1978). Pb, Nd and Sr isotopes in oceanic ferromanganese deposits and ocean floor basalts. *Nature*, 273(5662):435–438.

Orsi, A. H., Johnson, G., and Bullister, J. (1999). Circulation, mixing, and production of Antarctic Bottom Water. *Progress in Oceanography*, 43(1):55–109.

Orsi, A. H., Whitworth, T., and Jr, W. D. N. (1995). On the meridional extent and fronts of the Antarctic Circumpolar Current. *Deep Sea Research*, 42(5):641–673.

Orsi, A. H. and Wiederwohl, C. L. (2009). A recount of Ross Sea waters. *Deep-Sea Research Part II: Topical Studies in Oceanography*, 56(13-14):778–795.

Osborne, A. H., Newkirk, D. R., Groeneveld, J., Martin, E. E., Tiedemann, R., and Frank, M. (2014). The seawater neodymium and lead isotope record of the final stages of Central American Seaway closure. *Paleoceanography*, 29(7):715–729.

Ostlund, H. G., Craig, H., Broecker, W. S., and Spenser, D. (1987). GEOSECS Atlantic, Pacific and Indian Ocean expeditions: Shorebased data and graphics, vol. 7. *Tenchincl Reports, National Science Foundation*.

Pados, T., Spielhagen, R. F., Bauch, D., Meyer, H., and Segl, M. (2015). Oxygen and carbon isotope composition of modern planktic foraminifera and near-surface waters in the Fram Strait (Arctic Ocean) – a case study. *Biogeosciences*, 12(6):1733–1752.

Pahnke, K. and Zahn, R. (2005). Southern Hemisphere water mass conversion linked with North Atlantic climate variability. *Science*, 307(5716):1741–6.

Paillard, D., Labeyrie, L., and Yiou, P. (1996). Macintosh Program performs time-series analysis. *Eos, Transactions American Geophysical Union*, 77(39):379.

Palmer, M. and Elderfield, H. (1985). Variations in the Nd isotopic composition of foraminifera from Atlantic Ocean sediments. *Earth and Planetary Science Letters*, 73(2-4):299–305.

Palmer, M. R. and Elderfield, H. (1986). Rare earth elements and neodymium isotopes in ferromanganese oxide coatings of Cenozoic foraminifera from the Atlantic Ocean. 50(65).

Park, Y.-H., Vivier, F., Roquet, F., and Kestenare, E. (2009). Direct observations of the ACC transport across the Kerguelen Plateau. *Geophysical Research Letters*, 36(18):L18603.

Pena, L. D. and Goldstein, S. L. (2014). Thermohaline circulation crisis and impacts during the mid-Pleistocene transition. *Science*, 345(6194):318–322.

Peterson, C. D., Lisiecki, L. E., and Stern, J. V. (2014). Deglacial whole-ocean δ^{13}C change estimated from 480 benthic foraminiferal records. *Paleoceanography*, 29(6):549–563.

Piepgras, D. J. and Wasserburg, G. (1985). Strontium and neodymium isotopes in hot springs on the East Pacific Rise and Guaymas Basin. *Earth and Planetary Science Letters*, 72(4):341–356.

Piepgras, D. J. and Wasserburg, G. (1987). Rare earth element transport in the western North Atlantic inferred from Nd isotopic observations. *Geochimica et Cosmochimica Acta*, 51(5):1257–1271.

Piepgras, D. J., Wasserburg, G., and Dasch, E. J. (1979). The isotopic composition of Nd in different ocean masses. *Earth and Planetary Science Letters*, 45(2):223–236.

Piotrowski, A. M. (2005). Temporal relationships of carbon cycling and ocean circulation at Glacial boundaries. *Science*, 307(5717):1933–1938.

Piotrowski, A. M., Banakar, V. K., Scrivner, A. E., Elderfield, H., Galy, A., and Dennis, A. (2009). SOM Indian Ocean circulation and productivity during the last glacial cycle. *Earth and Planetary Science Letters*, (cm).

Piotrowski, A. M., Galy, A., Nicholl, J., Roberts, N. L., Wilson, D. J., Clegg, J., and Yu, J. (2012). Reconstructing deglacial North and South Atlantic deep water sourcing using foraminiferal Nd isotopes. *Earth and Planetary Science Letters*, 357-358:289–297.

Piotrowski, A. M., Goldstein, S. L., Hemming, S. R., Fairbanks, R. G., and Zylberberg, D. R. (2008). Oscillating glacial northern and southern deep water formation from combined neodymium and carbon isotopes. *Earth and Planetary Science Letters*, 272:394–405.

Pollard, D. and DeConto, R. M. (2009). Modelling West Antarctic ice sheet growth and collapse through the past five million years. *Nature*, 458(7236):329–332.

Pollard, D. and Deconto, R. M. (2012). Description of a hybrid ice sheet-shelf model, and application to Antarctica. *Geoscientific Model Development*, 5(5):1273–1295.

Pomiès, C., Davies, G. R., and Conan, S. M.-H. (2002). Neodymium in modern foraminifera from the Indian Ocean: implications for the use of foraminiferal Nd isotope compositions in paleo-oceanography. *Earth and Planetary Science Letters*, 203(3-4):1031–1045.

Pourmand, A., Dauphas, N., and Ireland, T. J. (2012). A novel extraction chromatography and MC-ICP-MS technique for rapid analysis of REE, Sc and Y: Revising CI-chondrite and Post-Archean Australian Shale (PAAS) abundances. *Chemical Geology*, 291:38–54.

Pudsey, C. J. and Camerlenghi, A. (1998). Glacial–interglacial deposition on a sediment drift on the Pacific margin of the Antarctic Peninsula. *Antarctic Science*, 10(03).

Pugh, R., McCave, I. N., Hillenbrand, C.-D., and Kuhn, G. (2009). Circum-Antarctic age modelling of Quaternary marine cores under the Antarctic Circumpolar Current: Ice-core dust–magnetic correlation. *Earth and Planetary Science Letters*, 284(1-2):113–123.

Quaia, T. and Cespuglio, G. (2000). Oxygen and carbon stable isotopes in foraminifers from cores ANTA91-8 and ANTA91-2 (Ross Sea). *Terra Antarctica Reports*, 4.

Rahmstorf, S. (2002). Ocean circulation and climate during the past 120,000 years. *Nature*, 419(6903):207–214.

Raymo, M. E., Lisiecki, L. E., and Nisancioglu, K. H. (2006). Plio-Pleistocene ice volume, Antarctic climate, and the global δ^{18}O record. *Science*, 313(July):492–495.

Raymo, M. E., Oppo, D. W., and Curry, W. B. (1997). The mid-Pleistocene climate transition: A deep sea carbon isotopic perspective. *Paleoceanography*, 12(4):546–559.

Raymo, M. E., Ruddiman, W. F., Backman, J., Clement, B. M., and Martinson, D. G. (1989). Late Pliocene variation in Northern Hemisphere ice sheets and North Atlantic deep water circulation. *Paleoceanography*, 4(4):413–446.

Reid, J. L. (1986). On the total geostrophic circulation of the South Pacific Ocean: Flow patterns, tracers and transports. *Progress in Oceanography*, 16(1):1–61.

Reid, J. L. and Lynn, R. J. (1971). On the influence of the Norweigen-Greenland and Weddel seas upon the bottom waters of the Indian and Pacific oceans. *Deep-Sea Research*, 18(March):1063–1088.

Reimer, P. J., Bard, E., Bayliss, A., Beck, J. W., Blackwell, P. G., Ramsey, C. B., Buck, C. E., Cheng, H., Edwards, R. L., Friedrich, M., Grootes, P. M., Guilderson, T. P., Haflidason, H., Hajdas, I., Hatté, C., Heaton, T. J., Hoffmann, D. L., Hogg, A. G., Hughen, K. A., Kaiser, K. F., Kromer, B., Manning, S. W., Niu, M., Reimer, R. W., Richards, D. A., Scott, E. M., Southon, J. R., Staff, R. A., Turney, C. S. M., and van der Plicht, J. (2013). IntCal13 and Marine13 Radiocarbon Age Calibration Curves 0–50,000 Years cal BP. *Radiocarbon*, 55(04):1869–1887.

Revel-Rolland, M., De Deckker, P., Delmonte, B., Hesse, P. P., Magee, J. W., Basile-Doelsch, I., Grousset, F., and Bosch, D. (2006). Eastern Australia: A possible source of dust in East Antarctica interglacial ice. *Earth and Planetary Science Letters*, 249(1-2):1–13.

Reynolds, B. C., Frank, M., and O'Nions, R. K. (1999). Nd- and Pb-isotope time series from Atlantic ferromanganese crusts: Implications for changes in provenance and paleocirculation over the last 8 Myr. *Earth and Planetary Science Letters*, 173(4):381–396.

Rickaby, R. E. M. and Elderfield, H. (2005). Evidence from the high-latitude North Atlantic for variations in Antarctic Intermediate water flow during the last deglaciation. *Geochemistry, Geophysics, Geosystems*, 6(5).

Rickli, J., Gutjahr, M., Vance, D., Fischer-Gödde, M., Hillenbrand, C.-D., and Kuhn, G. (2014). Neodymium and hafnium boundary contributions to seawater along the West Antarctic continental margin. *Earth and Planetary Science Letters*, 394:99–110.

Roberts, J., Gottschalk, J., Skinner, L. C., Peck, V. L., Kender, S., Elderfield, H., Waelbroeck, C., Vázquez Riveiros, N., and Hodell, D. A. (2016). Evolution of South Atlantic density and chemical stratification across the last deglaciation. *Proceedings of the National Academy of Sciences*, 113(3):514–519.

Roberts, N. L., Piotrowski, A. M., Elderfield, H., Eglinton, T. I., and Lomas, M. W. (2012). Rare earth element association with foraminifera. *Geochimica et Cosmochimica Acta*, 94:57–71.

Roberts, N. L., Piotrowski, A. M., McManus, J. F., and Keigwin, L. D. (2010). Synchronous deglacial overturning and water mass source changes. *Science*, 327(5961):75–8.

Robinson, R. S. and Sigman, D. M. (2008). Nitrogen isotopic evidence for a poleward decrease in surface nitrate within the ice age Antarctic. *Quaternary Science Reviews*, 27(9-10):1076–1090.

Rocchi, S., Armienti, P., D'Orazio, M., Tonarini, S., Wijbrans, J. R., and Di Vincenzo, G. (2002). Cenozoic magmatism in the western Ross Embayment: Role of mantle plume versus plate dynamics in the development of the West Antarctic Rift System. *Journal of Geophysical Research: Solid Earth*, 107(B9):ECV 5–1–ECV 5–22.

Rocholl, A., Stein, M., Molzahn, M., Hart, S. R., and Wörner, G. (1995). Geochemical evolution of rift magmas by progressive tapping of a stratified mantle source beneath the Ross Sea Rift, Northern Victoria Land, Antarctica. *Earth and Planetary Science Letters*, 131(3-4):207–224.

Ronge, T. A., Steph, S., Tiedemann, R., Prange, M., Merkel, U., Nürnberg, D., and Kuhn, G. (2015). Pushing the boundaries: Glacial/interglacial variability of intermediate and deep waters in the southwest Pacific over the last 350,000 years. *Paleoceanography*, 30(2):23–38.

Ronge, T. A., Tiedemann, R., Lamy, F., Köhler, P., Alloway, B. V., De Pol-Holz, R., Pahnke, K., Southon, J., and Wacker, L. (2016). Radiocarbon constraints on the extent and evolution of the South Pacific glacial carbon pool. *Nature Communications*, 7(May):11487.

Russon, T., Elliot, M., Kissel, C., Cabioch, G., De Deekker, P., and Corrège, T. (2009). Middle-late pleistocene deep water circulation in the southwest subtropical pacific. *Paleoceanography*, 24(4).

Russon, T., Paillard, D., and Elliot, M. (2010). Potential origins of 400-500 kyr periodicities in the ocean carbon cycle: A box model approach. *Global Biogeochemical Cycles*, 24(2).

Rutberg, R. R., Hemming, S. R., and Goldstein, S. L. (2000). Reduced North Atlantic Deep Water flux to the glacial Southern Ocean inferred from neodymium isotope ratios. *Nature*, 405:935–8.

Santoso, A., England, M. H., and Hirst, A. C. (2006). Circumpolar Deep Water Circulation and Variability in a Coupled Climate Model. *Journal of Physical Oceanography*, 36:1523–1552.

Sarmiento, J. L., Gruber, N., Brzezinski, M. A., and Dunne, J. P. (2004). High-latitude controls of thermocline nutrients and low latitude biological productivity. *Nature*, 427(6969):56–60.

Sarmiento, J. L. and Toggweiler, J. R. (1984). A new model for the role of the oceans in determining atmospheric pCO_2. *Nature*, 308(5960):621–624.

Schlitzer, R. (2000). Electronic atlas of WOCE hydrographic and tracer data now available. *Eos, Transactions American Geophysical Union*, 81(5):45–45.

Schlitzer, R. (2015). Ocean Data View. *http://odv.awi.de*.

Schmitt, J., Schneider, R., Elsig, J., Leuenberger, D., Lourantou, A., Chappellaz, J., Köhler, P., Joos, F., Stocker, T. F., Leuenberger, M., and Fischer, H. (2012). Carbon isotope constraints on the deglacial CO_2 rise from ice cores. *Science*, 336(6082):711–4.

Shackleton, N. J. (1974). Attainment of isotopic equilibrium ocean water and the benthic foraminifera genus *Uvigerina*: Isotopic changes in the ocean during the last glacial. In *Les methodes quantitative d'etude des variations due climat au cours du Pleistocene*, volume 219, pages 203–209. Colloques Internationaux du C.N.R.S, Paris.

Shackleton, N. J. and Opdyke, N. D. (1976). Oxygen-isotope and paleo- magnetic stratigraphy of Pacific core V28-239 late Pliocene to latest Pleistocene. In Cline, R. M. and Hays, J. D., editors, *Investigation of Late Quaternary Paleoceanography and Paleoclimatology*, pages 449–464. Geological Society of America Memoir.

Siani, G., Michel, E., De Pol-Holz, R., Devries, T., Lamy, F., Carel, M., Isguder, G., Dewilde, F., and Lourantou, A. (2013). Carbon isotope records reveal precise timing of enhanced Southern Ocean upwelling during the last deglaciation. *Nature communications*, 4(May):2758.

Siegel, D., Buesseler, K., Doney, S., Sailley, S., Behrenfeld, M., and Boyd, P. (2014). Global Biogeochemical Cycles. *Global Biogeochemical Cycles*, 28:181–196.

Siegenthaler, U. and Wenk, T. (1984). Rapid atmospheric CO_2 variations and ocean circulation. *Nature*, 308(5960):624–626.

Sigman, D. M. and Boyle, E. A. (2000). Glacial/interglacial variations in atmospheric carbon dioxide. *Nature*, 407(October):859–869.

Sigman, D. M., Hain, M. P., and Haug, G. H. (2010). The polar ocean and glacial cycles in atmospheric CO_2 concentration. *Nature*, 466(7302):47–55.

Sikes, E. L., Cook, M. S., and Guilderson, T. P. (2016). Reduced deep ocean ventilation in the Southern Pacific Ocean during the last glaciation persisted into the deglaciation. *Earth and Planetary Science Letters*, 438:130–138.

Sikes, E. L., Samson, C. R., Guilderson, T. P., and Howard, W. R. (2000). Old radiocarbon ages in the southwest Pacific Ocean during the last glacial period and deglaciation. *Nature*, 405(6786):555–559.

Simstich, J., Sarnthein, M., and Erlenkeuser, H. (2003). Paired δ^{18}O signals of *Neogloboquadrina pachyderma* (s) and *Turborotalita quinqueloba* show thermal stratification structure in Nordic Seas. *Marine Micropaleontology*, 48(1-2):107–125.

Singh, S. P., Singh, S. K., Goswami, V., Bhushan, R., and Rai, V. K. (2012). Spatial distribution of dissolved neodymium and εNd in the Bay of Bengal: Role of particulate matter and mixing of water masses. *Geochimica et Cosmochimica Acta*, 94:38–56.

Skinner, L. C., McCave, I. N., Carter, L., Fallon, S., Scrivner, A., and Primeau, F. (2015). Reduced ventilation and enhanced magnitude of the deep Pacific carbon pool during the last glacial period. *Earth and Planetary Science Letters*, 411:45–52.

Sloyan, B. M. and Rintoul, S. R. (2001). The Southern Ocean limb of the global deep overturning circulation. *Journal of Physical Oceanography*, 31(1):143–173.

Sloyan, B. M., Talley, L. D., Chereskin, T. K., Fine, R., and Holte, J. (2010). Antarctic Intermediate Water and Subantarctic Mode Water formation in the southeast Pacific: The role of turbulent mixing. *Journal of Physical Oceanography*, 40:1558–1574.

Smith, J. A., Hillenbrand, C.-D., Pudsey, C. J., Allen, C. S., and Graham, A. G. (2010). The presence of polynyas in the Weddell Sea during the Last Glacial Period with implications for the reconstruction of sea-ice limits and ice sheet history. *Earth and Planetary Science Letters*, 296(3-4):287–298.

Sosdian, S. and Rosenthal, Y. (2009). Deep-sea temperature and ice volume changes across the Pliocene-Pleistocene climate transitions. *Science*, 325(5938):306–310.

Speer, K. G., Rintoul, S. R., and Sloyan, B. M. (2000). The Diabatic Deacon Cell. *Journal of Physical Oceanography*, 30(12):3212–3222.

Staudigel, H., Doyle, P., and Zindler, A. (1985). Sr and Nd isotope systematics in fish teeth. *Earth and*, 76:45–56.

Stenni, B., Proposito, M., Gragnani, R., Flora, O., Jouzel, J., Falourd, S., and Frezzotti, M. (2002). Eight centuries of volcanic signal and climate change at Talos Dome (East Antarctica). *Journal of Geophysical Research: Atmospheres*, 107(D9):ACL 3–1–ACL 3–13.

Stephens, B. B. and Keeling, R. F. (2000). The influence of Antarctic sea ice on glacial-interglacial CO_2 variations. *Nature*, 404:171–174.

Stevens, I. G. and Stevens, D. P. (1999). Passive tracers in a general circulation model of the Southern Ocean. *Annales Geophysicae*, 17(7):971–982.

Stoll, H. M., Vance, D., and Arevalos, A. (2007). Records of the Nd isotope composition of seawater from the Bay of Bengal: Implications for the impact of Northern Hemisphere cooling on ITCZ movement. *Earth and Planetary Science Letters*, 255:213–228.

Stuiver, M. and Reimer, P. J. (1993). Extended ^{14}C data base and revised radiocarbon age calibration program. *Radiocarbon*, 35(01):215–230.

Sugden, D. E., McCulloch, R. D., Bory, A. J.-M., and Hein, A. S. (2009). Influence of Patagonian glaciers on Antarctic dust deposition during the last glacial period. *Nature Geoscience*, 2(4):281–285.

Sverdrup, H. U. (1940). Hydrology, Section 2, Discussion. *Reports of the B.A.N.Z. Antarctic Research Expedition 1921–1931, Series A, 3, Oceanography, Part 2, Section 2*, pages 88–126.

Tachikawa, K., Toyofuku, T., Basile-Doelsch, I., and Delhaye, T. (2013). Microscale neodymium distribution in sedimentary planktonic foraminiferal tests and associated mineral phases. *Geochimica et Cosmochimica Acta*, 100:11–23.

Talley, L. D. (1996). *Antarctic Intermediate Water in the South Atlantic*, pages 219–238. Springer Berlin Heidelberg.

Talley, L. D. (2013). Closure of the global overturning circulation through the Indian, Pacific and Southern Oceans: schematics and transports. *Oceanography*, 26:80–97.

Tanaka, T., Togashi, S., Kamioka, H., Amakawa, H., Kagami, H., Hamamoto, T., Yuhara, M., Orihashi, Y., Yoneda, S., Shimizu, H., Kunimaru, T., Takahashi, K., Yanagi, T., Nakano, T., Fujimaki, H., Shinjo, R., Asahara, Y., Tanimizu, M., and Dragusanu, C. (2000). JNdi-1: a neodymium isotopic reference in consistency with LaJolla neodymium. *Chemical Geology*, 168(3-4):279–281.

Taylor, S. R. and McLennan, S. M. (1985). *The Continental Crust: Its Composition and Evolution*, volume 94. Blackwell Scientific.

Thatje, S., Hillenbrand, C.-D., Mackensen, A., and Larter, R. D. (2008). Life hung by a thread: endurance of Antarctic fauna in glacial periods. *Ecology*, 89(3):682–692.

Thomas, D. J. (2004). Evidence for deep-water production in the North Pacific Ocean during the early Cenozoic warm interval. *Nature*, 430(6995):65–68.

Todd, C., Stone, J., Conway, H., Hall, B. L., and Bromley, G. (2010). Late Quaternary evolution of Reedy Glacier, Antarctica. *Quaternary Science Reviews*, 29(11-12):1328–1341.

Toggweiler, J. and Samuels, B. (1995). Effect of drake passage on the global thermohaline circulation. *Deep Sea Research Part I: Oceanographic Research Papers*, 42(4):477–500.

Toyota, T., Smith, I. J., Gough, A. J., Langhorne, P. J., Leonard, G. H., Van Hale, R. J., Mahoney, A. R., and Haskell, T. G. (2013). Oxygen isotope fractionation during the freezing of sea water. *Journal of Glaciology*, 59(216):697–710.

Tripati, A. K., Roberts, C. D., and Eagle, R. a. (2009). Coupling of CO_2 and ice sheet stability over major climate transitions of the last 20 million years. *Science*, 326(5958):1394–1397.

Ullermann, J., Lamy, F., Ninnemann, U. S., Lembke-Jene, L., Gersonde, R., and Tiedemann, R. (2016). Pacific-Atlantic Circumpolar Deep Water coupling during the last 500 ka. *Paleoceanography*, 31(6):639–650.

van de Flierdt, T. V. D., Griffiths, A. M., Lambelet, M., Little, S. H., Stichel, T., and Wilson, D. J. (2016). Subject Areas : Neodymium in the oceans: a global database , a regional comparison and implications for palaeoceanographic research. *Philosophical Transactions of the Royal Society A*, 374.

Vance, D. (2004). The use of foraminifera as a record of the past neodymium isotope composition of seawater. *Paleoceanography*, 19:1–17.

Venz, K. A. and Hodell, D. A. (2002). New evidence for changes in Plio-Pleistocene deep water circulation from Southern Ocean ODP Leg 177 Site 1090. *Palaeogeography, Palaeoclimatology, Palaeoecology*, 182:197–220.

Walter, H. J., Hegner, E., Diekmann, B., Kuhn, G., and Van der Loeff, M. M. R. (2000). Provenance and transport of terrrigenous sediment in the South Atlantic ocean and their relations to glacial and interglacial cycles: Nd and Sr isotopic evidence. *Geochimica et Cosmochimica Acta*, 64(22):3813–3827.

Wang, X. T., Sigman, D. M., Prokopenko, M. G., Adkins, J. F., Robinson, L. F., Hines, S. K., Chai, J., Studer, A. S., Martínez-García, A., Chen, T., and Haug, G. H. (2017). Deep-sea coral evidence for lower Southern Ocean surface nitrate concentrations during the last ice age. *Proceedings of the National Academy of Sciences*, pages 1–6.

Watson, A. J., Vallis, G. K., and Nikurashin, M. (2015). Southern Ocean buoyancy forcing of ocean ventilation and glacial atmospheric CO_2. *Nature Geoscience*, 8(11):861–864.

Weber, M. E., Clark, P. U., Kuhn, G., Timmermann, A., Sprenk, D., Gladstone, R., Zhang, X., Lohmann, G., Menviel, L., Chikamoto, M. O., Friedrich, T., and Ohlwein, C. (2014). Millennial-scale variability in Antarctic ice-sheet discharge during the last deglaciation. *Nature*, 510(7503):134–8.

Weber, M. E., Kuhn, G., Sprenk, D., Rolf, C., Ohlwein, C., and Ricken, W. (2012). Dust transport from Patagonia to Antarctica - A new stratigraphic approach from the Scotia Sea and its implications for the last glacial cycle. *Quaternary Science Reviews*, 36(February):177–188.

Wegner, W., Wörner, G., Harmon, R. S., and Jicha, B. R. (2011). Magmatic history and evolution of the Central American Land Bridge in Panama since Cretaceous times. *Bulletin of the Geological Society of America*, 123(3-4):703–724.

Wei, R., Abouchami, W., Zahn, R., and Masque, P. (2016). Deep circulation changes in the South Atlantic since the Last Glacial Maximum from Nd isotope and multi-proxy records. *Earth and Planetary Science Letters*, 434:18–29.

Whitworth III, T. (1988). The Antarctic Circmpolar Current. *Oceanus*, 35:53–58.

Williams, G. D., Aoki, S., Jacobs, S. S., Rintoul, S. R., Tamura, T., and Bindoff, N. L. (2010). Antarctic Bottom Water from the Adélie and George V Land coast, East Antarctica (140–149°E). *Journal of Geophysical Research*, 115(C4):C04027.

Wilson, D. J. (2011). *Investigating Nd and Pb isotopes as paleoceanographic proxies in the Indian Ocean: influences of water mass sourcing and boundary exchange*. Phd thesis, University of Cambridge.

Wilson, D. J., Galy, A., Piotrowski, A. M., and Banakar, V. K. (2015a). Quaternary climate modulation of Pb isotopes in the deep Indian Ocean linked to the Himalayan chemical weathering. *Earth and Planetary Science Letters*, 424:1–13.

Wilson, D. J., Piotrowski, A. M., Galy, A., and Banakar, V. K. (2015b). Interhemispheric controls on deep ocean circulation and carbon chemistry during the last two glacial cycles. *Paleoceanography*, 30(6):621–641.

Wilson, D. J., Piotrowski, A. M., Galy, A., and Clegg, J. A. (2013). Reactivity of neodymium carriers in deep sea sediments: Implications for boundary exchange and paleoceanography. *Geochimica et Cosmochimica Acta*, 109:197–221.

Wilson, D. J., Piotrowski, A. M., Galy, A., and McCave, I. N. (2012). A boundary exchange influence on deglacial neodymium isotope records from the deep western Indian Ocean. *Earth and Planetary Science Letters*, 341-344:35–47.

Winckler, G., Newton, R., Schlosser, P., and Crone, T. J. (2010). Mantle helium reveals Southern Ocean hydrothermal venting. *Geophysical Research Letters*, 37(5):1–5.

Winton, V., Dunbar, G., Atkins, C., Bertler, N., Delmonte, B., Andersson, P., Bowie, A., and Edwards, R. (2016). The origin of lithogenic sediment in the south-western Ross Sea and implications for iron fertilization. *Antarctic Science*, 28(February):1–11.

Woodruff, F., Savin, S. M., and Douglas, R. G. (1980). Biological fractionation of oxygen and carbon isotopes by recent benthic foraminifera. *Marine Micropaleontology*, 5:3–11.

Yamazaki, T. and Ikehara, M. (2012). Origin of magnetic mineral concentration variation in the Southern Ocean. *Paleoceanography*, 27(2):1–13.

Yokoyama, Y., Anderson, J. B., Yamane, M., Simkins, L. M., Miyairi, Y., Yamazaki, T., Koizumi, M., Suga, H., Kusahara, K., Prothro, L., Hasumi, H., Southon, J. R., and Ohkouchi, N. (2016). Widespread collapse of the Ross Ice Shelf during the late Holocene. *Proceedings of the National Academy of Sciences*, page 201516908.

You, Y. (2000). Implications of the deep circulation and ventilation of the Indian Ocean on the renewal mechanism of North Atlantic Deep Water. *Journal of Geophysical Research: Oceans*, 105(C10):23895–23926.

Yu, J., Anderson, R. F., Jin, Z., Menviel, L., Zhang, F., Ryerson, F. J., and Rohling, E. J. (2014). Deep South Atlantic carbonate chemistry and increased interocean deep water exchange during last deglaciation. *Quaternary Science Reviews*, 90:80–89.

Yu, J., Menviel, L., Jin, Z. D., Thornalley, D. J. R., Barker, S., Marino, G., Rohling, E. J., Cai, Y., Zhang, F., Wang, X., Dai, Y., Chen, P., and Broecker, W. S. (2016). Sequestration of carbon in the deep Atlantic during the last glaciation. *Nature Geoscience*, 9(4):319–324.

Zahn, R. and Mix, A. C. (1991). Benthic foraminiferal δ^{18}O in the oeans temperature-salinity-density field: constraints on ice age thermohaline circulation. *Paleoceanography*, 6(1):1–20.

Zahn, R., Winn, K., and Sarnthein, M. (1986). Benthic foraminiferal δ^{13}C and accumulation of organic carbon: *Uvigerina perigerina* and *Cibicidoides wuellerstorfi*. *Paleoceanography*, 1(1):27–42.

Zhang, J., Quay, P., and Wilbur, D. (1995). Carbon isotope fractionation during gas-water exchange and dissolution of CO_2. *Geochimica et Cosmochimica Acta*, 59(1):107–114.

Appendix A

Supplementary Figures

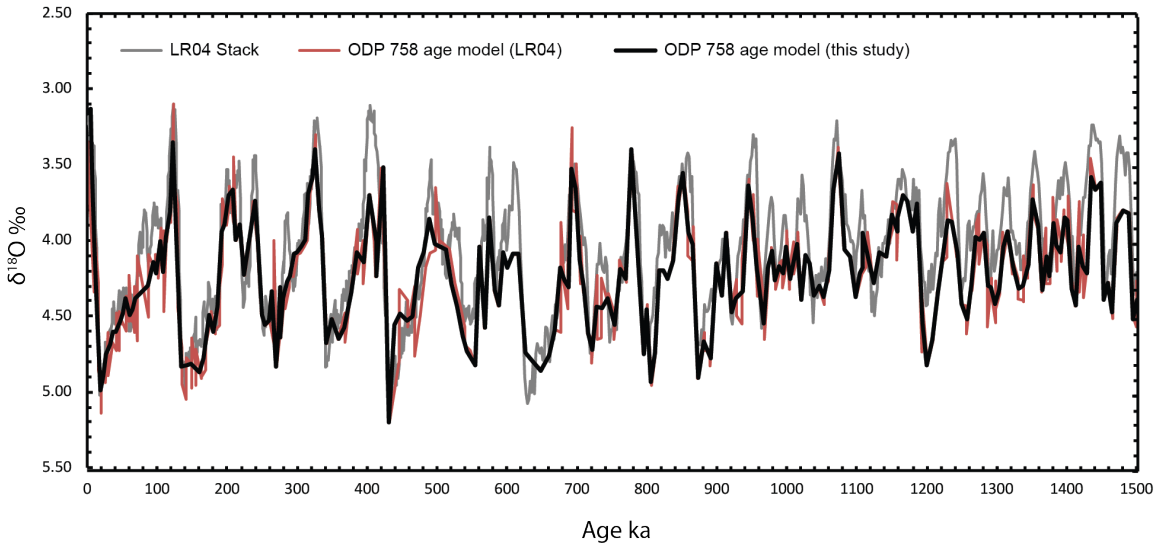

Fig. A.1 $\delta^{18}O_b$ from Ocean Drilling Project Leg 121 Site 758 plotted on the age model used in this thesis, the age model used for the LR04 stack, and the LR04 stack itself (Lisiecki and Raymo, 2005). Original $\delta^{18}O_b$ data from Site 758 published by Farrell and Janecek (1991); where multiple $\delta^{18}O_b$ data have been measured from the same depth, values have been averaged.

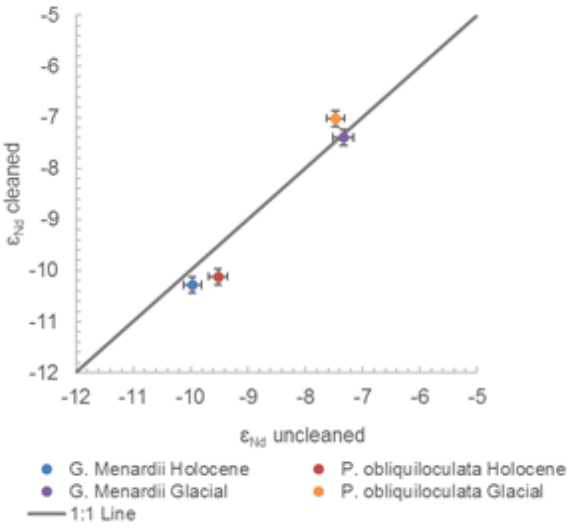

Fig. A.2 ε_{Nd} measurements made by Burton and Vance (2000) on reductively cleaned vs uncleaned planktonic foraminifera from Ocean Drilling Project Leg 121 Site 758. Results are inconclusive, with two results showing less radiogenic uncleaned values, one result showing a more radiogenic value, and one within error. The difference between clean and unclean values is much less than glacial-interglacial variability.

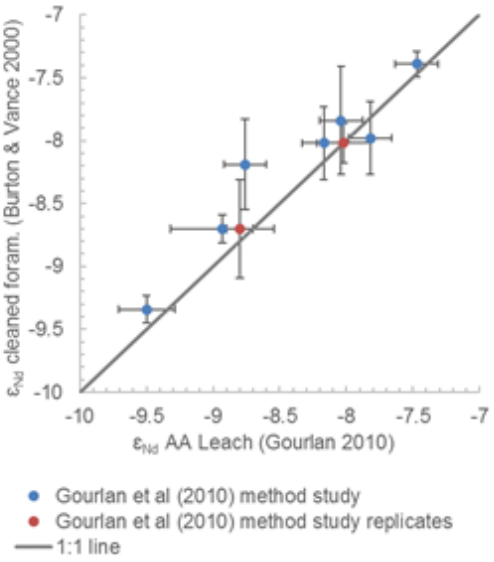

Fig. A.3 ε_{Nd} measurements made by Burton and Vance (2000) on reductively cleaned planktonic foraminifera vs measurements made by Gourlan et al. (2010) on 1N acetic acid leachates from Site 758. ε_{Nd} analyses made on cleaned planktonic foraminifera and a 1N acetic acid leach are largely within error of one another (n= 8 out of 9), suggesting they are measuring the same authigenic Fe-Mn phase. Gourlan et al. (2010) argue that this phase is acquired in the upper 1000 m. of the water column, however subsequent work has shown that it is actually acquired at or close to the sediment-water interface (Roberts et al., 2012; Tachikawa et al., 2013)

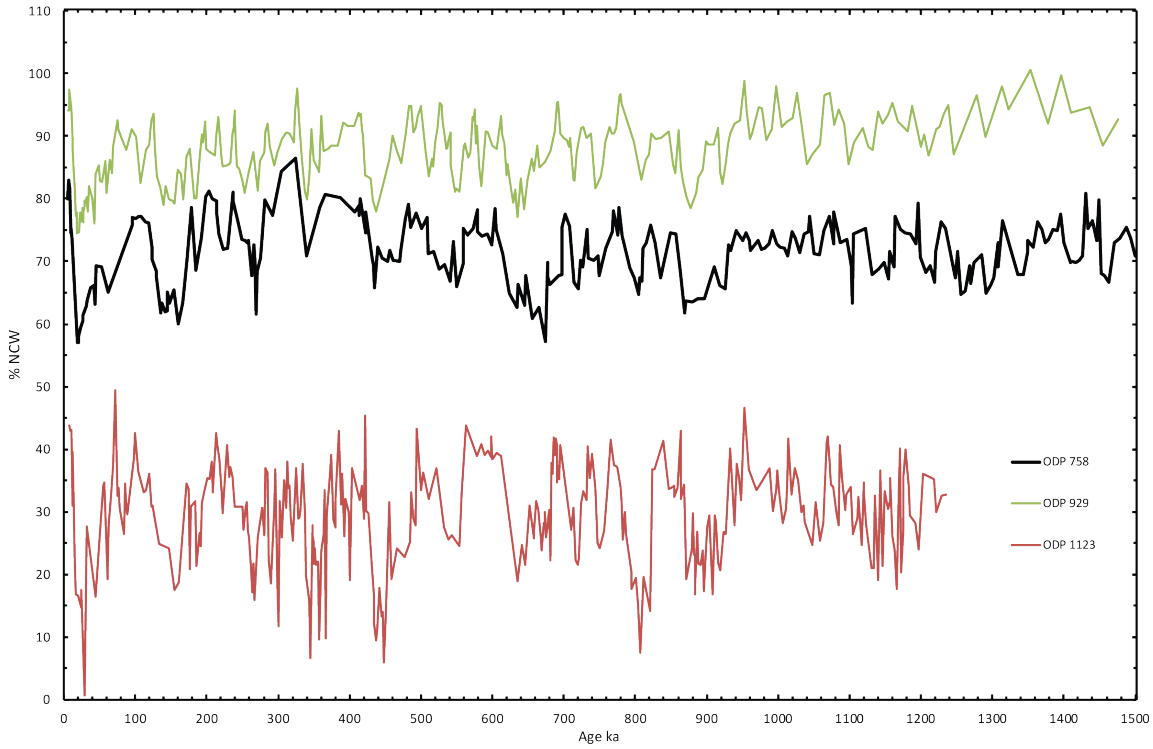

Fig. A.4 Percentages of Northern Component Water (NCW) bathing Ocean Drilling Program sites 929, 758 and 1123. Calculated using mixing calculation in section 4.4.3

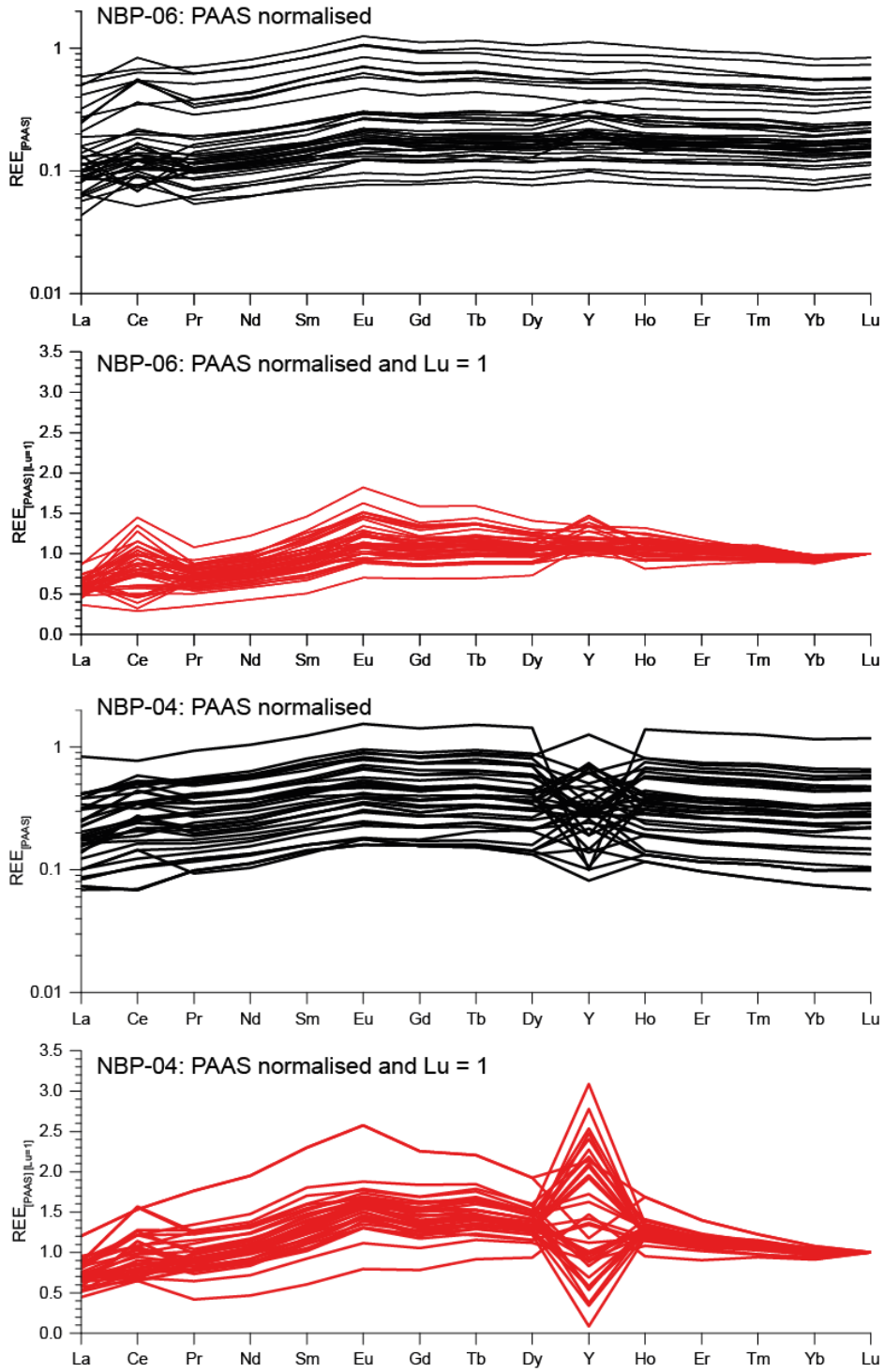

Fig. A.5 $REE^{leachate}$ data from sites NBP-04 and NBP-06, normalised to PAAS (black), and PAAS-normalised and Lu = 1 (red).

Appendix B

Supplementary Tables

Table B.1 Procedures for extraction of REE via column chromatography using 200 μL TRUSpec^{TM} resin (100-150 μm mesh size).

Step	Volume	Acids	Comments
(*sediment leachates/detrital samples only*) Redissolve samples in HNO_3 24 hours prior to starting TRU and dry down overnight	200-400 μL	3 N HNO_3	Forms a nitrate salt, allowing the sample to better stick to TRUSpec^{TM} resin
Prepare columns	c. 120 μL		Preparation of a new set of columns using TRUSpec^{TM} resin suspended in c. 120 μl Milli-Q
Wash column	1 mL (3x)	1 N HCl	Removes contaminant REE
Dissolve sample	1 mL	1 N HNO_3	
Flick acid from column			
Prime column	1 mL	1 N HNO_3	Charges the resin ready to load samples
(sediment leachates/detrital samples only) Centrifuge sample			20 minutes in 1.5 mL centrifuge tubes at 6000 rpm. Prevents particulates entering columns.
Flick acid HNO_3 from base of column			
Load sample	1 mL	1 N HNO_3	Pipette avoiding solids
Wash to microcentrifuge tube	0.5mL (2x)	1 N HNO_3	Collects Sr and other cations
Flick acid from column from base of column			Avoid capillary action
Elute to REE beaker	1 mL (3x)	1 N HCl	Collect REE

Table B.2 Procedures for purification of Nd via column chromatography using 5 mL LNSpec^{TM} resin (50-100 μm mesh size)

Step	**Volume**	**Acids**	**Comments**
Clean columns	4 mL	6N HCl	Removes contaminants from columns
Dissolve samples	100 μL	0.3 N HCl	
Equilibrate columns	1 mL (2x)	0.3 N HCl	Serves to re-equilibrate columns at a concentration of 0.3M after having washed them with 6M HCl
Load sample	100 μL	0.3 N HCl	
Rinse vial in HCl and load remaining sample	100 μL	0.3 N HCl	Ensures all cations get to column
Clean Teflon vials		Milli-Q; 6N HCl	Rinse in Milli-Q, scrub, fume in HCl with lid on for at least an hour, then re-rinse in Milli-Q
Wash to waste beaker	100 μL	0.3 N HCl	Removes unwanted cations
Wash to waste beaker	200 μL	0.3 N HCl	Removes unwanted cations
Wash to waste beaker	500 μL	0.3 N HCl	Removes unwanted cations
Elute to centrifuge tube	4.5 - 6 mL depending on column used.	0.3 N HCl	Removes unwanted cations. This step is collected in a 15 mL centrifuge tube in cases of error in column calibration
Elute to centrifuge tube	0.6 mL	0.3 N HCl	Collected in 15 mL centrifuge tube case of calibration error
Elute to cleaned Teflon vial	3.4 mL	0.3 N HCl	Collects Nd
Elute to centrifuge tube	0.5 mL	QD 6N HCl	Collected in 15 mL centrifuge tube in case of calibration error
Wash to waste beaker	2.5 mL	QD 6N HCl	Cleans remnant cations
Equilibrate and store	1 mL	0.3 N HCl	Fill columns and store in Teflon. Re-wrap columns in parafilm.

Table B.3 PC493 age model control points

Depth in core [cmbsf]	**Age [ka]**	**Description**	**Linear sed. rate (cm/ka)**
5.25	14	MIS 1/2 transition	0.38
40	71	MIS 4/5 transition	0.61
58.5	123	MIS 5e δ^{18}O minimum	0.36
66	130	MIS 5/6 transition	1.07
71.5	140	MIS 6 δ^{18}O maximum	0.55
99	191	MIS 6/7 transition	0.53
110.5	240	MIS 7.5 δ^{18}O minimum	0.23
112.5	252	MIS 8.2 δ^{18}O maximum	0.17
116	286	MIS 8.5 δ^{18}O minimum	0.1
118.5	294	MIS 8.6 δ^{18}O maximum	0.31
122	300	MIS 8/9 transition	0.58
148	337	MIS 9/10 transition	0.7
156.25	374	MIS 10/11 transition	0.22
166	424	MIS 11/12 transition	0.2
181	478	MIS 12/13 transition	0.28
193.5	533	MIS 13/14 transition	0.23
195.5	565	MIS 15 youngest δ^{18}O minimum	0.06
209	621	MIS 15/16 transition	0.24
250	676	MIS 16/17 transition	0.75
261	712	MIS 17/18 transition	0.31
269	761	MIS 18/19 transition	0.16
*282-287**	*780*	*Brunhes-Matuyama boundary*	n/a*
283	790	MIS 19/20 transition	0.48

*Not used as absolute tie point

Table B.4 ODP Leg 121 Ste 758 Age-depth tie points

Label	**Composite Depth [m]**	LR04 Age [ka]	**LSR cm/kyr**
121-758A-1-1,41	0.41	18	2.86
121-758A-1-2,1	1.51	69	2.16
121-758A-1-2,91	2.41	108	2.31
121-758A-1-2,121	2.71	123	2
121-758A-1-2,141	2.91	135	1.67
121-758A-1-3,71	3.71	186	1.57
121-758A-1-3,141	4.41	223	1.89
121-758A-1-4,11	4.61	239	1.25
121-758B-1-4,31	6.32	326	1.97
121-758B-1-4,61	6.62	341	2
121-758A-2H-1,25-27	7.67	435	1.11
121-758A-2-2,1	8.93	536	1.25
121-758A-2-2,11	9.03	543	1.46
121-758A-2-2,21	9.13	554	0.91
121-758A-2-2,61	9.53	582	1.43
121-758A-2-2,71	9.63	588	1.78
121-758A-2-2,101	9.93	608	1.44
121-758A-2-2,111	10.03	617	1.17
121-758A-2-2,121	10.13	626	1.08
121-758A-2-2,131	10.23	637	0.9
121-758A-2-2,141	10.33	649	0.85
121-758A-2-3,1	10.43	659	0.97
121-758A-2-3,11	10.53	668	1.1
121-758A-2-3,21	10.63	676	1.29
121-758A-2-3,91	11.33	716	1.78
121-758A-2-3,101	11.43	721	1.69
121-758A-2-3,121	11.63	736	1.42
121-758A-2-4,11	12.03	770	1.15
121-758A-2-4,21	12.13	778	1.34
121-758A-2-4,91	12.83	817	1.78
121-758A-2-4,101	12.93	823	1.66

121-758A-2-5,11	13.53	866	1.42
121-758A-2-5,21	13.63	873	1.3
121-758A-2-5,41	13.83	891	1.14
121-758A-2-5,51	13.93	899	1.18
121-758A-2-5,81	14.23	920	1.42
121-758A-2-5,101	14.43	937	1.24
121-758A-2-5,111	14.53	945	1.15
121-758A-2-5,121	14.63	952	1.58
121-758A-2-5,131	14.73	957	1.8
121-758A-2-6,111	16.03	1026	1.89
121-758A-2-6,121	16.13	1032	1.75
121-758A-2-7,31	16.73	1074	1.42
121-758A-2-7,41	16.83	1082	1.29
121-758A-2-7,61	17.03	1098	1.22
121-758A-2-7,71	17.13	1104	1.8
121-758B-2-5,21	17.21	1108	1.8
121-758B-2-5,31	17.31	1124	0.63
121-758B-2-5,71	17.71	1158	1.18
121-758A-3-1,141	18.92	1243	1.42
121-758A-3-2,11	19.12	1257	1.42
121-758A-3-2,21	19.22	1264	1.44
121-758A-3-2,91	19.92	1304	1.78
121-758A-3-2,101	20.02	1309	1.75
121-758A-3-3,21	20.72	1359	1.42
121-758A-3-3,31	20.82	1365	1.62
121-758A-3-3,41	20.92	1370	1.81
121-758A-3-4,1	22.02	1429	1.89
121-758A-3-4,11	22.12	1435	1.65
121-758A-3-4,21	22.22	1442	1.42
121-758A-3-4,31	22.32	1448	1.56
121-758A-3-4,61	22.62	1465	1.78
121-758A-3-4,71	22.72	1471	1.53
121-758A-3-4,91	22.92	1489	1.14
121-758A-3-4,101	23.02	1495	1.68

Table B.6 A list of tie points used in the construction of age models for cores NBP9802-04 and NBP9802-06. MS denotes tie points linking magnetic susceptibility records to the record of dust flux to the EPICA Dome C ice core

Core Depth cm NBP9802-06	Tie Point ka	Description
3.5	0.35±0.16	Planktic Radiocarbon UBA-32997
20.5	1.47±0.20	Chase et al 2003 bulk radiocarbon
55.5	3.611±0.26	Chase et al 2003 bulk radiocarbon
109.5	10.35±0.21	Planktic Radiocarbon UBA-32998
140.5	10.40±0.21	Planktic Radiocarbon UBA-32999
173.5	16.3	MS: MIS 2 End
210.5	22.55±0.35	Planktic radiocarbon: average of two dates, UBA-33000 + UBA-33001
219	25.75	MS: Main MIS 2 Peak
260	27.72	MS: Early MIS 2 Minima
282	30.13	MS: Late MIS 3 Peak
358	38.25	MS: Antarctic Warm Period 1 Minima
430.4	42.05	MS: MS Peak 1 (Pugh et al., 2009)
505.4	48.4	MS: MS Peak 2 (Pugh et al., 2009)
586.4	54.0562	MS: Antarctic Warm Period 3 Minima
641.4	56.125	MS: MS Peak 3 (Pugh et al., 2009)
NBP9802-04		
3.5	10.18±0.26	Planktic Radiocarbon UBA-33002
36.2	16.3	MS: MIS 2 End
46.5	26.00±0.34	Planktic Radiocarbon UBA-33005
52.5	26.10±0.35	Planktic Radiocarbon UBA-33006
62.5	26.87±0.49	Planktic Radiocarbon UBA-33007
80.5	32.94±0.94	Planktic Radiocarbon UBA-33008
122.8	62.48	MS: MIS 4 Peak End
146.8	67.91	MS: MIS 4 Peak Beginning
239.2	133.26	MS: MIS 6 Peak End
246.2	143.91	MS: MIS 6 Peak
273.2	154.89	MS: MIS 6 Peak
306.2	175.47	MS: MIS 6 Peak
329	186.64	MS: MIS 6 Peak Beginning
402	264.7	MS: MIS 8 Peak End
415	282.06	MS: MIS 8 First Rise
476	338.75	MS: MIS 10 End
503	355.65	MS: MIS 10 First Peak
566	427.39	MS: MIS 12 End
576	435.1	MS: MIS 12 Main Peak
628	470.67	MS: MIS 12 Beginning
723	539.64	MS: MIS 14 Main Peak

Appendix C

Data Tables

Table C.1 Data from core PC493: stable oxygen and carbon isotopes, inclination of the Characteristic Remanent Magnetization (ChRM), $CaCO_3$ content and total organic carbon.

Depth (cmbsf)	**Age (ka)**	**δ^{18}O *N. pach.* sin. (‰ PDB)**	**δ^{13}C *N. pach.* sin. +1.0 (‰ PDB)**	**δ^{18}O *Cib.* cf. *wuell.* (‰ PDB)**	**δ^{13}C *Cib.* cf. *wuell.* (‰ PDB)**	**ChRM Inclination (°)**	**$CaCO_3$ (wt.%)**	**Total Organic Carbon (wt.%)**
0	0					0.46		
0.5	0.93	3.7	2.33	3.83	0.43			
2	2.8					21.5		
2.5	3.73	4.14	1.78	4.31	0.24		18.5	0.87
3.5	6.53	4.1	1.79	3.91	0.41		20	0.42
4.2	9.33					-49.8		
4.5	11.2	4.1	2.11	4.18	0.41		17.9	0.17
5.5	14.39	4.39	1.89	4.46	-0.01		15.8	0.17
6.5	15.93	4.42	1.64	4.28	0.13		9.8	0.16
6.6	16.31					-58.1		
7.5	17.85	4.52	1.62	4.58	0.21		5	0.13
8.5	19.39	4.57	1.56	4.49	0.2		6.6	0.15
9.2	20.55					-50.9		
9.5	21.32	4.6	1.55	4.07	0.35		10.3	0.15
10.5	22.86	4.55	1.74	4.2	0.48		10.4	0.13
11.1	24.01					-76.5		
11.5	24.78	4.66	1.59	4.41	0.28		7.4	0.13
12.5	26.32	4.69	1.47	4.35	0.42		7.1	0.13

13.5	27.86	4.57	1.54	4.48	0.36		7.2	0.12
13.9	28.64					-75.8		
14.5	29.79	4.59	1.51	4.51	0.38		5.6	0.12
15.5	31.33	4.41	1.64	4.44	0.12		6.1	0.13
16.4	32.87					-85.3		
16.5	33.26	4.44	1.63	4.57	0.36		3.1	0.13
17.5	34.8	4.66	1.63	4.36	0.14		4.5	0.13
18.5	36.34	4.56	1.56	4.25	0.29		2.6	0.13
18.7	36.72					-53.1		
19.5	38.26	4.76	1.35	4.21	0.36		1.6	0.13
20.5	39.8	4.87	1.35	4.11	0.23		2.5	0.14
21	40.57					-27.2		
21.5	41.34	4.79	1.4				2.7	0.14
22.5	42.89	4.66	1.39	4.54	0.31		3.3	0.14
23.5	44.43	4.8	1.42	4.45	0.21	-34.2	2.4	0.13
24.5	45.97	4.98	1.45	4.51	0.45		2	0.14
25.5	47.51	4.8	1.36	4.77	0.19		1.9	0.14
25.9	48.28					21.1		
26.5	49.43	4.72	1.42	4.32	0.29		1.5	0.13
27.5	50.97	4.8	1.35	4.48	0.31		3.2	0.15
28.3	52.51					-15.7		
28.5	52.9	4.67	1.34				4.2	0.13
29.5	54.44	4.66	1.37	4.58	0.14		1	0.11
30.5	55.98	4.79	1.27	4.41	0.32		2.1	0.11
30.8	56.75					-65.8		

31.5	57.91	4.75	1.42	4.28	0.31		2.1	0.13
32.5	59.45	4.77	1.39	4.4	0.43		5	0.14
33	60.22					-36.5		
33.5	60.99	4.64	1.33	4.48	0.23		7.2	0.13
34.5	62.53	4.61	1.29	4.37	0.06		7.5	0.14
35	63.3					-27.3		
35.5	64.07	4.77	1.13	4.41	0.32		8.7	0.14
36.5	65.61	4.67	1.36	4.62	0.26		14.3	0.14
37.5	67.15	4.69	1.3	4.56	0.24		21.3	0.13
38	67.92					-5.9		
38.5	68.69	4.66	1.28	4.7	0.23		21.5	0.14
39.5	70.23	4.78	1.33	4.47	0.26		21.8	0.14
40.1	71.64					-12.9		
40.5	72.93	4.57	1.41	4.49	0.16		18.8	0.12
41.5	75.49	4.55	1.48	4.45	0.31		24.5	0.13
42.5	78.06	4.42	1.41	4.36	0.61		27.4	0.14
42.8	79.35					-2.1		
43.5	81.27	4.52	1.5	4.46	0.39		28.3	0.14
44.5	83.84	4.61	1.21	4.35	0.52		31.7	0.09
45	85.12					-24		
45.5	86.41	4.39	1.52	4.36	0.38		38.4	0.13
46.5	88.98	4.5	1.29	4.15	0.37		33.2	0.13
47.4	91.54					-1.4		
47.5	92.19	4.57	1.34	4.36	0.45		38.4	0.11
48.5	94.75	4.58	1.34	4.29	0.41		47.7	0.11

49.5	97.32	4.39	1.46	4.21	0.35		44.9	0.12
49.7	97.96					2.8		
50.5	100.53	4.33	1.52	4.22	0.57		45.3	0.13
51.5	103.1	4.43	1.51	4.3	0.39		43	0.13
52.1	105.02					27.1		
52.5	106.31	4.31	1.59	3.9	0.5		43.5	0.12
53.5	108.88	4.24	1.66	3.9	0.41		42	0.1
54.4	111.44					4.3		
54.5	112.09	4.26	1.64	4.06	0.49		42.1	0.1
55.5	114.65	4.25	1.47	3.94	0.47		37.3	0.1
56.5	117.22	4.09	1.56	3.86	0.41		34.6	0.09
56.8	118.51					-0.6		
57.5	120.43	4.16	1.52	3.52	0.54		34.4	0.09
58.5	123	4.02	1.68	3.77	0.53		35.8	0.09
59	123.45	4.46	1.45					
59.5	123.9	4.24	1.65	4.02	0.16		19.2	0.09
60.5	124.81	4.22	1.67	3.27	0.52		15.6	0.11
61	125.26					-53.6		
61.5	125.71	4.18	1.72	4.16	0.28		15.8	0.13
62.5	126.61	4.12	1.72	3.9	0.51		9.9	0.11
63.5	127.52	4.5	1.5	4.01	0.39		6.2	0.16
63.6	127.74					-50.6		
64.5	128.65	4.4	1.41	4.05	0.33		6	0.1
65.5	129.55	4.33	1.46	4.12	0.11		7.2	0.1
66.1	130.42					-28.1		

66.5	131.25	4.39	1.38	4.34	0.22		7.6	0.11
67.5	132.92	4.59	1.38	4.55	0.06		5.1	0.11
68.3	134.58					-39.1		
68.5	135	4.43	1.42	4.59	0.22		3.9	0.09
69.5	136.67	4.47	1.27	3.84	0.3		4.4	0.11
70.5	138.33	4.6	1.45	4.35	0.08	-2.1	3.9	0.08
71.5	140	4.99	1.41	4.25	0.25		3.6	0.1
72.5	141.76	4.87	1.21	4.56	0.26		5.3	0.1
73.1	143.08					-44.8		
73.5	143.96	4.7	1.27	4.69	0.12		6.7	0.1
74.5	145.72	4.87	1.3	4.62	0.19		7.3	0.1
75	146.59					-22.8		
75.5	147.47	4.88	1.2	4.7	0.06		6.2	0.11
76.5	149.23	4.58	1.35	4.41	0.12		5.5	0.13
77.5	150.99	4.75	1.14	4.65	0.18	-13.1	6	0.12
78.5	152.75	4.73	1.1	4.46	0.04		7.7	0.12
79.5	154.51	4.6	1.2	4.64	0.14		8.5	0.11
80.1	155.83					-4.9		
80.5	156.71	4.85	1.02	4.56	0.12		8.7	0.1
81.5	158.47	4.85	0.97	4.5	0.03		9.4	0.08
82.5	160.22	4.55	1.29	4.52	0.05	-64.6	10.8	0.09
83.5	161.98	4.86	1.06	4.43	0.08		7.6	0.1
84.5	163.74	4.74	1.09	4.53	0.12		6.4	0.11
84.7	164.18					-53.3		
85.5	165.94	4.73	0.99	4.53	0.03		7.5	0.09

86.5	167.7	4.66	0.98	4.33	0.19		9.3	0.09
87.1	169.02					-57.9		
87.5	169.9	4.78	0.93	4.35	0.26		12.9	0.09
88.5	171.66	4.42	1.1	4.42	0.22		22.6	0.09
89.5	173.41	4.56	1.21	4.4	0.11		25.5	0.11
89.6	173.85					-60.8		
90.5	175.61	4.42	1.29	4.46	0.05		27.4	0.1
91.5	177.37	4.97	1.18	4.36	0.12		28.1	0.08
92	178.25					-33.9		
92.5	179.13	4.92	1.16	4.46	-0.19		30.7	0.09
93.5	180.89	4.5	1.18	4.34	0.07		30.6	0.09
94.5	182.65	4.7	1.11	4.28	0.19	-50.1	39.2	0.08
95.5	184.41	5.01	1.38	4.44	0.02		36.7	0.08
96.5	186.16	4.84	1.02	4.22	0.17		37.6	0.07
96.9	187.04					-57.8		
97.5	188.36	4.46	1.3	4.34	0.06		39.8	0.08
98.5	190.12	4.53	1.14	4.03	0.4		40.3	0.09
99.1	192					-20.7		
99.5	194	4.43	1.29	3.98	0.42		38.4	0.11
100.5	198	4.54	1.09	3.67	0.51		35.4	0.12
101.5	202	4.33	1.42	4.18	0.09	-47.2	35.1	0.08
102.5	206	4.65	1.07	4.27	0.07		31.1	0.07
103.5	210	4.3	1.44	3.89	0.31		29.7	0.07
104.1	213					-43.5		
104.5	215	4.54	1.41	3.81	0.23		29.6	0.07

105.5	219	4.47	1.21	3.86	0.34		29.6	0.08
106.1	222					-29.3		
106.5	224	4.71	1.05	4.32	0.11		28.4	0.08
107.5	228	4.21	1.52	4.27	0.19		30.1	0.08
108.5	232	4.41	1.28	4.15	0.07		31.7	0.08
109.5	236	4.66	1.31	4.16	0.18		32.1	0.07
110.5	240	4.66	1.1	3.93	0.34		32.2	0.08
111.5	246	4.68	1.14	4.06	0.12		24.9	0.08
112.5	252	4.75	1.23	4.25	0.06		9.7	0.06
113.5	261.71	4.65	1.32	4.44	0.12		10	0.07
114.5	271.43	4.65	1.17	4.04	0.24	-72.2	15.5	0.08
115.5	281.14	4.62	1.27	4.09	0.2		23.9	0.09
116.5	287.45	4.43	1.46	4.24	0.19		24.5	0.08
117.1	289.64					-55.6		
117.5	291.09	4.59	1.34	4.39	0.12		30.6	0.08
118.5	294	4.79	1.12	4.01	0.25		36.3	0.08
119.5	295.6	4.69	1.19	4	0.41	-44.4	37.2	0.08
120.5	297.2	4.68	1.23	3.96	0.24		34.5	0.1
121.5	298.8	4.56	1.31	4.16	0.21		37.4	0.06
121.9	299.6					-36.7		
122.5	300.67	4.34	1.47	3.86	0.37		36.9	0.08
123.5	302.02	4.6	0.93	4.08	0.32		36.4	0.08
124.5	303.36	4.45	1.47	4.03	0.06	-74.4	34.1	0.08
125.5	304.71	4.48	0.81	3.96	0.29			
126.5	306.05						29	0.08

127	306.73					-39.9		
127.5	307.4	4.2	1.38	3.81	0.32		22.7	1.18
128.5	308.75	4.67	1.2	4.09	0.26			
129.5	310.09					-9.9	32.9	0.09
130.5	311.44	4.27	1.4	3.89	0.21			
131.5	312.78						26.8	0.07
131.6	313.12					-17.1		
132.5	314.46			4.08	0.18		31.8	0.09
133.5	315.81	4.41	1.05	4.18	0.12		35	0.09
133.9	316.48					-27.7		
134.5	317.49	4.16	1.37	3.42	0.57		40.5	0.07
135.5	318.84	4.17	1.5	3.54	0.32		39	0.07
136.5	320.18	4.35	1.48	3.42	0.13		37.8	0.08
136.6	320.52					-24.4		
137.5	321.86	4.13	1.48	3.5	0.11		36.3	0.08
138.5	323.21	4.35	1.29	3.48	0.28		32.8	0.08
138.9	323.88					-31.9		
139.5	324.89	4.09	1.36	3.26	0.38		26.9	0.07
140.5	326.24	4.25	1.28	3.59	0.19		20.8	0.08
141.5	327.58	4.24	1.25	3.49	0.25	52	18.4	0.08
142.5	328.93	4.21	1.13	3.48	0.12		18.1	0.07
143.5	330.27	4.2	1.37	3.57	0.21		12.5	0.08
144.3	331.62					-18.4		
144.5	331.95	4.23	1.45	4.1	0.09		12.9	0.08
145.5	333.3	4.43	1.16	4.12	0.22		17.1	0.08

146.5	334.65	4.41	1.09	3.96	0.18		13.5	0.07
146.9	335.32					-34.7		
147.5	336.33	4.4	1.1	4.31	-0.11		17.7	0.07
148.5	339.74	4.72	0.96	4.04	0.05		26.5	0.07
149.4	345.22					-2.2		
149.5	346.59	4.83	0.92	3.97	0.07		29.9	0.08
150.5	352.07	4.56	1.2	4.24	-0.1		34.6	0.08
151.5	357.56	4.54	0.97	4.36	-0.14		37.4	0.07
151.8	360.3					-33.6		
152.5	364.41	4.39	1.09	4.3	-0.09		33.4	0.07
153.5	368.52	4.65	0.88	4.26	-0.07		31.5	0.09
153.9	369.89					-36.3		
154.5	371.26	4.65	1.21	4	0.11		29.1	0.08
155.5	372.63	4.69	0.89	4.06	0.08		24.7	0.1
156.4	375.16					-75.5		
156.5	376.33	4.4	1.25	4.08	0.14		27.3	0.07
157.5	380.98	4.46	1.22	3.83	0.31		23.9	0.08
158.5	385.63	4.39	1.43	3.65	0.37		24.9	0.06
158.9	387.95					-70.9		
159.5	391.44	4.38	1.41	3.29	0.75		21.9	0.07
160.5	396.09	4.38	1.25	3.25	0.74		21.1	0.07
161.1	399.58					-83.7		
161.5	401.91	4.17	1.5	3.53	0.55		18.1	0.07
162.5	406.56	4.27	1.52	3.38	0.57		10.8	0.08
163.5	411.21	4.29	1.5	3.26	0.62		11.2	0.09

163.6	412.37					-79.4		
164.5	417.02	4.06	1.51	3.72	0.4		8.5	0.09
165.5	421.67	4.45	1.06	3.95	0.15		7.7	0.08
166.1	424.83					-61.5		
166.5	426.49	4.36	1.25	4.03	0.08		6.1	0.07
167.5	429.82	4.53	1.31	4.08	0.2		3.1	0.07
168.5	433.14	4.71	1.13	4.07	0.24	-73.4	3.9	0.07
169.5	436.46	4.18	1.42	4.12	0.3		3.8	0.07
170.5	439.78	4.47	1.2	4.37	0.08		4.2	0.08
170.8	441.45					-58.8		
171.5	443.94	4.79	0.89	4.51	-0.12		7.2	0.07
172.5	447.26	5	0.85	4.57	0.08		6.5	0.09
173.4	450.58					-82.4		
173.5	451.42	4.6	0.98	4.34	0.14		7	0.08
174.5	454.74	4.68	1.14	4.27	0.26		8.5	0.07
175.5	458.06	4.9	0.96	4.5	0		13.5	0.08
175.6	458.89					-81.4		
176.5	462.22	4.76	0.96	4.3	0.09		16.5	0.07
177.5	465.54	4.82	0.96	4.5	-0.15		20.7	0.08
178.1	468.03					-80.4		
178.5	469.69	4.81	1.01	4.41	0.04		23.5	0.07
179.5	473.02	4.6	1.13	4.62	-0.1		23.2	0.08
180.5	476.34	4.83	0.89	4.37	-0.03	-62.2	25.4	0.07
181.5	480.04	4.57	1.05	4.56	-0.03		24.1	0.08
182.5	484.11	4.68	0.95	4.01	0.35		26.4	0.07

182.7	485.13					-74		
183.5	489.2	4.54	1.12	4.23	0.48		31	0.07
184.5	493.28	4.41	1.47	4.01	0.54		31.3	0.07
185.2	496.33					-67.8		
185.5	498.37	4.51	1.43	4.13	0.23		30.6	0.08
186.5	502.44	4.64	1.01	4.17	0.33		32.5	0.07
187.5	506.52	4.57	1.24	3.97	0.45		30.1	0.08
187.6	507.54					-66.8		
188.5	511.61	4.57	1.47	4.1	0.41		33.6	0.07
189.5	515.69	4.54	1.59	4.23	0.43		35.9	0.08
190	517.72					-58.8		
190.5	519.76			4.13	0.64		37.3	0.06
191.5	523.83	4.4	1.75	4.27	0.69		36.3	0.08
192.4	527.91					-66.1		
192.5	528.93	4.4	1.46	4.08	0.68		35.4	0.07
193.5	533	4.37	1.52	4.29	0.63		38.3	0.08
194.5	547.22	4.53	1.21	4.59	0.32		32.7	0.09
194.7	550.78					-69		
195.5	565	4.44	1.26	3.99	0.45		31.7	0.07
196.5	568.93	4.37	1.42	4.26	0.73		29.1	0.07
196.9	570.89					-75.1		
197.5	573.84	4.36	1.23	4.02	0.54		27.2	0.07
198.5	577.77	4.25	1.52	4.3	0.43		29.1	0.07
199.5	581.7	4.5	1.32	4.01	0.51	-71.2	27	0.07
200.5	585.63	4.39	1.45	4.18	0.3		28	0.08

201.5	589.56	4.29	1.36	4.24	0.54		29.2	0.07
201.9	591.53					-84.5		
202.5	594.47	4.27	1.42	4.19	0.45		29.7	0.08
203.5	598.4	4.17	1.54	4.15	0.43		27.7	0.07
204	600.37					-69.6		
204.5	602.33	4.2	1.29	4.18	0.43		25.6	0.07
205.5	606.26	4.02	1.46	4.17	0.28		23.8	0.07
206.5	610.19	4.26	1.49	4.43	0.32	-63	24.4	0.06
207.5	614.12	4.2	1.42	4.37	0.44		20.9	0.06
208.5	618.05	4.32	1.38	4.42	0.37		20.3	0.06
208.9	620.02					-47		
209.5	621.62	4.47	1.37	4.52	0.34		14.4	0.06
210.5	622.86	4.43	1.41	4.74	0.22		9.9	0.06
211.5	624.11	4.46	1.18	4.48	0.25	-60.9	8.1	0.06
212.5	625.35	4.72	1.21	4.69	0.13		5.5	0.06
213.5	626.59	4.72	1.24	4.67	0.06		6.7	0.07
213.8	627.21					-62.9		
214.5	628.15	4.95	0.99	4.96	-0.01		9.4	0.07
215.5	629.39	5.04	1.02	4.52	0.2		9.9	0.06
216.2	630.32					-87.4		
216.5	630.94	5.09	0.52	4.78	0.22		8.1	0.07
217.5	632.19	4.99	1.02	4.82	0.06		7	0.06
218.5	633.43	5.01	0.96	4.93	0.19	-82.3	8	0.06
219.5	634.67	5.03	0.87	4.6	0.16		11	0.07
220.5	635.92	5.04	0.86	4.75	-0.01		11.6	0.06

220.9	636.54					-68.9		
221.5	637.47	4.98	0.83	4.51	-0.15		5.4	0.06
222.5	638.71	4.85	0.87	4.26	0.26		4.8	0.06
223.5	639.95	5.01	0.8	4.37	0.19		8.8	0.05
224.5	641.2	4.95	0.71	4.23	0.28		8.4	0.06
225.4	642.44					-79		
225.5	642.75	4.97	0.68	4.48	-0.1		9.9	0.05
226.5	643.99	4.93	0.82	4.67	-0.14		9.4	0.05
227.5	645.24	4.88	0.77	4.68	0.04		9.4	0.06
227.8	645.86					-80.6		
228.5	646.79	4.95	0.75	4.73	-0.18		9.9	0.06
229.5	648.03	4.96	0.73	4.64	-0.1		8.9	0.05
230.1	648.97					-85.6		
230.5	649.59	4.84	0.69	4.52	0.08		6.7	0.06
231.5	650.83	4.86	0.77	4.58	-0.23		7.5	0.06
232.4	652.07					-74		
232.5	652.38	4.6	0.87	4.76	-0.32		6	0.05
233.5	653.63	4.81	0.76	4.75	-0.2		4.7	0.05
234.5	654.87	4.81	0.76	4.64	0.03		3.5	0.05
235	655.49					-67.7		
235.5	656.11	4.55	0.95	4.8	-0.01		1.4	0.05
236.5	657.36	4.67	0.79	4.64	-0.19		3.4	0.05
237.1	658.29					-75.7		
237.5	658.91	4.81	0.89	4.74	-0.2		3	0.05
238.5	660.15	4.75	0.65	4.73	-0.44		2.2	0.06

239.4	661.4					-84.1		
239.5	661.71	4.62	0.96	4.31	0.18		1	0.05
240.5	662.95	4.61	0.95	4.96	-0.23		1.4	0.06
241.5	664.19	4.48	1.33				0.7	0.06
241.9	664.81					-75.4		
242.5	665.75	4.53	1.08	4.67	-0.63		2.6	0.06
243.5	666.99	4.73	0.83	4.86	-0.36		1.7	0.05
244.4	668.23					-71.5		
244.5	668.54	4.77	0.73	4.13	0.16		18.1	0.05
245.5	669.79	4.74	0.78	4.23	0.04		24.9	0.06
246.5	671.03	4.71	0.75	4.35	-0.12		31.6	0.06
246.7	671.34					-80.3		
247.5	672.58	4.73	0.87	4.37	0.06		30.8	0.07
248.5	673.82	4.63	0.79	4.44	-0.08		35.6	0.06
249.2	674.76					-84.3		
249.5	675.38	4.67	0.79	4.05	0.13		38.2	0.06
250.5	677.6	4.53	1.02	4.2	0.25		33	0.06
251.5	680.8	4.54	0.95	3.93	0.19		28.4	0.05
251.6	681.6					-82.5		
252.5	684.8	4.54	0.99	4.1	0.22		29.9	0.06
253.5	688	4.44	1.02	4.07	0.23		30.2	0.06
254	689.6					-77.8		
254.5	691.2	4.34	1.01	3.79	0.58		24.8	0.06
255.5	694.4	4.22	1.25	3.87	0.39		25.7	0.06
256.3	696					-53.3		

256.5	696.8	4.25	1.15	3.86	0.5		27.6	0.06
257.5	699.2	4.34	1.3	4.16	0.35		25.7	0.06
258.5	702.4	4.29	1.09	4.15	0.09		23.3	0.05
258.8	704					-10.9		
259.5	706.4	4.47	0.87	4.18	0.27		22.5	0.06
260.5	709.6	4.38	1.08	4.29	0.21		20.6	0.06
260.9	711.2					-18.4		
261.5	714.88	4.56	1.07	4.27	0.03		20.5	0.06
262.5	720.65	4.61	0.9	4.18	0.59		19.3	0.06
263	723.53					-81.8		
263.5	726.41	4.4	1.16	4.33	0.21		22.2	0.06
264.5	732.18	4.43	0.97	4.16	0.14		27.1	0.06
265.5	737.94	4.51	0.9	4.18	0.23		31.4	0.06
265.7	739.38					2.3		
266.5	745.15	4.57	0.97	4.44	0.05		32.4	0.06
267.5	750.91	4.53	0.98	4.35	-0.01		34.7	0.06
268.1	755.24					-28.2		
268.5	758.12	4.65	1	4.3	0.18		32.8	0.05
269.5	761.95	4.48	1.09	4.16	0.31		35.4	0.05
270.4	763.85					-49		
270.5	764.33	4.39	1.19	4.18	0.17		41.2	0.05
271.5	766.23	4.45	1.08	4.23	-0.12		39.7	0.05
272.5	768.13	4.44	1	3.89	0.23		38.5	0.05
272.8	769.08					-69.3		
273.5	770.51	4.61	0.84	3.95	0.11		38.5	0.05

274.5	772.41	4.48	0.91	4.18	0.1		37.3	0.06
275.1	773.84					-49.4		
275.5	774.79	4.65	0.84	4.06	0.07		37.3	0.06
276.5	776.69	4.4	1.12	3.59	0.44		36.4	0.06
277.5	778.59	4.43	1.26	3.82	0.26		34.5	0.05
277.6	779.07					-55.8		
278.5	780.97	4.22	1.33	3.67	0.31		35.4	0.05
279.5	782.87	4.05	1.49	3.69	0.5		32.3	0.06
280	783.82					0		
280.5	784.77	4.04	1.45	3.88	0.09		31.3	0.06
281.5	786.67	4.29	1.28	3.61	0.34		30.8	0.06
282.2	788.1					-26.3		
282.5	789.05	4.42	0.99	3.78	-0.01		27.4	0.05
283.5	791.3	4.42	0.99	4.17	-0.42		27.4	0.05
284.5	793.89	4.39	1.14	4.49	-0.37	50.5	26.4	0.05
285.5	796.49	4.48	0.95	4.22	-0.06		27.7	0.06
286.5	799.08	4.49	0.89	4.44	-0.32		28.6	0.06
287	800.38					54.4		

Table C.2 Details of sediment cores used in Holocene and LGM time slice compilations of *Cibicidoides* $\delta^{13}C_b$ in Figs. 3.8-3.10

Core	Lat. °N	Long. °E	Water Depth m.	Hol. $\delta^{13}C_b$	LGM $\delta^{13}C_b$	Deglacial $\Delta\delta^{13}C_b$	References	Sector
V16-51	-33.5	-17	898	0.61	0.9	-0.29	Lynch-Stieglitz et al., 2006	Atlantic
TN057-20	-42	1	1335	0.58	0.38	0.2	Ninnemann & Charles, 2002	Atlantic
Site 1087	-31.5	15.3	1372	0.45	0.39	0.06	Lynch-Stieglitz et al., 2006	Atlantic
Site 1088	-41.1	13.6	2082	0.55	0.26	0.3	Hodell et al., 2003	Atlantic
MD02-2594	-34.7	17.3	2440	0.74	0.04	0.7	Martínez-Méndez et al., 2009	Atlantic
PS1754-3	-46.8	7.6	2476	0.54	-0.33	0.87	Mackensen et al., 1994	Atlantic
MD96-2080	-36.3	19.5	2488	0.9	0.25	0.65	Rau et al., 2002	Atlantic
Site 704	-46.9	7.4	2543	-	0.2	-	Sarnthein et al., 1994; Hodell et al., 1993	Atlantic
GeoB2004-2	-30.9	14.3	2569	0.79	0.1	0.69	Bickert & Mackensen, 2004; Curry & Lohmann, 1985	Atlantic
MD02 2589	-41.4	25.3	2660	0.5	0	0.5	Molyneux, E.G et al., 2007	Atlantic
RC15-93	-46.1	-13.2	2714	0.29	-0.96	1.25	Charles et al., 1991	Atlantic

GeoB3603-2	-35.1	17.5	2840	0.55	0.05	0.5	Bickert & Mackensen, 2004	Atlantic
AII107-131	-30.9	-38.1	2925	0.95	0.85	0.1	Boyle et al 1992	Atlantic
CHN115-88	-30.9	-36.1	2941	0.68	0.54	0.15	Curry & Lohmann, 1982	Atlantic
PS2564 3	-46.1	35.9	3034	0.49	-0.83	1.32	Mackensen et al 2001	Atlantic
V19-240	-30.6	13.3	3103	0.66	0.05	0.61	Marchitto & Broecker, 2006	Atlantic
PS2495-3	-41.3	-14.5	3134	0.71	-0.67	1.38	Mackensen et al., 2001	Atlantic
CHN115-89	-30.9	-38.2	3152	-	0.41	-	Curry & Lohmann, 1982	Atlantic
PS2499-5	-46.5	-15.3	3175	0.31	-0.82	1.13	Mackensen et al., 2001	Atlantic
GeoB3808-6	-30.8	-14.7	3213	1.01	0.55	0.46	Bickert & Mackensen, 2004	Atlantic
RC12-294	-37.3	-10.1	3308	0.81	-0.23	1.04	Boyle et al 1992	Atlantic
CHN115-90	-30.9	-38.4	3384	-	0.22	-	Curry & Lohmann, 1982	Atlantic
GeoB2016-1	-31.9	-1.3	3385	0.77	0.42	0.35	Bickert & Mackensen, 2004	Atlantic
GeoB2819-1	-30.9	-38.3	3435	-	0.04	-	Bickert & Mackensen, 2004	Atlantic
GeoB1312-2	-31.7	-29.7	3436	-	-0.09	-	Bickert & Mackensen, 2004	Atlantic

CHN115-91	-30.8	-38.4	3576	0.47	0.54	-0.07	Curry & Lohmann, 1982	Atlantic
V34-157	-41.9	26.4	3636	-	-0.18	-	Matsumoto et al., 2001	Atlantic
RC11-80	-46	0	3656	-	-0.04	-	Matsumoto et al. 2001	Atlantic
Site 1090	-42.9	8.9	3699	0.2	-0.48	0.67	Hodell et al., 2003	Atlantic
AII60-13A	-32	-36.7	3739	1.18	-	-	Curry & Lohmann, 1982; Sarnthein et al., 1988	Atlantic
TN057-15	-51.9	4.5	3744	-0.02	-0.81	0.79	Ninnemann & Charles, 2002; Curry & Oppo, 2005	Atlantic
TTN057-6	-42.9	8.6	3751	0.5	-0.44	0.94	Hodell et al., 2003	Atlantic
RC15-94	-43	-20.9	3762	-0.18	-0.78	0.6	Charles & Fairbanks, 1990	Atlantic
MD07-3076	-44.2	-14.2	3770	-0.09	0	-0.09	Waelbroeck et al., 2011	Atlantic
PS2498-1	-44.2	-14.2	3783	0.22	-1.03	1.25	Mackensen et al., 2001	Atlantic
GeoB2019-1	-36.1	-8.8	3825	0.68	0.15	0.53	Bickert & Mackensen, 2004; Curry & Lohmann, 1985	Atlantic
CHN115-92	-30.8	-38.8	3934	-	-0.43	-	Curry & Lohmann, 1982	Atlantic

GeoB1306-1	-35.2	-26.8	4057	-	-0.45	-	Bickert & Mackensen, 2004	Atlantic
V22-108	-43.2	-3.3	4171	0.12	-0.83	0.95	Ninnemann & Charles, 2002; Curry & Oppo, 2005	Atlantic
GeoB3813-3	-32.3	-22	4331	0.55	0.08	0.47	Bickert & Mackensen, 2004	Atlantic
V29-105	-48	18	4350	-	-0.28	-	Matsumoto et al. 2001	Atlantic
PS2561-2	-41.9	28.5	4465	0.2	-0.73	0.93	Krueger et al 2012; Krueger et al 2008	Atlantic
Site 1089	-40.9	9.9	4621	0.27	-0.99	1.25	Hodell et al., 2001	Atlantic
PS2082	-43.2	11.8	4661	0.17	-0.78	0.95	McCorkle & Holder, 2001	Atlantic
RC11-83	-41.6	9.8	4718	0.22	-0.91	1.13	Charles et al., 1996	Atlantic
TN057-21	-41.1	7.8	4981	0.27	-0.83	1.1	Ninnemann & Charles, 2002; Curry & Oppo, 2005	Atlantic
RS67-GC27	-38.7	141.2	506	1.61	1.92	-0.31	Lynch-Stieglitz et al., 1994	Indian
RS102-GC09	-33.5	128	769	1.45	1.73	-0.28	McCorkle et al., 1998	Indian
RS78-GC18	-41.4	144.2	814	1.13	1.2	-0.07	Lynch-Stieglitz et al., 1994	Indian
RS102-GC13	-33.8	130.8	1008	1.11	1.01	0.1	McCorkle et al., 1998	Indian

SO36-SL17	-42.1	144.6	1042	1.03	0.7	0.33	Lynch-Stieglitz et al., 1994	Indian
SO36-SL7	-42.3	144.7	1085	-	0.66	-	Lynch-Stieglitz et al., 1994	Indian
RS102-GC14	-34.4	130.4	1502	0.66	0.43	0.23	McCorkle et al., 1998	Indian
RS102-GC15	-34.6	130.3	2003	0.53	0.31	0.22	McCorkle et al., 1998	Indian
RS102-GC16	-34.8	130.1	2495	0.36	0.11	0.25	McCorkle et al., 1998	Indian
RS102-GC17	-34.9	130.1	3001	0.47	0.11	0.36	McCorkle et al., 1998	Indian
RC11-120	-43.5	79.9	3193	0.43	-0.4	0.83	Curry & Lohmann, 1982	Indian
MD84-527	-43.5	51.2	3262	0.19	-0.38	0.58	Duplessy et al., 1988	Indian
MD972106	-45.2	146.3	3300	0.34	-0.36	0.7	Moy et al 2006	Indian
MD02-2488	-46.5	88	3420	0.1	-	-	Govin et al., 2009	Indian
MD88-769	-46	90	3420	-	-0.71	-	McCorkle et al., 1998	Indian
RS102-GC18	-35	130	3504	0.35	0.07	0.28	McCorkle et al., 1998	Indian
RS147GC34	-45.1	147.7	4001	0.29	-0.43	0.72	Moy et al 2006	Indian
SO136-003	-42	170	958	1.23	0.84	0.39	Ronge 2015 / Thiede, 1999	Pacific
SO213-84-1	-45	174	972	-	0.67	-	Ronge et al 2015	Pacific
MD97-2120	-45.5	174.9	1210	0.98	0.29	0.69	Pahnke & Zahn, 2005	Pacific
MD06-2986	-43	168	1477	0.72	0.23	0.49	Ronge et al 2015	Pacific
GL78-16	-76	-163	1937	1.07	-	-	Matsumoto et al. 2001	Pacific
SO213-82-1	-45	176	2066	0.49	-0.02	0.51	Ronge et al 2015	Pacific
PC493	-71	-120	2077	0.33	0.35	-0.01	This Study	Pacific

NBP9802-04GC1	-64	-170	2688	-	0.07	-	Matsumoto et al., 2001	Pacific
E20-18	-44.3	-111.2	2869	0.46	-0.35	0.81	Matsumoto & Lynch-Steiglitz, 1999	Pacific
E25-10	-50.1	-114.5	2891	0.49	-0.23	0.72	Matsumoto & Lynch-Steiglitz, 1999	Pacific
NBP9802-05GC1	-63	-170	2940	-	0.07	-	Matsumoto et al., 2001	Pacific
RC12-225	-53.4	-123.1	2964	0.46	-0.18	0.64	Matsumoto & Lynch-Steiglitz, 1999	Pacific
MD97-2121	-40.4	178	3014	0.3	-1.09	0.82	McCave et al., 2008	Pacific
E11-2	-56.1	-115.1	3094	0.21	0.09	0.12	Ninneman & Charles, 2002	Pacific
SO213-59-2	-44	-117	3161	-	0.06	-	Molina-Kescher et al 2016	Pacific
NBP9802-03GC1	-66	-170	3232	-	0	-	Matsumoto et al., 2001	Pacific
PS75_056-1	-55	-114	3581	-	-0.43	-	Ullermann et al 2016	Pacific
PS75_059-2	-54	-125	3613	0.12	-0.38	0.5	Ullermann et al 2016	Pacific
NBP9802-07MC2	-60	-170	4005	0.43	-	-	Matsumoto et al., 2001	Pacific
NBP9802-08MC1	-59	-170	4324	0.27	-	-	Matsumoto et al., 2001	Pacific

Table C.3 Authigenic $\varepsilon_{Nd}{}^{leachate}$ measurements made on the sediments of ODP Leg 121 Site 758 as part of this thesis

Sample	Composite Depth m	Age ka	Measured $^{143}\backslash^{144}Nd$	Corrected $^{143}\backslash^{144}Nd$	Internal error	$\varepsilon_{Nd}{}^{leachate}$	External Error	Reported error
U0758A-1H-1, 69.0 cm	0.70	31.2	0.512155	0.512232	0.0000034	-7.92	0.22	0.22
U0758A-1H-1, 96.5 cm	0.97	44.0	0.512146	0.512230	0.0000038	-7.96	0.18	0.18
U0758A-1H-1, 117.0 cm	1.18	53.5	0.512158	0.512199	0.0000067	-8.57	0.24	0.24
U0758A-1H-1, 136.0 cm	1.37	62.3	0.512142	0.512220	0.0000033	-8.16	0.22	0.22
U0758A-1H-3, 80 cm	3.80	190.8	0.512182	0.512189	0.0000071	-8.73	0.22	0.42
U0758A-1H-3, 110.5 cm	4.11	207.1	0.512053	0.512132	0.0000027	-9.88	0.22	0.22
U0758A-1H-4, 31.5 cm	4.82	249.7	0.512092	0.512173	0.0000036	-9.07	0.22	0.22
U0758A-1H-4, 69.5 cm	5.20	269.0	0.512162	0.512238	0.0000057	-7.81	0.28	0.14
U0758A-1H-4, 74 cm	5.23	270.5	0.512198	0.512201	0.0000029	-8.50	0.12	0.12
U0758A-1H-4, 84 cm	5.33	275.6	0.512186	0.512189	0.0000035	-8.73	0.20	0.20
U0758A-1H-4, 95 cm	5.44	281.2	0.512128	0.512133	0.0000049	-9.86	0.36	0.36
U0758A-1H-4, 118 cm	5.67	292.9	0.512142	0.512148	0.0000060	-9.55	0.20	0.84
U0758B-1H-3, 139.5 cm	5.90	304.6	0.512098	0.512101	0.0000029	-10.49	0.20	0.20
U0758B-1H-4, 29.5 cm	6.30	325.0	0.512079	0.512086	0.0000068	-10.80	0.20	0.60
U0758B-1H-4, 59.5 cm	6.60	340.0	0.512185	0.512187	0.0000024	-8.77	0.20	0.20
U0758B-1H-4, 80.5 cm	6.81	358.1	0.512138	0.512141	0.0000034	-9.69	0.26	0.26
U0758B-1H-4, 89.5 cm	6.90	366.2	0.512124	0.512126	0.0000029	-9.98	0.36	0.36
U0758B-1H-4, 112.5 cm	7.13	387.0	0.512126	0.512130	0.0000038	-9.90	0.14	0.14
U0758B-1H-4, 134 cm	7.35	406.8	0.512142	0.512145	0.0000032	-9.62	0.12	0.12
U0758A-2H-1, 1.5 cm	7.42	413.1	0.512137	0.512139	0.0000023	-9.74	0.16	0.16
U0758B-1H-4, 141 cm	7.42	413.1	0.512146	0.512149	0.0000025	-9.54	0.30	0.30

U0758A-2H-1, 9.5 cm	7.52	422.1	0.512089	0.512167	0.0000037	-9.19	0.22	0.22
U0758B-1H-5, 10 cm	7.62	432.0	0.512188	0.512191	0.0000023	-8.70	0.22	0.22
U0758A-2H-1, 47.5 cm	7.93	456.0	0.512110	0.512193	0.0000038	-8.68	0.30	0.30
U0758A-2H-1, 57.5 cm	8.00	461.6	0.512105	0.512193	0.0000034	-8.69	0.22	0.22
U0758A-2H-1, 67.5 cm	8.10	469.6	0.512106	0.512194	0.0000029	-8.66	0.22	0.22
U0758A-2H-1, 70.5 cm	8.13	472.0	0.512100	0.512183	0.0000034	-8.87	0.22	0.22
U0758A-2H-1, 78.5 cm	8.21	478.4	0.512073	0.512153	0.0000030	-9.45	0.22	0.22
U0758A-2H-1, 87.0 cm	8.30	485.2	0.512078	0.512161	0.0000030	-9.31	0.22	0.22
U0758A-2H-1, 97.5 cm	8.40	493.6	0.512067	0.512146	0.0000031	-9.59	0.22	0.22
U0758A-2H-1, 107.5 cm	8.50	501.6	0.512086	0.512163	0.0000034	-9.27	0.22	0.22
U0758A-2H-1, 117.5 cm	8.60	509.6	0.512106	0.512187	0.0000029	-8.81	0.22	0.22
U0758A-2H-1, 127.5 cm	8.70	517.6	0.512099	0.512184	0.0000031	-8.85	0.22	0.22
U0758A-2H-1, 137.5 cm	8.80	525.6	0.512110	0.512200	0.0000037	-8.54	0.22	0.22
U0758A-2H-1, 147.5 cm	8.90	533.6	0.512111	0.512196	0.0000055	-8.62	0.28	0.28
U0758A-2H-2, 7.5 cm	9.00	540.8	0.512129	0.512211	0.0000039	-8.33	0.20	0.20
U0758A-2H-2, 17.0 cm	9.10	550.0	0.512134	0.512216	0.0000057	-8.24	0.32	0.32
U0758A-2H-2, 27.5 cm	9.20	558.8	0.512109	0.512195	0.0000032	-8.64	0.22	0.22
U0758A-2H-2, 37.5 cm	9.30	565.9	0.512127	0.512169	0.0000045	-9.16	0.24	0.24
U0758A-2H-2, 47.5 cm	9.40	572.9	0.512083	0.512162	0.0000034	-9.28	0.22	0.22
U0758A-2H-2, 57.5 cm	9.50	579.8	0.512120	0.512166	0.0000052	-9.21	0.24	0.24
U0758A-2H-2, 67.5 cm	9.60	585.8	0.512087	0.512169	0.0000043	-9.14	0.18	0.18
U0758A-2H-2, 77.5 cm	9.70	592.2	0.512128	0.512168	0.0000047	-9.17	0.24	0.24
U0758A-2H-2, 87.5 cm	9.80	599.2	0.512134	0.512178	0.0000056	-8.97	0.24	0.24
U0758A-2H-2, 96.0 cm	9.89	605.2	0.512084	0.512164	0.0000033	-9.25	0.22	0.22
U0758A-2H-2, 107.5 cm	10.00	614.3	0.512107	0.512187	0.0000036	-8.80	0.22	0.22

U0758A-2H-2, 117.5 cm	10.10	623.3	0.512141	0.512221	0.0000023	-8.14	0.22	0.22
U0758A-2H-2, 127.5 cm	10.20	633.9	0.512149	0.512233	0.0000046	-7.90	0.22	0.22
U0758A-2H-2, 137.5 cm	10.30	645.4	0.512147	0.512231	0.0000062	-7.94	0.32	0.32
U0758A-2H-2, 147.5 cm	10.40	656.2	0.512151	0.512242	0.0000050	-7.73	0.22	0.22
U0758A-2H-3, 7.5 cm	10.50	665.6	0.512142	0.512233	0.0000073	-7.91	0.36	0.36
U0758A-2H-3, 17.5 cm	10.60	673.8	0.512188	0.512259	0.0000057	-7.39	0.32	0.32
U0758A-2H-3, 27.5 cm	10.70	680.0	0.512137	0.512213	0.0000057	-8.28	0.32	0.32
U0758A-2H-3, 49.0 cm	10.92	692.1	0.512162	0.512206	0.0000074	-8.43	0.38	0.38
U0758A-2H-3, 58.5 cm	11.01	697.5	0.512136	0.512205	0.0000057	-8.44	0.32	0.32
U0758A-2H-3, 67.5 cm	11.10	702.6	0.512063	0.512148	0.0000087	-9.57	0.38	0.38
U0758A-2H-3, 76.0 cm	11.19	707.3	0.512084	0.512160	0.0000045	-9.33	0.20	0.20
U0758A-2H-3, 87.5 cm	11.30	713.8	0.512137	0.512212	0.0000020	-8.31	0.08	0.08
U0758A-2H-3, 97.5 cm	11.40	719.6	0.512143	0.512218	0.0000047	-8.20	0.20	0.20
U0758A-2H-3, 107.5 cm	11.50	726.4	0.512123	0.512198	0.0000039	-8.58	0.18	0.18
U0758A-2H-3, 119.0 cm	11.62	734.4	0.512113	0.512191	0.0000047	-8.72	0.24	0.24
U0758A-2H-3, 127.5 cm	11.70	741.4	0.512146	0.512192	0.0000044	-8.70	0.24	0.24
U0758A-2H-3, 137.5 cm	11.80	750.1	0.512122	0.512206	0.0000036	-8.43	0.20	0.20
U0758A-2H-3, 147.5 cm	11.90	758.9	0.512099	0.512182	0.0000041	-8.90	0.18	0.18
U0758A-2H-4, 7.5 cm	12.00	767.7	0.512085	0.512165	0.0000037	-9.22	0.22	0.22
U0758A-2H-4, 17.5 cm	12.10	775.6	0.512121	0.512169	0.0000051	-9.14	0.24	0.24
U0758A-2H-4, 27.5 cm	12.20	781.8	0.512091	0.512170	0.0000031	-9.14	0.22	0.22
U0758A-2H-4, 47.5 cm	12.40	793.0	0.512126	0.512199	0.0000040	-8.56	0.22	0.22
U0758A-2H-4, 57.5 cm	12.50	798.6	0.512131	0.512208	0.0000039	-8.39	0.22	0.22
U0758A-2H-4, 67.5 cm	12.60	804.3	0.512158	0.512222	0.0000055	-8.11	0.28	0.28
U0758A-2H-4, 77.5 cm	12.70	809.9	0.512143	0.512211	0.0000047	-8.33	0.26	0.26

U0758A-2H-4, 87.5 cm	12.80	815.5	0.512108	0.512176	0.0000062	-9.00	0.30	0.30
U0758A-2H-4, 87.5 cm	12.80	815.5	0.512100	0.512182	0.0000065	-8.90	0.32	0.32
U0758A-2H-4, 97.5 cm	12.90	821.5	0.512091	0.512159	0.0000056	-9.35	0.28	0.28
U0758A-2H-4, 107.5 cm	13.00	828.2	0.512109	0.512177	0.0000052	-9.00	0.28	0.28
U0758A-2H-4, 117.5 cm	13.10	835.2	0.512139	0.512208	0.0000049	-8.39	0.26	0.26
U0758A-2H-4, 137.5 cm	13.30	849.3	0.512097	0.512166	0.0000048	-9.20	0.26	0.26
U0758A-2H-4, 137.5 cm	13.30	849.3	0.512087	0.512163	0.0000055	-9.26	0.28	0.28
U0758A-2H-4, 147.5 cm	13.40	856.4	0.512099	0.512168	0.0000056	-9.17	0.28	0.28
U0758A-2H-4, 147.5 cm	13.40	856.4	0.512085	0.512162	0.0000046	-9.29	0.26	0.26
U0758A-2H-5, 7.5 cm	13.50	863.4	0.512122	0.512202	0.0000037	-8.50	0.20	0.20
U0758A-2H-5, 16.0 cm	13.59	869.7	0.512157	0.512237	0.0000034	-7.83	0.20	0.20
U0758A-2H-5, 27.5 cm	13.70	879.3	0.512144	0.512228	0.0000028	-7.99	0.20	0.20
U0758A-2H-5, 37.5 cm	13.80	888.1	0.512142	0.512226	0.0000025	-8.04	0.20	0.20
U0758A-2H-5, 47.5 cm	13.90	896.7	0.512137	0.512225	0.0000028	-8.05	0.20	0.20
U0758A-2H-5, 67.5 cm	14.10	911.3	0.512110	0.512198	0.0000024	-8.57	0.20	0.20
U0758A-2H-5, 77.5 cm	14.20	918.3	0.512132	0.512214	0.0000032	-8.26	0.20	0.20
U0758A-2H-5, 87.5 cm	14.30	925.5	0.512135	0.512217	0.0000038	-8.21	0.20	0.20
U0758A-2H-5, 97.5 cm	14.40	933.9	0.512105	0.512184	0.0000049	-8.86	0.20	0.20
U0758A-2H-5, 106.5 cm	14.49	941.8	0.512086	0.512164	0.0000019	-9.24	0.20	0.20
U0758A-2H-5, 118.0 cm	14.61	950.0	0.512096	0.512174	0.0000040	-9.05	0.20	0.20
U0758A-2H-5, 128.0 cm	14.71	955.8	0.512085	0.512167	0.0000034	-9.20	0.20	0.20
U0758A-2H-5, 137.5 cm	14.80	960.9	0.512102	0.512183	0.0000023	-8.88	0.20	0.20
U0758A-2H-6, 7.5 cm	15.00	971.4	0.512093	0.512175	0.0000022	-9.04	0.20	0.20
U0758A-2H-6, 17.5 cm	15.10	976.7	0.512107	0.512183	0.0000052	-8.89	0.22	0.22
U0758A-2H-6, 27.5 cm	15.20	982.0	0.512092	0.512182	0.0000042	-8.90	0.18	0.18

U0758A-2H-6, 37.5 cm	15.30	987.3	0.512095	0.512177	0.0000041	-8.99	0.18	0.18
U0758A-2H-6, 46.5 cm	15.39	992.0	0.512092	0.512165	0.0000034	-9.23	0.20	0.20
U0758A-2H-6, 57.5 cm	15.50	997.8	0.512101	0.512177	0.0000050	-8.99	0.22	0.22
U0758A-2H-6, 67.5 cm	15.60	1003.1	0.512105	0.512181	0.0000059	-8.92	0.24	0.24
U0758A-2H-6, 77.5 cm	15.70	1008.4	0.512141	0.512181	0.0000044	-8.91	0.24	0.24
U0758A-2H-6, 87.5 cm	15.80	1013.7	0.512116	0.512188	0.0000051	-8.78	0.24	0.24
U0758A-2H-6, 97.5 cm	15.90	1018.9	0.512087	0.512165	0.0000034	-9.22	0.20	0.20
U0758A-2H-6, 107.5 cm	16.00	1024.3	0.512092	0.512172	0.0000039	-9.09	0.18	0.18
U0758A-2H-6, 117.5 cm	16.10	1029.9	0.512099	0.512185	0.0000042	-8.83	0.20	0.20
U0758A-2H-6, 127.5 cm	16.20	1036.6	0.512122	0.512168	0.0000036	-9.17	0.24	0.24
U0758A-2H-6, 137.5 cm	16.30	1043.6	0.512085	0.512150	0.0000039	-9.51	0.32	0.32
U0758A-2H-6, 147.5 cm	16.40	1050.7	0.512121	0.512187	0.0000030	-8.80	0.32	0.32
U0758A-2H-7, 7.5 cm	16.50	1057.7	0.512118	0.512188	0.0000033	-8.78	0.32	0.32
U0758A-2H-7, 17.5 cm	16.60	1064.8	0.512094	0.512165	0.0000031	-9.23	0.32	0.32
U0758A-2H-7, 27.5 cm	16.70	1071.8	0.512079	0.512150	0.0000035	-9.52	0.32	0.32
U0758A-2H-7, 36.5 cm	16.79	1078.5	0.512090	0.512178	0.0000035	-8.98	0.18	0.18
U0758A-2H-7, 47.5 cm	16.90	1087.8	0.512089	0.512177	0.0000033	-9.00	0.18	0.18
U0758A-2H-7, 57.5 cm	17.00	1095.7	0.512103	0.512173	0.0000036	-9.08	0.32	0.32
U0758A-2H-7, 67.5 cm	17.10	1101.9	0.512121	0.512197	0.0000034	-8.59	0.16	0.16
U0758A-2H-7, 74.0 cm	17.17	1105.5	0.512099	0.512168	0.0000034	-9.17	0.32	0.32
U0758B-2H-5, 29.5 cm	17.30	1122.3	0.512120	0.512163	0.0000056	-9.27	0.24	0.24
U0758B-2H-5, 39.5 cm	17.40	1131.8	0.512201	0.512204	0.0000035	-8.43	0.20	0.20
U0758B-2H-5, 49.5 cm	17.50	1140.6	0.512195	0.512199	0.0000033	-8.54	0.20	0.20
U0758B-2H-5, 58.0 cm	17.59	1148.1	0.512118	0.512195	0.0000026	-8.65	0.14	0.14
U0758B-2H-5, 68.5 cm	17.69	1156.4	0.512115	0.512185	0.0000041	-8.84	0.32	0.32

U0758A-3H-1, 28.5 cm	17.80	1164.2	0.512081	0.512150	0.0000038	-9.52	0.32	0.32
U0758A-3H-1, 38.5 cm	17.90	1171.3	0.512121	0.512163	0.0000059	-9.27	0.24	0.24
U0758A-3H-1, 48.5 cm	18.00	1178.3	0.512098	0.512167	0.0000038	-9.19	0.32	0.32
U0758A-3H-1, 58.5 cm	18.10	1185.3	0.512088	0.512168	0.0000038	-9.17	0.32	0.32
U0758A-3H-1, 68.5 cm	18.20	1192.4	0.512098	0.512178	0.0000031	-8.98	0.32	0.32
U0758A-3H-1, 78.5 cm	18.30	1199.4	0.512103	0.512189	0.0000039	-8.75	0.32	0.32
U0758A-3H-1, 88.5 cm	18.40	1206.5	0.512122	0.512203	0.0000038	-8.48	0.32	0.32
U0758A-3H-1, 98.5 cm	18.50	1213.5	0.512116	0.512197	0.0000032	-8.60	0.32	0.32
U0758A-3H-1, 108.5 cm	18.60	1220.5	0.512102	0.512184	0.0000032	-8.85	0.32	0.32
U0758A-3H-1, 118.5 cm	18.70	1227.6	0.512073	0.512156	0.0000039	-9.40	0.32	0.32
U0758A-3H-1, 128.5 cm	18.80	1234.6	0.512077	0.512162	0.0000033	-9.28	0.32	0.32
U0758A-3H-1, 138.5 cm	18.90	1241.7	0.512103	0.512188	0.0000036	-8.77	0.32	0.32
U0758A-3H-1, 147.5 cm	18.99	1248.0	0.512125	0.512208	0.0000031	-8.39	0.32	0.32
U0758A-3H-2, 8.5 cm	19.10	1255.7	0.512162	0.512222	0.0000033	-8.11	0.16	0.16
U0758A-3H-2, 18.5 cm	19.20	1262.7	0.512164	0.512219	0.0000043	-8.18	0.24	0.24
U0758A-3H-2, 28.5 cm	19.30	1268.6	0.512143	0.512198	0.0000039	-8.59	0.16	0.16
U0758A-3H-2, 38.5 cm	19.40	1274.2	0.512107	0.512194	0.0000067	-8.66	0.32	0.32
U0758A-3H-2, 58.5 cm	19.60	1285.5	0.512133	0.512187	0.0000028	-8.79	0.16	0.16
U0758A-3H-2, 68.5 cm	19.70	1291.1	0.512135	0.512221	0.0000043	-8.13	0.20	0.20
U0758A-3H-2, 78.5 cm	19.80	1296.8	0.512134	0.512215	0.0000025	-8.26	0.20	0.20
U0758A-3H-2, 88.5 cm	19.90	1302.4	0.512147	0.512208	0.0000027	-8.39	0.18	0.18
U0758A-3H-2, 98.5 cm	20.00	1308.1	0.512115	0.512176	0.0000030	-9.00	0.18	0.18
U0758A-3H-2, 108.5 cm	20.10	1314.9	0.512094	0.512154	0.0000037	-9.44	0.18	0.18
U0758A-3H-2, 138.5 cm	20.40	1336.0	0.512146	0.512206	0.0000031	-8.44	0.18	0.18
U0758A-3H-2, 148.0 cm	20.50	1342.7	0.512140	0.512205	0.0000023	-8.45	0.18	0.18

U0758A-3H-3, 8.5 cm	20.60	1350.1	0.512141	0.512185	0.0000044	-8.84	0.24	0.24
U0758A-3H-3, 18.5 cm	20.70	1357.1	0.512094	0.512180	0.0000041	-8.94	0.18	0.18
U0758A-3H-3, 28.5 cm	20.80	1363.5	0.512087	0.512155	0.0000066	-9.42	0.36	0.36
U0758A-3H-3, 38.5 cm	20.90	1369.1	0.512082	0.512163	0.0000042	-9.27	0.36	0.36
U0758A-3H-3, 38.5 cm	20.90	1369.1	0.512084	0.512164	0.0000038	-9.25	0.43	0.43
U0758A-3H-3, 48.5 cm	21.00	1374.5	0.512097	0.512176	0.0000036	-9.01	0.24	0.24
U0758A-3H-3, 68.5 cm	21.20	1385.0	0.512122	0.512164	0.0000048	-9.25	0.24	0.24
U0758A-3H-3, 78.5 cm	21.30	1390.3	0.512100	0.512165	0.0000053	-9.23	0.24	0.24
U0758A-3H-3, 88.5 cm	21.40	1395.6	0.512081	0.512148	0.0000101	-9.56	0.36	0.36
U0758A-3H-3, 98.5 cm	21.50	1400.9	0.512132	0.512176	0.0000051	-9.01	0.24	0.24
U0758A-3H-3, 109.5 cm	21.61	1406.7	0.512106	0.512189	0.0000036	-8.76	0.18	0.18
U0758A-3H-3, 118.5 cm	21.70	1411.4	0.512147	0.512193	0.0000053	-8.67	0.24	0.24
U0758A-3H-3, 128.5 cm	21.80	1416.7	0.512118	0.512194	0.0000035	-8.65	0.24	0.24
U0758A-3H-3, 137.5 cm	21.89	1421.5	0.512148	0.512193	0.0000029	-8.69	0.24	0.24
U0758A-3H-3, 147.5 cm	21.99	1426.9	0.512101	0.512188	0.0000046	-8.77	0.18	0.18
U0758A-3H-4, 8.5 cm	22.10	1433.4	0.512077	0.512163	0.0000036	-9.27	0.24	0.24
U0758A-3H-4, 18.5 cm	22.20	1440.2	0.512080	0.512155	0.0000063	-9.42	0.32	0.32
U0758A-3H-4, 28.5 cm	22.30	1446.8	0.512128	0.512174	0.0000057	-9.05	0.24	0.24
U0758A-3H-4, 38.5 cm	22.40	1452.6	0.512121	0.512205	0.0000041	-8.45	0.24	0.24
U0758A-3H-4, 47.0 cm	22.49	1457.3	0.512134	0.512206	0.0000059	-8.42	0.32	0.32
U0758A-3H-4, 58.5 cm	22.60	1463.8	0.512131	0.512212	0.0000027	-8.32	0.22	0.22
U0758A-3H-4, 78.5 cm	22.80	1478.5	0.512093	0.512172	0.0000062	-9.08	0.24	0.24
U0758A-3H-4, 88.5 cm	22.90	1487.3	0.512116	0.512161	0.0000015	-9.31	0.24	0.24
U0758A-3H-4, 98.5 cm	23.00	1493.8	0.512090	0.512172	0.0000035	-9.08	0.18	0.18
U0758A-3H-4, 108.5 cm	23.10	1499.5	0.512111	0.512189	0.0000036	-8.77	0.22	0.22

Table C.4 Authigenic $\varepsilon_{Nd}^{leachate}$ measurements made on the sediments of NBP9802-04PC1

Depth min. cm	**Depth max. cm**	**Measured ^{143}\$^{144}$Nd**	**Corrected ^{143}\$^{144}$Nd**	**Internal error**	**$\varepsilon_{Nd}^{leachate}$**	**External Error**	**Reported error**
1	6	0.512246	0.512284	0.0000026	-6.91	0.09	0.13
6.5	9.5	0.512247	0.512316	0.0000039	-6.27	0.14	0.21
13.5	16.5	0.512252	0.512321	0.0000038	-6.18	0.14	0.21
29	32	0.512263	0.512332	0.0000020	-5.98	0.14	0.14
42	45	0.512297	0.512369	0.0000023	-5.25	0.14	0.14
45	48	0.512314	0.512386	0.0000021	-4.93	0.14	0.14
51	54	0.512287	0.512359	0.0000029	-5.45	0.14	0.14
61	64	0.512334	0.512405	0.0000033	-4.54	0.14	0.14
71	74	0.512357	0.512428	0.0000028	-4.09	0.14	0.14
79	82	0.512378	0.512449	0.0000019	-3.69	0.14	0.14
89	92	0.512412	0.512482	0.0000030	-3.04	0.14	0.14
100	105	0.512460	0.512497	0.0000028	-2.75	0.09	0.14
111	114	0.512438	0.512509	0.0000022	-2.52	0.14	0.14
126	129	0.512439	0.512510	0.0000029	-2.51	0.14	0.14
140	143	0.512412	0.512483	0.0000029	-3.02	0.14	0.14
154	157	0.512396	0.512467	0.0000018	-3.33	0.14	0.14
169	172	0.512388	0.512460	0.0000022	-3.48	0.14	0.14
184	187	0.512375	0.512442	0.0000022	-3.82	0.14	0.14
194	197	0.512381	0.512449	0.0000016	-3.69	0.14	0.14
200	205	0.512404	0.512441	0.0000033	-3.84	0.09	0.15
212	215	0.512375	0.512443	0.0000039	-3.81	0.14	0.21

218.5	221.5	0.512309	0.512347	0.0000017	-5.68	0.09	0.09
226	229	0.512366	0.512427	0.0000027	-4.12	0.07	0.12
238	241	0.512375	0.512436	0.0000027	-3.93	0.07	0.13
245	248	0.512393	0.512455	0.0000030	-3.58	0.07	0.14
255	258	0.512387	0.512448	0.0000039	-3.71	0.07	0.16
269	272	0.512398	0.512459	0.0000022	-3.49	0.07	0.11
283	286	0.512396	0.512457	0.0000035	-3.53	0.07	0.15
293	296	0.512381	0.512444	0.0000028	-3.79	0.07	0.13
312	315	0.512325	0.512388	0.0000027	-4.88	0.07	0.12
326	329	0.512329	0.512391	0.0000027	-4.82	0.07	0.13
335	338	0.512336	0.512391	0.0000026	-4.81	0.12	0.12
345	348	0.512372	0.512408	0.0000035	-4.49	0.09	0.16
355	358	0.512395	0.512431	0.0000023	-4.04	0.09	0.13
369	372	0.512353	0.512409	0.0000026	-4.48	0.12	0.12
379	382	0.512386	0.512442	0.0000031	-3.83	0.12	0.17
388	391	0.512392	0.512448	0.0000022	-3.70	0.12	0.12
399	402	0.512412	0.512469	0.0000035	-3.31	0.12	0.18
408	411	0.512409	0.512466	0.0000024	-3.36	0.12	0.12
419	422	0.512419	0.512478	0.0000029	-3.13	0.12	0.12
428	431	0.512372	0.512431	0.0000032	-4.03	0.12	0.17
434	437	0.512371	0.512407	0.0000037	-4.51	0.09	0.17
446	449	0.512365	0.512400	0.0000026	-4.64	0.09	0.13
456	459	0.512371	0.512407	0.0000029	-4.52	0.09	0.14
467	470	0.512380	0.512416	0.0000034	-4.33	0.09	0.16
479	482	0.512404	0.512440	0.0000031	-3.87	0.09	0.15

490	493	0.512368	0.512404	0.0000027	-4.57	0.09	0.14
502	505	0.512359	0.512395	0.0000030	-4.75	0.09	0.14
510	513	0.512370	0.512406	0.0000024	-4.52	0.09	0.13
520	523	0.512366	0.512404	0.0000026	-4.56	0.09	0.13
529	532	0.512358	0.512397	0.0000040	-4.71	0.09	0.18

Table C.5 ε_{Nd}^{foram} measurements made on NBP9802-04PC1

Depth min. cm	**Depth max. cm**	**Measured $^{143}\backslash^{144}$Nd**	**Corrected $^{143}\backslash^{144}$Nd**	**Internal error**	**$\varepsilon_{Nd}^{leachate}$**	**External Error**	**Reported error**
1	6	0.512237	0.512291	0.0000057	-6.78	0.12	0.26
22.5	27.5	0.512273	0.512327	0.0000060	-6.03	0.12	0.27
35	40	0.512295	0.512350	0.0000027	-5.61	0.14	0.14
42	45	0.512242	0.512329	0.0000055	-6.02	0.12	0.25
45	48	0.512344	0.512404	0.0000036	-4.57	0.14	0.27
51	54	0.512283	0.512369	0.0000043	-5.28	0.14	0.22
61	64	0.512347	0.512407	0.0000040	-4.52	0.12	0.20
71	74	0.512369	0.512455	0.0000026	-3.61	0.17	0.17
79	82	0.512400	0.512444	0.0000029	-3.78	0.17	0.17
100	105	0.512389	0.512457	0.0000030	-3.55	0.17	0.17
300	305	0.512350	0.512414	0.0000053	-4.37	0.12	0.24
312	315	0.512332	0.512393	0.0000021	-4.75	0.14	0.14
326	329	0.512333	0.512394	0.0000106	-4.76	0.14	0.44
335	338	0.512292	0.512373	0.0000059	-5.19	0.14	0.27

Table C.6 $\varepsilon_{Nd}^{detrital}$ measurements made on the sediments of NBP9802-04PC1

Depth min. cm	Depth max. cm	Measured $^{143}\backslash^{144}Nd$	Corrected $^{143}\backslash^{144}Nd$	Internal error	$\varepsilon_{Nd}^{leachate}$	External Error	Reported error
1	6	0.512396	0.512396	0.0000034	-4.72	0.20	0.20
61	64	0.512453	0.512453	0.0000037	-3.60	0.20	0.20
226	229	0.512456	0.512456	0.0000041	-3.54	0.20	0.20
226	229	0.512450	0.512450	0.0000058	-3.67	0.18	0.29

Table C.7 Authigenic $\varepsilon_{Nd}^{leachate}$ measurements made on the sediments of NBP9802-06PC1

Depth min. cm	Depth max. cm	Measured $^{143}\backslash^{144}Nd$	Corrected $^{143}\backslash^{144}Nd$	Internal error	$\varepsilon_{Nd}^{leachate}$	External Error	Reported error
1	6	0.512167	0.512115	0.0000017	-8.44	0.10	0.10
18.5	21.5	0.512170	0.512115	0.0000018	-8.38	0.10	0.10
38.5	41.5	0.512174	0.512115	0.0000018	-8.30	0.10	0.10
53.5	56.5	0.512179	0.512115	0.0000016	-8.20	0.10	0.10
61.5	64.5	0.512191	0.512115	0.0000019	-7.97	0.10	0.10
70	75	0.512222	0.512115	0.0000015	-7.36	0.10	0.10
85.5	88.5	0.512242	0.512115	0.0000018	-6.97	0.10	0.10
98.5	101.5	0.512259	0.512115	0.0000046	-6.69	0.15	0.23
108.5	111.5	0.512248	0.512115	0.0000015	-6.86	0.10	0.10
118.5	121.5	0.512307	0.512115	0.0000026	-5.75	0.15	0.15
125	130	0.512234	0.512115	0.0000020	-7.11	0.10	0.10
138.5	142.5	0.512238	0.512115	0.0000019	-7.02	0.10	0.10

148.5	153.5	0.512253	0.512115	0.0000038	-6.80	0.15	0.15
158.5	163.5	0.512321	0.512115	0.0000019	-5.40	0.10	0.10
168.5	171.5	0.512335	0.512115	0.0000031	-5.30	0.15	0.15
178.5	181.5	0.512352	0.512115	0.0000020	-4.80	0.10	0.10
188.5	191.5	0.512377	0.512115	0.0000023	-4.30	0.10	0.10
198.5	201.5	0.512351	0.512115	0.0000023	-4.81	0.10	0.10
205	210	0.512332	0.512115	0.0000022	-5.17	0.10	0.10
211.5	214.5	0.512325	0.512115	0.0000016	-5.39	0.10	0.10
218.5	221.5	0.512309	0.512115	0.0000017	-5.68	0.09	0.09
238.5	241.5	0.512327	0.512115	0.0000031	-5.47	0.15	0.15
248.5	251.5	0.512321	0.512115	0.0000034	-5.58	0.15	0.15
264.5	267.5	0.512329	0.512115	0.0000034	-5.34	0.15	0.15
278.5	281.5	0.512311	0.512115	0.0000019	-5.78	0.15	0.15
300	305	0.512322	0.512115	0.0000013	-5.37	0.10	0.10
300	305	0.512321	0.512115	0.0000019	-5.45	0.09	0.09
318.5	321.5	0.512344	0.512115	0.0000047	-5.12	0.15	0.24
333.5	336.5	0.512373	0.512115	0.0000018	-4.46	0.10	0.10
344.5	347.5	0.512378	0.512115	0.0000027	-4.46	0.15	0.15
356.5	359.5	0.512377	0.512115	0.0000023	-4.38	0.10	0.10
383.5	386.5	0.512393	0.512115	0.0000033	-4.09	0.15	0.15
398.5	401.5	0.512397	0.512115	0.0000020	-4.08	0.15	0.15
418.5	421.5	0.512382	0.512115	0.0000061	-4.31	0.15	0.28
439.5	442.5	0.512393	0.512115	0.0000032	-4.15	0.15	0.15
448.5	451.5	0.512381	0.512115	0.0000062	-4.33	0.15	0.29
458.5	461.5	0.512402	0.512115	0.0000020	-3.99	0.15	0.15

474.5	477.5	0.512402	0.512115	0.0000067	-3.86	0.15	0.30
485.5	488.5	0.512425	0.512115	0.0000016	-3.54	0.15	0.15
503.5	506.5	0.512439	0.512115	0.0000034	-3.13	0.15	0.15
516.5	519.5	0.512447	0.512115	0.0000028	-3.02	0.09	0.14
524.5	527.5	0.512437	0.512115	0.0000031	-3.18	0.15	0.15
527.5	530.5	0.512433	0.512115	0.0000031	-3.25	0.15	0.15
577.5	580.5	0.512438	0.512115	0.0000033	-3.19	0.15	0.15
612.5	615.5	0.512400	0.512115	0.0000030	-3.93	0.09	0.14
638.5	641.5	0.512372	0.512115	0.0000031	-4.47	0.09	0.15

Table C.8 Authigenic ε_{Nd}^{foram} measurements made on NBP9802-06PC1

Depth min. cm	**Depth max. cm**	**Measured $^{143}\backslash^{144}$Nd**	**Corrected $^{143}\backslash^{144}$Nd**	**Internal error**	**$\varepsilon_{Nd}^{leachate}$**	**External Error**	**Reported error**
1	6	0.512257	0.512202	0.0000053	-8.50	0.16	0.26
18.5	21.5	0.512306	0.512220	0.0000026	-8.16	0.17	0.17
38.5	41.5	0.512291	0.512211	0.0000036	-8.34	0.15	0.15
53.5	56.5	0.512287	0.512225	0.0000038	-8.07	0.15	0.15
61.5	64.5	0.512303	0.512242	0.0000042	-7.74	0.15	0.22
125	130	0.512317	0.512257	0.0000033	-7.44	0.16	0.16
205	210	0.512429	0.512369	0.0000028	-5.29	0.16	0.16

Table C.9 Authigenic $\varepsilon_{Nd}^{detrital}$ measurements made on the sediments of NBP9802-06PC1

Depth min. cm	**Depth max. cm**	**Measured $^{143}\backslash^{144}$Nd**	**Corrected $^{143}\backslash^{144}$Nd**	**Internal error**	**$\varepsilon_{Nd}^{leachate}$**	**External Error**	**Reported error**
1	6	0.512237	0.512316	0.0000141	-6.29	0.42	0.69
108.5	111.5	0.512342	0.512406	0.0000129	-4.52	0.25	0.56
138.5	142.5	0.512349	0.512439	0.0000032	-3.89	0.20	0.20
188.5	191.5	0.512336	0.512426	0.0000029	-4.13	0.20	0.20
248.5	251.5	0.512290	0.512377	0.0000033	-5.09	0.20	0.20
344.5	347.5	0.512397	0.512477	0.0000195	-3.15	0.22	0.79
439.5	442.5	0.512331	0.512406	0.0000109	-4.53	0.11	0.44
524.5	527.5	0.512371	0.512460	0.0000052	-3.48	0.20	0.28
612.5	615.5	0.512203	0.512294	0.0000078	-6.71	0.18	0.35

Table C.10 Values used for PAAS-normalisation of REE concentrations. From Pourmand et al. (2012)

Element	**Concentration**
La	44.56
Ce	88.25
Pr	10.15
Nd	37.32
Sm	6.884
Eu	1.215
Gd	6.043
Tb	0.8914
Dy	5.325
Ho	1.053
Er	3.075
Tm	0.451
Yb	3.012
Lu	0.4386

Table C.11 PAAS-normalised $REE^{leachate}$ data from core NBP9802-04PC1

Depth Min. cm	Depth Max. cm	Sediment Age	Age ±	Y ppm	La ppm	Ce ppm	Pr ppm	Nd ppm	Sm [ppm]	Eu ppm	Gd ppm	Tb ppm	Dy ppm	Ho ppm	Er ppm	Tm ppm	Yb ppm	Lu ppm
1	6	10.24	0.46	8.3	7.3	15.2	1.8	7.3	1.6	0.4	1.7	0.2	1.4	0.3	0.7	0.1	0.6	0.1
6.5	9.5	11.07	0.28	13.2	11	38.9	3.6	13.8	3.1	0.6	2.7	0.4	2.3	0.4	1	0.1	0.8	0.1
13.5	16.5	12.37	0.28	11.9	6.4	19.3	1.9	7.9	1.7	0.4	1.6	0.3	1.4	0.3	0.7	0.1	0.6	0.1
29	32	15.24	0.28	9	4.4	12.8	0.9	3.9	0.9	0.2	1.1	0.2	1.1	0.2	0.6	0.1	0.6	0.1
42	45	23.38	0.92	19.4	11.4	30.6	3.2	12.8	2.8	0.6	2.6	0.4	2.4	0.4	1.2	0.2	1	0.1
45	48	26.01	0.92	16.9	10.1	30.3	2.7	11.1	2.4	0.5	2.2	0.4	1.9	0.3	0.9	0.1	0.8	0.1
51	54	26.13	0.44	16.9	9.1	22.5	3	12.6	2.9	0.6	2.8	0.4	2.2	0.4	1.1	0.1	0.9	0.1
61	64	27.03	0.69	19	8.1	22	2.9	12.6	3	0.7	2.9	0.4	2.4	0.4	1.1	0.2	1	0.1
71	74	30.29	0.88	18.3	6.2	24.3	2	8.3	2	0.4	1.8	0.3	1.6	0.3	0.8	0.1	0.7	0.1
79	82	32.84	0.88	13.8	16.9	51.7	5.2	21	4.8	1	4.5	0.7	3.9	0.7	1.9	0.3	1.7	0.2
89	92	39.76	0.88	7.6	14.2	31.5	4.2	16.4	3.5	0.7	3.2	0.5	2.7	0.5	1.2	0.2	1	0.1
100	105	48.2	1.46	8	5.5	14.4	1.7	6.8	1.5	0.3	1.4	0.2	1.1	0.2	0.5	0.1	0.4	0.1
111	114	55.23	0.88	5.9	3.1	6.1	1	4.2	1	0.2	1	0.1	0.8	0.1	0.4	0.1	0.3	0
126	129	63.55	0.34	7	3.3	6	1	4.2	1	0.2	0.9	0.1	0.8	0.1	0.4	0.1	0.3	0
140	143	66.71	0.34	8.8	3.9	9.2	1.2	4.9	1.1	0.2	1	0.2	0.8	0.1	0.4	0.1	0.3	0
154	157	74.03	1.05	3.8	4.5	10.9	1.4	5.8	1.3	0.3	1.3	0.2	1.1	0.2	0.5	0.1	0.5	0.1
169	172	84.57	1.05	2.7	37.3	68.2	9.5	39	8.5	1.9	8.6	1.4	7.6	1.5	4	0.6	3.5	0.5
184	187	95.11	1.05	2.8	3.3	6	1	4.2	1	0.2	0.9	0.1	0.8	0.1	0.4	0.1	0.3	0
194	197	102.55	1.05	2.9	11.2	38.8	3.5	13.8	3	0.6	2.6	0.4	2.2	0.4	1	0.1	0.8	0.1
200	205	107.47	1.76	5.2	8.5	23.5	3	12	2.7	0.5	2.4	0.4	1.8	0.3	0.8	0.1	0.7	0.1

212	215	115.2	1.05	4	10	30.9	3.5	14.1	3.2	0.6	2.8	0.4	2.2	0.4	1	0.1	0.8	0.1
226	229	125.04	1.05	7.5	7.7	16.6	2.5	10.1	2.3	0.5	2.2	0.3	1.9	0.4	1	0.1	0.8	0.1
238	241	133.72	1.79	2.2	3.7	9.4	1.2	5	1.1	0.2	0.9	0.1	0.7	0.1	0.3	0	0.2	0
245	248	144.03	1.28	4	3.7	9.4	1.2	5	1.1	0.2	0.9	0.1	0.7	0.1	0.3	0	0.2	0
255	258	148.1	0.61	6.6	4.5	12.7	1.5	6.4	1.5	0.3	1.4	0.2	1.2	0.2	0.5	0.1	0.5	0.1
269	272	153.79	0.61	9.4	6.9	19.1	2.3	9.5	2.2	0.5	2	0.3	1.7	0.3	0.8	0.1	0.7	0.1
283	286	161.94	0.94	8.6	8.1	21.2	2.3	9.4	2.2	0.5	2.2	0.4	2.1	0.4	1.1	0.2	1	0.2
293	296	168.17	0.94	20.2	6.9	23.9	2.2	9.3	2.3	0.5	2.2	0.3	1.9	0.4	1	0.1	0.9	0.1
312	315	179.11	0.78	34.5	16.9	37.3	5.2	21.3	5.1	1.1	5.1	0.8	4.5	0.9	2.3	0.3	2	0.3
326	329	185.91	0.73	11.8	13.8	31	4.1	17.1	3.8	0.9	3.9	0.6	3.2	0.6	1.5	0.2	1.3	0.2
335	338	194.66	1.6	10	8	18.2	2.1	8.8	1.9	0.4	1.9	0.3	1.7	0.3	0.9	0.1	0.8	0.1
345	348	205.35	1.6	5.2	18.5	46.8	4.9	20.5	4.5	1	4.4	0.7	3.8	0.7	1.9	0.3	1.6	0.2
369	372	231.02	1.6	7.3	13.9	44.6	3.9	16.2	3.7	0.8	3.6	0.6	3.2	0.6	1.7	0.2	1.4	0.2
388	391	251.33	1.6	8.5	15.2	27.9	4	16.7	3.6	0.8	3.6	0.5	3	0.6	1.6	0.2	1.3	0.2
399	402	263.1	1.6	9.3	18.4	44.4	5.3	22.2	5.1	1.1	4.9	0.8	4.3	0.8	2.1	0.3	1.7	0.3
408	411	274.72	2	7.4	6.2	24.3	2	8.3	2	0.4	1.8	0.3	1.6	0.3	0.8	0.1	0.7	0.1
419	422	287.09	1.37	7.4	18.6	46	5.6	22	4.9	1	4.5	0.7	3.7	0.7	1.7	0.2	1.5	0.2
428	431	295.32	1.37	16.7	18.8	41.6	5.7	23.7	5.5	1.2	5.4	0.8	4.7	0.9	2.2	0.3	1.9	0.3

Table C.12 PAAS-normalised $REE^{leachate}$ data from core NBP9802-04PC1

Depth Min. cm	Depth Max. cm	Sediment Age	Age ±	Y ppm	La ppm	Ce ppm	Pr ppm	Nd ppm	Sm [ppm]	Eu ppm	Gd ppm	Tb ppm	Dy ppm	Ho ppm	Er ppm	Tm ppm	Yb ppm	Lu ppm
1	6	0.38	0.16	8.5	7	9.2	1.7	7.1	1.5	0.4	1.6	0.2	1.4	0.3	0.7	0.1	0.6	0.1
18.5	21.5	1.37	0.1	8.4	5.9	6	1.4	6.3	1.4	0.3	1.5	0.2	1.3	0.3	0.7	0.1	0.6	0.1
38.5	41.5	2.61	0.09	7.1	5.2	6.1	1.2	5.2	1.1	0.3	1.2	0.2	1	0.2	0.6	0.1	0.5	0.1
53.5	56.5	3.53	0.09	5.9	4.2	6.4	1	4.3	0.9	0.2	1	0.1	0.9	0.2	0.5	0.1	0.5	0.1
61.5	64.5	4.41	0.18	5.5	4.1	6.8	1	4.3	0.9	0.2	1	0.1	0.9	0.2	0.5	0.1	0.4	0.1
70	75	5.55	0.3	6	5.1	11.1	1.3	5.4	1.2	0.3	1.2	0.2	1.1	0.2	0.6	0.1	0.6	0.1
85.5	88.5	7.29	0.18	4.6	3.9	9.1	1	4.3	0.9	0.2	0.9	0.1	0.8	0.2	0.5	0.1	0.4	0.1
98.5	101.5	9.07	0.18	5.7	4.9	11.9	1.3	5.2	1.1	0.3	1.1	0.2	1	0.2	0.6	0.1	0.5	0.1
108.5	111.5	10.28	0.13	5.2	3.8	7.8	0.9	3.8	0.8	0.2	0.9	0.1	0.8	0.2	0.5	0.1	0.5	0.1
118.5	121.5	10.37321	0	7.6	5.8	12.4	1.4	5.7	1.2	0.3	1.3	0.2	1.2	0.2	0.7	0.1	0.7	0.1
125	130	10.39	0.01	10.3	8.4	17.4	1.9	8	1.7	0.4	1.7	0.3	1.6	0.3	1	0.1	0.9	0.1
138.5	142.5	10.43	0.08	5.5	2.9	4.5	0.6	2.8	0.6	0.2	0.7	0.1	0.7	0.2	0.5	0.1	0.5	0.1
148.5	153.5	12.1	0.44	3.6	2.9	8.7	0.7	3	0.7	0.1	0.7	0.1	0.6	0.1	0.4	0.1	0.4	0.1
158.5	163.5	13.88	0.44	5.1	4	12.2	1.1	4.5	1	0.2	1	0.2	0.9	0.2	0.5	0.1	0.5	0.1
168.5	171.5	15.48	0.27	5.1	4.5	13.6	1.2	4.8	1	0.2	1.1	0.2	1	0.2	0.6	0.1	0.5	0.1
178.5	181.5	17.21	0.25	4.9	3.6	14.9	1	4.4	1	0.2	1	0.2	1	0.2	0.5	0.1	0.5	0.1
188.5	191.5	18.9	0.25	12.8	11.4	47.6	3.6	14.9	3.5	0.7	3.2	0.5	2.7	0.5	1.3	0.2	1.1	0.2
198.5	201.5	20.59	0.25	15.2	12.2	30.7	3.8	16	3.9	0.9	3.7	0.6	3	0.6	1.5	0.2	1.3	0.2
205	210	21.86	0.42	21.2	22.1	73.7	6.3	26.3	5.8	1.3	5.5	0.8	4.3	0.8	2.1	0.3	1.7	0.3
211.5	214.5	23.26	0.63	30.6	26	59.5	7.2	30	6.7	1.5	6.7	1	5.6	1.1	2.9	0.4	2.5	0.4

218.5	221.5	25.75	0.3	24	22.9	56	6.3	25.9	5.8	1.3	5.7	0.9	4.9	0.9	2.5	0.4	2.2	0.3
238.5	241.5	26.71	0.07	14.1	10.9	49.5	3.3	14.4	3.4	0.8	3.2	0.5	2.8	0.5	1.5	0.2	1.3	0.2
264.5	267.5	28.27	0.16	14.4	14.3	48.6	3.9	16.5	3.9	0.8	3.8	0.6	3.1	0.6	1.6	0.2	1.4	0.2
300	305	32.21	0.27	16.8	18.5	47.9	5.2	21.1	4.7	1	4.6	0.7	3.7	0.7	1.9	0.3	1.7	0.2
333.5	336.5	35.68	0.16	7.7	7.1	18.5	2	7.7	1.7	0.4	1.7	0.3	1.5	0.3	0.8	0.1	0.7	0.1
356.5	359.5	38.14	0.16	4.3	3.8	9.3	1	4.1	0.9	0.2	0.9	0.1	0.8	0.2	0.4	0.1	0.4	0.1
383.5	386.5	39.63	0.08	5.5	4.4	10.9	1.2	5	1.1	0.2	1.1	0.2	1	0.2	0.6	0.1	0.5	0.1
398.5	401.5	40.42	0.08	7.4	5.6	16.5	1.6	6.7	1.5	0.3	1.5	0.2	1.4	0.3	0.8	0.1	0.7	0.1
418.5	421.5	41.46	0.08	9.7	9.3	31.9	2.9	12.1	2.7	0.6	2.5	0.4	2.2	0.4	1.1	0.2	1	0.2
439.5	442.5	42.86	0.13	4.1	4.3	13.8	1.1	4.7	1	0.2	1	0.1	0.8	0.2	0.5	0.1	0.4	0.1
448.5	451.5	43.62	0.13	4.5	4.9	14.6	1.3	5.4	1.2	0.2	1.1	0.2	0.9	0.2	0.5	0.1	0.5	0.1
474.5	477.5	45.83	0.13	2.7	1.9	8.1	0.5	2.3	0.5	0.1	0.5	0.1	0.5	0.1	0.3	0	0.2	0
485.5	488.5	46.76	0.13	3.3	2.9	10.7	0.9	3.5	0.8	0.2	0.7	0.1	0.6	0.1	0.4	0.1	0.3	0
503.5	506.5	48.28	0.13	3.4	4.6	11.9	1	4	0.9	0.2	0.8	0.1	0.7	0.1	0.4	0.1	0.3	0.1
516.5	519.5	49.21	0.1	2.3	2.5	6.8	0.6	2.3	0.5	0.1	0.5	0.1	0.4	0.1	0.2	0	0.2	0
524.5	527.5	49.77	0.1	2.8	2.7	8.3	0.7	2.8	0.6	0.1	0.6	0.1	0.5	0.1	0.3	0	0.3	0
527.5	530.5	49.98	0.1	3.9	3.7	10.7	1	3.9	0.8	0.2	0.8	0.1	0.7	0.1	0.4	0.1	0.4	0.1
577.5	580.5	53.47	0.1	4.6	3.7	9.6	1	4.2	0.9	0.2	0.9	0.1	0.8	0.2	0.5	0.1	0.4	0.1
612.5	615.5	55.06	0.06	4.6	4	10.8	1.1	4.4	1	0.2	1	0.2	0.9	0.2	0.5	0.1	0.4	0.1
638.5	641.5	56.03	0.06	7.6	6.3	19.3	1.8	7.7	1.7	0.4	1.8	0.3	1.6	0.3	0.8	0.1	0.7	0.1